INTERNATIONAL ATOMIC ENERGY AGENCY

INDC(BLR)-015
Distr. J+TU/EL

I N D C INTERNATIONAL NUCLEAR DATA COMMITTEE

Neutron Data Evaluation of ^{232}U

V.M. Maslov[1], Yu.V. Porodzinskij[1], N.A. Tetereva[1]
A.B. Kagalenko[1*], N.V. Kornilov[1*]
M. Baba[2], A. Hasegawa[3]

[1]) Joint Institute of Nuclear and Energy Research – SOSNY
220109, Minsk-Sosny, Belarus
[2]) Cyclotron and Radioisotope Center, Tohoku University,
Sendai, Japan
[3]) Department of Nuclear Energy System, Tokai Research
Establishment, Japan Atomic Energy Research Institute,
Tokai-mura, Naka-gun, Ibaraki-ken

*) Permanent address: Institute of Physics and Power Engineering,
249020, Obninsk, Russia

March 2003

IAEA NUCLEAR DATA SECTION, WAGRAMER STRASSE 5, A-1400 VIENNA

Documents in the EL series are available in only limited quantities in hardcopy form. They may be downloaded in electronic form from http://www-nds.iaea.or.at/indc_sel.html or sent as an e-mail attachment. Requests for hardcopy or e-mail transmittal should be directed to services@iaeand.iaea.org or to:

Nuclear Data Section
International Atomic Energy Agency
PO Box 100
Wagramer Strasse 5
A-1400 Vienna
Austria

Produced by the IAEA in Austria
March 2003

INDC(BLR)-015
Distr. J+TU/EL

Neutron Data Evaluation of ^{232}U

V.M. Maslov[1], Yu.V. Porodzinskij[1], N.A. Tetereva[1]
A.B. Kagalenko[1*], N.V. Kornilov[1*]
M. Baba[2], A. Hasegawa[3]

[1]) Joint Institute of Nuclear and Energy Research – SOSNY
220109, Minsk-Sosny, Belarus
[2]) Cyclotron and Radioisotope Center, Tohoku University,
Sendai, Japan
[3]) Department of Nuclear Energy System, Tokai Research
Establishment, Japan Atomic Energy Research Institute,
Tokai-mura, Naka-gun, Ibaraki-ken

*) Permanent address: Institute of Physics and Power Engineering,
249020, Obninsk, Russia

Abstract

Consistent evaluation of ^{232}U measured data base is performed. Hauser-Feshbach-Moldauer theory, coupled channel model and double-humped fission barrier model are employed. Total, differential scattering, fission and (n,*x*n) data are consistently reproduced as a major constraint for inelastic scattering cross section estimate. The direct excitation of ground state and higher band levels is calculated within rigid rotator and soft (deformable) rotator model, respectively. Prompt fission neutron spectra data are described. Average resonance parameters are provided, which reproduce evaluated cross sections in the range of 10-150 keV.

This work is performed under the Project Agreement B-404 with the International Science and Technology Center (Moscow). The Financing Party for the Project is Japan.

March 2003

Contents

1 Introduction

Uranium-232 has a half-life of 69.9 years. It can be produced in uranium- and uranium-thorium-fueled nuclear reactors by high-energy neutrons in (n,xn) reactions and in capture reactions after subsequent $\alpha-$ and β-decay of residual nuclei. Uranium-232 is a very hazardous waste itself due to hard γ-emission of its α- and β- decay products. High α-activity of the ^{232}U sample has hindered extensive measurements of its neutron-induced reaction cross sections. Only one total cross section measurement [1] and a few fission cross sections measurements exist, which are rather discrepant with each other. Brief survey of the fission data available [2, 3, 4, 5] reveals rather peculiar feature in the neutron-induced fission cross section of ^{232}U target nuclide. It undergoes a substantial thermal neutron fission and exhibits a non-threshold behavior at low incident neutron energies in contrast with the other even-even U isotopes. Since only one spin state is excited by neutrons with incident energies up to $\sim$200 eV, a Reich-Moore resonance parameters, fitting total and fission data, could be provided. As was demonstrate earlier [6], this behavior could be interpreted within a statistical model, employed recently for the description of the neutron-induced fission cross sections of actinide nuclei [7]. It turns out that fission data analysis maintains almost the only constraint for ^{232}U capture, neutron elastic and inelastic scattering and other cross section evaluation. This approach was validated recently in case of simultaneous ^{238}U neutron data description [8].

2 Resolved resonance energy range

Here we will briefly review the status of resolved neutron resonance parameters of ^{232}U and provide a cross section parameterization of total, capture, elastic and inelastic scattering cross sections in unresolved resonance energy range.

Resolved resonance region of ENDF/B-VI [9] data file extends up to 53 eV. Resolved resonance parameters are adopted from BNL-325 [10], however resolved resonance parameters are assumed to be single level Breit-Wigner parameters, instead of Reich-Moore. Thermal capture and fission cross sections are equal to 72.7 barns and 77.2 barns and are compatible with BNL-325 estimates (73.1 $\pm$1.5 barns and 75.2 $\pm$4.7 barns, respectively).

Region of resolved resonances in JENDL-3.2 [11] extends up 200 eV. Parameters recommended in BNL-325 [10] also were adopted as a multilevel Breit-Wigner parameters, discrepancies of calculated and measured fission data in the valleys between resonances were compensated by adding background cross section. Smooth cross section energy region starts at 200 eV.

Recently new data file became available [12], which accepted basically BNL-325 [10] Reich-Moore parameters up to 194 eV. Initially two Reich-Moore parameter sets were available: the first one up to ∼28 eV [1] and the second one up to ∼80 eV [2]. Main conclusion of these parameterization attempts is the inadequacy of single fission channel Reich-Moore formalism for total and fission data fitting. Mughabghab et al. [10] proposed a two fission channel Reich-Moore parameter set to fit measured data up to 200 eV (see Table 1). We will compare present and Wright et al. [12] calculated total and fission cross sections with measured data taking into account only a temperature broadening for T=300°K.

Figures 1-12 demonstrate a comparison of calculated total and fission cross sections with measured data. We demonstrate how Reich-Moore parameter set, corresponding to two fission channels, proposed by Mughabghab et al. [10], could be modified to improve total and fission data fit (see Table 1). Cross sections calculated with one fission channel Reich-Moore parameter set by Auchampaugh et al. [2] are also included. Total cross section data description at thermal point of 0.00253 eV and below first resonance is shown on Fig. 1. Total, fission and capture thermal cross sections [1, 13, 14] were fitted with negative resonance parameters after obtaining proper description of total data by Simpson et al. [1] and first fission resonance data by Auchampaugh et al. [2] (see Fig. 6). At higher incident neutron energies measured total (see Figs. 2, 3 and 4) and fission (see Figs. 7, 8, 9, 11 and 12) data description much depends on the fission resonance interference. Basically resonance parameters recommended in BNL-325 [10] might be accepted, though much improved fission data description in the valleys between resonances might be obtained changing the character of interference between resonances, i.e. the signs of fission resonance widths. Valley between first and second positive resonances is somewhat overestimated using the fission width signs recommended in BNL-325 [10]. However, the next valley, that between second and third positive resonances is severely underestimated with recommended set of resonance parameters of BNL-325 [10]. Including instrumental resolution one would not change the fission data fit with BNL-325 [10] resonance parameters essentially. Actually, poor fit of the fission data between these 12.67 and 20.85 resonances, instrumental resolution included, was one of the main reasons to conclude that fission data by Auchampaugh et al. [2] cannot be fitted with one channel Reich-Moore formula. Nonetheless, we see that two fission channel parameter set of BNL-325 [10] leads to the more poor total (see Fig. 3) and fission (see Fig. 8) data fit. One could take advantage of two-fission channel Reich-Moore formalism to improve the fission data description between resonances starting from the second positive 12.7-eV resonance. Changing the sign of fission width of the third, 20.8-eV resonance, gives a constructive interference with the preceding 12.7-eV resonance and improves the description of the valley between these resonances. To improve the description of the valley between next two strong resonances of 27.6-eV and 34.2-eV, the interference of 34.2-eV resonance with 29.65-eV resonance of large fission width, should be con-

structive. The latter resonance was introduced by Auchampaugh et al. [2] to fit the asymmetric right shoulder of 27.60-eV resonance. For this the only option is changing the sign of 34.2-eV resonance. Then this 34.2-eV resonance would interfere constructively with the 40-eV resonance having large fission width, since they would have different signs. However, to make these changes we should first check what happens with higher energy resonances. The survey of the energy region between 43.13-eV and 74.4-eV resonances shows that the fission data [2] description also could be much improved (see Fig. 9), the total data description also would be improved (see Fig. 4). To get a fair description of the valley between 52.48-eV and 74.4-eV resonances, the interference of strong 74.4-eV resonance with 52.48-eV resonance should be constructive. For this we have changed the sign of fission width of 52.48-eVresonance from negative to positive. To get fair description of the valley between 43.3-eV and 52.48-eV resonances we have changed to opposite the signs of 40-, 43.13-, 47.61- and 52.48-eV resonances (see Fig. 9), total data description also improved (see Fig. 4). In case of resonance parameters of BNL-325 [10], strong 74.4-eV resonance interferes destructively with 52.48-eV resonance, producing a strong dip at the left shoulder of the 52.48-eV resonance, but constructively with neighboring 72.35-eV resonance. In other words, constructive interference of 74.4-eV resonance both with 52.48-eV and 72.35-eV resonances much improves the data fit in the respective valleys. Figure 11 shows what would happen in case of changing the sign of 74.4-eV resonance in the present combination shown in Table 1, so that it would interfere destructively with both preceding 72.35-eV and 52.48-eV resonances.

Returning to the valley between 34.2-eV and strong 43.13-eV resonances (see Fig. 12) we see that the interference of 34.2-eV and 40-eV resonances, after changing the signs of 40-, 43.13-, 47.61- and 52.48-eV resonances, is again destructive, since they both have negative signs of fission widths. One should avoid changing the sign of 40-eV resonance without changing the sign of 43.13-eV resonance to keep interference unaffected. We suppose that the sign of 43.13-eV resonance fission width is fixed by fitting the higher resonance valleys. Changing the sign of 40-eV resonance would improve the data description at the right slope of the 34.2-eV resonance, but would produce a strong dip at the left shoulder of 43.13-eV resonance (see Fig. 12). To compensate this deficiency, we would add another 35-eV weak resonance with comparatively large fission width. Being assigned a positive sign it would interfere constructively both with 34.2- and 40-eV resonances. Adding a resonance with relatively small neutron and large fission width is a routine procedure in fitting resonance shapes, to compensate similar data fitting deficiencies, 24.75-eV and 29.65-eV resonances were added by Auchampaugh et al. [2], we further decreased the neutron width value of the 29.65-eV resonance.

Table 1

Resonance parameters

N	E_0	Γ_n	Γ_{f1}	Γ_{f2}	Γ_n,[10]	Γ_{f1},[10]	Γ_{f2},[10]
1	-0.06	1.28E-4	-0.05965	0.00	1.28E-4	-.0311	0.00
2	5.980	1.5E0-3	0.0250	0.00	1.5E0-3	0.025	0.00
3	12.70	7.00E-3	0.00	0.264	7.00E-3	0.00	0.264
4	20.80	1.90E-3	0.00	-0.50	1.90E-3	0.00	0.50
5	23.75	5.50E-3	-0.08	0.00	5.50E-3	-.08	0.00
6	24.75	5.00E-4	1.15	0.00	5.00E-4	1.15	0.00
7	27.60	2.40E-3	-0.15	0.00	2.40E-3	-0.15	0.00
8	29.65	2.50E-4	0.90	0.00	8.50E-4	0.90	0.00
9	34.20	5.90E-4	-0.36	0.00	5.90E-4	0.36	0.00
10	35.00	2.50E-4	0.675	0.00	2.50E-4	-	-
11	40.00	2.50E-4	-2.60	0.00	2.50E-4	2.60	0.00
12	43.13	7.90E-3	0.178	0.00	7.90E-3	-0.178	0.00
13	47.61	1.06E-3	-0.34	0.00	1.06E-3	0.34	0.00
14	52.48	2.00E-3	0.284	0.00	2.00E-3	-0.284	0.00
15	72.35	3.70E-4	0.938	0.05	3.70E-4	0.938	0.05
16	74.40	2.13E-2	-0.518	0.05	2.13E-2	-0.518	0.05
17	81.50	2.70E-5	0.00	0.05	2.70E-5	0.00	0.05
18	82.10	6.30E-6	-0.8	0.00	6.30E-6	-0.8	0.00
19	90.65	1.40E-5	-0.10	0.00	1.40E-5	-0.10	0.00
20	91.85	2.50E-5	-0.05	0.00	2.50E-5	-0.05	0.00
21	102.9	2.40E-3	-0.15	0.04	2.40E-3	-0.15	0.04
22	106.3	7.00E-3	-0.15	-0.015	7.00E-3	-0.15	-0.015
23	107.3	3.60E-3	-0.10	0.00	3.60E-3	-0.1	0.00
24	112.8	3.80E-3	0.028	0.128	3.80E-3	0.028	0.128
25	118.0	1.90E-5	0.00	0.10	1.90E-5	0.00	0.1
26	124.4	2.60E-3	-0.05	0.015	2.60E-3	-0.05	0.015

Table 1 (continued)

N	E_0	Γ_n	Γ_{f1}	Γ_{f2}	Γ_n,[10]	Γ_{f1},[10]	Γ_{f2},[10]
27	128.2	2.15E-2	-0.40	0.00	2.15E-2	-0.40	0.00
28	131.5	1.90E-3	-0.20	-0.05	1.90E-3	-0.20	-0.05
29	141.7	2.24E-2	-0.35	0.05	2.24E-2	-0.35	0.05
30	149.4	2.20E-3	-0.10	-0.20	2.20E-3	-0.10	-0.20
31	155.3	1.06E-2	-0.975	0.025	1.06E-2	-0.975	0.025
32	156.7	1.75E-3	0.00	0.084	1.75E-3	0.00	0.084
33	160.0	6.30E-6	0.00	0.20	6.30E-6	0.00	0.20
34	163.6	2.90E-4	0.75	0.05	2.90E-4	0.75	0.05
35	165.6	2.20E-4	1.90	-0.10	2.20E-4	1.90	-0.10
36	168.0	7.80E-5	0.125	0.025	7.80E-5	0.125	0.025
37	174.1	5.50E-3	-1.47	0.025	5.50E-3	-1.47	0.025
38	185.6	2.53E-2	-0.95	-0.05	2.53E-2	-0.95	-0.05
39	188.0	2.40E-3	-0.025	0.15	2.40E-3	-0.025	0.15
40	197.3	1.00E-3	0.30	0.20	1.00E-3	0.30	0.20
41	202.0	2.03E-3	-0.85	0.05	2.03E-3	-0.85	0.05
42	206.5	4.20E-4	-1.45	0.05	4.20E-4	-1.45	0.05
43	210.5	1.50E-4	-1.50	0.00	1.50E-4	-1.50	0.00
44	213.2	6.90E-3	0.475	0.025	6.90E-3	0.475	0.025

Capture and fission resonance integrals are compared with measured data in Table 2. Present and evaluated by Wright et al. [12] capture and fission thermal cross sections are compatible with measured data. Total resonance integral is compatible with data measured by Simpson et al. [1], while the measured capture resonance integral value by Halperin et al. [14] seems to be overestimated. In summary, present Reich-Moore resonance parameter set (see Table 1) provides a reasonable description of total and fission data up to 200 eV.

The resonance parameters accepted in data file of ^{232}U, might provide a test of neutron width and spacing distributions. We performed a resonance parameter analysis based on maximum likelihood estimates both of mean level spacing $\langle D_{l=0}\rangle$ and neutron strength function S_o [16]. Cumulative sum of $s-$resonances up to 200 eV is shown on Fig. 13, it seems resonance missing starts above $\sim$50 eV. Proper account of missing of levels based on analysis of level spacing distribution and neutron width distribution gives estimate of average $s-$wave neutron resonance spacing as 4.717 eV.

Cumulative sum of reduced neutron widths of $s-$resonances Γ_n^o is described with strength function estimate of S_o =1.17$\times 10^{-4}$ (see Fig. 14). The resolution function parameters as well as $\langle\Gamma_n^o\rangle$ and $\langle D_{l=0}\rangle$ are obtained by maximum likelihood method when comparing experimental distributions of reduced neutron width and resonance spacing with Porter-Thomas and Wigner distributions, modified for the resonance missing. The latter distributions will be called expected distributions. Figures 15 and 16 demonstrate the comparison of predicted

level spacing $D_{l=0}$ and reduced neutron width Γ_n^o distributions with present resonance parameter set. Quantiles on Fig. 15 show five equal probability intervals ($P(x \leq x_{0.2}) = \int p(x)dx$ =0.2) for level spacing distribution of $s-$wave resonances $D_{l=0}$. Expected distribution, which takes into account missing of weak resonances and unresolved doublets, is not much different from Wigner distribution. This conclusion is supported by the reduced neutron width distribution. Quantiles on Fig. 16 show five equal probability ($P(x \leq x_{0.2} = \int p(x)dx$ =0.2) intervals for Γ_n^o distribution. Figure 17 shows a comparison of cumulative Porter-Thomas distribution of reduced neutron widths.

Table 2

Thermal cross sections and resonance integrals

N	Reaction	σ^{th}	RI	σ^{th}	RI	σ^{th}	RI
		Present		Wright et al. [12]			
1	Total	163.45	-	162.77	-	168±17 [1]	
2	Elastic	10.37	-	10.79	-		
3	Fission	77.61	370.18	76.76	383.53	81±15[13]	
4	Capture	75.47	184.44	75.21	181.22	78±4 [14]	280±15 [14]

3 Unresolved resonance region

The unresolved resonance energy region of ENDF/B-VI [9] extends from 53 eV up to 1 keV. Provided are energy independent average resonance parameters $\langle D_{l=0} \rangle$ =4.2528 eV, $\langle \Gamma_n^{0,1/2} \rangle$ =5.463400$\times 10^{-4}$ (eV)$^{-1/2}$, $\langle \Gamma_\gamma \rangle$ = 0.045 eV, $\langle \Gamma_f \rangle$ = 0.6 eV for $s-$wave. In JENDL-3.2 [11] unresolved resonance region is missing. In evaluated data file by Wright et al. [12] energy independent average resonance parameters for $s-$wave resonances are provided from 194 eV up to 2 keV.

The assumed lower energy of unresolved resonance energy region in present evaluation is the end-point of resolved resonance region, i.e. 200 eV, the upper energy is 150 keV, the same as in our recent evaluations of ^{238}U and ^{232}Th [8]. We suppose $s-$, $p-$ and $d-$wave neutron-nucleus interactions to be effective.

3.1 Average resonance parameters

Average resonance parameters $S_o = 1.17 \pm 0.08 \times 10^{-4}$, $\langle D_{l=0} \rangle$= 4.717 eV, $\langle \Gamma_\gamma \rangle$ =40 meV are applied for the cross section calculation from 0.2 keV up to 150 keV.

3.1.1 Neutron resonance spacing

Neutron resonance spacing $\langle D_J \rangle$ was calculated with the phenomenological model, which takes into account the shell, pairing and collective effects. The main parameter of the model $\widetilde{a}$ was normalized to the observed neutron resonance spacing $\langle D_{l=0} \rangle = 4.717$ eV.

3.1.2 Neutron width

Average neutron width is calculated as follows

$$\langle \Gamma_n^{lJ} \rangle = S_l \langle D_J \rangle E_n^{1/2} P_l \nu_n^{lJ}, \tag{1}$$

where P_l is the transmission factor for the $l-$th partial wave, which was calculated within black nucleus model, ν_n^{lJ} is the number of degrees of freedom of Porter-Thomas distribution (see Table 3). The p-wave neutron strength function $S_1 = 2.15\times10^{-4}$ at 0.2 keV was calculated with the optical model, using the deformed optical potential, described below.

3.1.3 Radiative capture width

Energy and angular momentum dependence of radiative capture width are calculated within a two-cascade γ-emission model with allowance for the (n,γn') and (n,γf) reactions competition to the (n,$\gamma\gamma$) reaction. The (n,$\gamma\gamma$) reaction is supposed to be a radiative capture reaction. The radiative capture width was normalized to the value of $\langle \Gamma_\gamma \rangle$.

3.1.4 Neutron inelastic width

Average neutron inelastic width is calculated as follows

$$\langle \Gamma_{n'}^{lJ} \rangle = S_l \langle D_J \rangle (E_n - E_1)^{1/2} P_l (E_n - E') \nu_{n'}^{lJ}, \tag{2}$$

where $\nu_{n'}^{lJ}$ is number of degrees of freedom of Porter-Thomas distribution (see Table 3). For actual compound nucleus states, formed by $s-$, $p-$ and $d-$wave neutrons one obtains

$$\begin{aligned}
\langle \Gamma_{n'}^{0,1/2} \rangle &= S_2 \langle D_{1/2} \rangle (E_n - E_1)^{1/2} P_2 (E - E_1) \cdot 2, \\
\langle \Gamma_{n'}^{1,1/2} \rangle &= S_1 \langle D_{1/2} \rangle (E_n - E_1)^{1/2} P_1 (E_n - E_1), \\
\langle \Gamma_{n'}^{1,3/2} \rangle &= S_1 \langle D_{3/2} \rangle (E_n - E_1)^{1/2} P_1 (E_n - E_1) \cdot 2
\end{aligned} \tag{3}$$

$$\langle\Gamma^{2,3/2}_{n'}\rangle = S_0\langle D_{3/2}\rangle(E_n-E_1)^{1/2}+S_2\langle D_{3/2}\rangle(E_n-E_1)^{1/2}P_2(E_n-E_1)\cdot 2$$
$$\langle\Gamma^{2,5/2}_{n'}\rangle = S_0\langle D_{5/2}\rangle(E_n-E_1)^{1/2}+S_2\langle D_{5/2}\rangle(E_n-E_1)^{1/2}P_2(E_n-E_1)\cdot 2$$

3.1.5 Fission width

Fission widths are calculated within a double-humped fission barrier model. Energy and angular momentum dependence of fission width is defined by the transition state spectra at inner and outer barrier humps. We constructed transition spectra by supposing the axiality of inner saddle and mass asymmetry at outer saddle. Number of degrees of freedom ν_f^{lJ} of Porter-Thomas distribution is defined in see Table 3. They will be described below.

Table 3.

Number of degrees of freedom

l, J	ν_n^{lJ}	$\nu_{n'}^{lJ}$	ν_f^{lJ}
0,1/2	1	2	3
1,1/2	1	1	3
1,3/2	1	2	4
2,3/2	1	1	4
2,5/2	1	1	4

3.2 Average cross sections in the region 0.2-150 keV

3.2.1 Total cross section

Total cross section was measured by Simpson et al. [1] up to 10 keV. Figure 18 shows the description of averaged measured total cross section data by Simpson et al. [1]. Above 10 keV total cross section was estimated assuming a decreasing trend of S_o and S_1 strength function values as the latter and potential radii, which was adopted from optical calculations, define total cross section up E_n =150 keV. To reproduce total cross section, calculated with optical model, we assume S_o value linearly decreasing starting from 50 keV to 1.0×10^{-4},while S_1 - to 1.8×10^{-4} at 150 keV (see Fig. 18). That is consistent with the results of coupled channel optical model calculations. The d-wave neutron strength function was assumed to be equal to $S_2 = 1.17\times10^{-4}$. In recent evaluation by Wright et al. [12] as well as in that of JENDL-3.2 [11], potential scattering radius is R =0.98 fm, we assumed $R = 0.9608$ fm.

3.2.2 Fission cross section

Only 4 sets of the measured fission cross section data are available. In the lower energy region, below 2 keV, the data of Auchampaugh et al. [2] measured with linac are essentially higher than bomb-shot data of Farrel [3], covering the energy range from 4 eV up to 21 keV. Though these data are discrepant, both show unusually high fission cross sections, while the other even-even U isotopes exhibit rather low subthreshold values in this energy region.

In the higher energy region, above ∼100 keV, the data of Vorotnikov et al. [5] are much discrepant with those by Fursov et al. [4], particularly as regards the cross section shape below E_n ∼1 MeV, both data sets were measured with Van de Graaf accelerator. Considering the trends of the cross section shape, we rely on the data by Auchampaugh et al. [2] and by Fursov et al. [4]. It is possible to reconcile the data by Auchampaugh et al. [2] with data by Fursov et al. [4] using statistical model calculation (see Fig. 19). Our estimate of fission cross section is lower than ENDF/B-VI data file predicts below 3 keV, but higher than estimate of JENDL-3.2 below ∼20 keV.

3.2.3 Elastic scattering cross section

Elastic scattering cross section estimates seem to be very sensitive to the fission cross section estimate. The discrepancy of present, ENDF/B-VI [9] and JENDL-3.2 [11] estimates from ∼1 keV and up to ∼30 keV, shown on Fig. 20, appears to be correlated with the difference of fission cross section estimates (see Fig. 19).

3.2.4 Inelastic scattering cross section

Calculated inelastic scattering cross section increases not that fast as in case of ^{238}U target nuclide, it reaches ∼0.35 b at 150 keV. Direct scattering contribution seems to be rather important even at this low incident neutron energies, since it comprises ∼25% at 150 keV, this contribution is twice as large as in case of ^{238}U+n interaction. Conventional ENDF/B processing codes (i.e. RECENT [17], NJOY [18]) exemplify Hauser-Feshach-Moldauer formalism and do not take into account direct scattering component of inelastic scattering. Total and capture data could be described within Hauser-Feshach-Moldauer formalism, adopted in these codes, while it fails in case of inelastic scattering cross section because of appreciable direct scattering contribution. This discrepancy above ∼100 keV could be compensated by increasing inelastic neutron widths $\langle \Gamma_{n'}^{lJ} \rangle$ for the channels giving major contributions to inelastic scattering. Figure 21 shows partial contributions to the inelastic scattering coming from different (l, J)-channels. Major contribution, like in case of ^{238}U+n interaction, comes from $p-$wave channels $(l = 1, J = 1/2)$ and $(l = 1, J = 3/2)$, the lowest comes from $s-$wave channel $(l = 0, J = 1/2)$, since only $d-$wave neutrons could excite 2^+ excited level of ^{232}U. The intermediate contribution comes from $(l = 2, J = 3/2)$ and

($l = 2, J = 5/2$) entrance channels, since both $s-$wave and $d-$wave neutrons contribute to exit channel. The direct contribution missing could be compensated by linear increase of S_1 neutron strength function in the exit channels from 1.65×10^{-4} (eV)$^{-1/2}$ up to 3.0×10^{-4} (eV)$^{-1/2}$ at 150 keV. To keep capture cross section unaffected we should increase capture widths in the same linear manner, up to ~15% at 150 keV. Evaluated inelastic scattering cross sections of JENDL-3.2 [11] and ENDF/B-VI [9] are much different from present calculation, the latter being systematically higher, while the former has completely different shape, steeply rising around a threshold energy, but almost flat up to 150 keV.

3.2.5 Capture cross section

We adopted $s-$wave radiative strength function $S_{\gamma 0} = 84.8\times10^{-4}$ ($\Gamma_\gamma = 40$ meV and $\langle D_{l=0}\rangle = 4.717$ eV). The important peculiarity of the calculated ^{238}U(n,γ) capture cross section, Wigner cusp above first excited level threshold, is not that pronounced in case of ^{232}U(n,γ) reaction cross section (see Fig. 22). It could be explained by the fact that major competition to capture reaction comes from fission decay channel. The pattern of $s-, p-$and $d-$wave channel contributions to the capture cross section is also rather different from that of ^{238}U target nuclide. The contributions of $s-, p-, d-$wave neutrons to ^{232}U(n,γ) capture cross section are shown on Fig. 22. The $p-$wave contribution is higher than that of $s-$wave only above ~30 keV, while that of $d-$wave neutrons is the lowest. In case of ^{238}U(n,γ) reaction main contribution comes from $p-$wave neutrons above 5 keV, while that of $d-$wave neutrons becomes higher than that of $s-$wave above ~130 keV. These peculiarities might be attributed to the increased fission competition in $p-$ and $d-$wave entrance channels. The decrease of S_1 strength function above ~45 keV is essential for consistent description of capture and total cross section, calculated with a Hauser-Feshbach-Moldauer approach. Capture cross sections in present data file, JENDL-3.2 [11] and ENDF/B-VI [9] are only slightly different below 1 keV, while for higher incident neutron energies the estimate of JENDL-3.2 [11] is much lower than present and ENDF/B-VI [9] estimates (see Fig. 22). It is lower even than $s-$wave channel contribution of present calculation. Competition of (n,γf) reaction [15] to capture reaction is also essential (see Fig. 22).

The advantage of present evaluation is that it provides average energy dependent resonance parameters, which reproduce cross sections, calculated with optical and statistical models, fission cross section included, using conventional ENDF/B processing codes [17, 18]. The price paid for that is slight increase of inelastic and capture widths for $p-$wave channels. Without that increase the competitive inelastic width would correspond to inelastic scattering cross section, which is lower than inelastic cross section of smooth cross section file above 150 keV. That would be pronounced as a step in total cross section at 150 keV, since according to ENDF/B conventions, total cross section is calculated as a sum of elastic, capture, fission and inelastic scattering cross section, the latter is

taken from tabulated cross section data file. The other partial cross sections are calculated using average energy dependent parameters.

4 Optical Potential

A coupled channel model is employed for estimating differential scattering and total cross sections. Another important application of coupled channel model is calculation of direct inelastic scattering contribution of discrete levels, five levels of ground state band are assumed coupled. The direct excitation of ground state rotational band levels 0^+-2^+-4^+-6^+-8^+ is estimated within rigid rotator model. To calculate the direct excitation cross sections for β-vibration ($K^\pi = 0^+$), γ-vibration ($K^\pi = 2^+$), as well as octupole ($K^\pi = 0^-$) band levels a soft rotator model [34] was used.

We adopted here the optical potential parameters obtained for ^{232}Th [8] by fitting total cross section data, angular distributions and $s-$wave strength function. Then we fitted ^{232}U $s-$wave strength function $S_o = 1.17 \pm 0.08 \times 10^{-4}$ with β_2 and β_4 deformation parameters. The optical potential parameters are as follows:

$$W_D = \begin{cases} V_R = 45.722 - 0.334E_n, MeV, r_R = 1.2668\ fm, a_R = 0.6468\ fm \\ 3.145 + 0.455E_n, MeV, \quad E_n \leq 10MeV, r_D = 1.25\ fm, a_D = 0.5246\ fm \\ 7.695\ MeV, \qquad 10 < E_n < 20\ MeV \end{cases}$$
$$V_{SO} = 6.2\ MeV, r_{SO} = 1.120\ fm, a_{SO} = 0.47\ fm,$$
$$\beta_2 = 0.220, \beta_4 = 0.071$$

4.1 Total cross section

Present total cross section is compared with JENDL-3.2 [11] and ENDF/B-VI [9] evaluated cross section on Fig. 23. Present and JENDL-3.2 [11] estimates are not much discrepant, while shape of ENDF/B-VI [9] cross section is rather different from both evaluations. Figure 24 shows the comparison of reaction cross sections, calculated with present coupled channels optical potential and spherical optical potential of JENDL-3.2 [11]. Figure 25 compares elastic cross sections estimates of coupled channels optical potential and spherical optical potential of JENDL-3.2 [11] with estimate of elastic scattering cross section of ENDF/B-VI [9] as a difference of total and partial reaction cross sections.

5 Statistical Model

As distinct from the previous evaluations JENDL-3.2 [11] and ENDF/B-VI [9] we proceed within Hauser-Feshbach theory, coupled channel optical model and double-humped fission barrier model. The relative importance of direct excitation of rotational and vibrational levels is much increased even in a few MeV incident

neutron energy range due to the lowered compound scattering to the ^{232}U discrete and continuum levels.

Hauser-Feshbach-Moldauer [19] statistical theory is employed for partial cross section calculations below emissive fission threshold. Fissioning and residual nuclei level densities as well as fission barrier parameters are key ingredients, involved in neutron-induced actinide cross section calculations. First, level density parameters are defined, using neutron resonance spacing $\langle D_{obs} \rangle$ estimate for ^{232}U target nuclide. Constant temperature level density parameters T_o, E_o, U_c are defined by fitting cumulative number of low-lying levels of ^{233}U and ^{232}U (see Fig. 26, 27). Level density parameter estimates for ^{232}U, ^{231}U, ^{230}U nuclides, which emerge in neutron emission cascade reactions, could be defined only by parameter systematics [16]. At incident neutron energies when continuum levels are excited, width fluctuation correction is treated within Tepel et al. [20] approach. Cross sections, calculated with statistical theory by Tepel et al. [20] cross sections are matched to those calculated with Hauser-Feshbach-Moldauer statistical theory at the incident neutron energy equal to the energy of last discrete level. At higher incident neutron energies Hauser-Feshbach code STAPRE [21] is employed.

In case of fast neutron ($E_n \leq 6$ MeV) interaction with ^{232}U target nucleus, the main reaction channel is fission, fission cross section description serves as a major constraint for the neutron inelastic scattering and radiative neutron capture cross section estimate. Below there is an outline of the statistical model [22, 23] employed.

Neutron-induced reaction cross section (n, x) for excitation energies up to emissive fission threshold is defined as

$$\sigma_{nx}(E_n) = \frac{\pi \, \acute{\lambda}^2}{2(2I+1)} \sum_{ljJ\pi} (2J+1) T_{lj}^{J\pi}(E_n) P_x^{J\pi}(E_n) S_{nx}^{ljJ\pi}, \tag{4}$$

the compound nucleus decay probability $P_x^{J\pi}$ $(x = n, f, \gamma)$ is

$$P_x^{J\pi}(E_n) = \frac{T_x^{J\pi}(U)}{T_f^{J\pi}(U) + T_n^{J\pi}(U) + T_\gamma^{J\pi}(U)}, \tag{5}$$

where $U = B_n + E_n$ is the excitation energy of the compound nucleus, B_n is the neutron binding energy, E_n is the incident neutron energy, $T_{lj}^{J\pi}$ are the entrance neutron transmission coefficients for the channel $(ljJ\pi)$, I is the target nucleus spin. Decay probability $P_x^{J\pi}(E)$ of the compound nucleus with excitation energy U for given spin J and parity π, depends on $T_f^{J\pi}$, $T_n^{J\pi}(U)$ and $T_\gamma^{J\pi}(U)$, transmission coefficients of the fission, neutron scattering and radiative decay channels, $S_{nx}^{ljJ\pi}$ denotes partial widths Porter-Thomas fluctuation factor. Below incident neutron energy equal to the cut-off energy of discrete level spectra, neutron cross sections are calculated within Hauser-Feshbach approach with correction for width fluctuation by Moldauer [19]. For width fluctuation correction calculation only Porter-Thomas fluctuations are taken into account. Effective

number of degrees of freedom for fission channel is defined at the higher fission barrier saddle as $\nu_f^{J\pi} = T_f^{J\pi}/T_{f\,\max}^{J\pi}$, where $T_{f\,\max}^{J\pi}$ is the maximum value of the fission transmission coefficient $T_f^{J\pi}$. At higher incident neutron energies the Tepel et al. [20] approach is employed, it describes cross section behavior in case of large number of open channels correctly.

5.1 Level Density

Level density is the main ingredient of statistical model calculations. Level density of fissioning, residual and compound nuclei define transmission coefficients of fission, neutron scattering and radiative decay channels, respectively. We will briefly discuss here level densities of even-even ^{232}U and even-odd ^{233}U nuclides.

The level densities were calculated with a phenomenological model by Ignatyuk et al. [24], which takes into account shell, pairing and collective effects in a consistent way

$$\rho(U, J, \pi) = K_{rot}(U, J) K_{vib}(U) \rho_{qp}(U, J, \pi), \tag{6}$$

where quasiparticle level density

$$\rho_{qp}(U, J, \pi) = \frac{(2J+1)\omega_{qp}(U)}{4\sqrt{2\pi}\sigma_\perp^2 \sigma_\parallel} \exp\left(-\frac{J(J+1)}{2\sigma_\perp^2}\right), \tag{7}$$

$\omega_{qp}(U, J, \pi)$ is state density, $K_{rot}(U, J)$ and $K_{vib}(U)$ are factors of rotational and vibrational enhancement of the level density. The collective contribution of the level density of deformed nuclei is defined by the nuclear deformation order of symmetry. The actinide nuclei at equilibrium deformation are axially symmetric. The order of symmetry of nuclear shape at inner and outer saddles were adopted from calculations within shell correction method (SCM) by Howard & Möller [25]. Uranium nuclei of interest (A$\leq$233)are assumed to be axially symmetric, then

$$K_{rot}(U) = \sigma_\perp^2 = F_\perp t, \tag{8}$$

where $\sigma_\perp^2$ is the spin cutoff parameter, $F_\perp$ is the nuclear momentum of inertia (perpendicular to the symmetry axis), which equals the rigid-body value at high excitation energies, where the pairing correlations are destroyed, experimental value at zero temperature and is interpolated in between, using the pairing model, $F_\parallel = 6/\pi^2 < m^2 > (1 - 2/3\varepsilon)$, where $< m^2 >$ is the average value of the squared projection of the angular momentum of the single-particle states, and ε is quadrupole deformation parameter. The closed-form expressions for thermodynamic temperature and other relevant equations which one needs to calculate $\rho(U, J, \pi)$ are provided by Ignatyuk et al. model [24].

To calculate the residual nucleus level density at the low excitation energy, i.e. just above the last discrete level excitation energy where $N^{exp}(U) \sim N^{theor}(U)$,

we employ a Gilbert-Cameron-type approach. The constant temperature approximation of

$$\rho(U) = dN(U)/dU = T^{-1}\exp((U - U_o)/T) \tag{9}$$

is extrapolated up to the matching point U_c to the $\rho(U)$ value, calculated with a phenomenological model by Ignatyuk et al. [24] with the condition

$$U_c = U_o - Tln(T\rho(U_c)). \tag{10}$$

In this approach $U_o \simeq -n\triangle_o$, where $\triangle_o$ is the pairing correlation function, $\triangle_o = 12/\sqrt{A}$, A is the mass number, $n = 0$ for even-even, 1 for odd nuclei, i.e. U_o has the meaning of the odd-even energy shift. The value of nuclear temperature parameter T is obtained by the matching conditions at the excitation energy U_c.

In present approach the modelling of total level density

$$\rho(U) = K_{rot}(U)K_{vib}(U)\frac{\omega_{qp}(U)}{\sqrt{2\pi}\sigma} = T^{-1}\exp((U - U_o)/T) \tag{11}$$

in Gilbert-Cameron-type approach looks like a simple renormalization of quasiparticle state density $\omega_{qp}(U)$ at excitation energies $U < U_c$. The cumulative number of observed levels for even-even ^{232}U and even-odd ^{233}U are compared with constant temperature approximation on Figs. 26 and 27. In case of ^{232}U missing of levels above pairing gap ($\sim$1.2 MeV) is markedly pronounced. In case of ^{233}U nuclide missing seems to be pronounced above excitations of $\sim$0.65 MeV.

Few-quasiparticle effects which are due to pairing correlations are essential for state density calculation at low intrinsic excitation energies either for equilibrium or saddle deformations. The step-like structure in ^{238}Pu(n,f) reaction cross section above fission threshold was shown to be a consequence of threshold excitation of three-quasiparticle states in fissioning ^{239}Pu nuclide and two-quasiparticle configurations in residual even-even nuclide ^{238}Pu [26]. Fission threshold is not observed in the reaction ^{232}U(n,f), nonetheless we argue that step-like irregularity in fission cross section around $\sim$1 MeV incident neutron energy also might be attributed to the step in the level density of fissioning nuclide ^{233}U. We argue that few-quasiparticle effects are important also for reasonable prediction of inelastic scattering cross section for even-even target nuclide ^{232}U at low energies.

The partial $n-$quasiparticle state densities, which sum-up to intrinsic state density of quasiparticle excitations could be modelled using the Bose-gas model prescriptions [27, 28]. The intrinsic state density of quasiparticle excitations $\omega_{qp}(U)$ could be represented as a sum of $n-$quasiparticle state densities $\omega_{nqp}(U)$:

$$\omega_{qp}(U) = \sum_n \omega_{nqp}(U) = \sum_n \frac{g^n(U - U_n)^{n-1}}{((n/2)!)^2(n-1)!}, \tag{12}$$

where $g = 6a_{cr}/\pi^2$ is a single-particle state density at the Fermi surface, n is the number of quasiparticles. The important model parameters are threshold values

U_n for excitation of $n-$quasiparticle configurations $n = 2, 4...$ for even-even nuclei and $n = 1, 3...$ for odd-A nuclei [28]. The detailed treatment of this approach and approximations employed, as applied for fission, inelastic scattering or capture reaction calculations, is provided in [29].

Nuclear level density $\rho(U)$ of even-even nuclei above the pairing gap up to the four-quasiparticle excitation threshold was extracted by fitting fission cross section data of ^{232}U. The total level density for even nuclide ^{232}U at equilibrium deformation, as compared with the Gilbert-Cameron-type approximation of $\rho(U)$ is shown on Fig. 28. The arrows on the horizontal axis of Fig. 28 indicate the excitation thresholds of even $n-$quasiparticle configurations. Below the excitation threshold U_2, i.e. within pairing gap the constant temperature model fits cumulative number of ^{232}U levels [30].

In case of even-odd nuclei the partial contributions of $n-$quasi-particle states $\omega_{nqp}(U)$ to the total intrinsic state density $\omega_{qp}(U)$ produces distinct "jump" only below three-quasiparticle excitation threshold U_3 (see Fig. 29). The arrows on the horizontal axis of Fig. 29 indicate the excitation thresholds of odd $n-$quasiparticle configurations. Nuclear level density $\rho(U)$ up to the three-quasiparticle excitation threshold U_3 is virtually independent on the excitation energy, since the intrinsic state density ($\omega_1 \sim g$) is constant. The numerical values of nuclear level density $\rho(U)$ parameters, defining one- and three quasiparticle state densities are fitted to ^{232}U(n,f) cross section data by Fursov et al. [4].

Main parameters of the level density model for equilibrium, inner and outer saddle deformations are as follows: shell correction δW, pairing correlation functions Δ and Δ_f, at equilibrium deformations $\Delta = 12/\sqrt{A}$, quadrupole deformation ε and momentum of inertia at zero temperature $F_o/\hbar^2$ are given in Table 4. For ground state deformations the shell corrections were calculated as $\delta W = M^{exp} - M^{MS}$, where M^{MS} denotes liquid drop mass (LDM), calculated with Myers-Swiatecki parameters [31], and M^{exp} is the experimental nuclear mass. Shell correction values at inner and outer saddle deformations $\delta W_f^{A(B)}$ are adopted following the comprehensive review by Bjornholm and Lynn [32].

Table 4

Level density parameters of fissioning nucleus and residual nucleus

Parameter	inner saddle	outer saddle	neutron channel
δW, MeV	1.5	0.6	LDM
$\triangle$, MeV	$\triangle_o + \delta^*$	$\triangle_o + \delta^*$	$\triangle_o$
ε	0.6	0.8	0.24
$F_0/\hbar^2$, MeV^{-1}	100	200	73

*)$\delta = \Delta_f - \Delta$ value is defined by fitting fission cross section in the plateau region.

6 Fission Cross Section

Fission data fit is used as a major constraint for capture, elastic and inelastic scattering, (n,2n) and (n,3n) cross sections estimation. Description of measured fission might justify a validity of level density description and fission barrier parameterization.

6.1 Fission Channel

Neutron-induced fission in a double humped fission barrier model could be viewed as a two-step process, i.e. a successive crossing over the inner hump A and over the outer hump B. Hence, the transmission coefficient of the fission channel $T_f^{J\pi}$ (U) can be represented as

$$T_f^{J\pi}(U) = \frac{T_{fA}^{J\pi}(U) T_{fB}^{J\pi}(U)}{(T_{fA}^{J\pi}(U) + T_{fB}^{J\pi}(U))}. \tag{13}$$

The transmission coefficient $T_{fi}^{J\pi}(U)$ is defined by the level density $\rho_{fi}(\varepsilon, J, \pi)$ of the fissioning nucleus at the inner and outer humps (i = A,B, respectively):

$$T_{fi}^{J\pi}(U) = \sum_{K=-J}^{J} T_{fi}^{JK\pi}(U) + \int_0^U \frac{\rho_{fi}(\epsilon, J, \pi) d\epsilon}{(1 + \exp(2\pi(E_{fi} + \epsilon - U)/h\omega_i))}, \tag{14}$$

where the first term denotes the contribution of low-lying collective states and the second term that from the continuum levels at the saddle deformations, ϵ is the intrinsic excitation energy of fissioning nucleus. The first term contribution due to discrete transition states depends upon saddle symmetry. The total level density $\rho_{fi}(\epsilon, J, \pi)$ of the fissioning nucleus is determined by the order of symmetry of nuclear saddle deformation.

Inner and outer fission barrier heights and curvatures as well as level densities at both saddles are the model parameters. They are defined by fitting fission cross section data at incident neutron energies below emissive fission threshold. Fission barrier height values and saddle order of symmetry are strongly interdependent. The order of symmetry of nuclear shape at saddles was defined by Howard and Möller [25] within shell correction method (SCM) calculation. We adopt the saddle point asymmetries from SCM calculations. According to shell correction method (SCM) calculations of Howard and Möller [25] the inner barrier was assumed axially symmetric. This helps to interpret the non-threshold fission cross section behavior of ^{232}U(n,f) [6] assuming a lowered height of axially symmetric inner hump of ^{233}U, as anticipated by Howard and Möller [25] with SCM calculations. Outer barrier for uranium nuclei is assumed mass-asymmetric.

6.1.1 Fission transmission coefficient, level density and transition state spectrum

Fission cross section data of ^{232}U exhibits non-threshold shape. Adopted level density description allows to fit measured data shape (see Fig. 30). Incident neutron energy $E_3 = U_3 + E_{fA(B)} - B$ correspondent to excitation of three-quasiparticle states is $\sim$ 1.5 MeV. The one-quasiparticle neutron states of even-odd fissioning nuclide, lying below the three-quasiparticle states excitation threshold define the shape of fission cross section below incident neutron energy of $E_n \leq E_{fA(B)} + U_3 - B_n$. At higher excitation energies three-quasiparticle states are excited. Two-quasiparticle states in even residual nuclide ^{232}U could be excited at incident neutron energies $E_n > U_2$. At lower energies fission cross section shape is controlled by one-quasiparticle state density. The transition state spectra were constructed using values of $F_0/\hbar^2$ at the inner and outer saddles shown in Table 5.

Each one-quasiparticle state in odd fissioning nucleus is assumed to have a rotational band built on it with a rotational constant, dependent upon the respective saddle deformation. We construct the discrete transition spectra up to $\sim$100 keV, using one-quasiparticle states by Bolsterli et al. [33] (see Table 5). The discrete transition spectra, as well as continuous level contribution to the fission transmission coefficient are dependent upon the order of symmetry for fissioning nucleus at inner and outer saddles. The negative parity bands $K^\pi = 1/2^-$,$3/2^-$, $5/2^-$ ... at outer saddle are assumed to be doubly degenerate due to mass asymmetry. With transition state spectra thus defined the fission barrier parameters are obtained.

Table 5.

Transition spectra band-heads, Z-even, N-odd nuclei

inner saddle		outer saddle	
K^π	E_{K^π}, MeV	K^π	E_{K^π}, MeV
$1/2^+$	0.0	$1/2^+$	0.0
$5/2^+$	0.08	$1/2^-$	0.0
$1/2^-$	0.05	$3/2^+$	0.08
$3/2^-$	0.0	$3/2^-$	0.08
		$5/2^+$	0.0
		$5/2^-$	0.0

6.2 Fission Data Analysis

Measured data for ^{232}U(n,f) cross section by Fursov et al. [4] and Vorotnikov et al. [5] are incompatible below E_n ~1 MeV (see Figs. 30, 31, 32). The most peculiar feature of measured data by Fursov et al. [4] is a step-like irregularity around ~1 MeV neutron energy. One-quasiparticle neutron states of even-odd ^{233}U fissioning nuclide, lying below three-quasiparticle states excitation threshold define the shape of ^{232}U fission cross section below incident neutron energy of ~1.5 MeV. At higher energies three-quasiparticle states are excited. We fit the decreasing trend of data by Fursov et al. [4] with above E_n ~2 MeV increasing the correlation function value at outer saddle, which controls the cross section shape. Below E_n ~2 MeV neutron energy the step-like irregularity is reproduced by varying the density of one- and three-quasiparticle states at saddle deformations (see Figs. 30, 31, 32).

6.3 Inelastic Scattering

Fission data fit defines the compound inelastic scattering contribution to the total inelastic scattering cross section. The relative contribution of direct discrete level excitation cross sections is much higher than in case of ^{238}U target nuclide because of much stronger fission competition.

6.4 Neutron Channel

The lumped transmission coefficient of the neutron scattering channel is given by

$$T_n^{J\pi}(U) = \sum_{l'j'q} T_{l'j'}^{J\pi}(E_n - E_{q'}) + \sum_{l'j'I'} \int_0^{U-U_c} T_{l'j'}^{J\pi}(E'_n)\rho(U - E'_n, I', \pi)dE'_n, \quad (15)$$

where $\rho(U - E'_n, I', \pi)$ is the level density of the residual nucleus. Levels of residual nuclide ^{232}U [30] are provided in Table 6. The entrance channel neutron transmission coefficients $T_{lj}^{J\pi}$ are calculated within a rigid rotator coupled channel approach. For the compound nucleus formation cross section calculation, the cross sections of the direct excitation of ground state band levels were subtracted from the reaction cross section. The compound and direct inelastic scattering components are added incoherently.

The exit neutron transmission coefficients $T_{l'j'}^{J\pi}(E'_n)$ were calculated using the re-normalized deformed optical potential of entrance channel without coupling, which describes a neutron absorption cross section.

Table 6.

Levels of ^{232}U

E, MeV	J^π	K^π
0.866792	2^+	2^+
0.83307	4^+	0^+
0.8058	10^+	0^+
0.7469	5^-	1^-
0.73456	2^+	0^+
0.69121	0^+	0^+
0.628967	3^-	1^-
0.563194	1^-	1^-
0.541	8^+	0^+
0.3226	6^+	0^+
0.15657	4^+	0^+
0.047572	2^+	0^+
0.0000	0^+	0^+

6.5 Ground State Rotational Band

Predicted discrete level excitation cross section shape, calculated within a rigid rotator model, depends upon optical potential used. Calculated compound contribution is controlled mainly by fission competition. Due to low fission threshold of ^{233}U, compound and direct inelastic scattering make almost equal contributions to excitation cross sections of 1st, 2nd and 3d levels of ^{232}U around $E_n \sim$1 MeV (see Figs. 33, 34, 35). Figure 36 shows that direct scattering essentially defines the excitation cross section of $J^\pi = 8^+$ level. The discrepancies with previous evaluations are due to both compound and missing (in previous evaluations) direct contribution estimates. The compound component tends to be zero above $\sim$3 MeV incident neutron energy.

6.6 Soft rotator model

We assume strong missing of levels above excitations of $\sim$0.870 MeV, so only levels up to this excitation energy were included when calculating inelastic scattering cross sections. Four bands with $K^\pi = 0^+_1$, $K^\pi = 0^+_2$, $K = 0^-$ and $K^\pi \simeq 2^+$ could be distinguished in ^{232}U level scheme (see Table 6) within a soft rotator model [34] for excitation energies up to $\sim$0.870 MeV. Excitation energies of members of even-parity collective bands $K^\pi = 0^+_1$, $K^\pi = 0^+_2$, and $K^\pi \simeq 2^+$ and first octupole band $K^\pi = 0^-$, are reproduced. Direct excitation of vibrational levels $K = 0^+_2$, $K = 0^-$ and $K \simeq 2^+$ could be described within a soft rotator model

[34]. Specifically, direct excitation cross sections for the second $K^\pi = 0_2^+$ band, anomalous rotational band $K^\pi = 2^+$ as well as first octupole ($K^\pi = 0^-$) band levels are calculated for deformed non-axial, soft to quadrupole vibrations rotator (see Figs. 37-44). Values of coupling strength parameters were fixed as follows: octupole deformation parameter β_3 was adopted to be the same as for the ^{238}U nuclide, then level positions of $K = 0^-$ band were fitted with softness parameter μ_ξ. Levels of second $K^\pi = 0_2^+$ band (0.69121 MeV) are classified as quadrupole longitudinal $\beta-$vibrations, excitation energies are defined by softness parameter μ_β (see Table 7). Levels of this $K^\pi = 0_2^+$ band could be reproduced also assuming different nature of these vibrations, i.e. transversal $\gamma-$vibrations. However, in that case the parameter of softness for this vibrations μ_γ should be anomalously high as compared with ^{238}U and ^{232}Th nuclides (see Tables 7, 8). That means γ-vibration $K^\pi = 0_2^+$ band should be at higher excitations than $\sim$0.87 MeV, this is correlated with rather low position of $K^\pi \simeq 2^+$ band-head. In other words, ^{232}U turns out to be less soft to $\gamma-$vibrations, than ^{238}U nuclide. The same effect is observed in case of ^{232}Th, since γ-vibration $K^\pi = 0^+$ band is positioned at excitation above $\sim$1 MeV, while β-vibration $K^\pi = 0^+$ band is $\sim$0.25 MeV lower than in case of ^{238}U. These peculiarities might be correlated with positions of anomalous rotational band $K^\pi = 2^+$ in ^{232,238}U and ^{232}Th nuclides. Anomalous rotational $K^\pi = 2^+$ band levels are defined by non-axiality parameter γ_0.

Table 7.

Deformation parameter values of soft rotator model

Nuclide	β_2	β_3	β_4	$\hbar\omega_o$,	μ_ξ	μ_β	μ_γ	γ_o
^{232}Th	0.188	0.052	0.071	0.725	0.626	0.279	0.279	0.187
^{232}U(n_γ=1)	0.220	0.052	0.071	0.667	0.626	0.278	0.456	0.167
^{232}U(n_β=1)	0.220	0.052	0.071	0.691	0.626	0.273	0.294	0.168
^{238}U	0.195	0.052	0.078	0.989	0.626	0.216	0.290	0.146

Table 8.
Comparison of β-vibration band-head positions

^{238}U		^{232}U		^{232}U	
	1.0603;2^+		0.867; 2^+		0.867; 2^+
0.993;0^+		0.69121;0^+		0.69121; 0^+	
$K^\pi = 0^+$	$K^\pi \simeq 2^+$	$K^\pi = 0^+$;	$K^\pi \simeq 2^+$	$K^\pi = 0^+$;	$K^\pi \simeq 2^+$
n_β=1, μ_β =0.294,		n_β=1, μ_β =0.273,		n_γ=1, μ_β =0.278,	
γ_0=0.146; μ_γ=0.294		γ_0=0.168; μ_γ=0.294		γ_0=0.167; μ_γ=0.456	

Actually the calculations of direct inelastic scattering cross sections were made adding each of 7 levels of $K^\pi = 0_2^+$, $K^\pi = 0^-$ and $K^\pi \simeq 2^+$ bands (see Table 9), one by one, to the 0^+-2^+-4^+-6^+-8^+ coupling basis, instead of the last 8^+-member, since the coupling with ground state band levels is the strongest for any band level. This procedure was checked in case of ^{238}U and ^{232}Th target nuclides. However, coupling basis could be extended to include all 13 level (see Table 9) simultaneously. This procedure influences only slightly on the calculated direct excitation cross sections.

Table 9.

Coupling scheme for ^{232}U

			0.866797; 2^+
		0.83307; 4^+	
0.8058;10^+			
	0.7469;5^-		
		0.73456;2^+	
		0.69121; 0^+	
	0.628967; 3^-		
	0.563194; 1^-		
0.5410;8^+			
0.32261; 6^+			
0.15657; 4^+			
0.047572; 2^+			
0.0000; 0^+			
$K^\pi = 0^+$	$K^\pi = 0^-$	$K^\pi = 0_2^+$	$K^\pi \simeq 2^+$

6.6.1 Octupole band

The most pronounced is the direct excitation contribution for the K^π=0^- band head state 0.563 MeV (J^π=1^-) (see Figs. 37). Relative contribution of direct level excitation increases for the higher lying members of the band (see Figs. 38, 41). Previous estimates of excitation cross sections of these levels are rather discrepant, the inconsistencies for $E_n \lesssim 3$ MeV are due to compound scattering contribution.

6.6.2 Quadrupole bands

Discrepancies of present calculation of excitation cross sections of K^π=0_2^+ β-vibration band levels with JENDL-3.2 and ENDF/B-VI estimates, which are

observed below ∼4 MeV, are due to different compound and missing direct scattering components (see Figs. 39, 40, 43). At higher incident neutron energies direct scattering makes major contribution to the inelastic scattering cross section.

The comparison of calculated excitation cross section of $K^\pi \simeq 2^+$ anomalous rotation band-head with previous evaluations is shown on Fig. 44. Noticeable discrepancy of present calculation and JENDL-3.2 [11] and ENDF/B-VI [9] evaluations with measured data is also observed.

6.7 Total inelastic cross section

Calculated total inelastic cross section is compared with previous evaluated data on Fig. 45. Lumped contribution of direct excitation of ground state band levels, octupole, β-vibration and anomalous rotation band levels is shown to attain ∼50% of total inelastic cross section at $E_n \gtrsim 2$ MeV. The calculated curve is drastically discrepant with JENDL-3.2 evaluation [11], while it is roughly compatible with ENDF/B-VI [9] evaluation up to E_n ∼1.5 MeV. Shape of calculated continuum inelastic scattering cross section is rather similar to that of JENDL-3.2 evaluated total inelastic scattering cross section (see Fig. 46). The differences of total inelastic scattering cross sections are defined by rather large relative direct inelastic scattering contribution, which almost doubles inelastic scattering cross section in a few MeV incident neutron energy range.

Above emissive fission threshold evaluations of inelastic scattering cross section differ severely, present estimate being the highest (see Fig. 47). In our calculations pre-equilibrium neutron emission contribution is defined by description of secondary neutron spectra and consistent description of ^{238}U(n,f), ^{238}U(n,2n) and ^{238}U(n,3n) reaction cross sections [29].

7 Capture cross section

We have demonstrated by the analysis of measured capture cross sections of ^{238}U(n,γ) and ^{232}Th(n,γ) [8] that capture data could be described within a statistical model. Specifically, in a few-keV energy region calculated capture cross section is defined by the radiative strength function value $S_\gamma = \Gamma_\gamma/D$. At incident neutron energies above ∼100 keV calculated capture cross section shape is defined by the energy dependence of radiative strength function S_γ. Energy dependence of S_γ is controlled mainly by the energy dependence of the level density of the compound nuclide ^{233}U. Low fission threshold for the ^{233}U nuclide necessitates the inclusion of the competition of fission alongside with neutron emission at the second $\gamma-$cascade, i.e. after first $\gamma-$quanta emission [15]. Then "true" capture reaction cross section (n,$\gamma\gamma$) is defined using transmission coefficient $T^{J\pi}_{\gamma\gamma}(U)$

defined in a two-cascade approximation as

$$T_{\gamma\gamma}^{J\pi} = \frac{2\pi C_{\gamma 1}}{3(\pi hc)^2} \int \varepsilon_\gamma^2 \sigma_\gamma(\varepsilon_\gamma) \sum_{I=|J-1|}^{I=J+1} \rho(U-\varepsilon_\gamma, I, \pi) \frac{T_\gamma^{I\pi}}{T_f^{I\pi} + T_{n'}^{I\pi} + T_\gamma^{I\pi}} d\varepsilon_\gamma \ , \quad (16)$$

The last term of the integrand describes the competition of fission, neutron emission and γ-emission at excitation energy $(U - \varepsilon_\gamma)$ after emission of first γ-quanta, $C_{\gamma 1}$ is the normalizing coefficient. That means that transmission coefficients $T_\gamma^{I\pi}$, $T_{n'}^{I\pi}$ and $T_f^{I\pi}$ are defined at excitation energy $(U - \varepsilon_\gamma)$. The neutron emission after emission of first $\gamma-$quanta strongly depends on the ^{232}U residual nuclide level density at excitations just above paring gap. The contribution of (n,γf)$-$reaction [15] to fission cross section is defined by $T_{\gamma f}^{J\pi}$ value. The energy dependence of (n,γf) reaction transmission coefficient $T_{\gamma f}^{J\pi}$ was calculated with the expression

$$T_{\gamma f}^{J\pi} = \frac{2\pi C_{\gamma 1}}{3(\pi hc)^2} \int \varepsilon_\gamma^2 \sigma_\gamma(\varepsilon_\gamma) \sum_{I=|J-1|}^{I=J+1} \rho(U-\varepsilon_\gamma, I, \pi) \frac{T_f^{I\pi}}{T_f^{I\pi} + T_{n'}^{I\pi} + T_\gamma^{I\pi}} d\varepsilon_\gamma \ , \quad (17)$$

The capture data description is shown on Fig. 48. The (n,γf) reaction competition to the "true" capture (n,$\gamma\gamma$) reaction competition is rather strong above $\sim$1 MeV incident neutron energy. The competition of (n,γn') reaction to the "true" capture (n,$\gamma\gamma$) reaction is much less essential below $\sim$.5 MeV incident neutron energy. We adopted here radiative capture strength function, which actually corresponds to $\langle\Gamma_\gamma\rangle$ = 40 meV and $\langle D_{l=0}\rangle$ = 4.717 eV. The important peculiarity of the calculated ^{238}U(n,γ) capture cross section - Wigner cusp above first excited level threshold, is not that pronounced in case of ^{232}U(n,γ) reaction cross section (see Fig. 48). This could be explained by the fact that major competition to capture reaction comes from fission decay channel. Another capture cross section drop is observed from $\sim$600 keV up to $\sim$1 MeV. It might be correlated with strong increase of inelastic scattering competition due to vibrational levels of $K^\pi = 0_2^+$, $K^\pi = 0^-$ and $K^\pi \simeq 2^+$ bands. Above $E_n \sim$1 MeV capture cross section decrease is defined mainly by (n,γf) reaction competition.

Previous evaluated capture cross sections are rather discrepant with present calculation. Some consistency is observed only with JENDl-3.2 evaluation up to $\sim$10 keV. For higher incident neutron energies competition of fission and inelastic scattering with $\gamma-$emission seems to modelled correctly within present approach.

8 Cross sections above emissive fission threshold

At higher incident neutron energies when fission reaction of ^{232}U or ^{231}U compound nuclides is possible after emission of 1 or 2 neutrons, the observed ^{232}U(n,f)

fission cross section is a superposition of non-emissive or first chance fission of ^{233}U and xth-chance fission contributions. These contributions are weighted with a probability of x neutrons emission before fission. For fixed statistical model parameters of residual nuclei ^{232}U and ^{231}U, fissioning in (n,nf) or (n,2nf) reactions, the behavior of the first-chance fission cross section σ_{f1} should make it possible to reproduce the measured fission cross section σ_f of ^{232}U. A consistent description of a most complete set of measured data on the (n,f), (n,2n), (n,3n) and (n,4n) reaction cross sections for the ^{238}U target nuclide up to 20 MeV enables one to consider the estimates of first neutron spectra of initial ^{233}U nuclide as fairly realistic.

8.1 Fission cross section

Fission cross section of ^{232}U, shown on the Fig. 49 demonstrates a step-like structure, relevant to contribution of (n,nf) reaction to the total fission cross section. We fitted the ^{232}U(n,f) fission data by Fursov et al. [4] above emissive fission threshold with fission probability of ^{232}U, fissioning in ^{232}U(n,nf) reaction. Calculated fission cross section at $E_n \sim$15 MeV remains much lower than measured data by Fursov et al. [4], actually the latter data point is much higher than neutron absorption cross section σ_r (see Fig. 24). Contribution of first-chance fission is defined by the pre-equilibrium emission of first neutron and level densities of fissioning ^{233}U and residual ^{232}U nuclides. The behavior of the first-chance fission cross section σ_{f1} is obviously related to the energy dependence of the fission probability of the $A+1$ nucleus P_{f1}:

$$\sigma_{f1} = \sigma_r(1 - q(E_n))P_{f1}. \tag{18}$$

Once the contribution of first neutron pre-equilibrium emission $q(E_n)$ is fixed [8], the first-chance fission probability P_{f1} of the ^{233}U compound nuclide depends only on the level density parameters of fissioning and residual nuclei. Actually, it depends on the ratio of shell correction values $\delta W_{fA(B)}$ and δW_n. The results of different theoretical calculations of the shell corrections as well as of the fission barriers vary by $1 \sim 2\ MeV$. The same is true for the experimental shell corrections, which are obtained with a smooth component of potential energy calculated according to the liquid-drop or droplet model. However the isotopic changes of $\delta W_{fA(B)}$ and δW_n [32] are such that P_{f1} viewed as a function of the difference $(\delta W_{fA(B)} - \delta W_n)$ is virtually independent on the choice of smooth component of potential energy. Therefore, we shall consider the adopted $\delta W_{fA(B)}$ estimates (see Table 4) to be effective, provided that δW_n are obtained with the liquid drop model. The trend of the first-chance fission cross section σ_{f1} shown in Fig. 49 corresponds to estimate of σ_{f1} obtained by fit of ^{238}U(n,f), ^{238}U(n,2n), ^{238}U(n,3n) and ^{238}U(n,4n) reaction cross section data. Contribution of second-chance fission of ^{232}U nuclide is defined by pre-equilibrium contribution

of first neutron spectrum and subsequent sharing of $\sigma_r = \sigma_{n,f1} + \sigma_{n,nx}$ reaction cross section into first-chance fission and neutron emission cross sections. First-, second- and third-chance fission contributions to the total neutron-induced fission cross section of ^{232}U is compared with relevant contributions for neutron-induced fission of ^{238}U target nuclide on Fig. 50. The contribution of first-chance fission to the ^{232}U(n,f) reaction cross section is rather smooth function of incident neutron energy, as distinct from ^{238}U(n,f) reaction. In the latter case a local minimum is observed near ^{238}U(n,nf) reaction threshold. The second-chance fission contribution ^{232}U(n,nf) is a smooth increasing function of excitation energy. The contribution of ^{232}U(n,2nf) reaction to the total fission cross section is much lower than in case of ^{238}U(n,2nf) reaction. Calculated with present level density and fission barrier parameters cross section of ^{231}U(n,f) reaction is shown on Fig. 51. It is compared with simulated fission data, obtained using fission probability of ^{232}U nuclide [35]. Rather large discrepancy is observed above incident neutron energy of ∼0.5 MeV. Contribution of (n,2nf) reaction corresponds to neutron-induced fission cross section of ^{230}U(n,f) reaction. Calculated with present level density and fission barrier parameters cross section of ^{230}U(n,f) reaction is shown on Fig. 52. It is also compared with simulated fission data, obtained using fission probability of ^{231}U nuclide [35], measured with transfer reactions. As distinct from ^{231}U(n,f) reaction, calculated and simulated ^{230}U(n,f) cross sections are compatible.

8.2 ^{232}U(n,xn) cross section

There is no measurements of ^{232}U(n,2n) or ^{232}U(n,3n) reaction cross section. These cross sections would be estimated using ^{232}U(n,f) fission cross section fit up to ∼7.5 MeV as the only constraint. Present estimate of ^{232}U(n,2n) cross section around maximum is about twice lower than that of JENDL-3.2 [11], the estimate of ENDF/B-VI seems unrealistically high (see Fig. 53). Present estimate of ^{232}U(n,3n) cross section is compatible with that of JENDL-3.2 [11], except the threshold region, the estimate of ENDF/B-VI also seems unrealistically high (see Fig. 54).

9 Neutron emission spectra

Neutron emission spectra are inclusive of both fission and scattered neutrons. First we will describe the approach used for prompt fission neutron number ν and prompt fission neutron spectrum calculation and then return to the discussion on neutron emission spectra. A brief survey of the model used to estimate prompt fission neutron number ν value and PFNS is provided below.

9.1 Prompt fission neutron number ν

Figure 55 shows the neutron multiplicity ν values for actinide nuclei at thermal incident neutron energy [36, 37, 38, 39, 40, 41, 42, 43, 44, 45, 46, 47, 48, 49, 50, 51, 52, 53, 54]. One can see that thermal energy data point ν^{th} =3.13±0.06 [42] of the prompt neutron multiplicity for ^{232}U(n,f), is discrepant with other actinide nuclei measurements. The systematics [55] predicts ν^{th} =2.506 for ^{232}U(n,f) reaction. Systematic trend predicted in [55] for actinide nuclei is compatible with most of measured data. The systematics reproduces the general tendency for the ν dependence on the mass number of the compound nuclei, though for some nuclei the discrepancy with systematics is beyond ∼3 variances. Data for two reactions, ^{232}U(n,f) and ^{236}Np(n,f), deviate remarkably from the predicted [55] compound nucleus mass number dependence of ν. Measured ν values for the thermal point energy of uranium isotopes are shown on Fig. 56. Similar discrepancy could be viewed, though a slight upward trend is predicted for neutron-deficient uranium nuclei.

In the systematics [55] the νth value is defined by the fission energy balance. The following values were assumed for the following quantities: energy release E_r =185.67 MeV, total kinetic energy TKE =169.52 MeV and energy removed by emitted prompt fission neutron $E = B_n + \langle E \rangle$ =8.746 MeV. Total kinetic energy TKE value makes major influence on the calculated ν^{th} value. There is only one experiment [56], in which TKE =169±0.5 MeV was measured, this value is compatible with the estimate of [55]. The semi-empirical equation, used to estimate TKE [57]

$$TKE = 0.104 * (Z^2/A^{0.333}) + 24.7, \tag{19}$$

gives TKE =167.4 MeV, ν^{th} =2.75 corresponds to this TKE value. Zamyatnin et al. [58] recommend to use TKE =169.5 MeV. Reducing TKE value by ∼ 5 MeV, calculated estimate of νth at thermal energy point could be increased and made compatible with measured data by Jaffey et al.[42]. It might be assumed that ν^{th} measured data [42] point contains some systematic error, otherwise systematics [55] should be rejected, at least for the ^{232}U(n,f) and ^{236}Np(n,f) reactions. On the basis of the TKE data scatter, the uncertainty for the evaluated data of νth =2.506±0.24 [55] could be estimated.

At incident neutron energies above emissive fission threshold the number of prompt fission neutron $\nu(E_n)$ was calculated as

$$\begin{aligned} \nu(E_n) &= \beta_o\nu_o(E_n) + \beta_1(1 + \nu_1(E_n - B_{nA} - \overline{E}_1)) + \\ &\quad \beta_2(2 + \nu_2(E_n - B_{nA} - B_{nA-1} - \overline{E}_1 - \overline{E}_2)). \end{aligned} \tag{20}$$

Here, $\nu_i(E_n)$ is a prompt fission neutron number for ith fissioning nucleus, B_{nA} - neutron binding energy for the A nucleus, $\overline{E}_i$- average energy of ith neutron. To

calculate the ν-value energy dependence for ^{232}U(n,f) up to 20 MeV we should know also ν-values for ^{231}U and ^{230}U target nuclides, which contribute to the observed ν-value via emissive fission processes (see Fig. 57). The energy dependence of ν versus incident neutron energy estimated with this equation is compared on Fig. 58 with previous evaluations. Bump in $\nu-$value above (n,nf) reaction threshold is once again due to pre-fission neutrons emitted in ^{232}U(n,nf) reaction. The similar behavior was measured in experiments for ^{232}Th(n,f) and ^{238}U(n,f) and was reproduced in the framework of present model. The first-chance ν_p-values [55] for ^{230,231,232}U target nuclides are shown in Table 10.

9.2 Prompt fission neutron spectra

Prompt Fission Neutron Spectra (PFNS) for ^{232}U have been calculated with the model that was previously applied for ^{238}U and ^{232}Th PFNS data analysis [8]. Here is enclosed a brief description of the PFNS model.

Table 10.

The evaluated first chance ν-values for ^{230,231,232}U target nuclides.

Target	ν^{th}	ν(E, MeV)	ν(6 MeV)
^{230}U	2.632	2.679 (0.57 MeV)	3.307
^{231}U	2.632	2.679 (0.57 MeV)	3.307
^{232}U	2.506	2.667(1.92 MeV)	3.196

9.2.1 Model for PFNS evaluation

In the energy range of first chance fission ($E_n \lesssim 5$ MeV) the PFNS are calculated as sum of two Watt distributions [59]:

$$S_i(E, E_n) = 0.5 \cdot \sum_{j=1,2} W_i(E, E_n, T_{ij}(E_n), \alpha) \tag{21}$$

where

$$T_{ij} = k_{ij} \cdot \sqrt{E^*} = k_{ij} \cdot \sqrt{E_r - TKE + B_n + E_n} \tag{22}$$

is the temperature parameters for nucleus "i" and light and heavy fragments (j=1,2) for nucleus "i", E_n is the incident neutron energy, α is the ratio of the total kinetic energy (TKE) at the moment of the neutron emission to the TKE value at full acceleration. Free parameter α was fitted to the PFNS experimental data for a number of nuclei, values for the specific nuclei scatter not much. The ratio of "temperatures" for light and heavy fragment r=1.248 is the second semi-empirical fitting parameter, it also varies from one target nucleus to another

only slightly, so we assumed r=1.248 for all actinide nuclei. Present model exhibits some deviations from the Maxwellian (see Fig. 59) for E_n =3 MeV. The Maxwellian distribution underestimates the low ($E \lesssim 2$ MeV) and high ($E \gtrsim 12$ MeV) energy tail contributions. Present model predicts also higher average energy $\langle E \rangle$=2.070 MeV instead of 2.026 MeV for JENDL-3.2 and ENDF/B-VI for E_n =3 MeV.

Above emissive fission threshold the PFNS are described by the equation:

$$\begin{aligned} S(E,E_n) &= \nu^{-1}(E_n)(\nu_o(E_n)\cdot\beta_o(E_n)\cdot S_o(E,E_n) + \\ &\quad \nu_1(E_n)\cdot\beta_1(E_n)\cdot S_1(E,E_n) + \beta_1(E_n)\cdot P_{11}(E,E_n) + \\ &\quad \nu_2(E_n)\cdot\beta_2(E_n)\cdot S_2(E,E_n) + \\ &\quad \beta_2(E_n)\cdot[P_{21}(E,E_n) + P_{22}(E,E_n)] + ...), \end{aligned} \tag{23}$$

$$\int P_{ij}(E,E_n)dE = 1,$$

$$\nu(E_n) = \sum_{i=0}[\nu_i(E_n) + i)\cdot\beta_i(E_n)], \tag{24}$$

where subscript i =0, 1, 2 denotes i-th chance fission reaction of the $A+1$, A, $A-1$ nucleus after emission of i pre-fission neutrons, $\beta_i(E_n)$ is the i-th chance fission contribution to the observed fission cross section (see Fig. 50), $\nu_i(E_n)$ is the number of the prompt fission neutron for these nuclei, $S_i(E,E_n)$ is PFNS spectrum without pre-fission neutrons, $P_{ik}(E,E_n)$ is the spectrum of k-th pre-fission neutron for $i-$th chance fission. To calculate total PFNS, $\nu_i(E_n)$, $\beta_i(E_n)$ and T_{ij} values should be known.

The pre-fission neutron spectra $P_{ik}(E,E_n)$ and average neutron energy $<E_{ik}>$ were calculated as described in [60]. The pre-equilibrium pre-fission neutron emission was also taken into account.

The excitation energy U_i of the nucleus $A_i = A+1-i$ after emission of i-neutrons was calculated as:

$$U_i = E_{ri} + B_n + E_n - \sum_j (B_j + \langle E_{ij}\rangle), \tag{25}$$

where B_j is the neutron binding energy. This allows to estimate the excitation energy of fission fragments as $E^* = E_r + U - TKE$ and calculate the $T_{ij}(E_n)$ energy for each nucleus in the chain. We assumed that excitation energy U_i is brought into A_i nucleus with the reaction: $n+A_i-1 \rightarrow fission$. Incident neutron energy in this hypothetical reaction equals to $U_i - B_{i-1}$. In this way the $\nu_i(E_n)$ functions for all isotopes in the chain $A+1, A, A-1$ were evaluated (see above).

For incident neutron energies $E_n \gtrsim 10$ MeV we incorporated an additional correction to remove a discrepancy between measured and calculated data for PFNS

of ^{238}U(n,f) and ^{232}Th(n,f) reactions [8]. We assume that the same correction for CMS energy per one nucleon E_{v0} should be introduced for ^{232}U(n,f) reaction. The CMS energy was calculated according to the equation:

$$E_v = \alpha \cdot \alpha_1 \cdot E_{v0}, \tag{26}$$

α_1=1 for E_n<10 MeV and α_1=0.7 for E_n >12 MeV and linearly interpolated for 10< E_n <12 MeV. This correction was made either for non-emissive and emissive fission reactions.

9.2.2 Spectrum of pre-fission neutrons

To calculate neutron energy distributions of (n,$x$nf) and (n,xnγ), x = 1, 2, 3 reactions we use a simple Weisscopf-Ewing evaporation model taking into account fission and gamma-emission competition to neutron emission. The pre-equilibrium emission of first neutron is fixed by the description of high energy tail of ^{238}U(n,2n) reaction cross section and ^{238}U(n,f) reaction cross section. This feature was parameterized within a conventional exciton model similar to that used in STAPRE [21] code, we obtained the main parameter of the exciton model, that is the matrix element $M^2 = 10/A^3$. We accepted this pre-equilibrium model parameters for the ^{232}U+n interaction modelling. Partial contributions of emissive and non-emissive fission reactions to the observed fission cross section, shown on Fig. 50, were fitted. First neutron spectrum of the ^{232}U(n,nf) reaction is the sum of evaporated and pre-equilibrium emitted neutron contributions. Second and third neutron spectra for ^{232}U(n,$x$nf) fission reactions are assumed to be evaporative. Pre-fission neutron spectrum, especially hard energy tail of ^{232}U(n,nf) reaction, is sensitive to the description of fission probability of ^{232}U compound nuclide near fission threshold (see below).

9.2.3 Comparison with calculated ^{238}U PFNS

In ENDF/B-VI data file prompt fission neutron spectra are similar to those of JENDL-3.2, i.e. Maxwellian spectrum was employed up to 20 MeV in both evaluations. Calculated PFNS of ^{238}U(n,f) spectra reproduce available measured data. We will compare with them calculated PFNS of ^{232}U(n,f) to define the influence of different partial chance fission contributions.

In the domain of emissive fission rather different contribution of (n,nf) reaction for the ^{232}U(n,f) reaction, than in case of ^{238}U(n,f) reaction [8] is observed. Relative contribution of ^{232}U (n,nf) reaction is lower than in case of ^{238}U (n,nf) reaction for $E_n \lesssim 9$ MeV. At the other hand, relative contribution of ^{232}U (n,nf) reaction is much higher than in case of ^{238}U (n,nf) reaction for $E_n \gtrsim 9$ MeV. The low energy spectrum component due to pre-fission neutrons makes a strong influence on the PFNS shape. For ^{232}U(n,f) reaction the contribution of pre-fission neutrons from (n,nf) reaction to the observed PFNS in fission neutron energy

range $E_{th} \sim \ E_n - B_f$ should be less pronounced than in case of ^{238}U(n,f) for $E_n \lesssim$9 MeV and more pronounced for higher incident neutron energies (see Figs. 60, 61, 62 and 63, where PFNS for ^{232}U(n,f) and ^{238}U(n,f) reactions at $E_n = 7$, 10, 14 and 20 MeV are compared). Actually, the energy dependence of PFNS for ^{232}U(n,f) and ^{238}U(n,f) reactions at fission neutron energies $E_n \lesssim E_{th}$ resembles the shape of fission probability of ^{232}U or ^{238}U nuclide, respectively. Figure 50 shows the comparison of emissive chance fission contributions to the total fission cross section of ^{232}U (n,f) and ^{238}U (n,f) reactions. Data on fission probability of ^{232}U, measured in transfer reaction [35] are compared with calculated fission probability of ^{232}U for the reaction ^{231}U(n,f) on Fig. 51. The decreasing trend of ^{232}U(n,f) above $E_n \gtrsim$7.5 MeV (see Fig. 49) is correlated with the absorption reaction cross section. The contribution of ^{232}U(n,nf) reaction cross section to the observed fission cross section ^{232}U(n,f) is shown on Fig. 50. For $E_n \lesssim 9$ MeV contribution of (n,nf) reaction to the total fission cross section in case of ^{232}U target is lower than in case of ^{238}U target, while for $E_n > 9$ MeV it is much higher. The latter peculiarity is a direct consequence of high ^{232}U target nuclide fissility with neutrons and consequent high non-emissive fission contribution to the observed fission cross section. At E_n =7 MeV (see Fig. 60) low energy components due to pre-fission neutrons from (n,nf) reaction reduce average energy very much as it was observed for ^{238}U(n,f) and ^{232}Th(n,f) reactions. Since the contribution of (n,nf) reaction at E_n =7 MeV is higher in case of ^{238}U(n,f), than in case of ^{232}U(n,f), it is pronounced in the low energy part of PFNS (see Fig. 60). At $E_n = 10$ MeV the (n,nf) contributions of PFNS are similar for ^{232}U(n,f) and ^{238}U(n,f) reactions (see Fig. 61). However, the situation is quite different for higher incident energies $E_n \gtrsim$10 MeV (see Fig. 62, 63), the contribution of (n,nf) reaction in PFNS now is higher in case of ^{232}U(n,f) reaction. As shown on Figs. 50, 57 the contribution of (n,2nf) reaction to the observed $\nu-$value is rather small, it is much smaller than in case of ^{238}U(n,f) reaction.

The average energy of the fission neutron versus incident energy is shown in Fig. 64. At incident neutron energy $E_n \lesssim 6$ MeV, the $\nu-$value energy dependence is proportional to $\sqrt{U_i}$, however, at higher excitations we have more complicated excitation energy dependence. At $E_n \sim$7 MeV the average energy reduces by $\sim$150 keV due to the contribution of low energy neutrons from (n,nf) reaction. The tendency visible in measured data for the ^{238}U(n,f) PFNS is predicted for the ^{232}U(n,f) reaction.

9.3 Neutron emission spectra data analysis

There are no measured data on neutron emission spectra for ^{232}U+n interaction. Relative contribution of prompt fission neutron spectra to the neutron emission spectra is much higher than in case of ^{238}U+n interaction. In case of ^{238}U calculated neutron emission spectra reproduce structures in measured data, these structures are correlated with excitation of first octupole band ($K^\pi = 0^-$) levels

and levels of $\beta-$ vibration ($K^\pi = 0^+$) and $\gamma-$bands ($K^\pi = 0_2^+, 2^+$). Estimates of inelastic scattering to vibrational levels of first octupole band and higher lying $\beta-$ and $\gamma-$ bands of ^{238}U were shown to be extremely important for incident neutron energies $E_n \leq 3$ MeV. In case of ^{232}U there is no measured data to define a resolution function. The parameters of resolution function usually are fitted to the elastic peak shape. Using the parameters obtained for ^{238}U+n data description in case of ^{232}U+n, one can observe that the structures due to discrete level excitation is no longer visible. They could be revealed introducing a better secondary neutron energy resolution. Figures 65–71 show emission spectra, calculated for 1.2, 2.6, 3.55, 6.1, 11.8. 14.05 and 18 MeV, these energies were selected because for these energies emission neutron spectra were measured for ^{238}U target nuclide [61, 62, 63].

The direct excitation of ground state rotational band levels 0^+, 2^+, 4^+, $6^+$and 8^+ was estimated within rigid rotator model. To calculate the direct excitation cross sections for $\beta-$ vibration ($K^\pi = 0^+$) and anomalous rotation band (K^π= 2^+) as well as octupole (K^π=0^-) band levels a soft rotator model was employed. Due to strong fission reaction competition in case of ^{232}U+n interaction, compound inelastic scattering is rather low and direct contribution to inelastic scattering is appreciable. For ground state band levels the direct and compound components became comparable above ~1.5 MeV, for octupole (K^π=0^-) band levels - above ~2.5 MeV, while for $\beta-$ vibration ($K^\pi = 0^+$) levels - above ~3 MeV. With increase of incident energy the influence of discrete level excitation diminishes, while the role of continuum level excitation grows.

Figures 65-67 show the comparison of present calculations with JENDL-3.2 evaluated emission spectra below emissive fission threshold. Bumps evident in neutron emission spectra for E_n ~2 - 4 MeV could be correlated with excitation of discrete levels of various collective bands. The elastic as well as inelastic scattering to 2^+, 4^+ and 6^+ levels of ground state rotational band contribution was added to the other inelastic scattered and fission neutrons. They were broadened using model resolution function of Gaussian type with a constant resolution width. PNFS labels prompt neutron fission spectra. Arrows on figures show emitted neutron energy, corresponding to excitation of octupole and $\beta-$vibration levels.

To calculate neutron energy distributions of (n,xnγ) and (n,$x$nf), x = 1, 2, 3 reactions we use a simple Weisscopf-Ewing evaporation model taking into account fission and gamma-emission competition to neutron emission. The pre-equilibrium emission of first neutron is included. The hard component of neutron scattering spectra and high energy tail of ^{232}U(n,2n) reaction cross section are interpreted as being due to the pre-equilibrium evaporation of neutrons. This feature is parameterized within a conventional exciton model, used in STAPRE [21] code. Pre-equilibrium contribution of first neutron spectrum was fixed by consistent description of (n,f), (n,2n) and (n,3n) reaction cross sections up to 20 MeV, we get the main parameter of the exciton model, that is the matrix element $M^2 = 10/A^3$. The charge conservation and transition rates renormalization were

also employed. With all that in mind and in the STAPRE code [21] a pre-equilibrium emission fraction $q(E)$ leading to depletion of compound nucleus states population is obtained. It equals ∼0.05 at $E_n = 4$ MeV and increases up to ∼0.35 at $E_n = 20$ MeV. First neutron spectra for the (n,nx) reaction is the sum of evaporated and pre-equilibrium emitted neutron contributions. Second and third neutron spectra are assumed to be evaporative.

For incident neutron energy higher than emissive fission threshold, emissive neutron spectrum is deconvoluted, components of 1st, 2nd and 3d neutron spectra are provided, where applicable. We have calculated 1st, 2nd and 3d neutron spectra for the (n,nγ), (n,2n) and (n,3n) reactions. According to the ENDF/B-VI format specifications the secondary neutron spectra are included in the following way. Calculated spectra were summed up and tabular spectra for the (n,nγ), (n,2n) and (n,3n) reactions were obtained. To clarify the competition of neutron, γ-emission and fission in case of (n,nx) and (n,2nx) reactions the following presentation of spectra is provided. Figures 72 and 73 show secondary neutron spectra of the reaction (n,nx) and its partial contributions for (n,nγ), (n,2n), (n,nf) (n,2nf) and (n,3n) reactions at incident neutron energy of 20 and 14 MeV. The partial neutron spectra are normalized to the contributions of appropriate cross sections to the (n,nx) reaction cross sections. Above ∼5 MeV energy of first emitted neutron, neutron spectrum is of pre-equilibrium nature. Spectrum of (n,nγ) reaction actually is just hard energy tail of 'pre-equilibrium' component of first neutron spectrum. Spectrum of the first neutron of (n,2n) reaction is much softer, although 'pre-equilibrium' component still comprise appreciable part of it. First neutron spectrum of (n,3n) reaction is actually of evaporative nature. First neutron spectrum of (n,nf) reaction has rather long pre-equilibrium high-energy tail . First neutron spectrum of (n,2nf) reaction, as that of (n,3n) reaction, is of evaporative nature.

Figures 74, 75, 76 and 77 compare neutron spectra of (n,nγ) reaction of JENDL-3.2 [11] and ENDF/B-VI [9] with present calculation. Neutron spectra of JENDL-3.2 [11] and ENDF/B-VI [9] are evaporative. Average energies of first neutron spectra for JENDL-3.2 and ENDF/B-VI are much lower than that of present evaluation.

Figures 78 and 79 show spectra of 2nd neutron of the reaction (n,2nx) and its partial contributions for (n,2n), (n,3n), (n,2nf) etc. reactions for 14 and 20 MeV incident neutron energy. Spectrum of (n,2n) reaction neutron seems to be the hardest one at 20 MeV. Figures 80 and 81 show the comparison of (n,2n) reaction spectra of JENDL-3.2, ENDF/B-VI and present evaluation at 20 and 14 MeV. The discrepancies above ∼5 MeV and ∼3 MeV, respectively, are due to first neutron spectra of (n,2n) reaction in present calculation (see Figs. 72, 73) being of pre-equilibrium nature. In JENDL-3.2 and ENDF/B-VI spectrum of (n,2n) reaction is evaporative. Figure 82 shows the comparison of (n,2n) reaction spectra of JENDL-3.2 and present evaluation at 8 MeV. In contrast to first neutron spectra, present (n,2n) reaction spectrum seems to be softer than those

of JENDL-3.2 and ENDF/B-VI. The same happens with spectrum of (n,3n) reaction (see Figs. 83, 84), shown on Fig. 84 for incident neutron energy of 14 MeV.

In summary, inclusion of pre-equilibrium emission changes significantly the average energies of emitted neutron spectra. That is shown in Table 11, where the average secondary neutron energies for current, ENDFB-VI and JENDL-3.2 evaluations are compared. The most significant is the change of neutron spectra of (n,nγ) reaction. First neutron spectra of (n, n'f) reaction also becomes harder, that influences prompt fission neutron spectra. On the other hand, the spectra of 2nd and 3d neutrons become softer.

Table 11.

Average energies of secondary neutron spectra for ^{232}U+n

1st neutron average energy, MeV							
E_n, MeV	(n,n')			(n,2n)	(n,n'f)	(n,3n)	(n,2n'f)
	Pres.	J-3.2	B-VI	Present	Present	Present	Present
2.0	0.496	0.510	0.500				
8.0	2.872	1.016	1.331	0.45	1.16		
14.0	9.544	1.385	1.744	2.37	2.66	0.31	0.58
20.0	15.58	1.672	2.077	8.58	4.13	1.76	2.45

$\langle E \rangle$ for (n,2n), MeV				$\langle E \rangle$ for (n,3n), MeV		
E_n, MeV	Present	J-3.2	B-VI	Present	J-3.2	B-VI
8.0	0.321	0.407	0.428			
14.0	1.646	1.116	1.720	0.256	0.450	0.485
20.0	4.841	1.462	2.076	1.241	1.236	2.015

10 Conclusions

The statistical Hauser-Feshbach-Moldauer model calculation of neutron-induced reaction cross sections for ^{232}U target nucleus shows the fair description of available data base on total and fission cross sections. Statistical calculations were employed for predicting capture, inelastic, (n,2n), (n,3n) and fission reaction (above (n,nf) threshold) cross sections. Rigid and soft rotator coupled channel models were used to predict inelastic scattering cross sections for level excitation. Prompt fission neutron spectra are predicted with the model, tested on the PFNS description of ^{238}U(n,f) and ^{232}Th(n,f) reactions. Reich-Moore and average unresolved resonance parameters are provided.

11 Acknowledgments

This work was supported within the Project B-404 "Actinide Nuclear Data Evaluation" of International Science and Technology Center (Funding Party Japan).

*) Permanent address: Institute of Physics and Power Engineering, 249020, Obninsk, Russia

References

[1] Simpson,O.D., Moore M.S., Berreth J.R., Nucl. Sci. Eng. 29, 415 (1967).

[2] Auchampaugh G.F., Bowman C.D., Evans J.E., Nucl. Phys., A112, 329 (1968).

[3] Farrell, J.A. LA-4420,3 (1970).

[4] Fursov B.I. Samylin B.F., Klemyshev et al.,Sov.Journ. of Atomic Energy,61,963 (1986).

[5] Vorotnikov, P.E., Dubrovina, S.M., Otroshchenko, G.A., et al. . Yadernaya Fizika, 12(3), 474 (1970).

[6] Maslov V.M., Kikuchi Y., Nucl. Sci. Eng. 124, 492 (1996).

[7] Maslov V.M., INDC(BLR)-13, IAEA, Vienna (1998).

[8] V.M. Maslov, Yu. V. Porodzinskij, M. Baba, A. Hasegawa, N.V. Kornilov, A.B. Kagalenko "Neutron Scattering on ^{238}U and ^{232}Th", Abstracts of International Conference on Nuclear Data for Science and Technology, October 7-12, 2001, Tsukuba, Japan (2001).

[9] Roussin R.W., Young P.G., McKnight R., Proc. Int. Conf. Nuclear Data for Science and Technology, Gatlinburg, USA, May 9-13, 1994, p. 692, J.K. Dickens (Ed.), ANS (1994).

[10] Mughabghab S.F.and Garber D.I., BNL-325, VOL. 1, BRookhaven National Laboratory (1973)

[11] JAERI-Data/Code, 98-006 (Part II), (Eds.) K. Shibata and T. Narita (1998).

[12] Wright R.C., Ohsawa T., Nakagawa T., ENDF/B-VI, Rev. 2. Mod. (1999).

[13] Elson R. et al., Phys. Rev., 89, 320 (1953).

[14] Halperin HJ., Baldock C.R., Oliver J.H., Nucl. Sci. Eng., 21, 257 (1965).

[15] Stavinskij V.S., Shaker M.O., Nucl. Phys., 62, 667 (1965).

[16] Maslov V.M.,Porodzinskij Yu.V. JAERI-Research 98-038, Japan (1998).

[17] Cullen D. PREPRO2000: 2000 ENDF/B Pre-Processing Codes.

[18] NJOY 94.10 Code System for Producing Pointwise and Multigroup Neutron and Photon Cross Sections from ENDF/B Data, RSIC Peripheral Shielding Routine Collection, ORNL, PSR-355, LANL, Los Alamos, New Mexico (1995).

[19] Moldauer P.A., Phys. Rev., C11, 426 (1975).

[20] Tepel J.W., Hoffman H.M., Weidenmuller H.A. Phys. Lett. 49, 1 (1974).

[21] Uhl M., Strohmaier B., IRK-76/01, IRK, Vienna (1976).

[22] Ignatjuk A.V., Maslov V.M., Proc. Int. Symp. Nuclear Data Evaluation Methodology, Brookhaven,USA, October 12-16, 1992, p.440, World Scientific (1993).

[23] Maslov V.M., Kikuchi Y., JAERI-Research 96-030 (1996).

[24] Ignatjuk A.V., Istekov K.K., Smirenkin G.N. Sov. J. Nucl. Phys. 29, 450 (1979).

[25] Howard W.M., Möller P. Atomic Data and Nuclear Data Tables, 25, 219 (1980).

[26] Maslov V.M., Physics of Atomic Nuclei, 63, 161 (2000).

[27] Maslov V.M., Zeit. Phys. A, Hadrons & Nuclei, 347, 211 (1994).

[28] Fu C. Nucl. Sci. Engng. 86, 344 (1984).

[29] Maslov V.M., Porodzinskij Yu.V., Hasegawa A., Shibata K. JAERI-Research 98-040, Japan (1998).

[30] Shmorack M.K., Nucl. Data Sheets, 20, No.2 (1977).

[31] Myers W.O., Swiatecky W.J., Ark. Fyzik, 36, 243 (1967).

[32] Bjornholm S., Lynn J.E. Rev. Mod. Phys., 52, 725 (1980).

[33] Bolsterli M., Fiset E.O., Nucl. Sci.Eng., 63, 250 (1977).

[34] Porodzinskij Yu.V., Sukhovitskij E.Sh, Yadernaya Fyzika, 59, 247 (1996).

[35] A. Gavron, Britt H.C., Konecny E. et al., Phys. Rev. C13, 2374 (1978).

[36] Malinovskij V.V, Vorobeva V.G., Kuzminov B.D., Voprosy Atomnoi Nauki i Tekhniki, Ser. Yadernye Konstanty, 5(54), (1983).

[37] Crane W. W. T., Higgins G. H., Bowman H. R., Phys. Rev. 1804 (1956) .

[38] Hicks D. A., Ise, J., Pyle R.V., Phys. Rev. 1016, (1956) .

[39] Lebedev V. I., Kalashnikova V. I., Atomnaya Energiya 176 (1958).

[40] Lebedev V. I., Kalashnikova V. I., JETP 535 (1958) .

[41] Jaffey, A. H. , Lerner. J., Report ANL-6600, p. 124 (1961).

[42] Jaffey A.H., Lerner J.L., Nuclear Physics A145, 1 (1970).

[43] Kroshkin, N. I. , Zamyatnin Yu. S., Atomnaya Energiya 95, (1970) .

[44] Volodin K. E., Nesterov V. G., Nurpeisov, B. et al., Yadernaya Fizika 29 (1972) .

[45] Zhuravlev K. D., Zamyatnin Yu. S., Kroshkin N. I., Proc. 2nd All-Union Conf. on Neutron Phys. Kiev, 1973, Part 4, p. 57 (1973).

[46] Flynn K. F., Gindler J. E., Sjoblom R. K., Glendenin L. E., Phys. Rev. C 1676 (1975) .

[47] Thierens H., Jacobs E., D'Hondt P., DeFrenneD., DeClercq A., DeGelder P., Deruytter A. J., Blachot J., Perrin P., Nucl. Phys. A 229 (1980) .

[48] Gindler J. E., Glendenin L. E., Krapp E. L., Fernandez S. J., Flynn K. F., Henderson D. J., Journ. Inorg. Nucl. Chem. 445 (1981) .

[49] Gindler J. E. , Glendenin, L. E. , Henderson, D. J., Journ. Inorg. Nucl. Chem. 1433 (1981).

[50] Howe R. E., Nucl. Sci. Eng. 157 (1984).

[51] Holden N. E. Proc. Int. Conf. on Nucl. Data for Sci. and Technol., Mito, 1988, p. 795 (1988).

[52] Solonkin A. A. , Teplykh V. F. , Platygina E. V., Petrzhak K. A., Mosesov A. V., Atomnaya Energiya, 435 (1988) .

[53] Tellier, H. , in: Nuclear Data Standards for Nuclear Measurements, NEA OECD, p. 90 (1992).

[54] Hoffman D. C., Hamilton T. M., Lane M. R., Report LBL-33001, UC-113 (1992).

[55] Malinovskij V.V. Voprosy Atomnoi Nauki i Tekhniki, Ser. Yadernye Konstanty, 2, 25 (1987).

[56] Asghar M, Caitucoli F., et al., Nuclear Physics A368, 328 (1988).

[57] Rusanov A. Ya., Itkis M.G., Okolovich V.N., Physics of Atomic Nuclei, 60, 773 (1997).

[58] Zamyatnin Yu. S, Konovalov V.Yu, Low energy Neutron Physics, editor H. Schopper, Landolt-Bornstein, vol. 16(A), sec. 9 (2000).

[59] Kornilov N.V., Kagalenko A.B., Hambsch F.-J. Physics of Atomic Nuclei, 62, 173 (1999).

[60] Kornilov N.V., Kagalenko A.B., Maslov V.M. et. al. In: Proceedings of Trieste Conference on Nuclear Data for Science and Techology, Trieste, v. 1, p940 (1997).

[61] Baba M. et al., J. Nucl. Sci. Technol. 27, 7, 601 (1990).

[62] Miura T., Baba M., Ibaraki M. et al. Proc. of the 1998 Symp. on Nuclear Data, November 19-20, 1999, JAERI, Tokai, Japan, JAERI-Conf., 99-002, p. 101 (1999).

[63] Baba M., Matsuyama S., Ito T., et al. Proc. Int. Conf. Nucl. Data for Sci. and Technology, Julich, Germany, May 13-19, 1991, p.349 (1991).

12 Figure captions

Fig. 1 Total cross section of ^{232}U.
Fig. 2 Total cross section of ^{232}U.
Fig. 3 Total cross section of ^{232}U.
Fig. 4 Total cross section of ^{232}U.
Fig. 5 Total cross section of ^{232}U.
Fig. 6 Fission cross section of ^{232}U.
Fig. 7 Fission cross section of ^{232}U.
Fig. 8 Fission cross section of ^{232}U.
Fig. 9 Fission cross section of ^{232}U.
Fig. 10 Fission cross section of ^{232}U.
Fig. 11 Fission cross section of ^{232}U.
Fig. 12 Fission cross section of ^{232}U.
Fig. 13 Cumulative sum of levels of ^{232}U.
Fig. 14 Cumulative sum of reduced neutron width of ^{232}U.
Fig. 15 Level spacing distribution of ^{232}U.
Fig. 16 Reduced neutron width distribution of ^{232}U.
Fig. 17 Cumulative distribution of reduced neutron widths of ^{232}U.
Fig. 18 Total cross section of ^{232}U.
Fig. 19 Fission cross section of ^{232}U.
Fig. 20 Elastic scattering cross section of ^{232}U.
Fig. 21 Inelastic scattering cross section of ^{232}U.
Fig. 22 Capture cross section of ^{232}U.
Fig. 23 Total cross section of ^{232}U.
Fig. 24 Reaction cross section of ^{232}U.
Fig. 25 Elastic scattering cross section of ^{232}U.
Fig. 26 Cumulative number of levels of ^{232}U.
Fig. 27 Cumulative number of levels of ^{233}U.
Fig. 28 Level density of ^{232}U.
Fig. 29 Level density of ^{233}U.
Fig. 30 Fission cross section of ^{232}U.
Fig. 31 Fission cross section of ^{232}U.
Fig. 32 Fission cross section of ^{232}U.
Fig. 33 Cross section of ^{232}U: 0.047572 MeV, 2^+ level excitation.
Fig. 34 Cross section of ^{232}U: 0.15657 MeV, 4^+ level excitation.
Fig. 35 Cross section of ^{232}U: 0.3226 MeV, 6^+ level excitation.
Fig. 36 Cross section of ^{232}U: 0.541 MeV, 8^+ level excitation.
Fig. 37 Cross section of ^{232}U: 0.563194 MeV, 1^- level excitation.
Fig. 38 Cross section of ^{232}U: 0.628967 MeV, 3^- level excitation.

Fig. 76 Comparison of (n,n'γ) reaction neutron spectra of ^{232}U for incident neutron energy 8 MeV.
Fig. 77 Comparison of (n,n'γ) reaction neutron spectra of ^{232}U for incident neutron energy 6 MeV.
Fig. 78 Components of second neutron spectrum of ^{232}U for incident neutron energy 20 MeV.
Fig. 79 Components of second neutron spectrum of ^{232}U for incident neutron energy 14 MeV.
Fig. 80Comparison of (n,2n) reaction neutron spectra of ^{232}U for incident neutron energy 20 MeV.
Fig. 81 Comparison of (n,2n) reaction neutron spectra of ^{232}U for incident neutron energy 14 MeV.
Fig. 82 Comparison of (n,2n) reaction neutron spectra of ^{232}U for incident neutron energy 8 MeV.
Fig. 83 Comparison of (n,3n) reaction neutron spectra of ^{232}U for incident neutron energy 20 MeV.
Fig. 84 Comparison of (n,3n) reaction neutron spectra of ^{232}U for incident neutron energy 14 MeV.

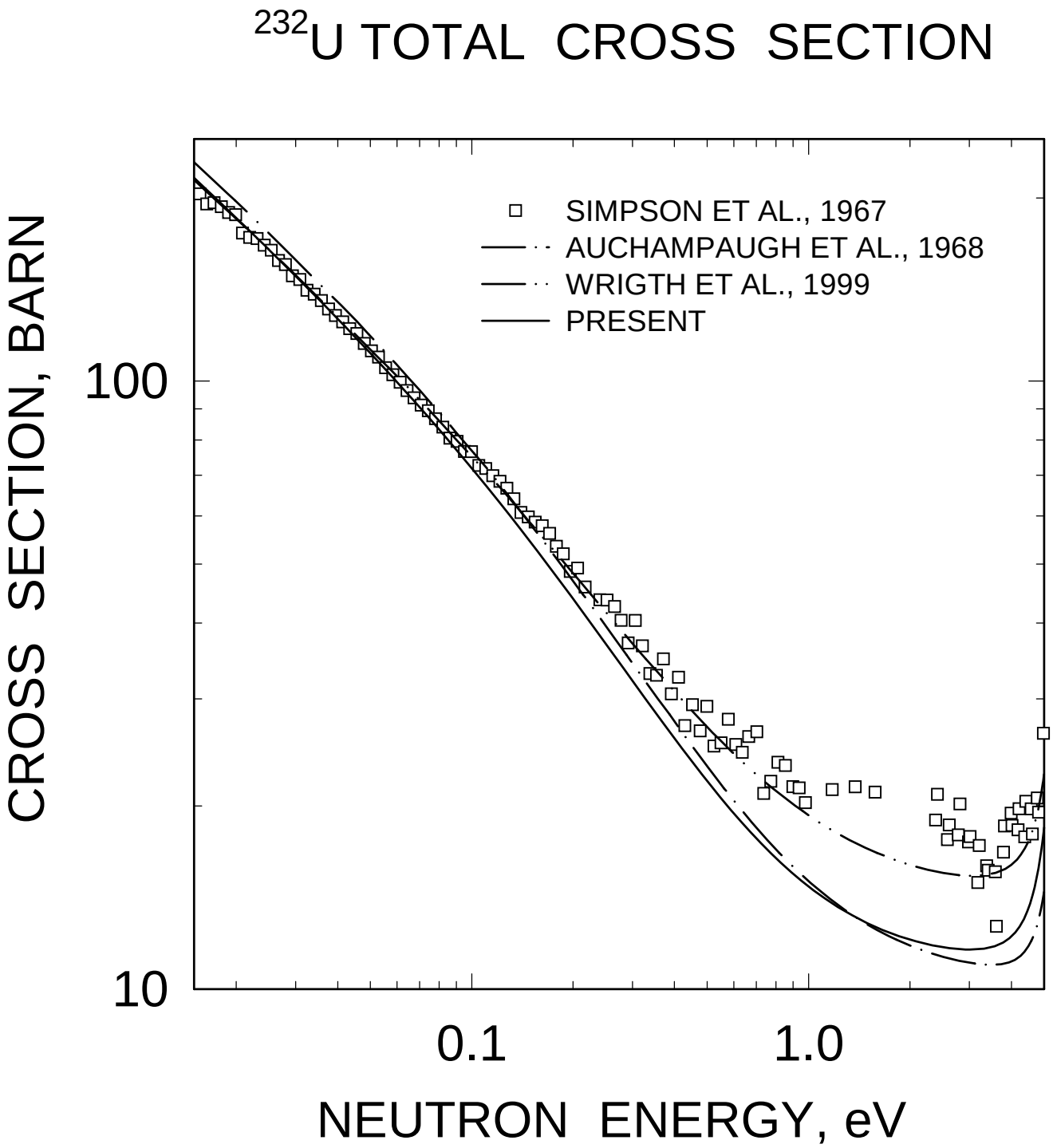
232U TOTAL CROSS SECTION
SIMPSON ET AL., 1967
AUCHAMPAUGH ET AL., 1968
WRIGTH ET AL., 1999
PRESENT
CROSS SECTION, BARN
100
10
0.1
1.0
NEUTRON ENERGY, eV

FIG. 1

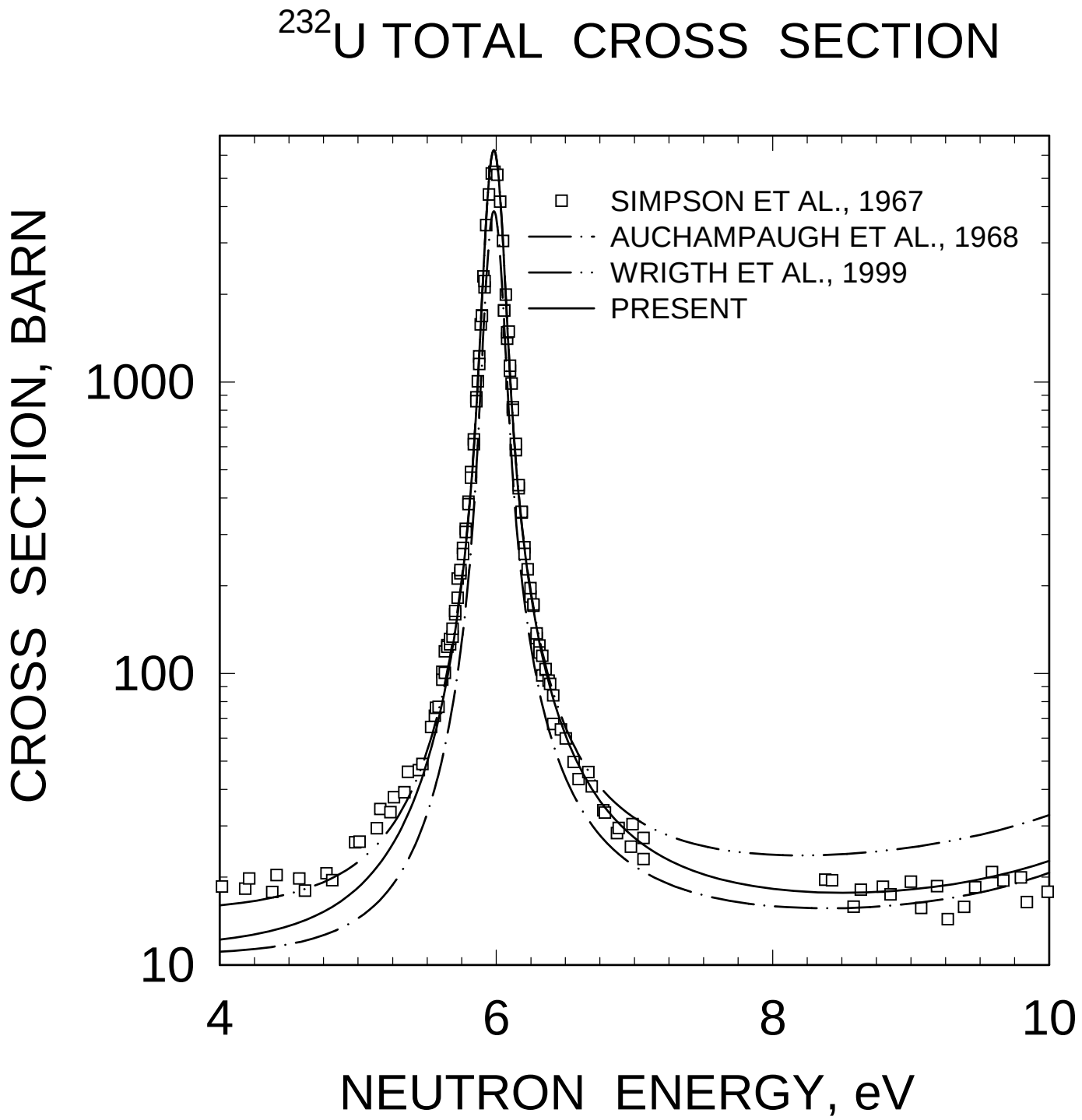
^{232}U TOTAL CROSS SECTION
SIMPSON ET AL., 1967
AUCHAMPAUGH ET AL., 1968
WRIGTH ET AL., 1999
PRESENT
CROSS SECTION, BARN
1000
100
10
4
6
8
10
NEUTRON ENERGY, eV

FIG. 2

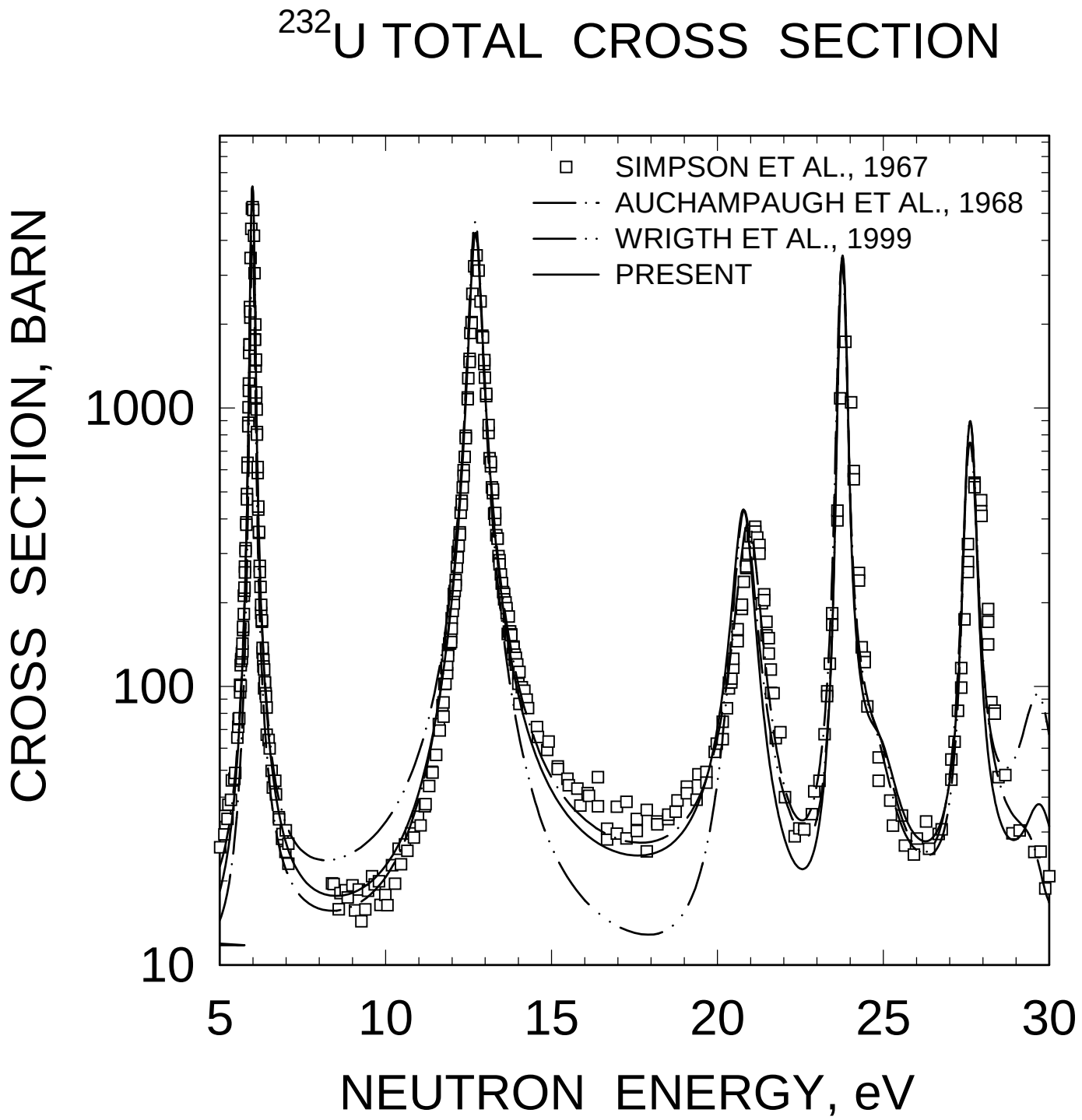
^{232}U TOTAL CROSS SECTION
SIMPSON ET AL., 1967
AUCHAMPAUGH ET AL., 1968
WRIGTH ET AL., 1999
PRESENT
CROSS SECTION, BARN
1000
100
10
5
10
15
20
25
30
NEUTRON ENERGY, eV

FIG. 3

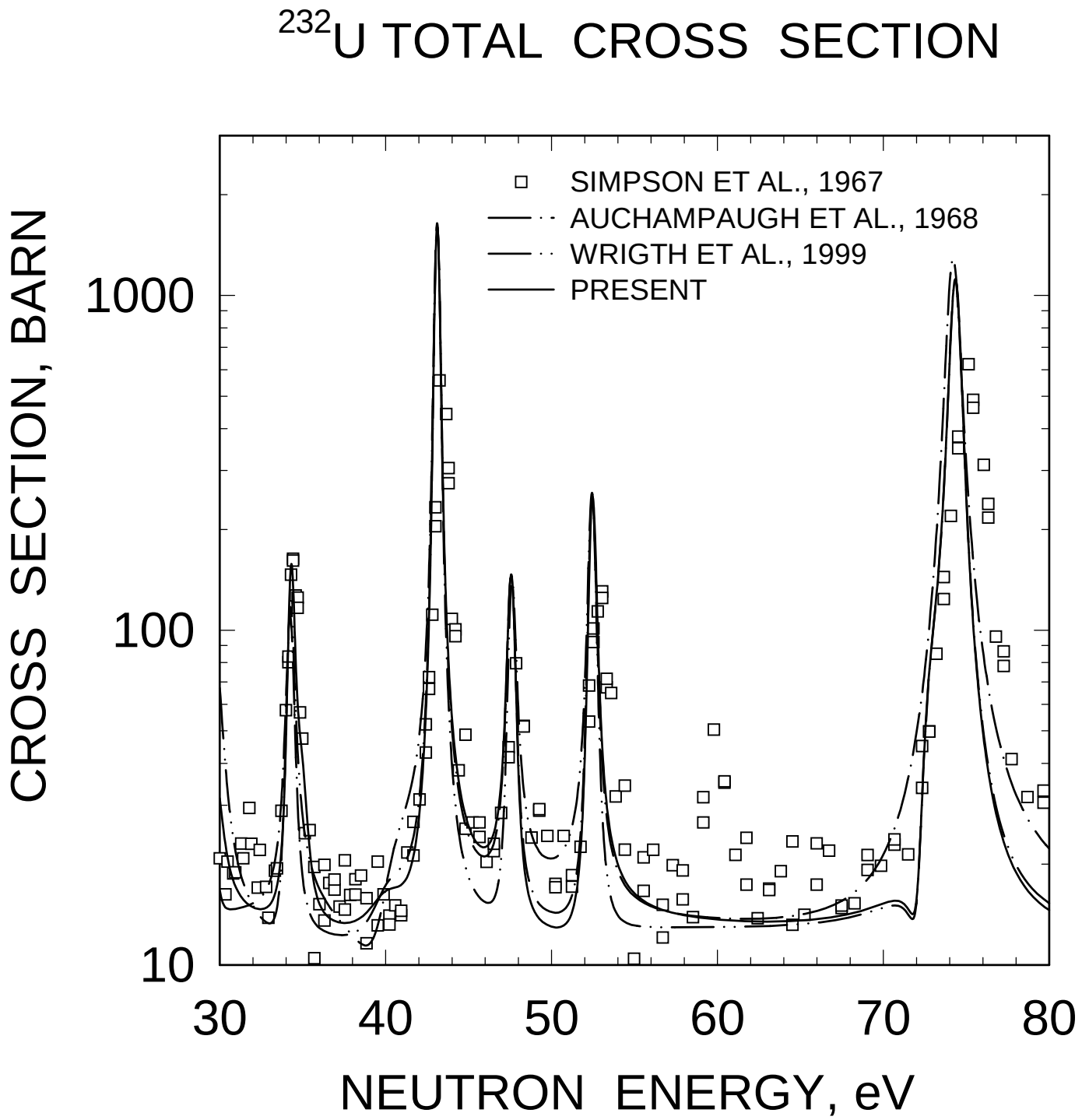
232U TOTAL CROSS SECTION
SIMPSON ET AL., 1967
AUCHAMPAUGH ET AL., 1968
WRIGTH ET AL., 1999
PRESENT
CROSS SECTION, BARN
1000
100
10
30
40
50
60
70
80
NEUTRON ENERGY, eV

FIG. 4

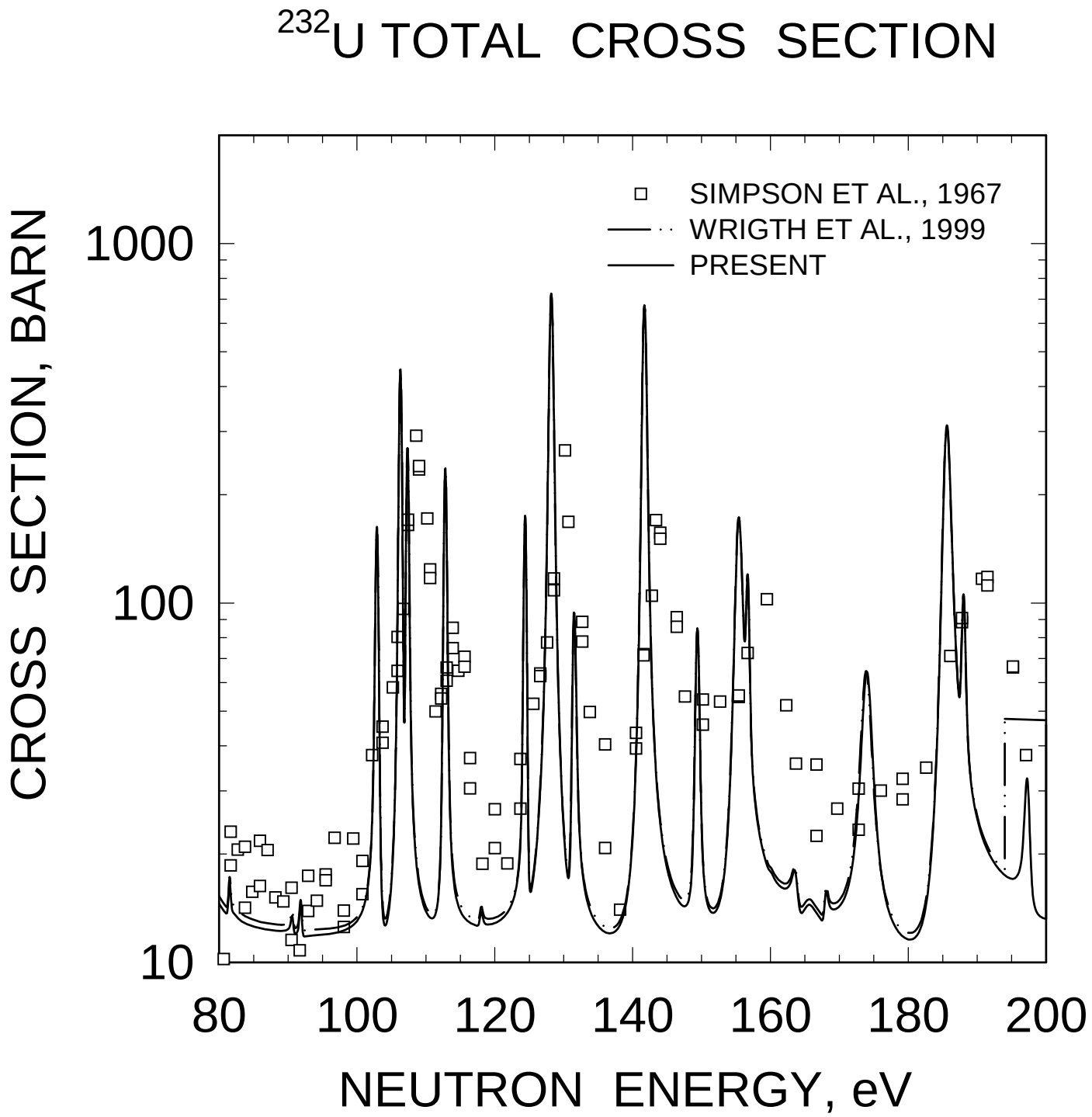
232U TOTAL CROSS SECTION
SIMPSON ET AL., 1967
WRIGTH ET AL., 1999
PRESENT
CROSS SECTION, BARN
1000
100
10
80
100
120
140
160
180
200
NEUTRON ENERGY, eV

FIG. 5

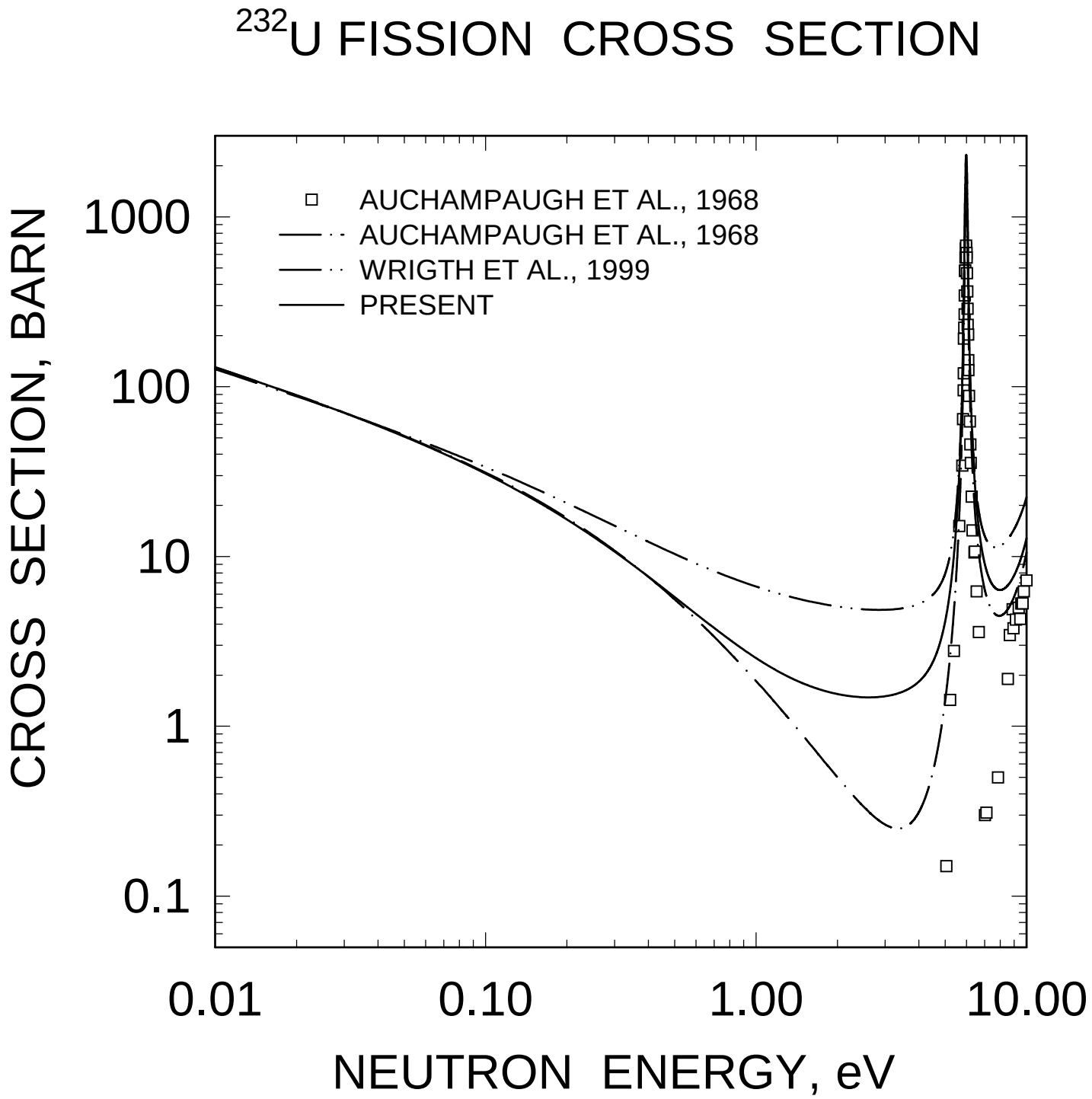
232U FISSION CROSS SECTION
AUCHAMPAUGH ET AL., 1968
AUCHAMPAUGH ET AL., 1968
WRIGTH ET AL., 1999
PRESENT
CROSS SECTION, BARN
1000
100
10
1
0.1
0.01
0.10
1.00
10.00
NEUTRON ENERGY, eV

FIG. 6

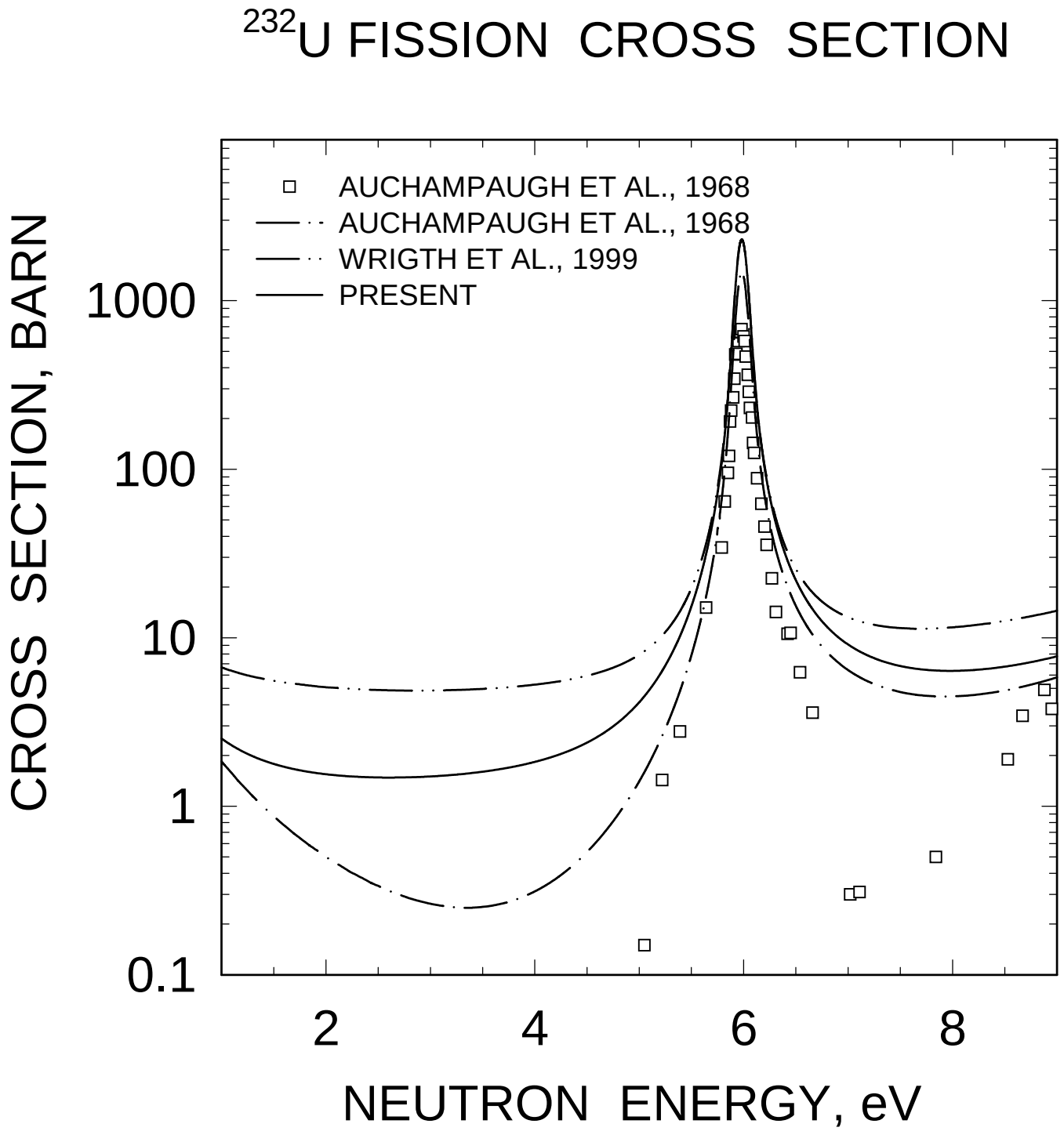
232U FISSION CROSS SECTION
AUCHAMPAUGH ET AL., 1968
AUCHAMPAUGH ET AL., 1968
WRIGTH ET AL., 1999
PRESENT
CROSS SECTION, BARN
1000
100
10
1
0.1
2
4
6
8
NEUTRON ENERGY, eV

FIG. 7

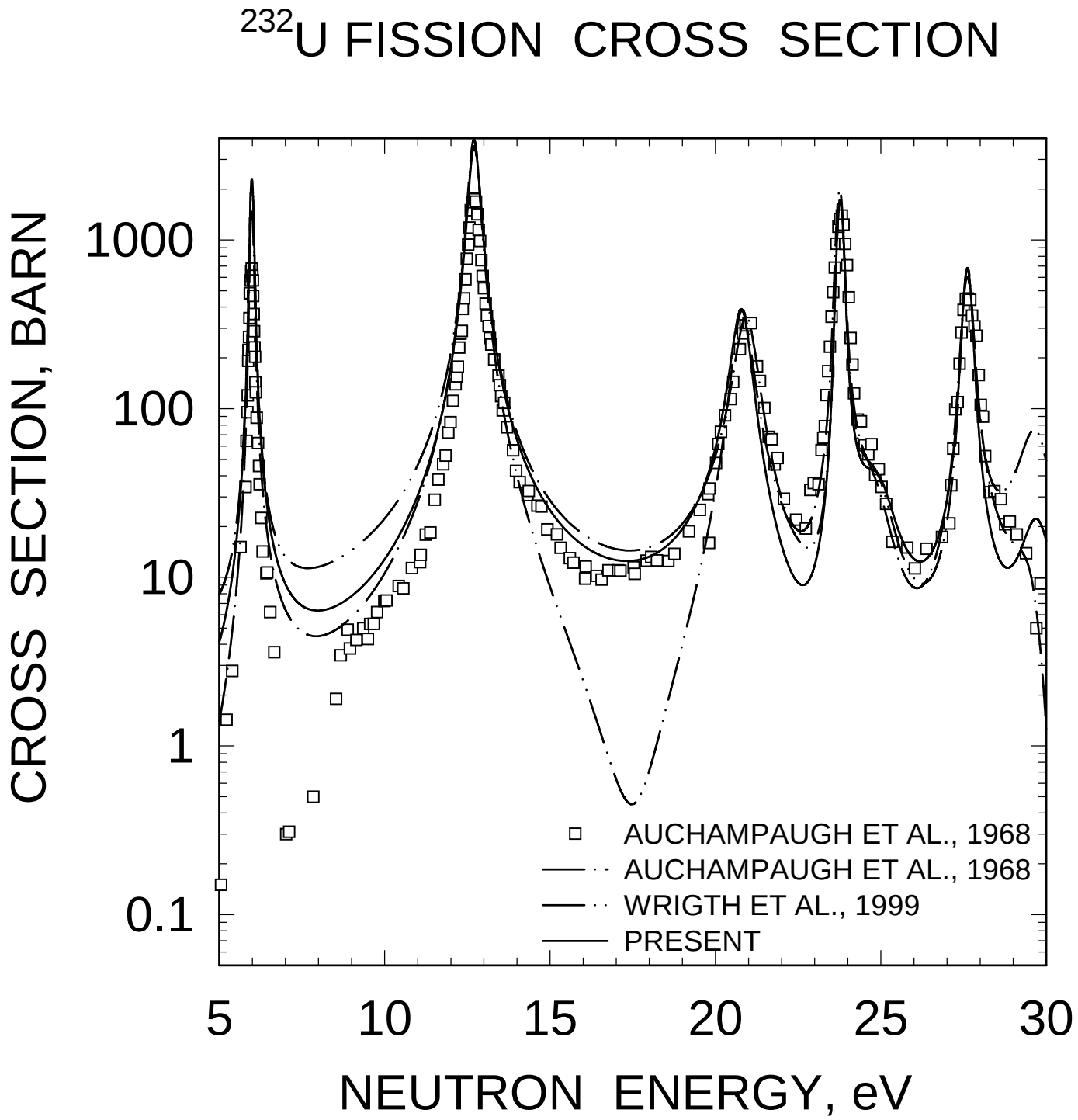
^{232}U FISSION CROSS SECTION
CROSS SECTION, BARN
1000
100
10
1
0.1
5
10
15
20
25
30
NEUTRON ENERGY, eV
AUCHAMPAUGH ET AL., 1968
AUCHAMPAUGH ET AL., 1968
WRIGTH ET AL., 1999
PRESENT

FIG. 8

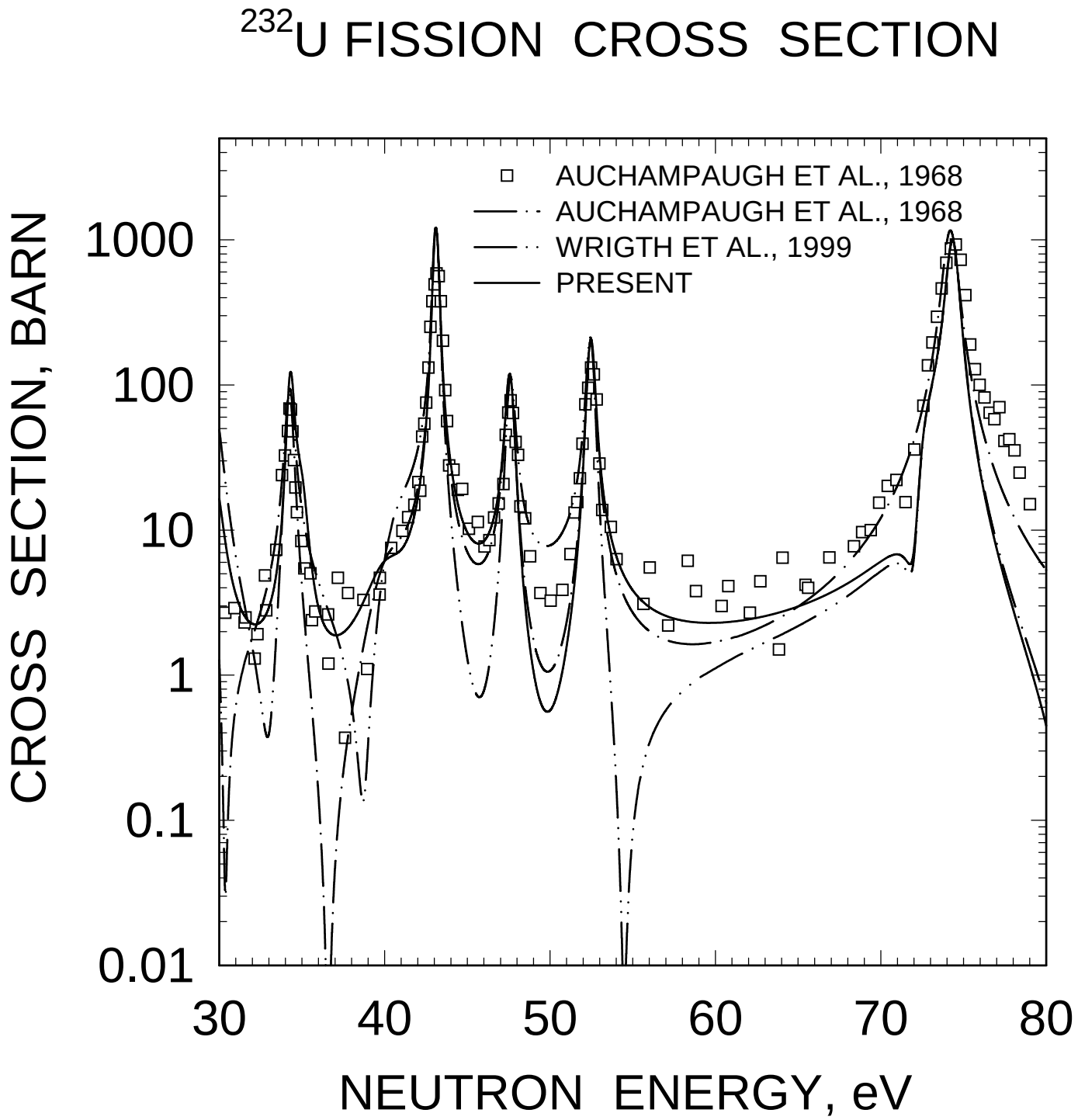
232U FISSION CROSS SECTION
AUCHAMPAUGH ET AL., 1968
AUCHAMPAUGH ET AL., 1968
WRIGTH ET AL., 1999
PRESENT
CROSS SECTION, BARN
1000
100
10
1
0.1
0.01
30
40
50
60
70
80
NEUTRON ENERGY, eV

FIG. 9

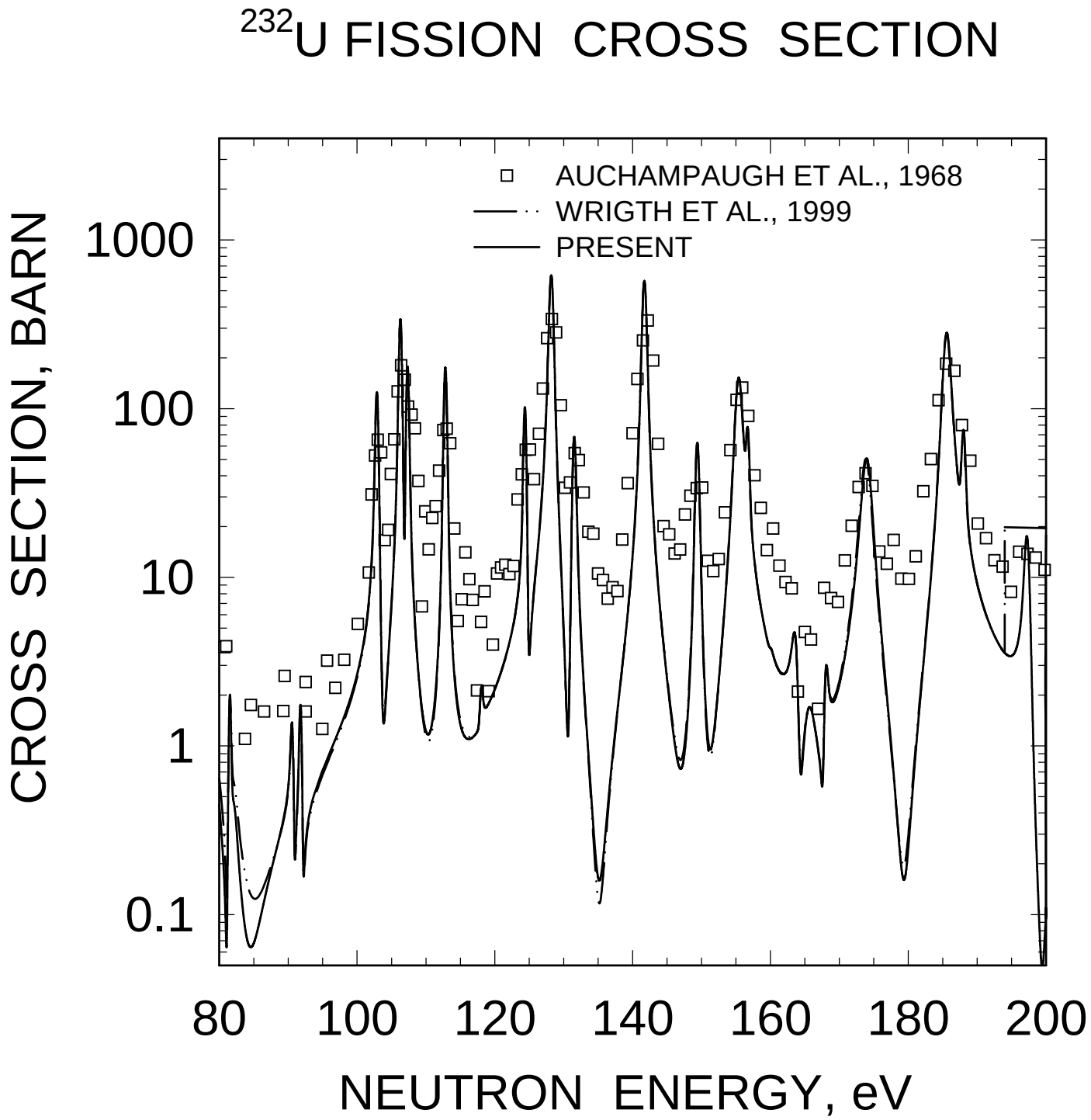
^{232}U FISSION CROSS SECTION
AUCHAMPAUGH ET AL., 1968
WRIGTH ET AL., 1999
PRESENT
CROSS SECTION, BARN
1000
100
10
1
0.1
80
100
120
140
160
180
200
NEUTRON ENERGY, eV

FIG. 10

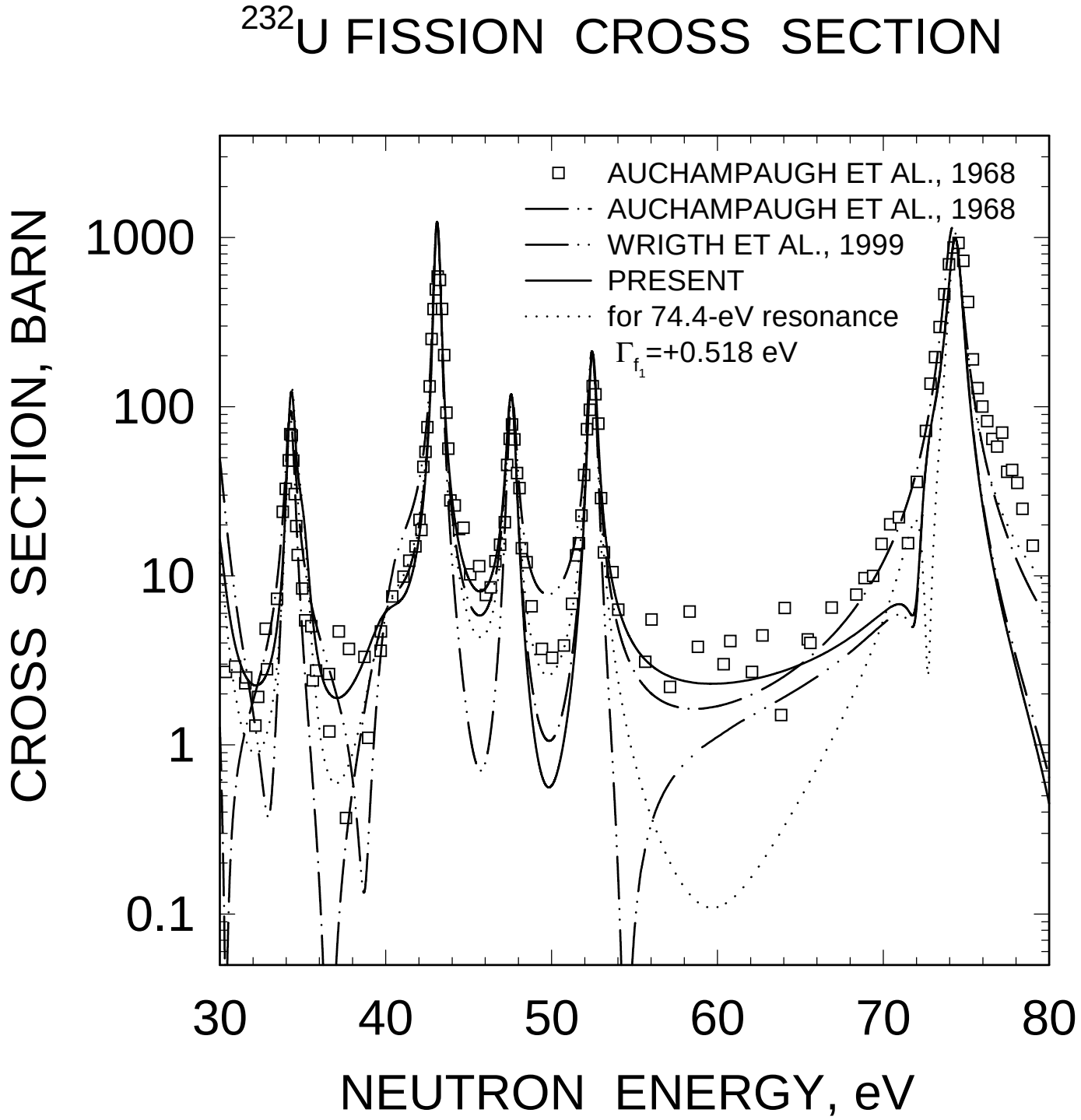
232U FISSION CROSS SECTION
AUCHAMPAUGH ET AL., 1968
AUCHAMPAUGH ET AL., 1968
WRIGTH ET AL., 1999
PRESENT
for 74.4-eV resonance
Γf1=+0.518 eV
CROSS SECTION, BARN
1000
100
10
1
0.1
30
40
50
60
70
80
NEUTRON ENERGY, eV

FIG. 11

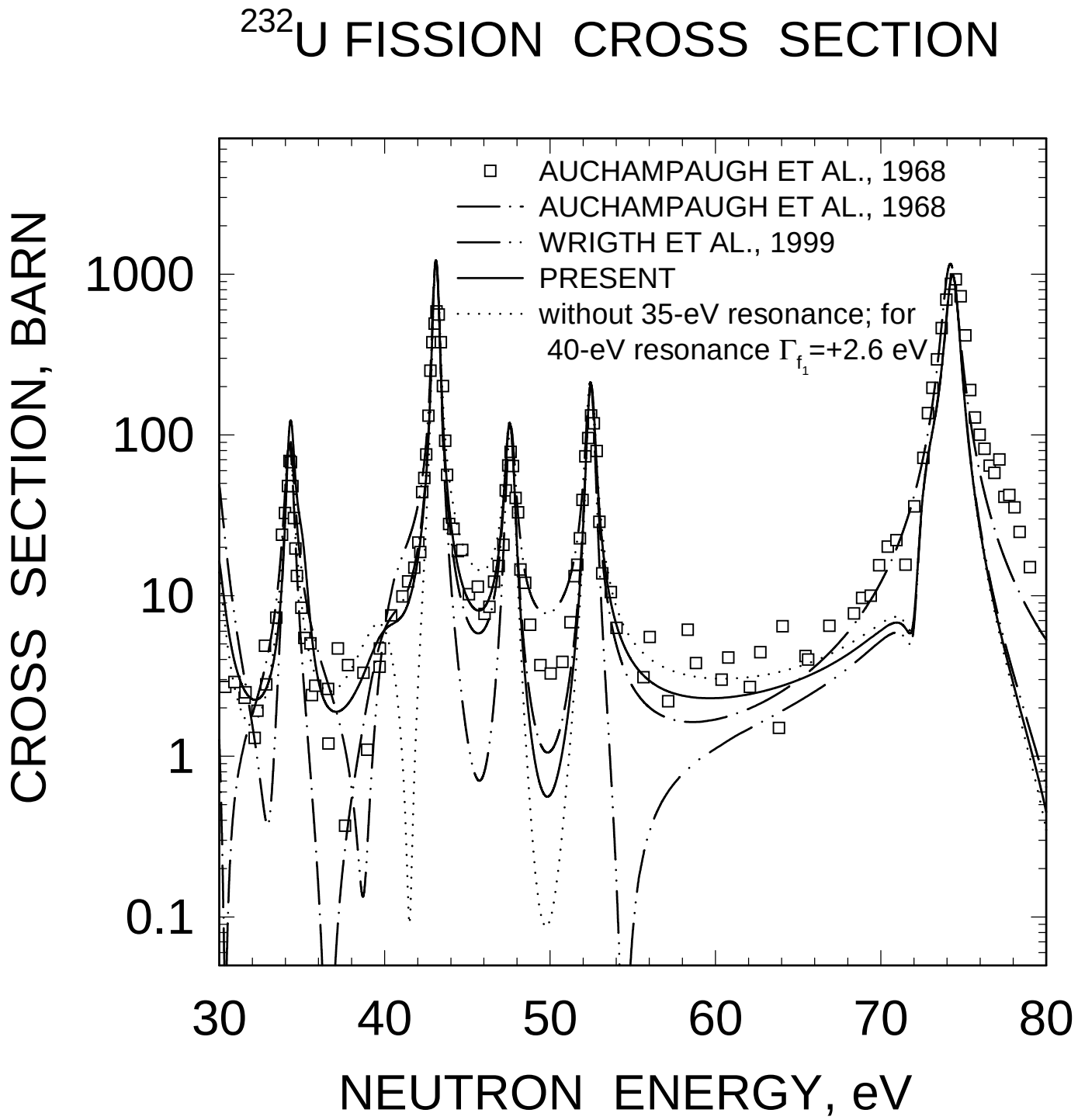
232U FISSION CROSS SECTION
AUCHAMPAUGH ET AL., 1968
AUCHAMPAUGH ET AL., 1968
WRIGTH ET AL., 1999
PRESENT
without 35-eV resonance; for
40-eV resonance Γf1=+2.6 eV
CROSS SECTION, BARN
1000
100
10
1
0.1
30
40
50
60
70
80
NEUTRON ENERGY, eV

FIG. 12

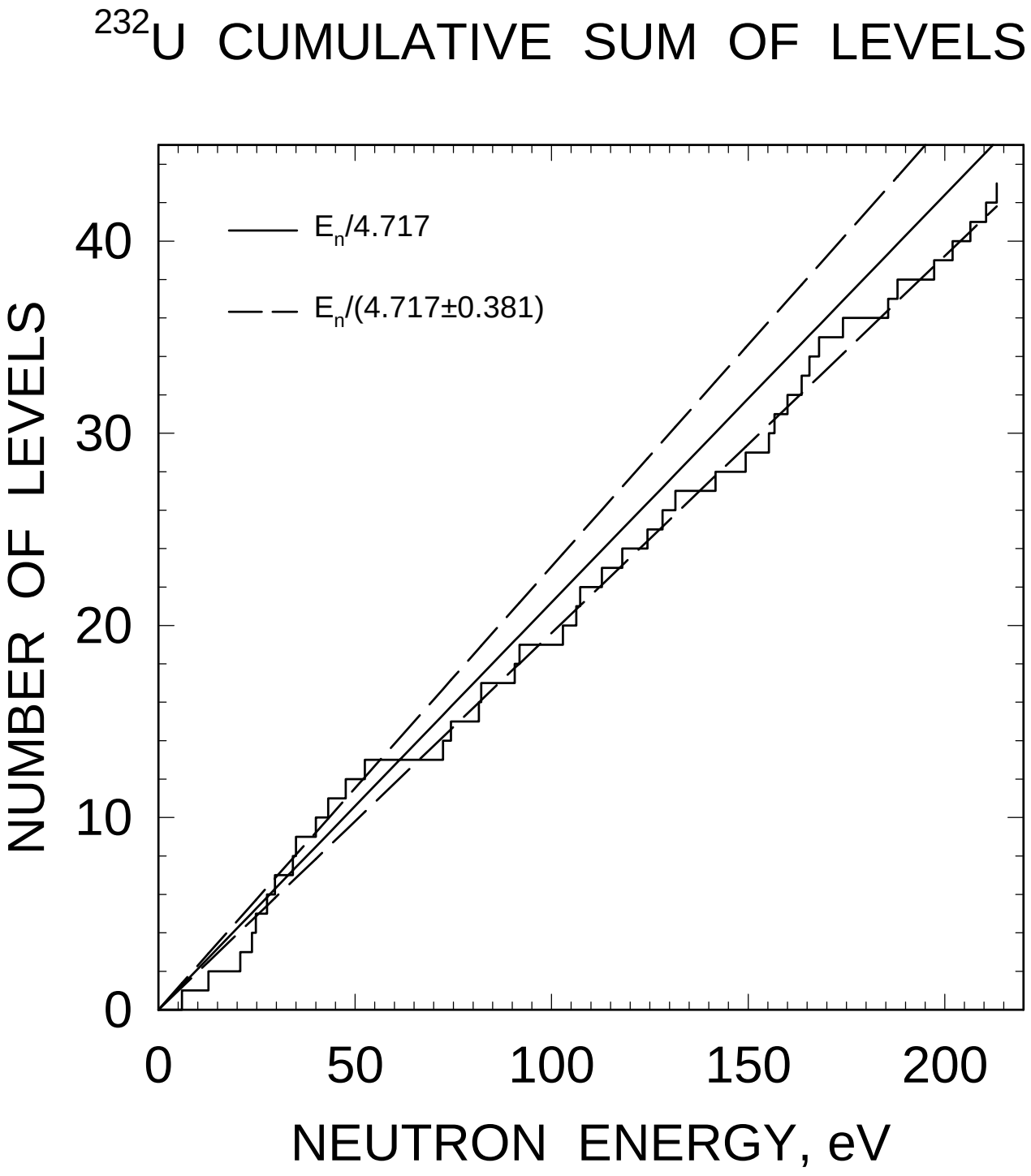
232U CUMULATIVE SUM OF LEVELS
En/4.717
En/(4.717±0.381)
NUMBER OF LEVELS
0
10
20
30
40
0
50
100
150
200
NEUTRON ENERGY, eV

FIG. 13

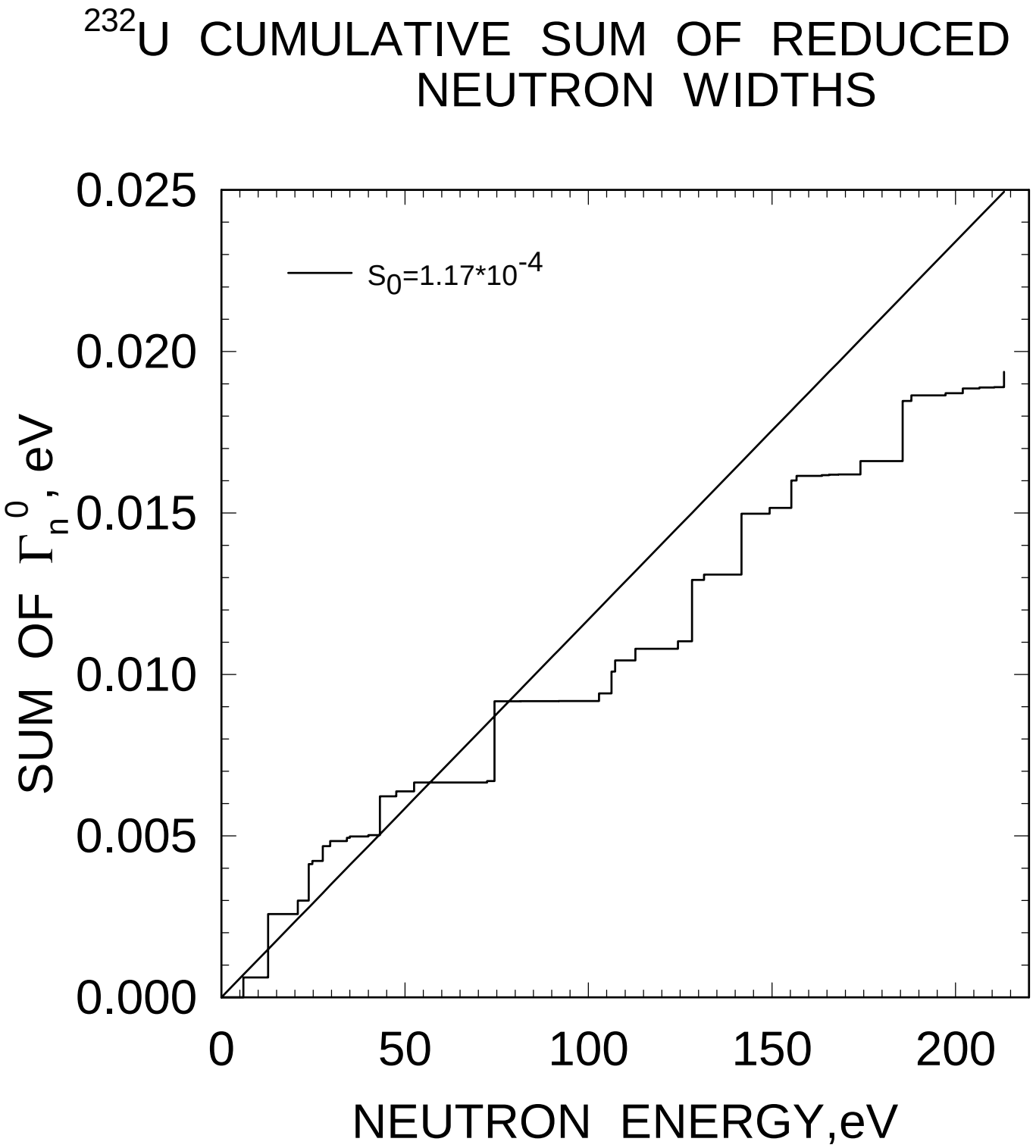
^{232}U CUMULATIVE SUM OF REDUCED NEUTRON WIDTHS
S_0=1.17*10^{-4}
SUM OF Γ_n^0, eV
0.025
0.020
0.015
0.010
0.005
0.000
0
50
100
150
200
NEUTRON ENERGY,eV

FIG. 14

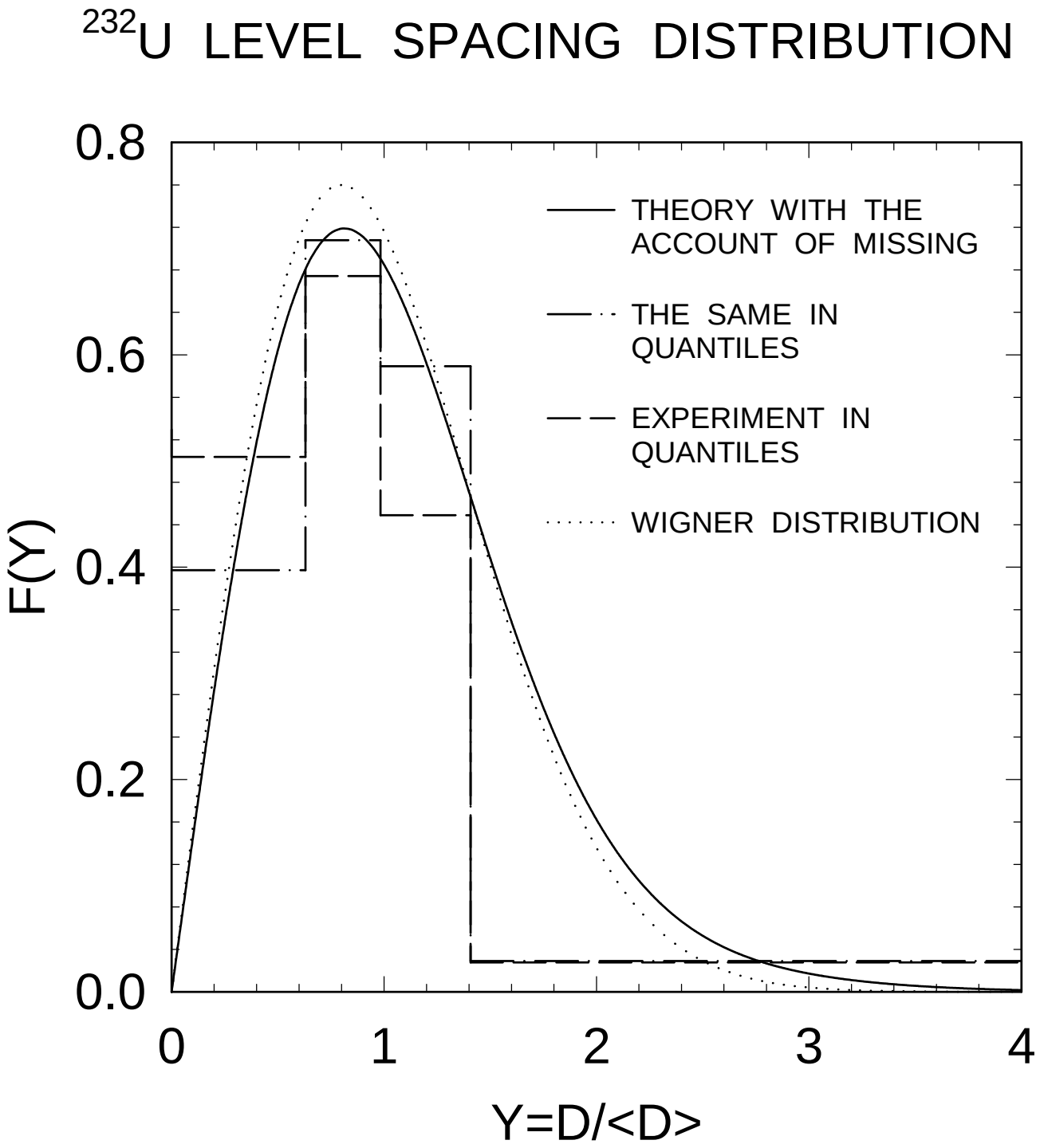
^{232}U LEVEL SPACING DISTRIBUTION
0.8
0.6
0.4
0.2
0.0
F(Y)
0
1
2
3
4
Y=D/<D>
THEORY WITH THE ACCOUNT OF MISSING
THE SAME IN QUANTILES
EXPERIMENT IN QUANTILES
WIGNER DISTRIBUTION

FIG. 15

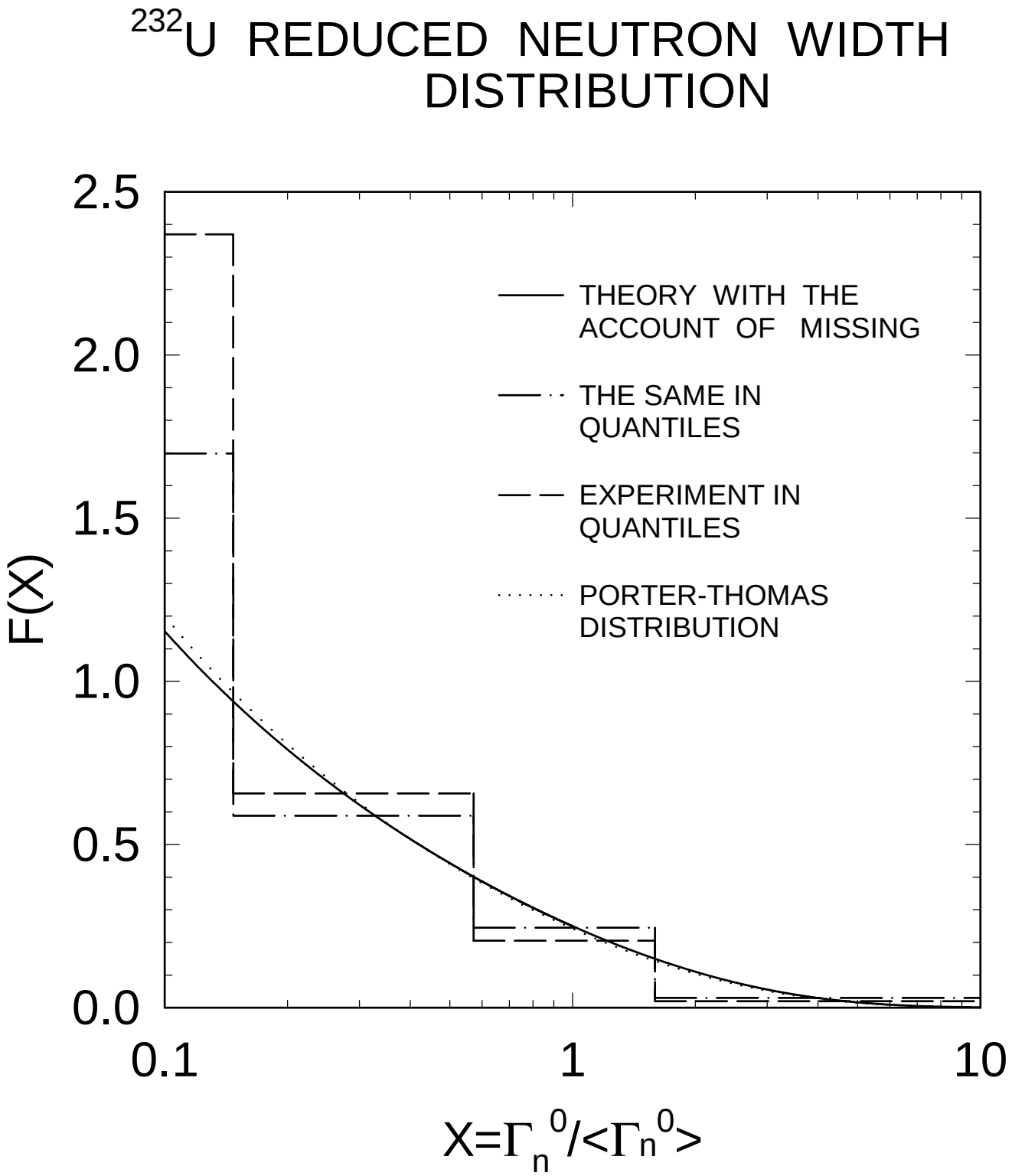
232U REDUCED NEUTRON WIDTH DISTRIBUTION
2.5
2.0
1.5
1.0
0.5
0.0
F(X)
0.1
1
10
X=Γn0/<Γn0>
THEORY WITH THE ACCOUNT OF MISSING
THE SAME IN QUANTILES
EXPERIMENT IN QUANTILES
PORTER-THOMAS DISTRIBUTION

FIG. 16

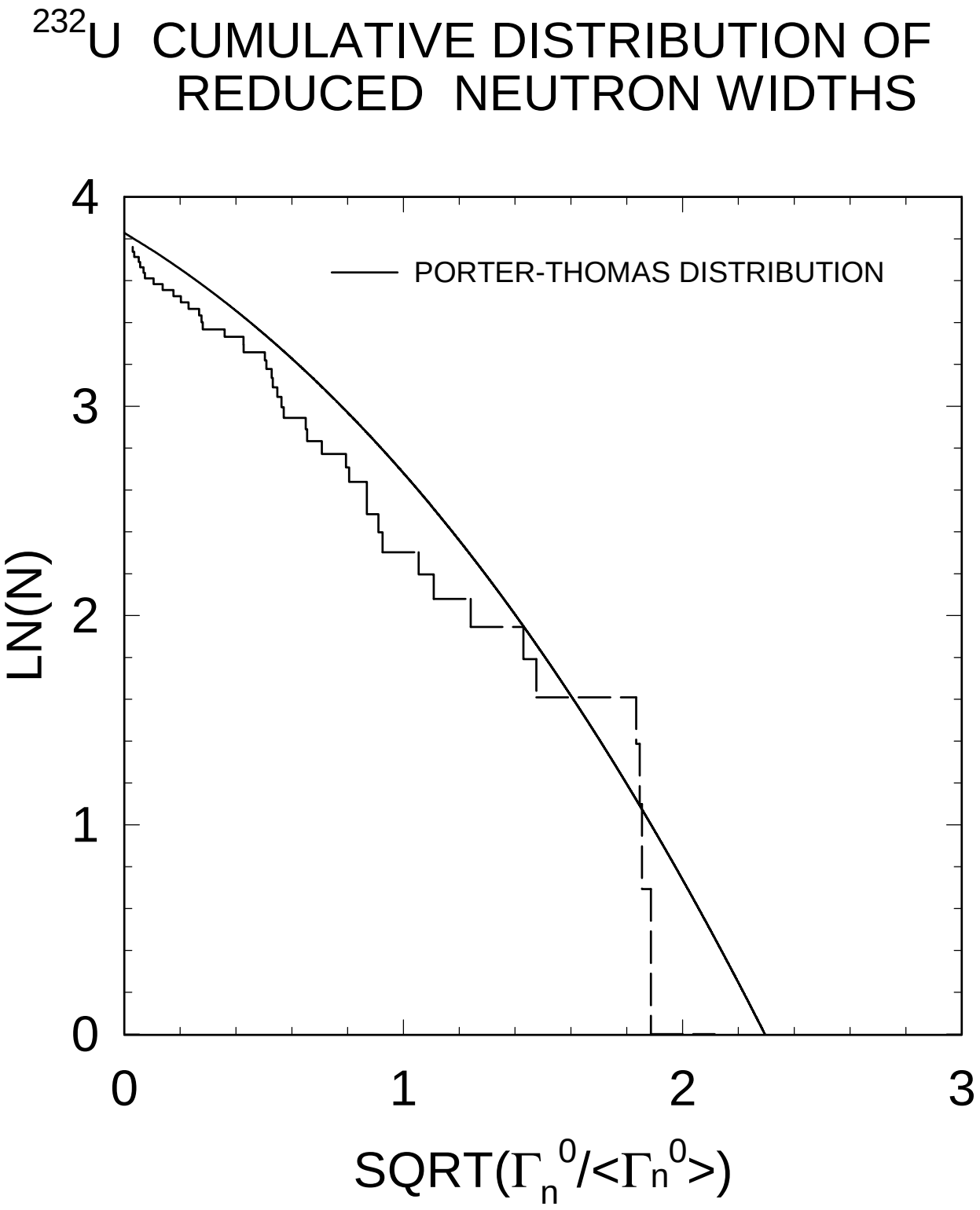
^{232}U CUMULATIVE DISTRIBUTION OF REDUCED NEUTRON WIDTHS
PORTER-THOMAS DISTRIBUTION
LN(N)
0
1
2
3
4
0
1
2
3
SQRT(Γ_n^0/<Γ_n^0>)

FIG. 17

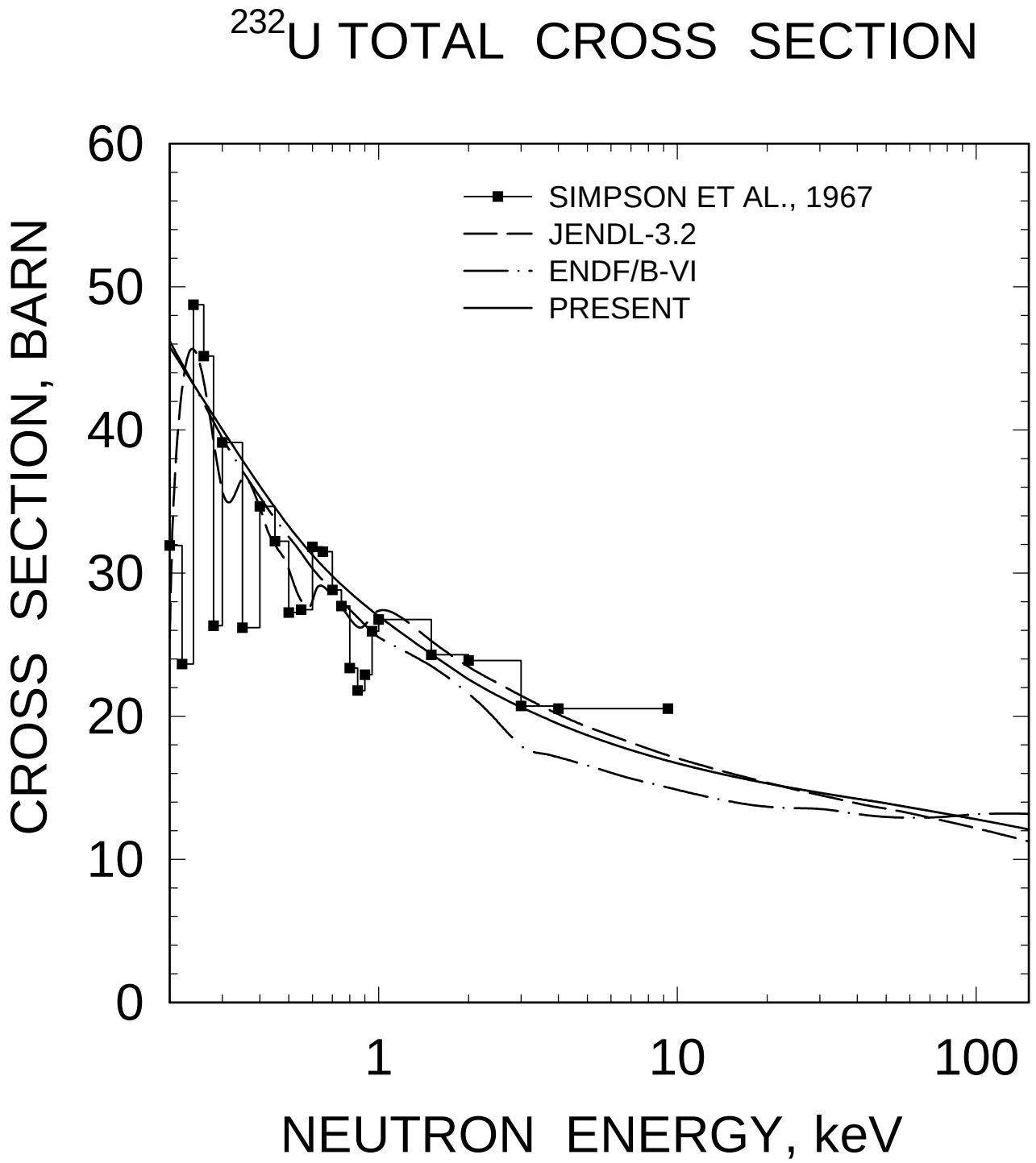
232U TOTAL CROSS SECTION
SIMPSON ET AL., 1967
JENDL-3.2
ENDF/B-VI
PRESENT
CROSS SECTION, BARN
60
50
40
30
20
10
0
1
10
100
NEUTRON ENERGY, keV

FIG. 18

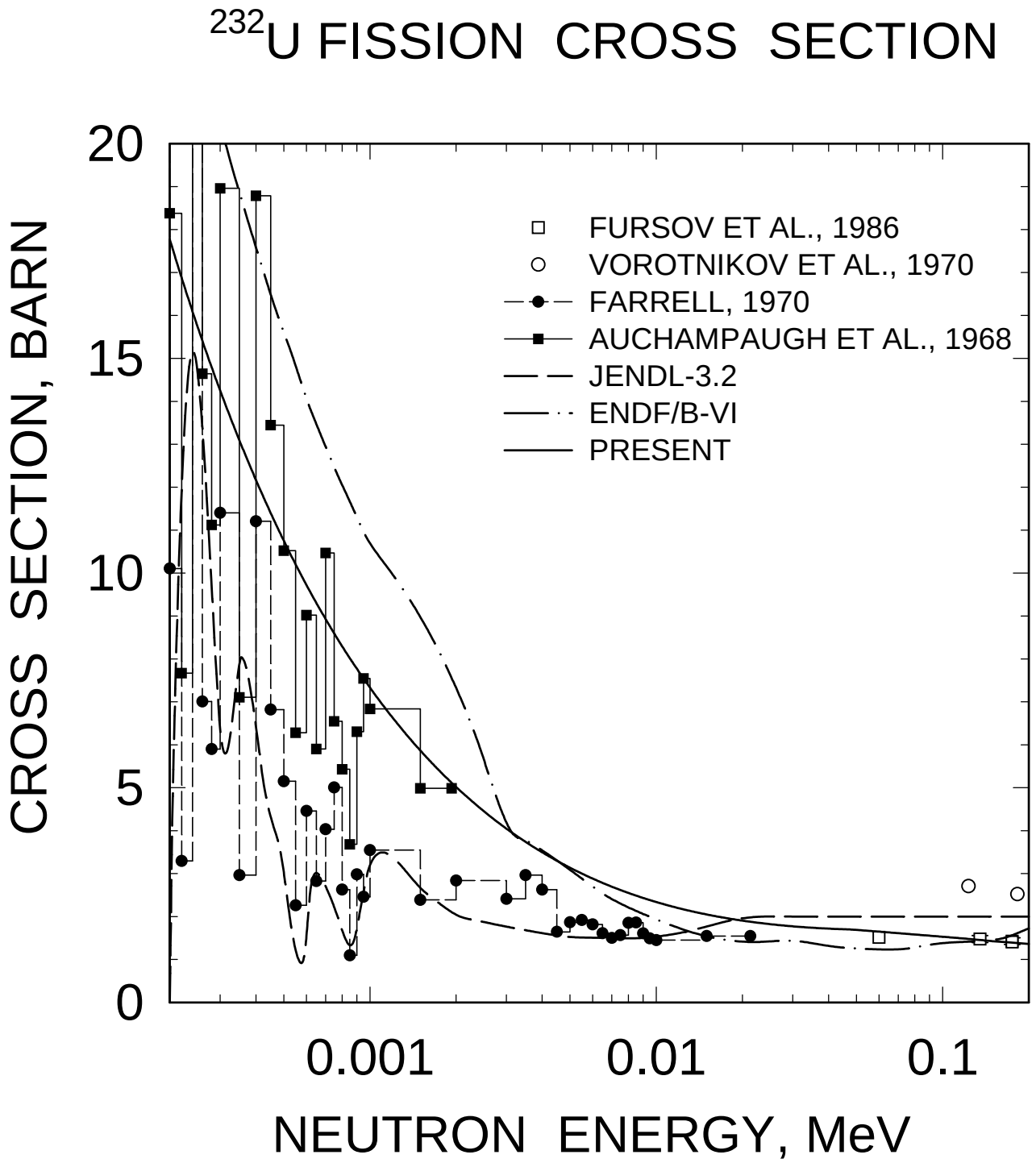
232U FISSION CROSS SECTION
CROSS SECTION, BARN
NEUTRON ENERGY, MeV
0
5
10
15
20
0.001
0.01
0.1
FURSOV ET AL., 1986
VOROTNIKOV ET AL., 1970
FARRELL, 1970
AUCHAMPAUGH ET AL., 1968
JENDL-3.2
ENDF/B-VI
PRESENT

FIG. 19

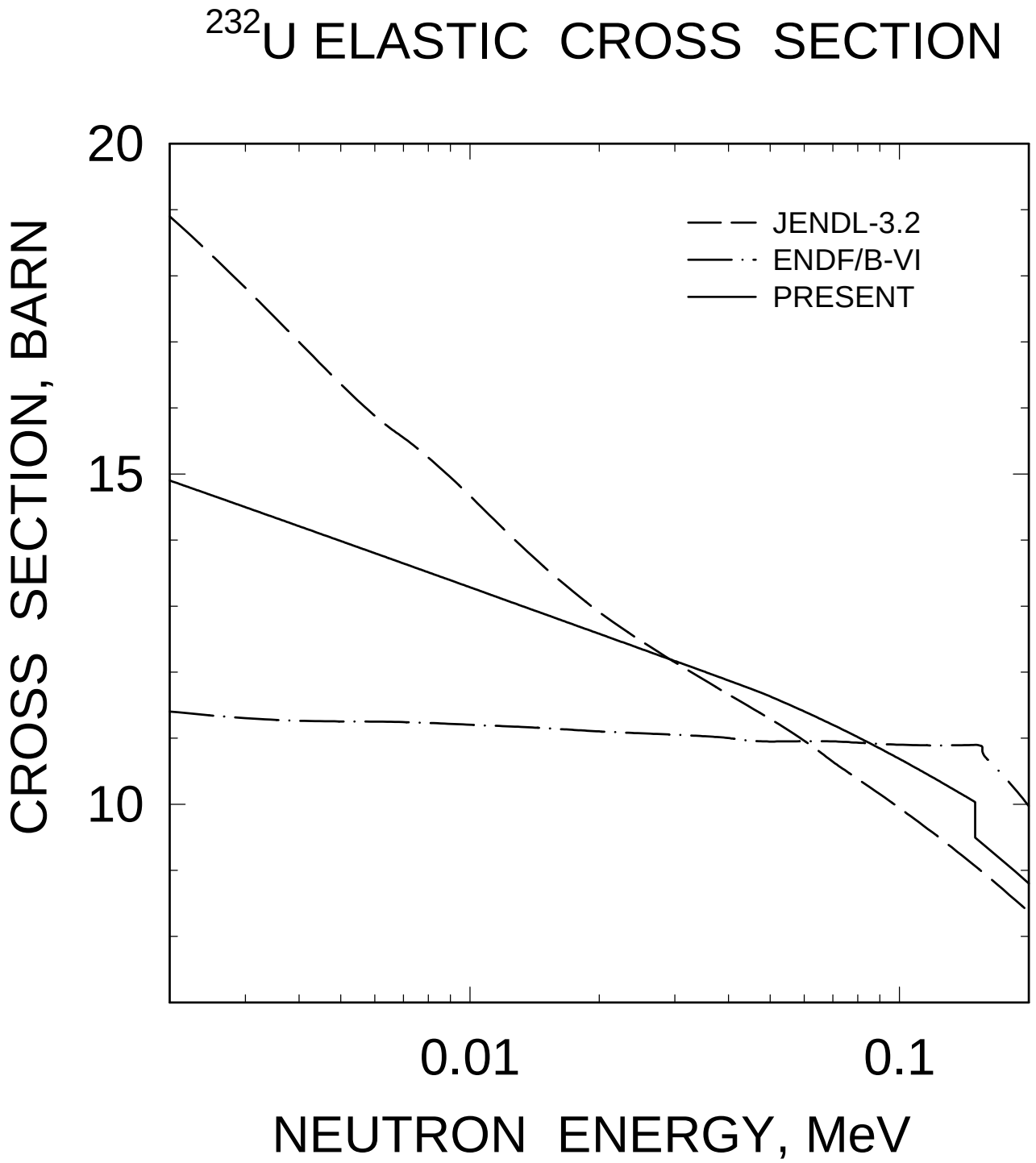
^{232}U ELASTIC CROSS SECTION
20
15
10
CROSS SECTION, BARN
JENDL-3.2
ENDF/B-VI
PRESENT
0.01
0.1
NEUTRON ENERGY, MeV

FIG. 20

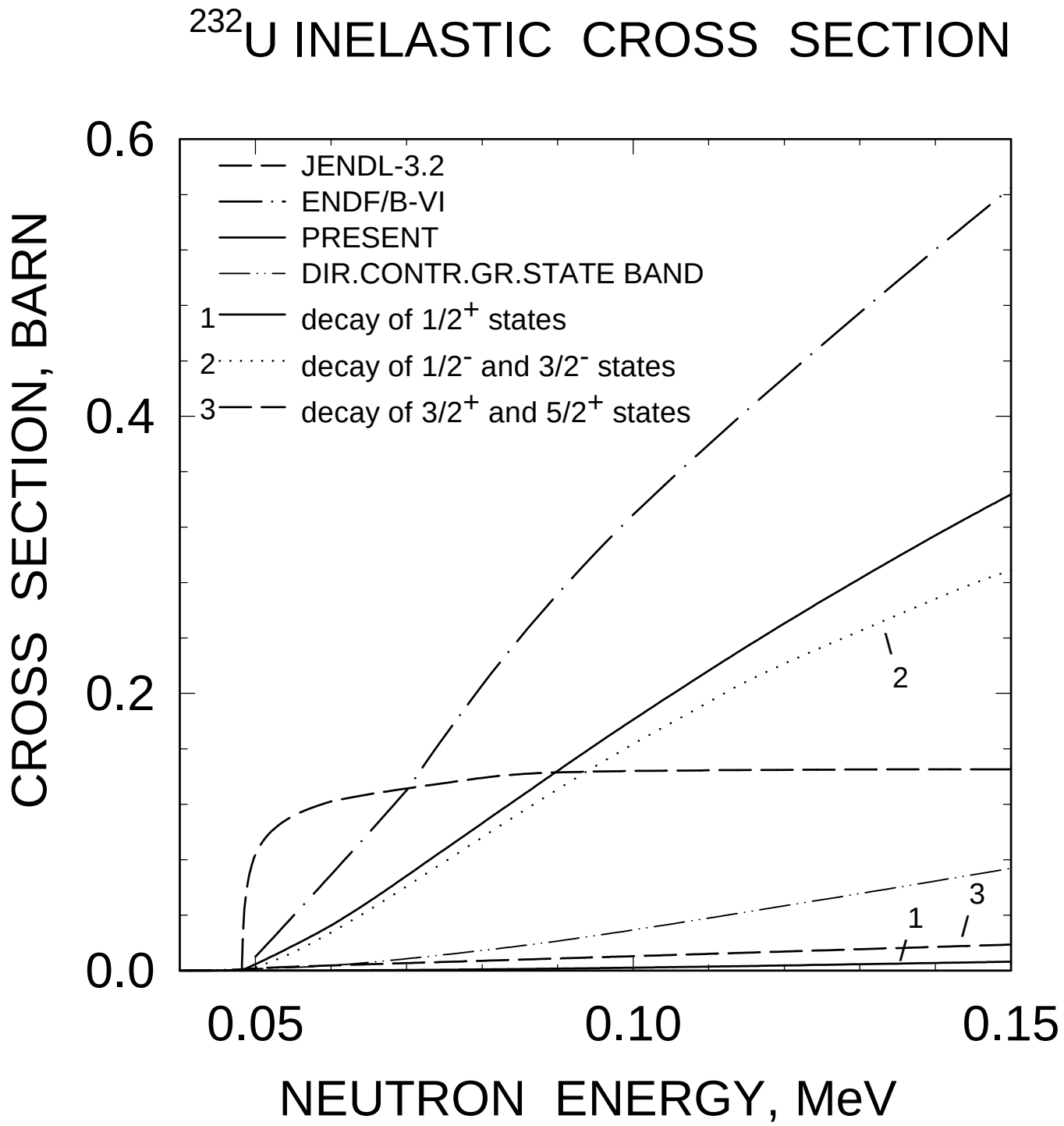
232U INELASTIC CROSS SECTION
JENDL-3.2
ENDF/B-VI
PRESENT
DIR.CONTR.GR.STATE BAND
1 decay of 1/2+ states
2 decay of 1/2- and 3/2- states
3 decay of 3/2+ and 5/2+ states
CROSS SECTION, BARN
0.6
0.4
0.2
0.0
0.05
0.10
0.15
NEUTRON ENERGY, MeV
1
2
3

FIG. 21

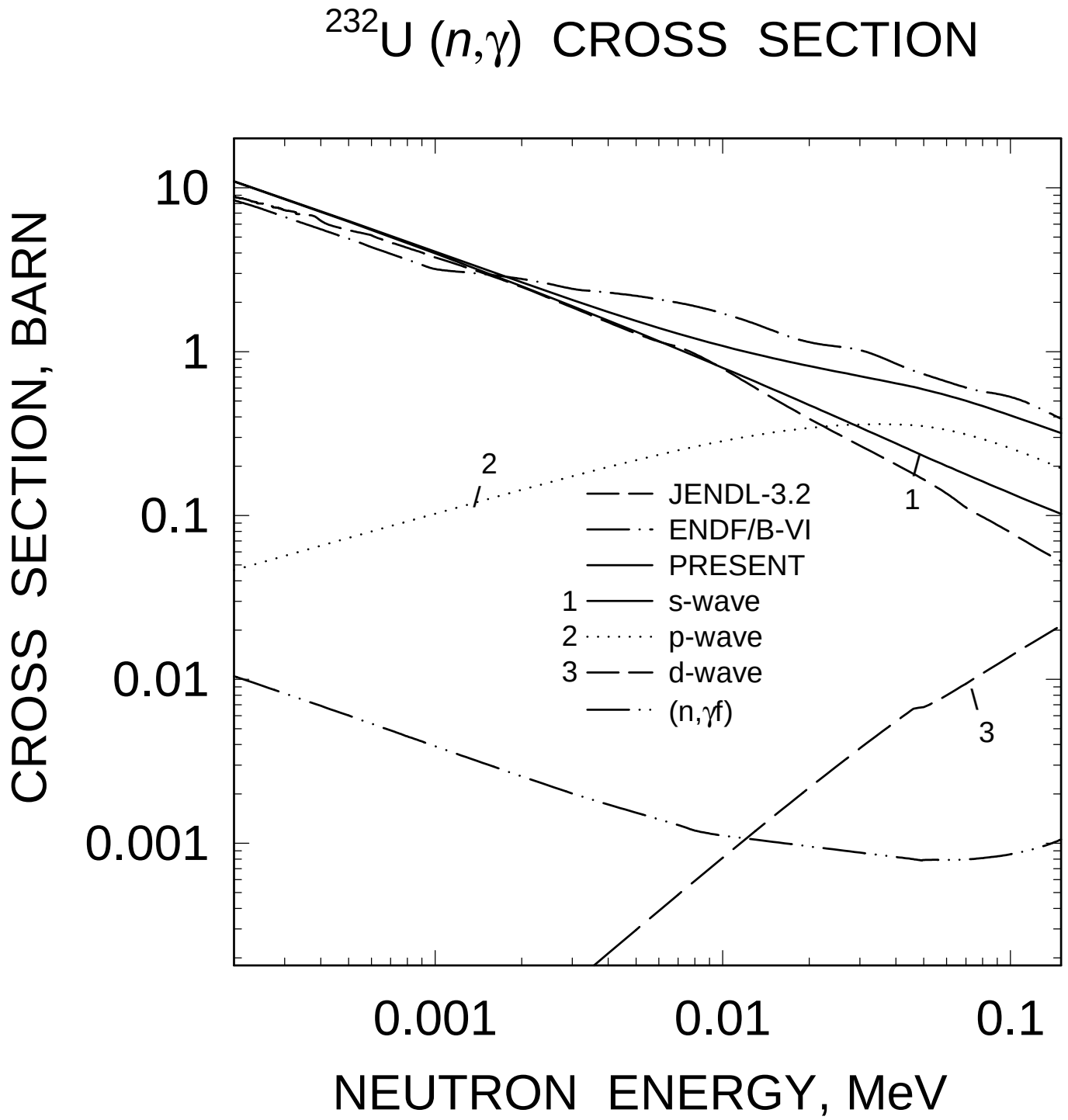
232U (n,γ) CROSS SECTION
CROSS SECTION, BARN
10
1
0.1
0.01
0.001
0.001
0.01
0.1
NEUTRON ENERGY, MeV
JENDL-3.2
ENDF/B-VI
PRESENT
1 s-wave
2 p-wave
3 d-wave
(n,γf)
1
2
3

FIG. 22

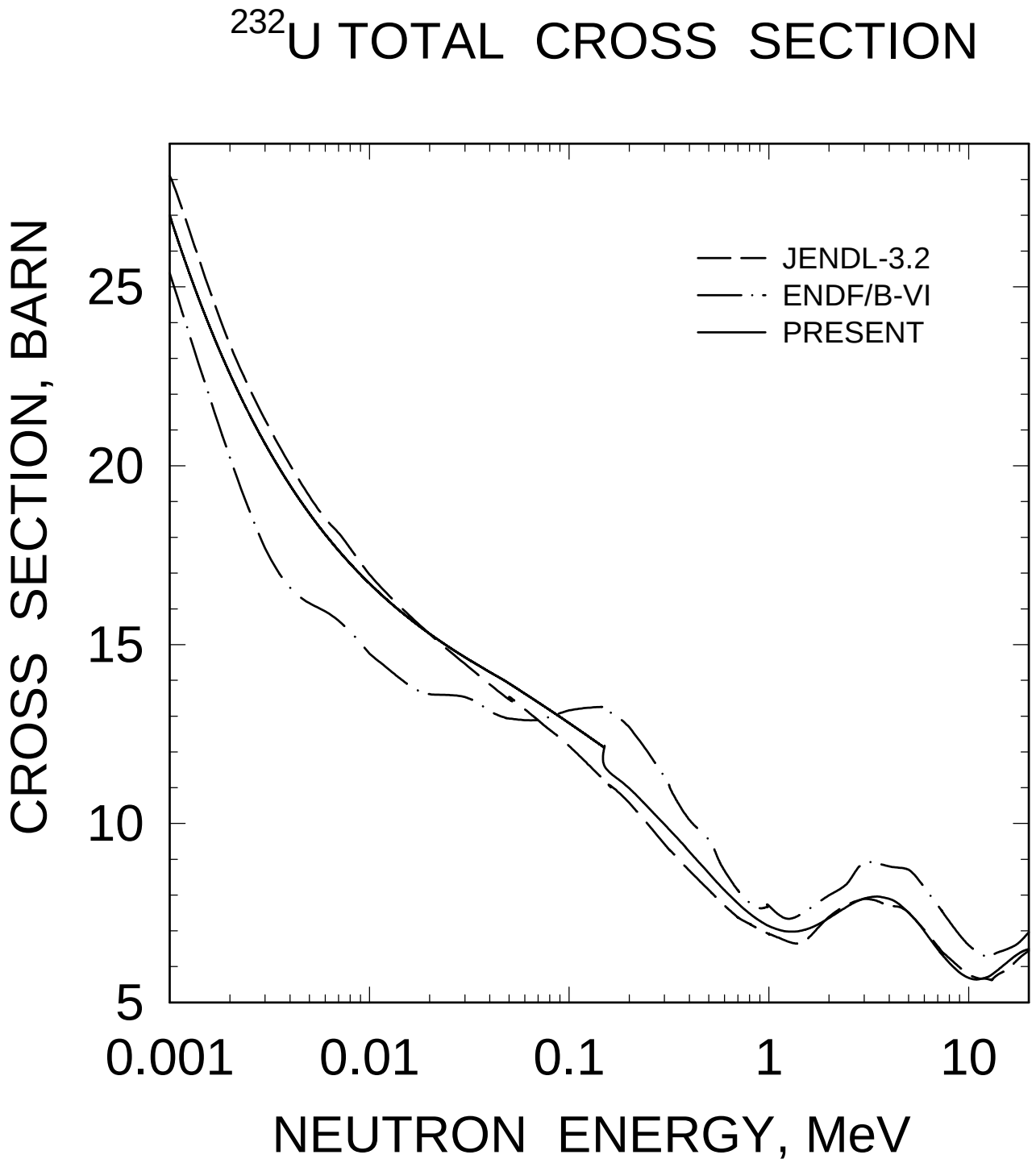
232U TOTAL CROSS SECTION
JENDL-3.2
ENDF/B-VI
PRESENT
CROSS SECTION, BARN
25
20
15
10
5
0.001
0.01
0.1
1
10
NEUTRON ENERGY, MeV

FIG. 23

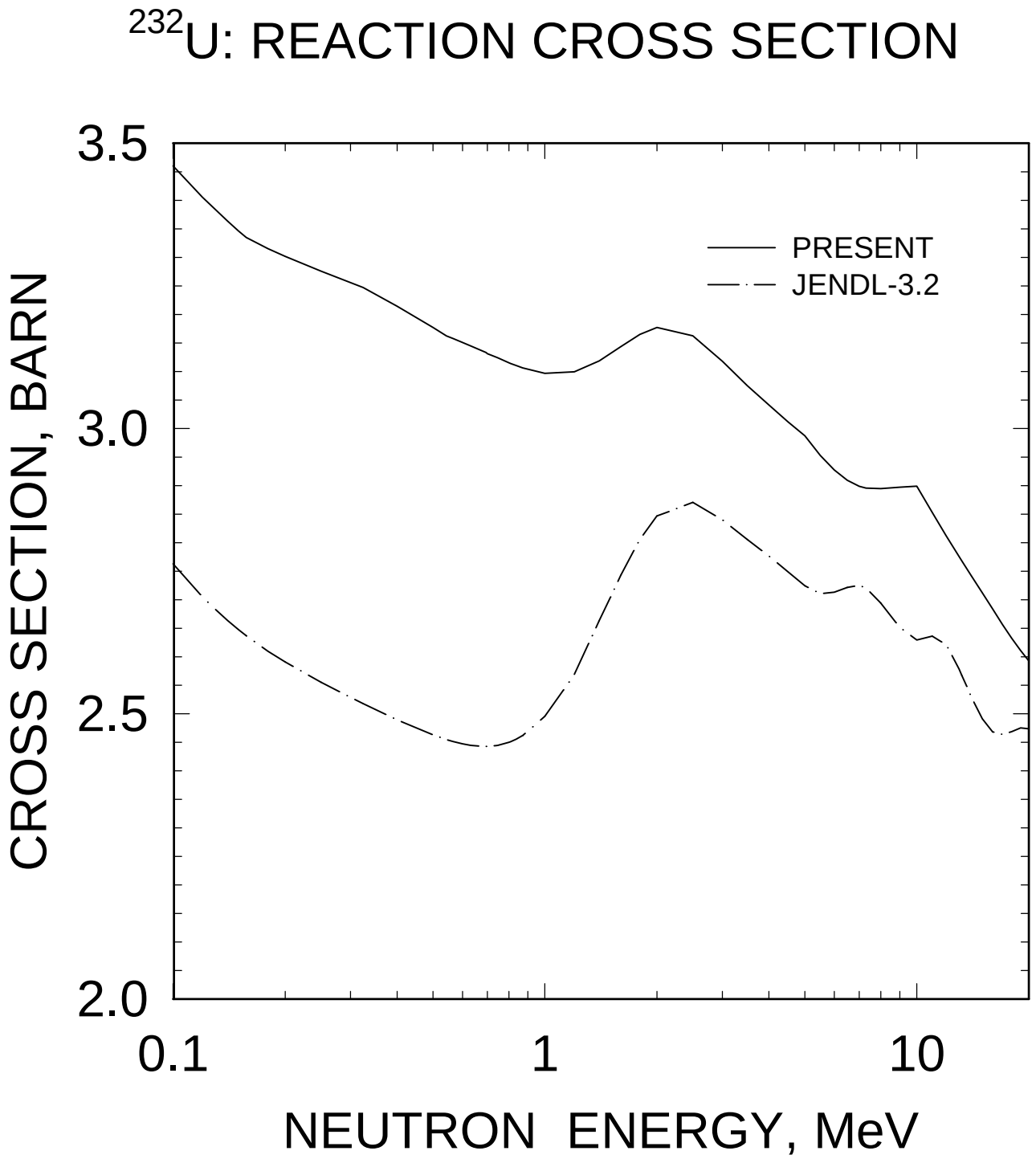
^{232}U: REACTION CROSS SECTION
3.5
3.0
2.5
2.0
CROSS SECTION, BARN
PRESENT
JENDL-3.2
0.1
1
10
NEUTRON ENERGY, MeV

FIG. 24

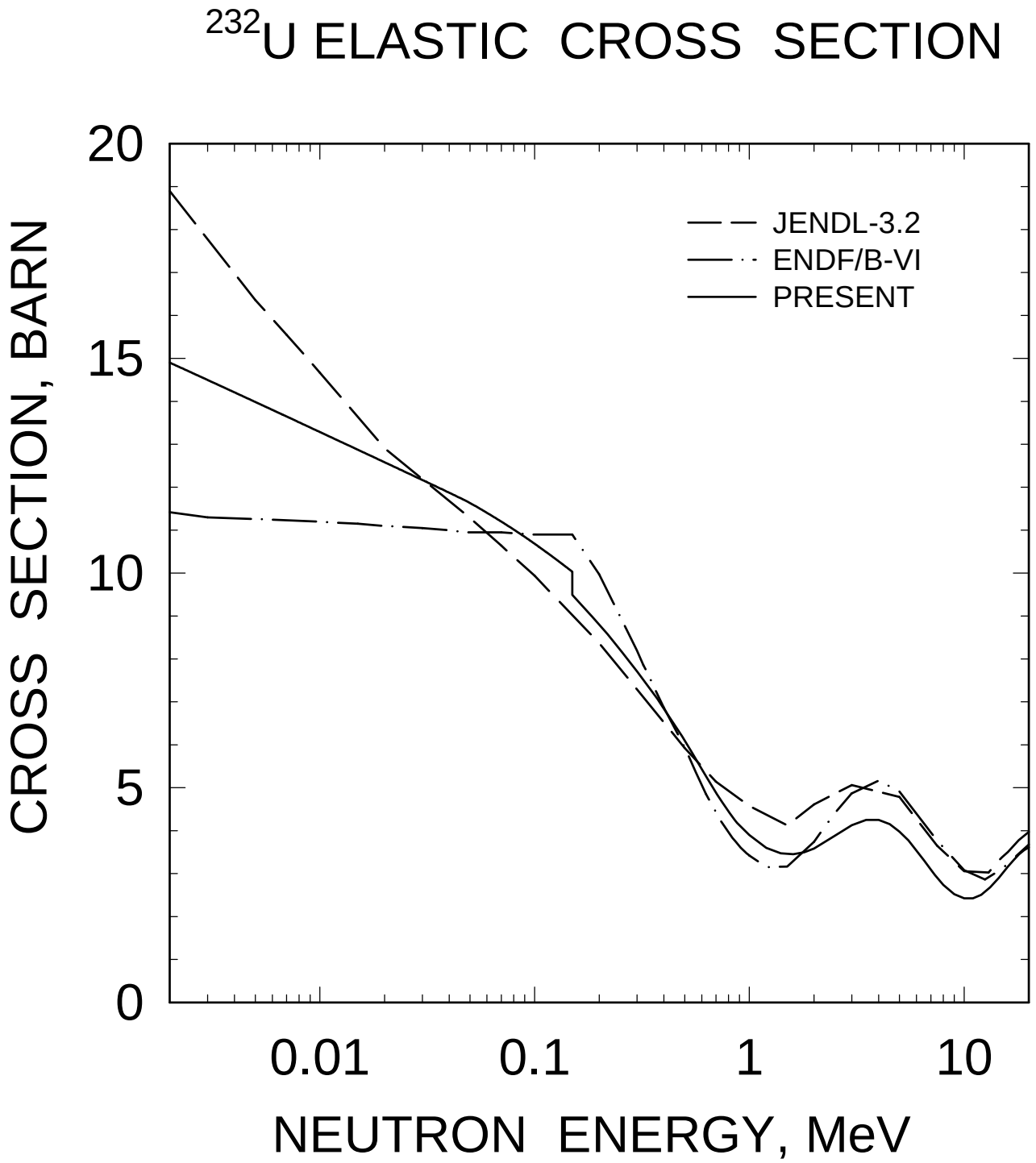
232U ELASTIC CROSS SECTION
CROSS SECTION, BARN
20
15
10
5
0
0.01
0.1
1
10
NEUTRON ENERGY, MeV
JENDL-3.2
ENDF/B-VI
PRESENT

FIG. 25

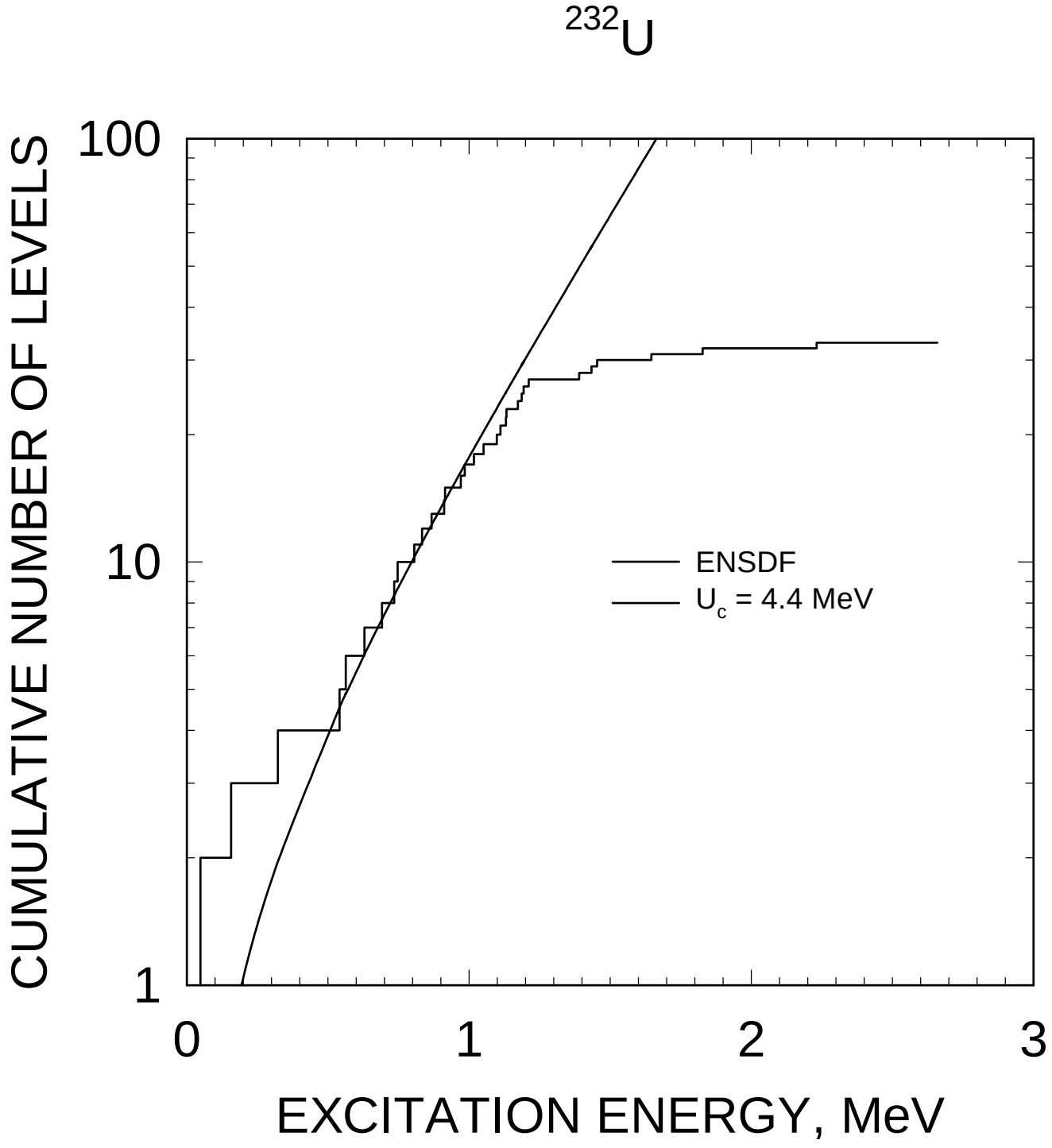
232U
100
10
1
CUMULATIVE NUMBER OF LEVELS
0
1
2
3
EXCITATION ENERGY, MeV
ENSDF
Uc = 4.4 MeV

FIG. 26

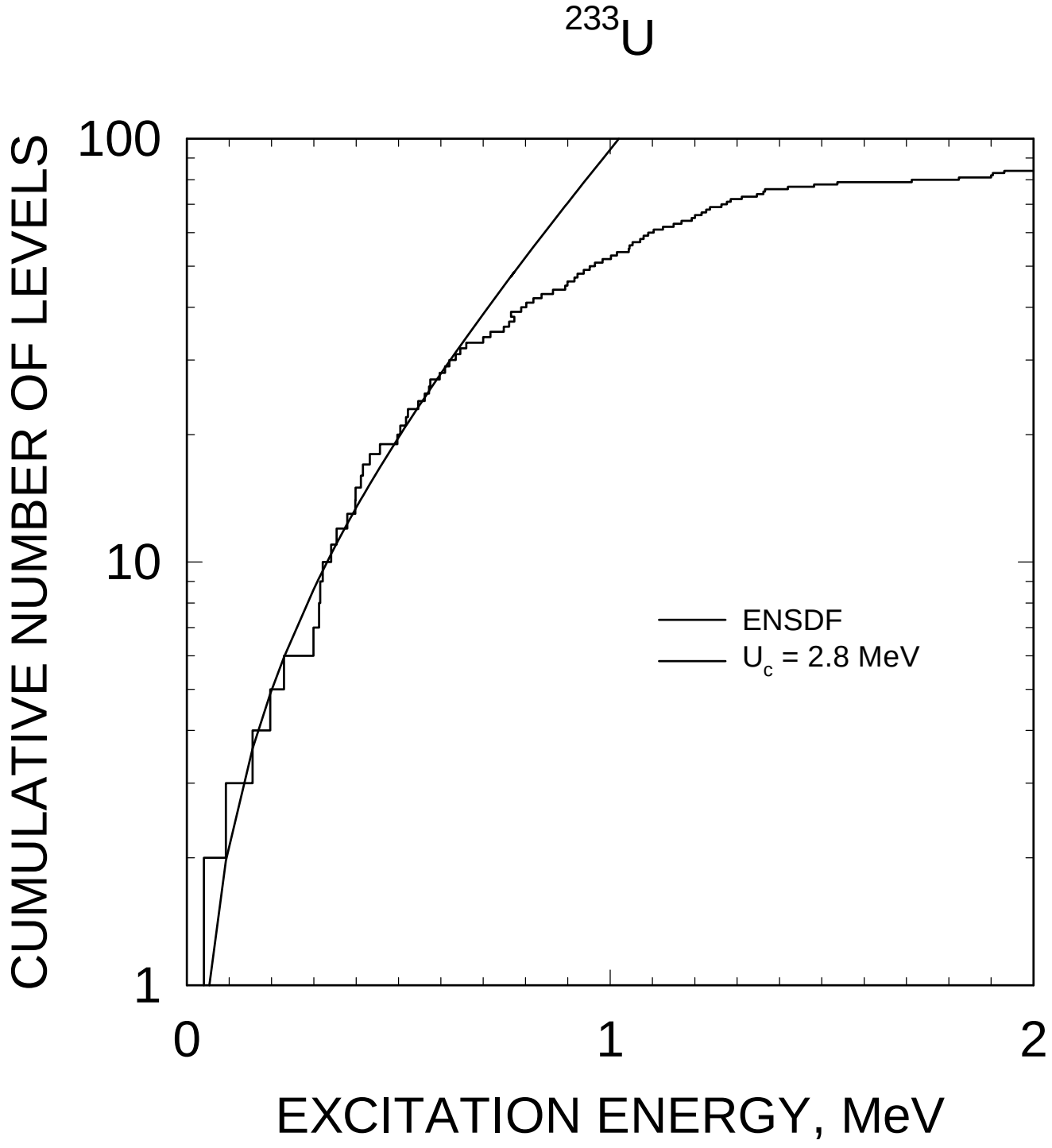
233U
100
10
1
CUMULATIVE NUMBER OF LEVELS
0
1
2
EXCITATION ENERGY, MeV
ENSDF
Uc = 2.8 MeV

FIG. 27

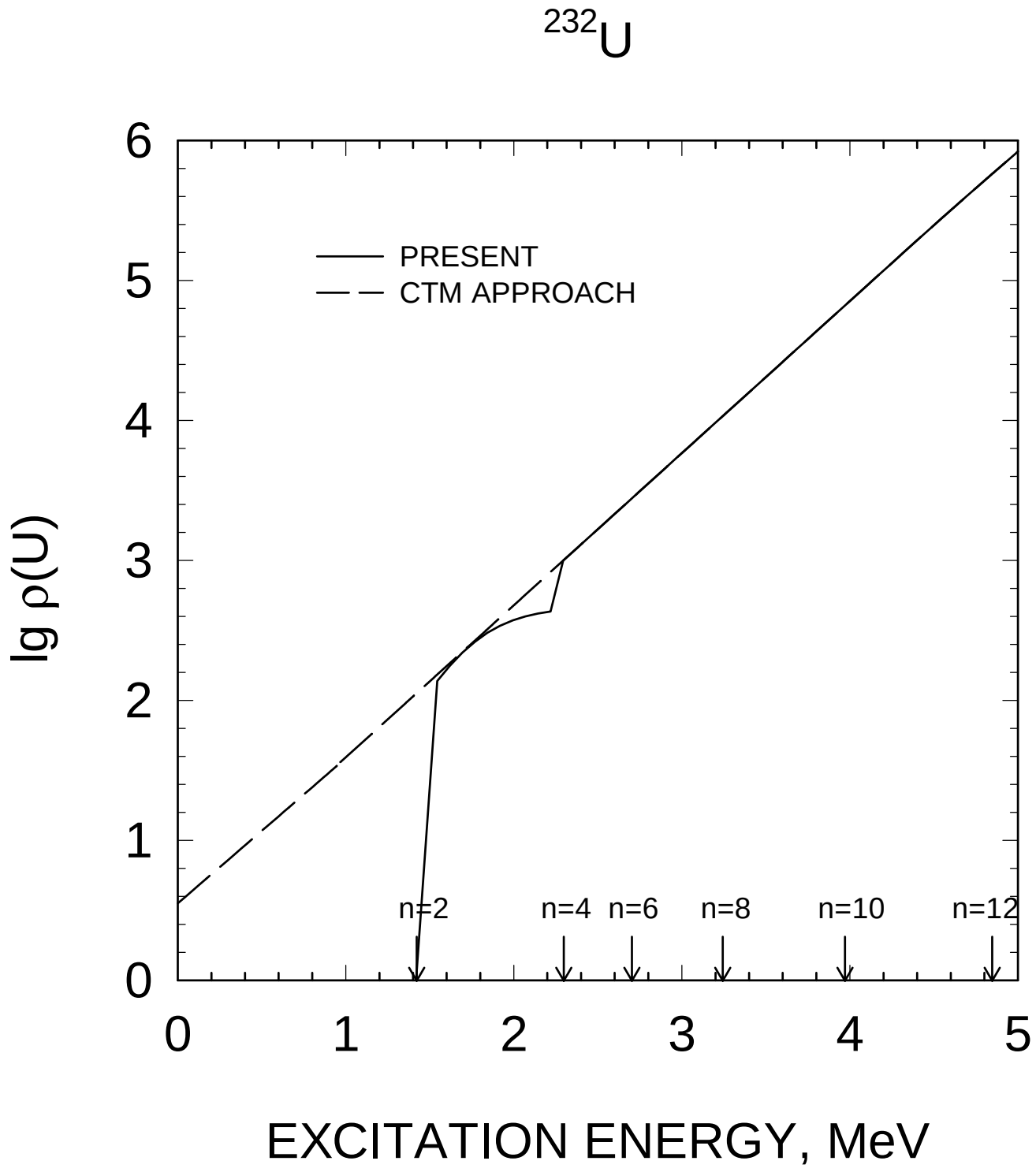
232U
PRESENT
CTM APPROACH
lg ρ(U)
n=2
n=4
n=6
n=8
n=10
n=12
0
1
2
3
4
5
6
EXCITATION ENERGY, MeV

FIG. 28

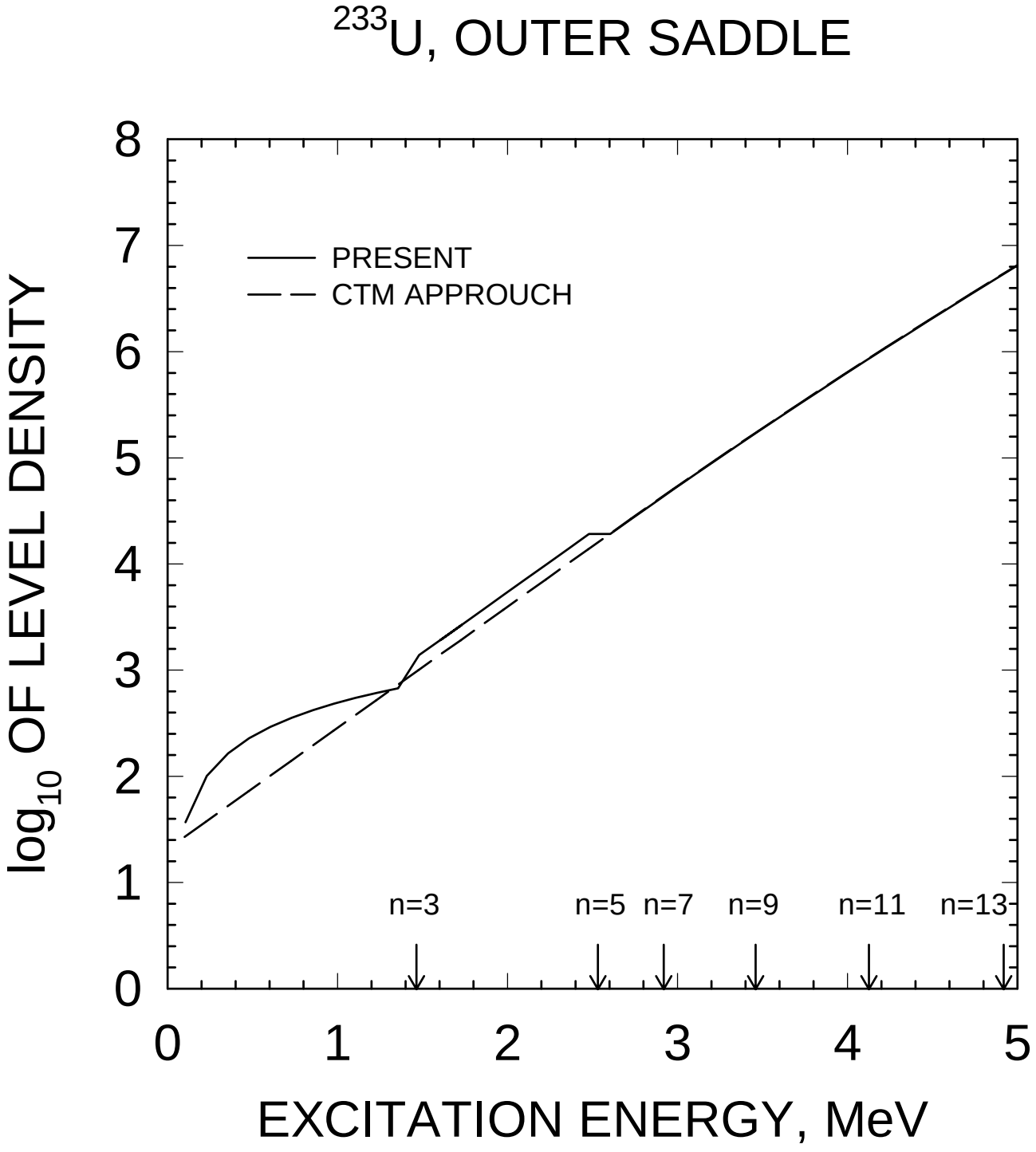
^{233}U, OUTER SADDLE
PRESENT
CTM APPROUCH
log$_{10}$ OF LEVEL DENSITY
EXCITATION ENERGY, MeV
n=3
n=5
n=7
n=9
n=11
n=13
0
1
2
3
4
5
6
7
8

FIG. 29

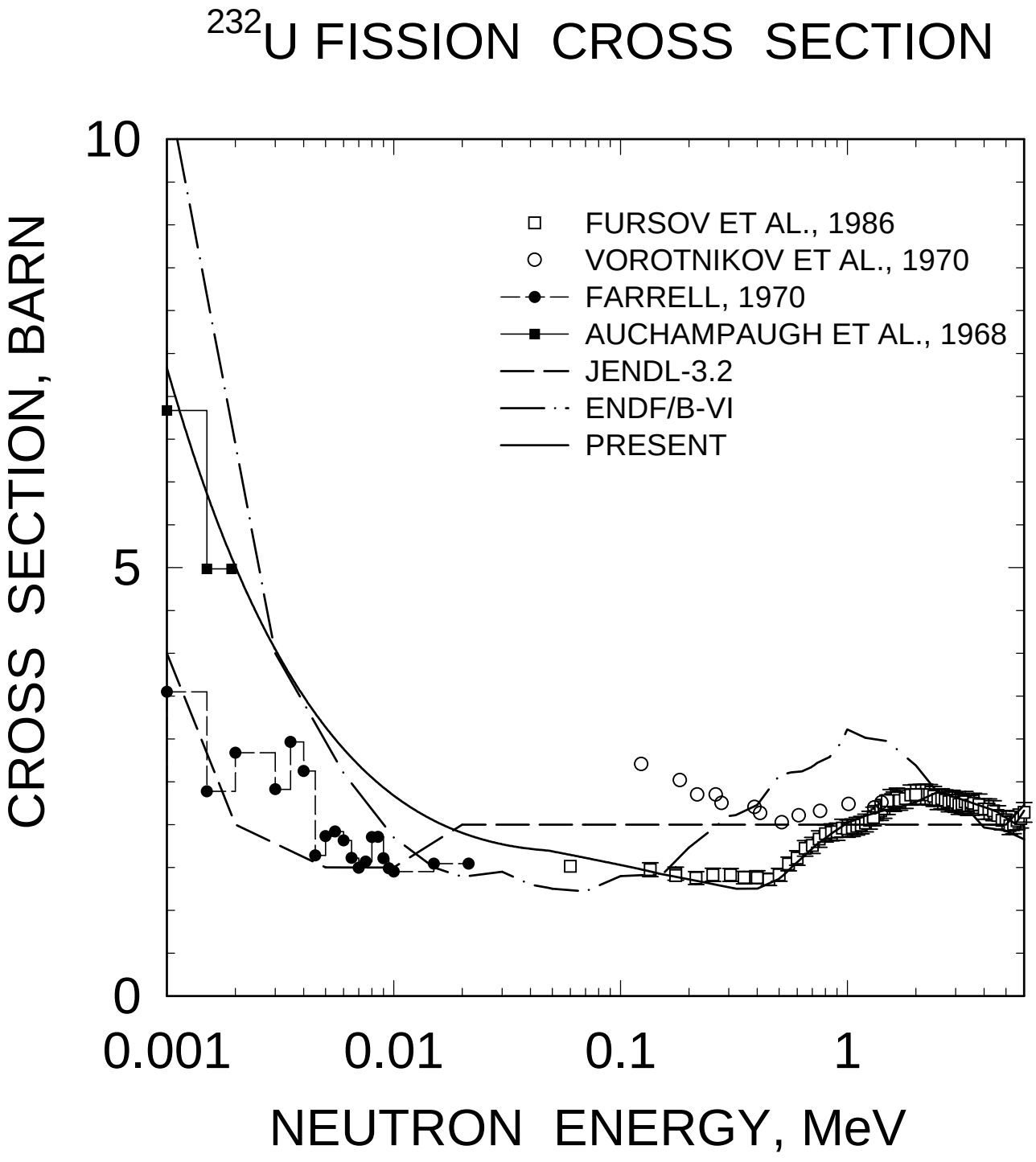
232U FISSION CROSS SECTION
FURSOV ET AL., 1986
VOROTNIKOV ET AL., 1970
FARRELL, 1970
AUCHAMPAUGH ET AL., 1968
JENDL-3.2
ENDF/B-VI
PRESENT
CROSS SECTION, BARN
10
5
0
0.001
0.01
0.1
1
NEUTRON ENERGY, MeV

FIG. 30

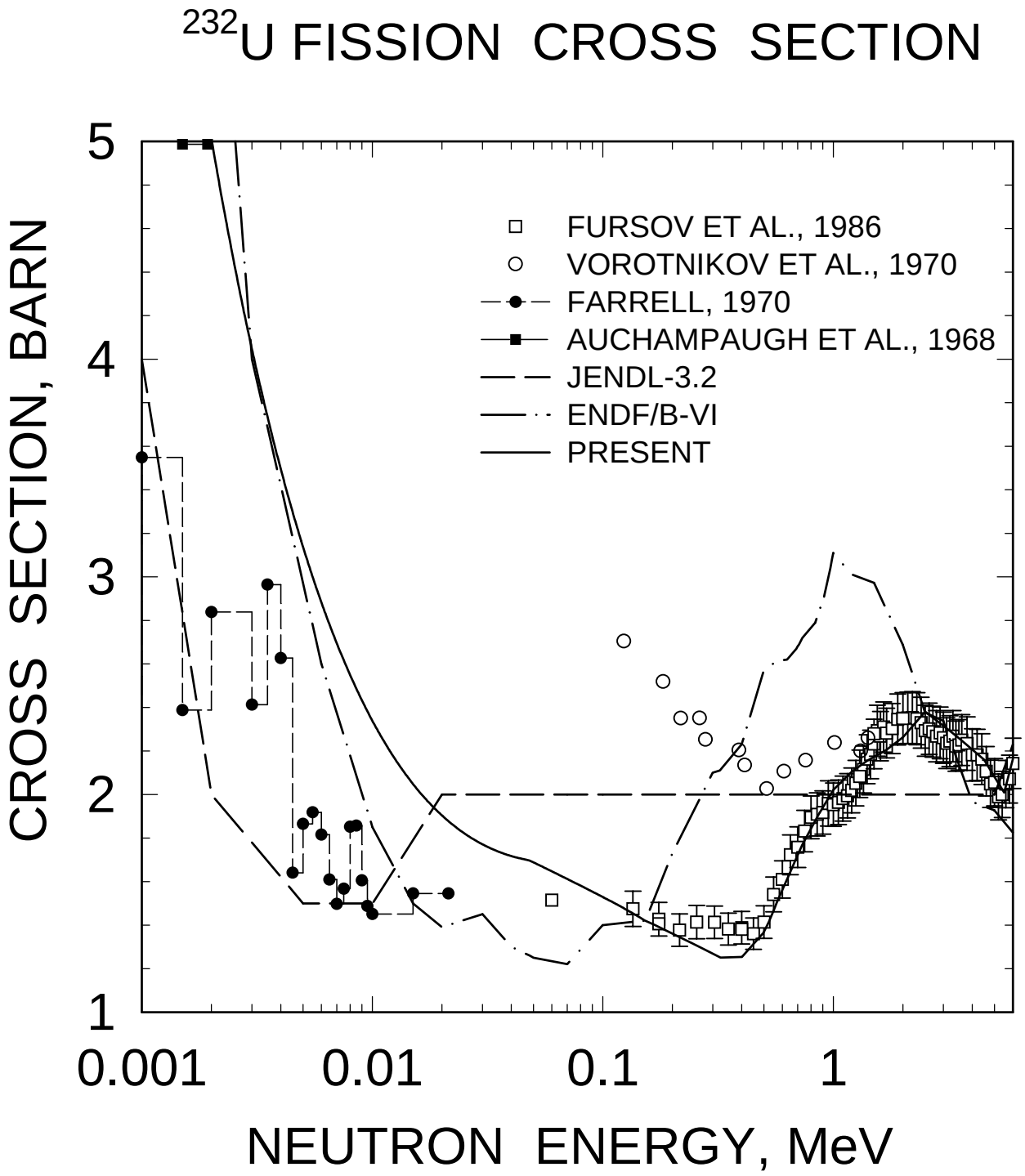
232U FISSION CROSS SECTION
FURSOV ET AL., 1986
VOROTNIKOV ET AL., 1970
FARRELL, 1970
AUCHAMPAUGH ET AL., 1968
JENDL-3.2
ENDF/B-VI
PRESENT
CROSS SECTION, BARN
NEUTRON ENERGY, MeV
5
4
3
2
1
0.001
0.01
0.1
1

FIG. 31

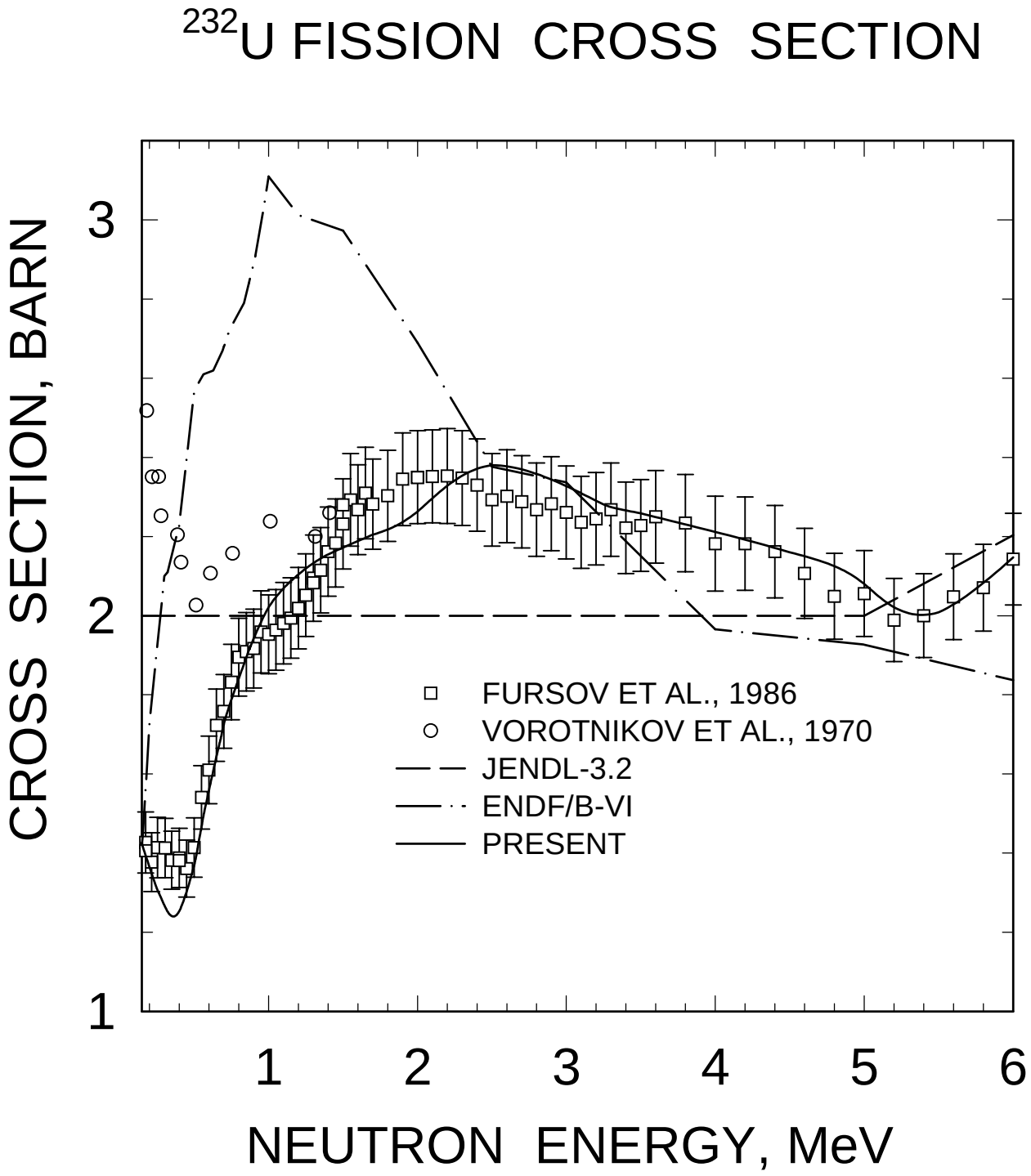
^{232}U FISSION CROSS SECTION
CROSS SECTION, BARN
3
2
1
1
2
3
4
5
6
NEUTRON ENERGY, MeV
FURSOV ET AL., 1986
VOROTNIKOV ET AL., 1970
JENDL-3.2
ENDF/B-VI
PRESENT

FIG. 32

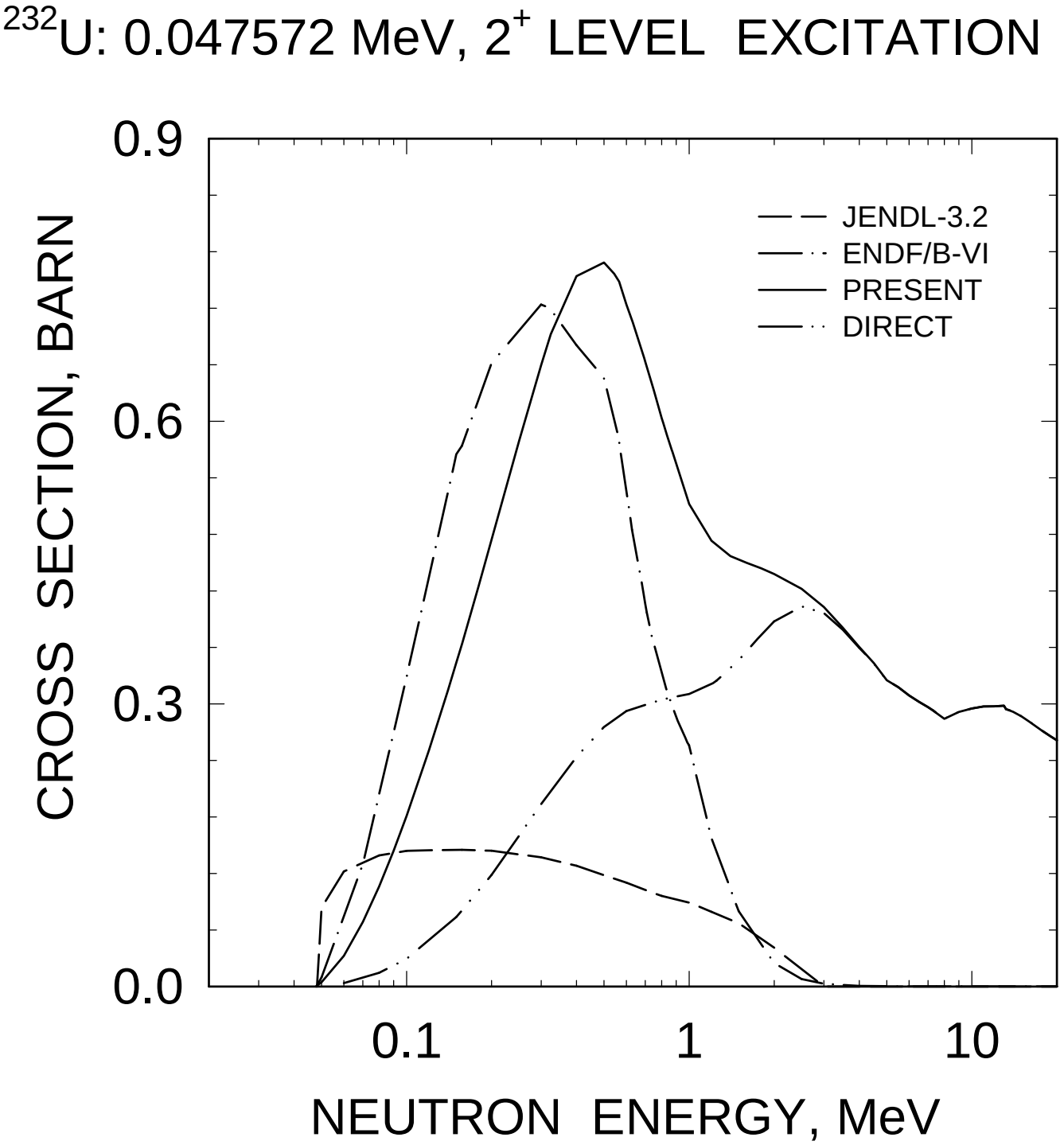
^{232}U: 0.047572 MeV, 2^{+} LEVEL EXCITATION
0.9
0.6
0.3
0.0
CROSS SECTION, BARN
JENDL-3.2
ENDF/B-VI
PRESENT
DIRECT
0.1
1
10
NEUTRON ENERGY, MeV

FIG. 33

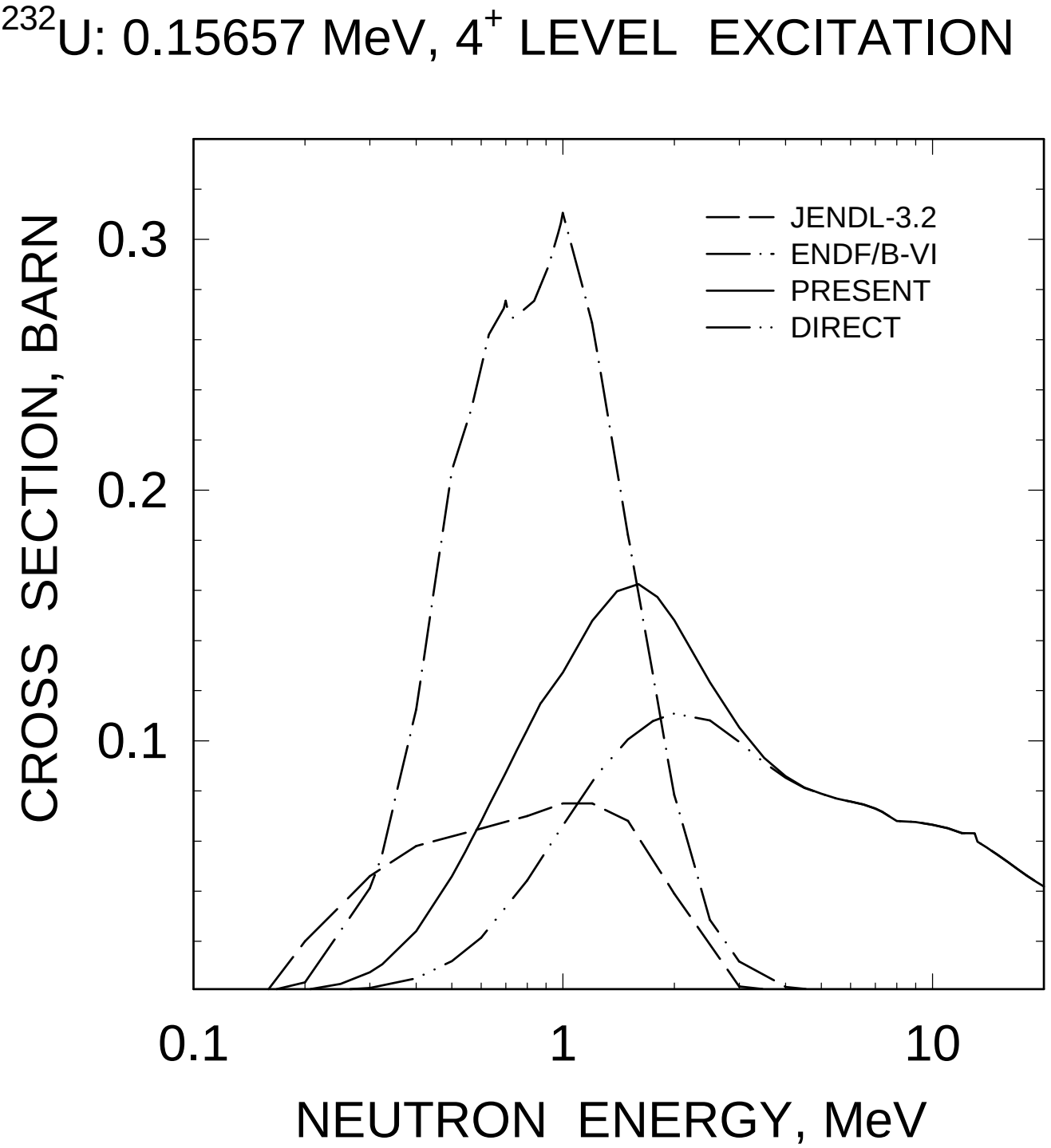
^{232}U: 0.15657 MeV, 4^{+} LEVEL EXCITATION
JENDL-3.2
ENDF/B-VI
PRESENT
DIRECT
CROSS SECTION, BARN
0.3
0.2
0.1
0.1
1
10
NEUTRON ENERGY, MeV

FIG. 34

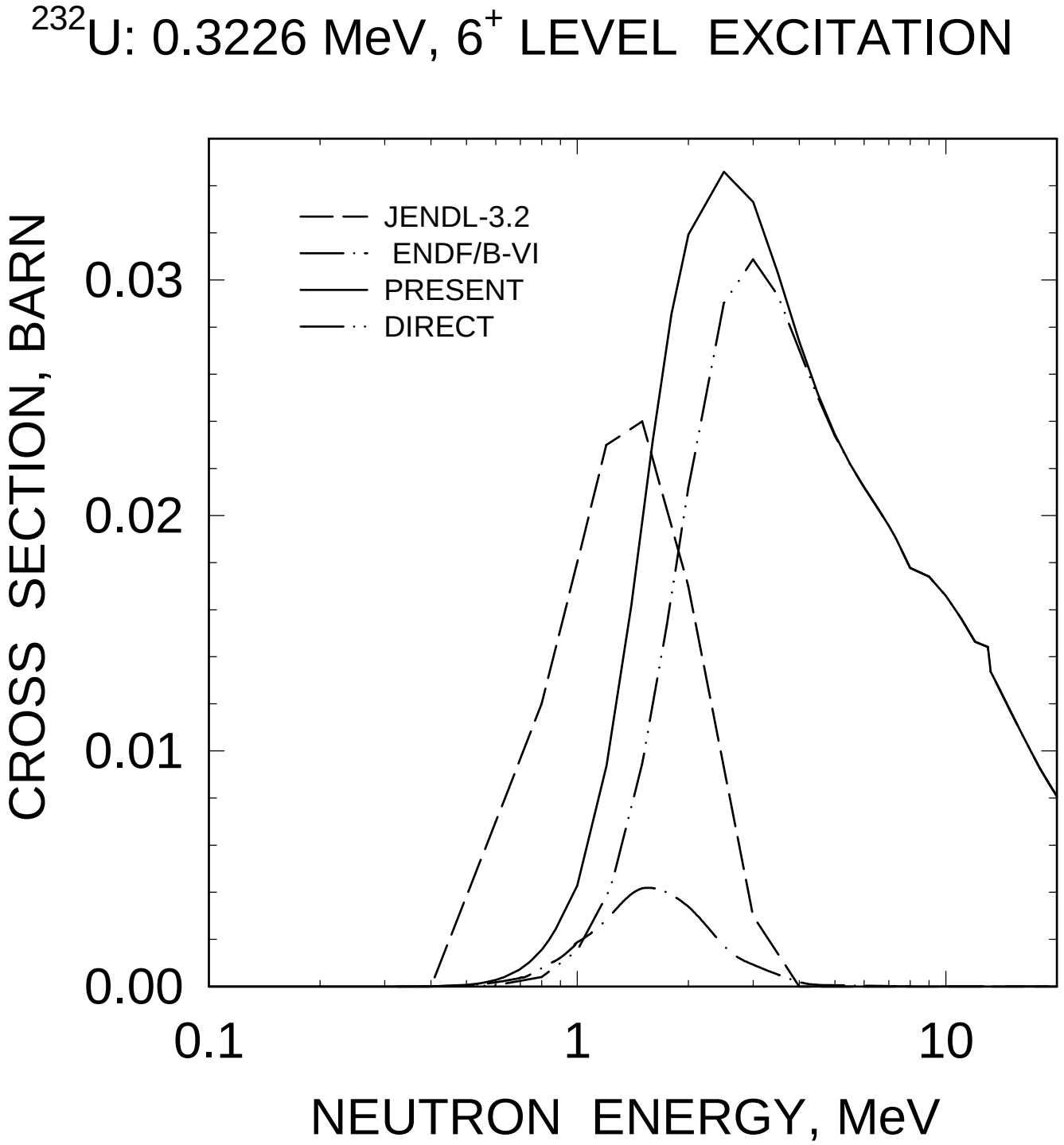
^{232}U: 0.3226 MeV, 6^{+} LEVEL EXCITATION
JENDL-3.2
ENDF/B-VI
PRESENT
DIRECT
CROSS SECTION, BARN
0.03
0.02
0.01
0.00
0.1
1
10
NEUTRON ENERGY, MeV

FIG. 35

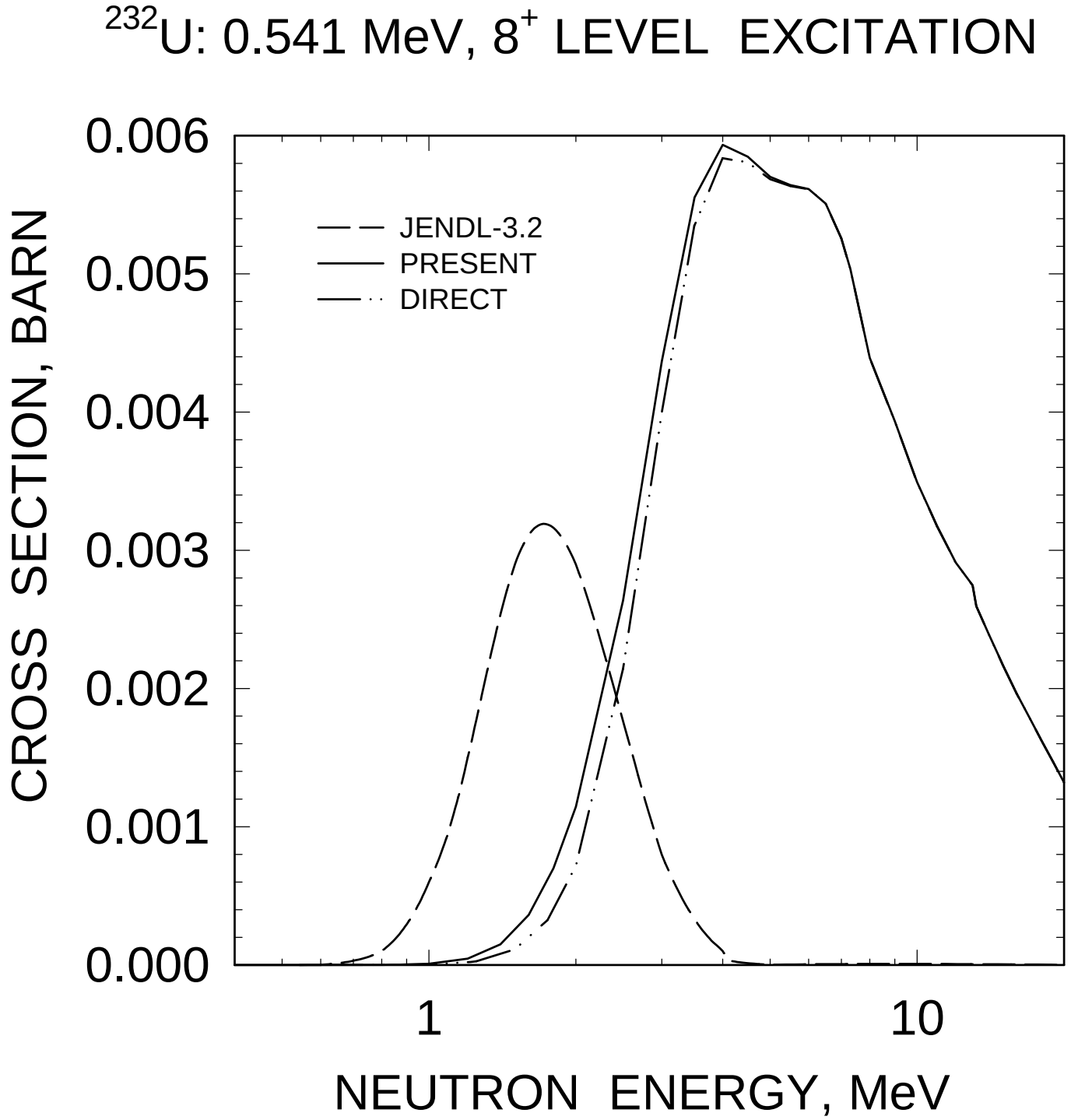
^{232}U: 0.541 MeV, 8^{+} LEVEL EXCITATION
JENDL-3.2
PRESENT
DIRECT
CROSS SECTION, BARN
0.006
0.005
0.004
0.003
0.002
0.001
0.000
1
10
NEUTRON ENERGY, MeV

FIG. 36

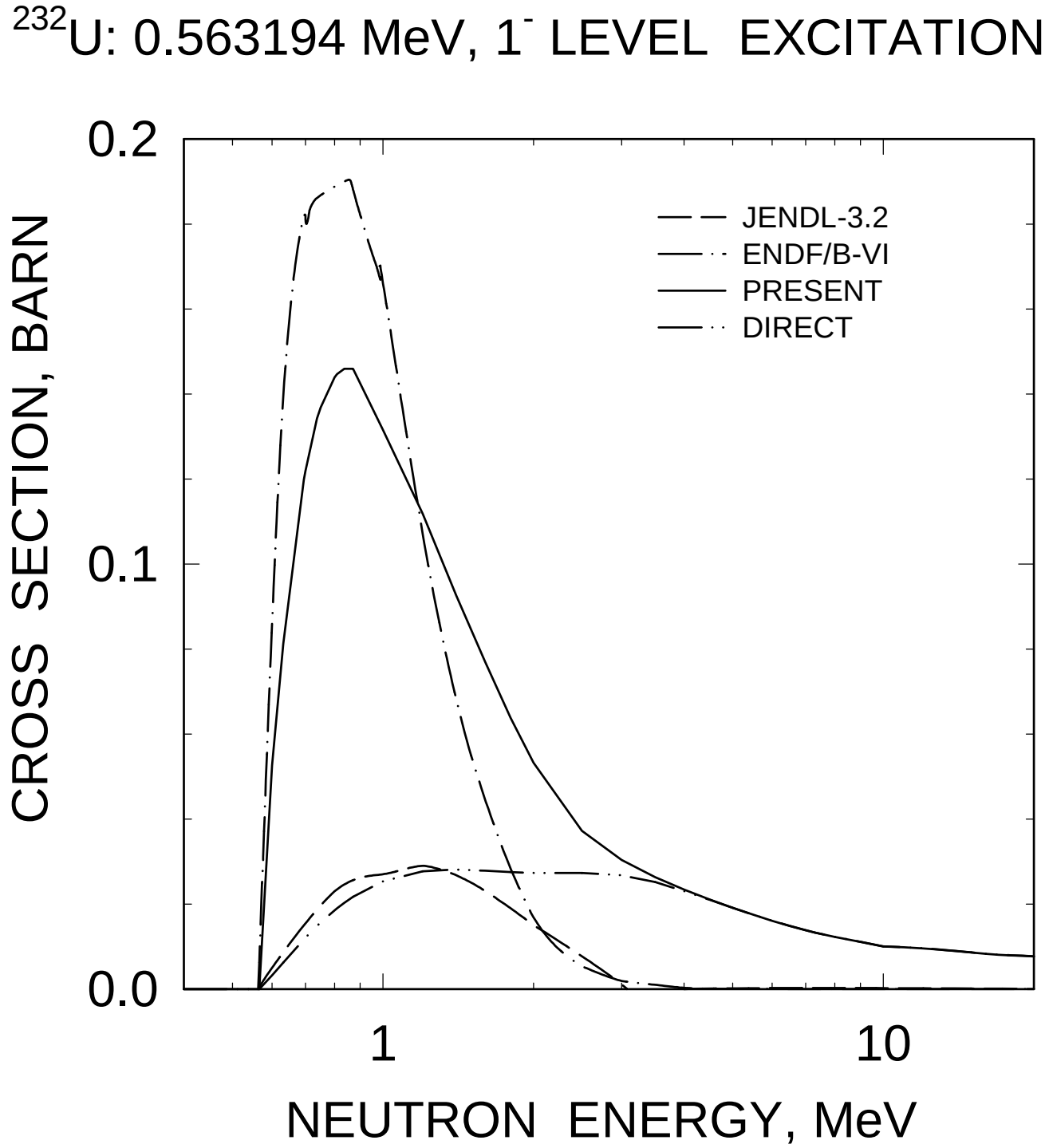
^{232}U: 0.563194 MeV, 1$^-$ LEVEL EXCITATION
0.2
0.1
0.0
CROSS SECTION, BARN
JENDL-3.2
ENDF/B-VI
PRESENT
DIRECT
1
10
NEUTRON ENERGY, MeV

FIG. 37

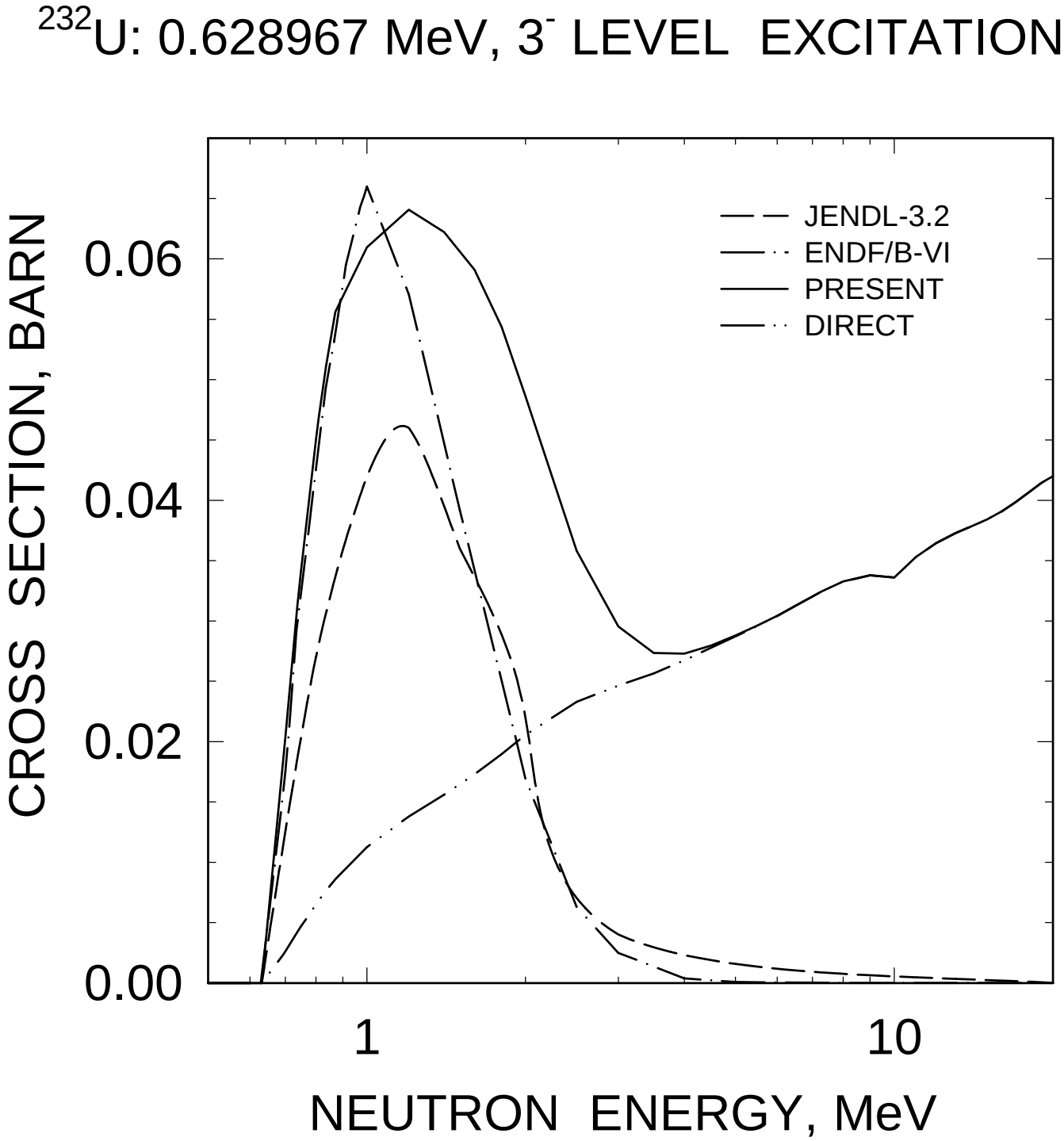
^{232}U: 0.628967 MeV, 3$^-$ LEVEL EXCITATION
JENDL-3.2
ENDF/B-VI
PRESENT
DIRECT
CROSS SECTION, BARN
0.06
0.04
0.02
0.00
1
10
NEUTRON ENERGY, MeV

FIG. 38

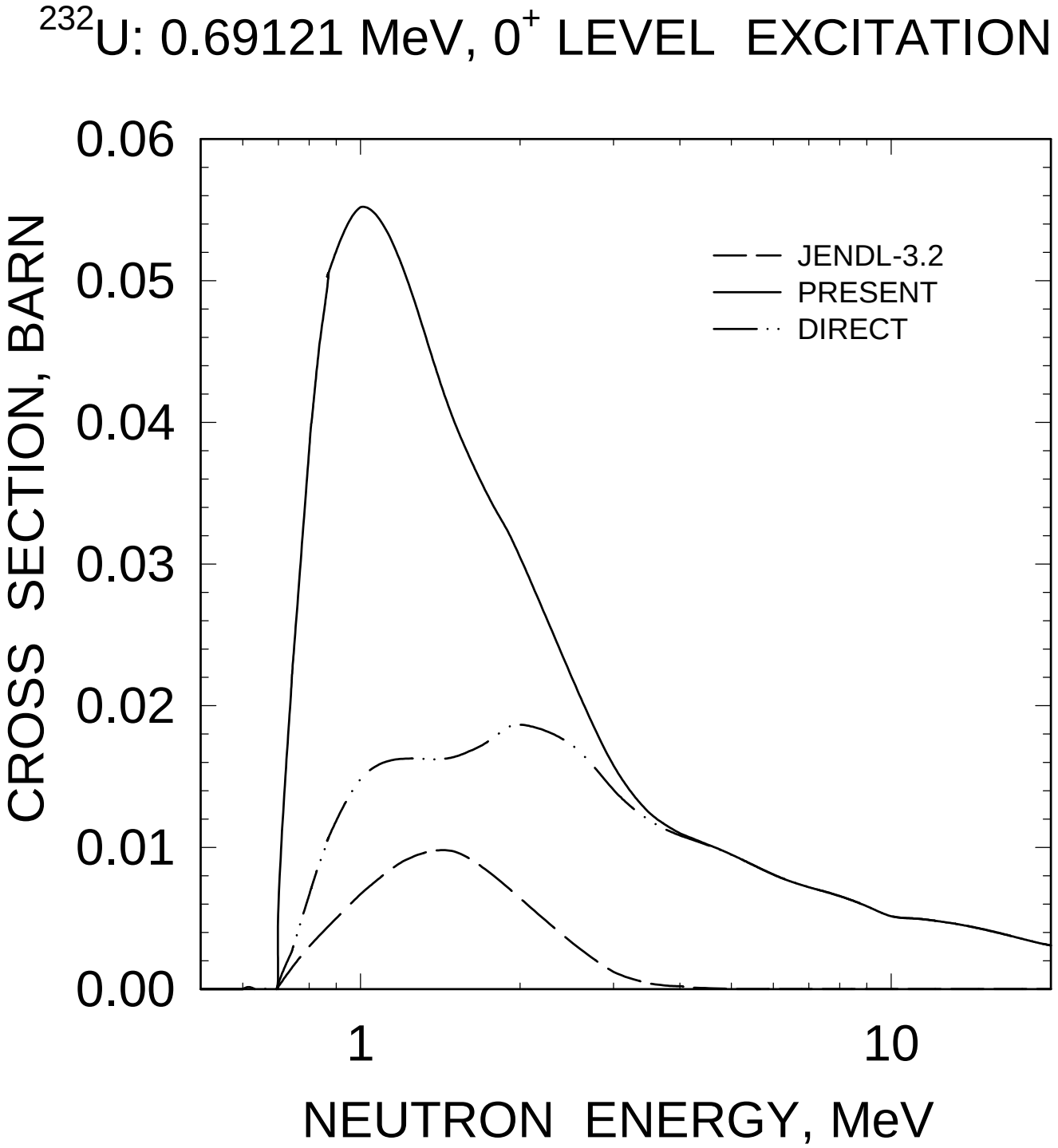
^{232}U: 0.69121 MeV, 0^{+} LEVEL EXCITATION
CROSS SECTION, BARN
0.06
0.05
0.04
0.03
0.02
0.01
0.00
1
10
NEUTRON ENERGY, MeV
JENDL-3.2
PRESENT
DIRECT

FIG. 39

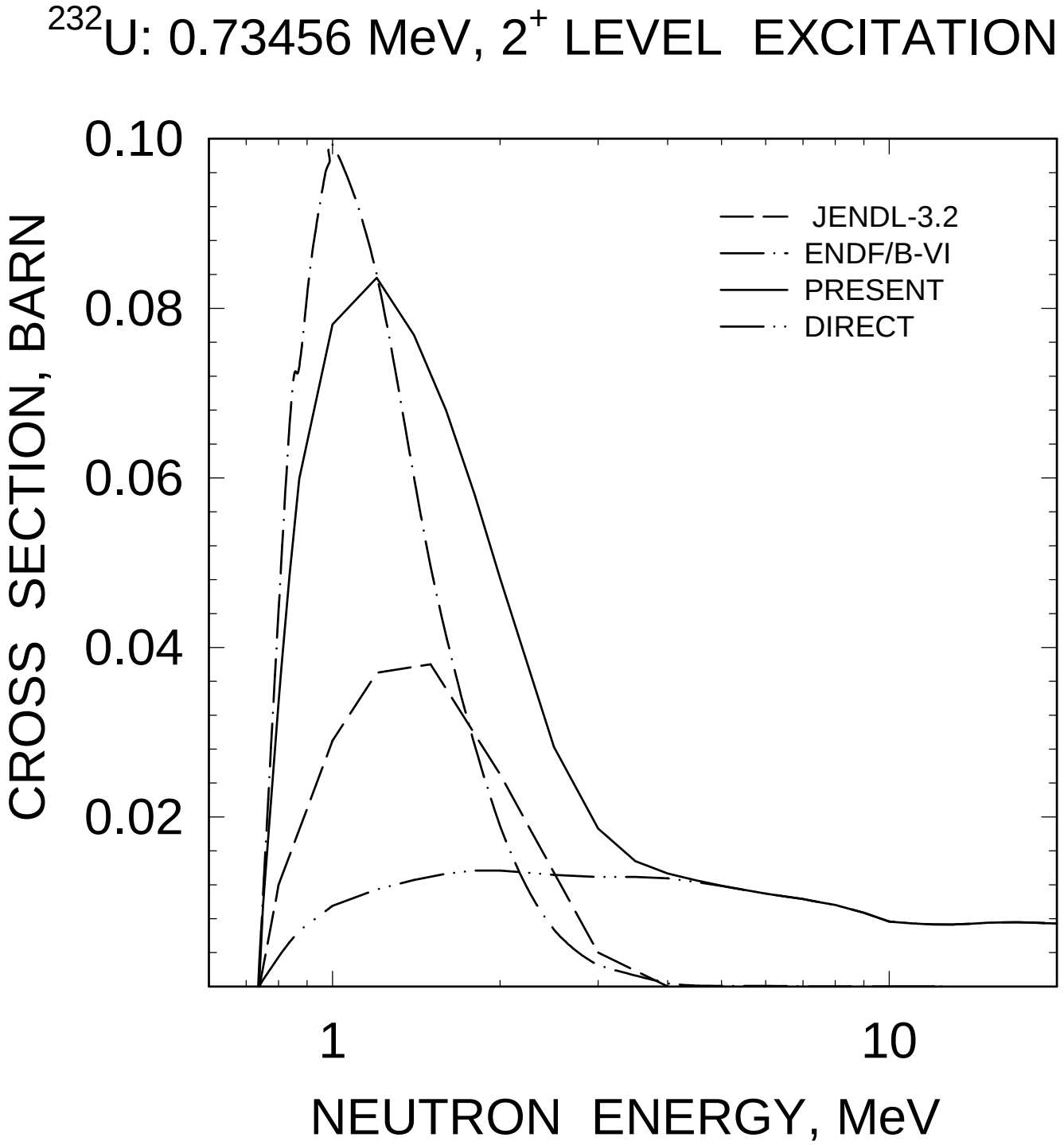
^{232}U: 0.73456 MeV, 2^{+} LEVEL EXCITATION
0.10
0.08
0.06
0.04
0.02
CROSS SECTION, BARN
JENDL-3.2
ENDF/B-VI
PRESENT
DIRECT
1
10
NEUTRON ENERGY, MeV

FIG. 40

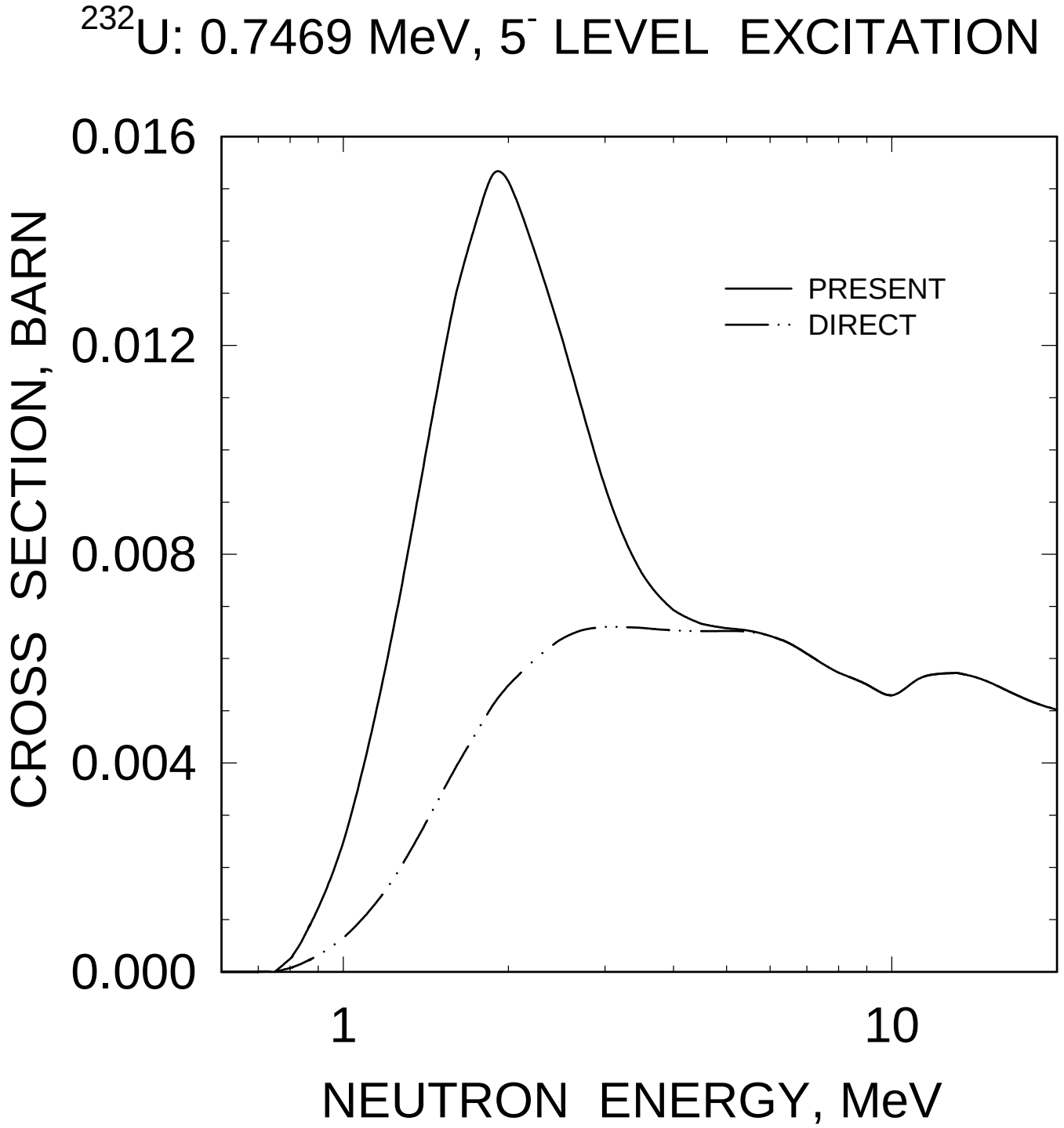
^{232}U: 0.7469 MeV, 5$^-$ LEVEL EXCITATION
0.016
0.012
0.008
0.004
0.000
CROSS SECTION, BARN
PRESENT
DIRECT
1
10
NEUTRON ENERGY, MeV

FIG. 41

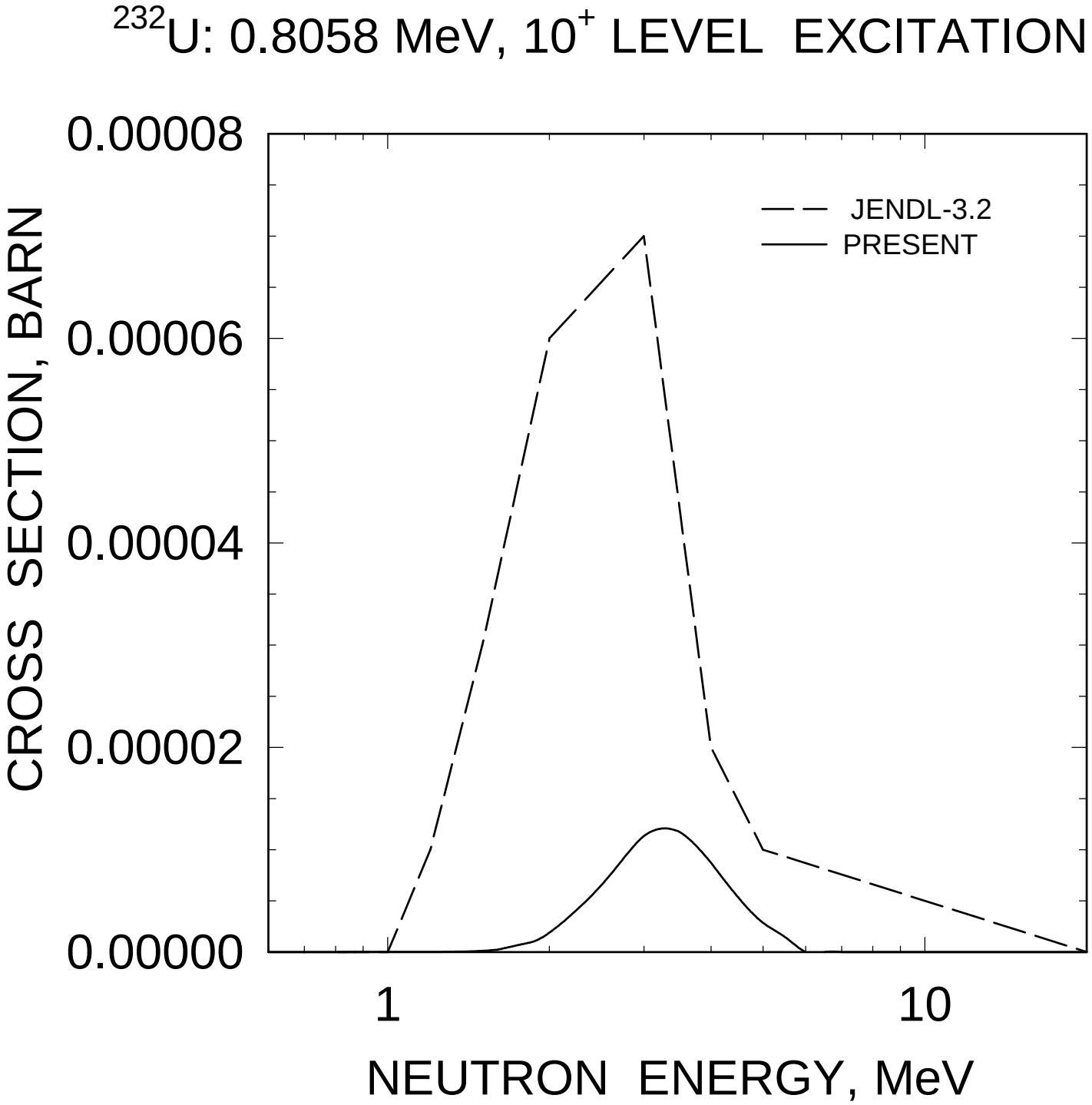
^{232}U: 0.8058 MeV, 10^{+} LEVEL EXCITATION
0.00008
0.00006
0.00004
0.00002
0.00000
CROSS SECTION, BARN
JENDL-3.2
PRESENT
1
10
NEUTRON ENERGY, MeV

FIG. 42

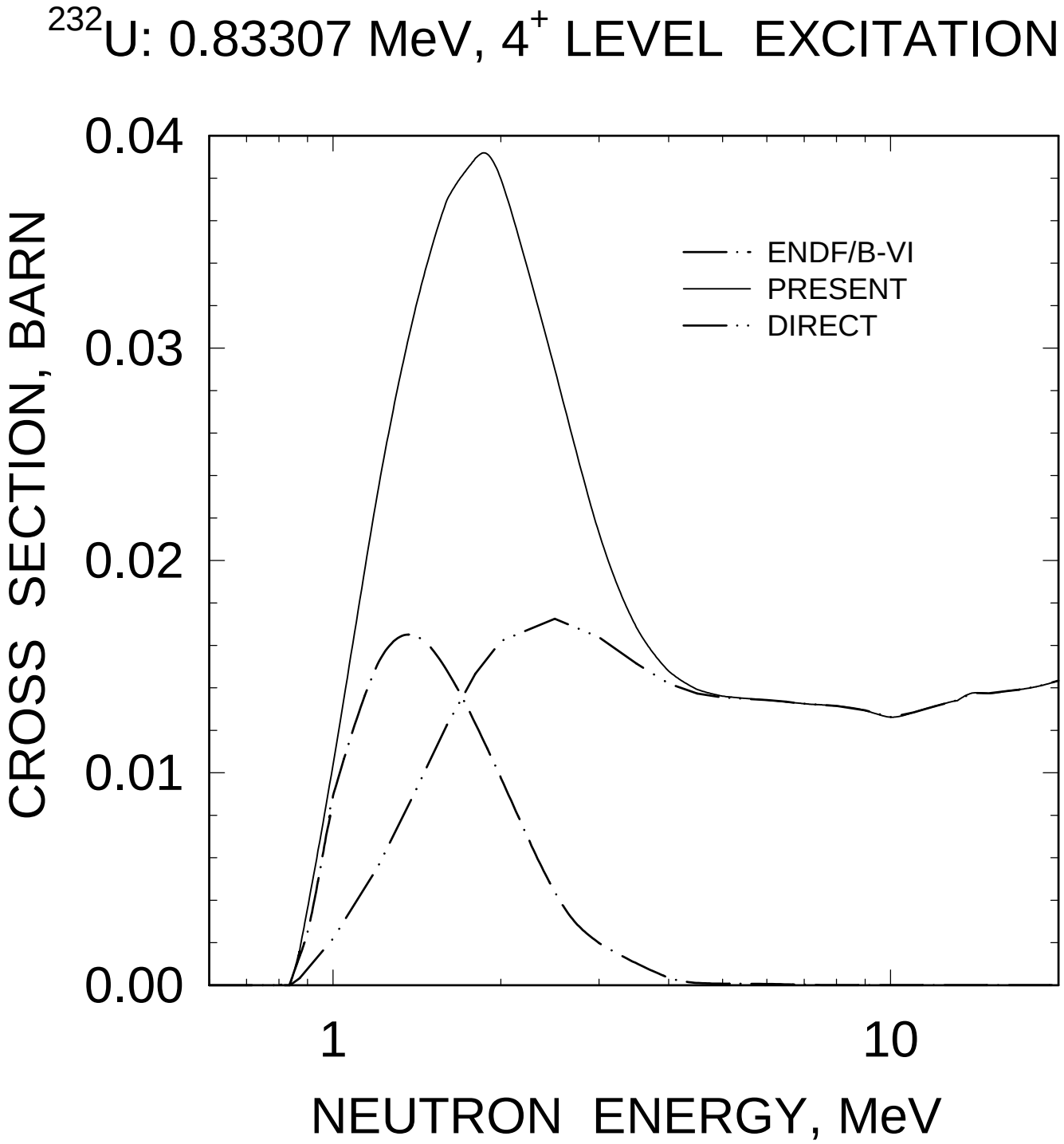
^{232}U: 0.83307 MeV, 4^{+} LEVEL EXCITATION
0.04
0.03
0.02
0.01
0.00
CROSS SECTION, BARN
ENDF/B-VI
PRESENT
DIRECT
1
10
NEUTRON ENERGY, MeV

FIG. 43

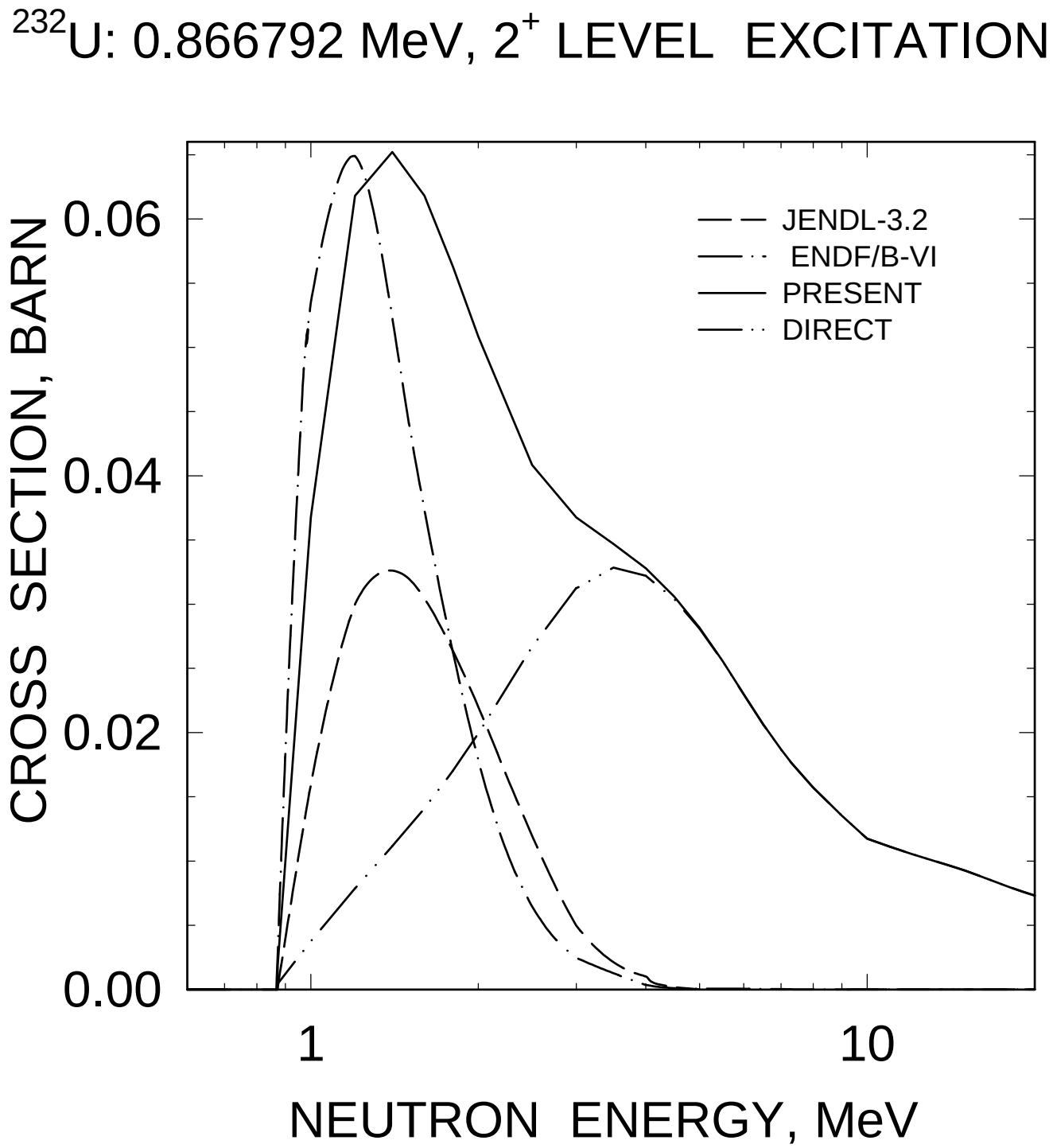
^{232}U: 0.866792 MeV, 2^{+} LEVEL EXCITATION
CROSS SECTION, BARN
0.06
0.04
0.02
0.00
1
10
NEUTRON ENERGY, MeV
JENDL-3.2
ENDF/B-VI
PRESENT
DIRECT

FIG. 44

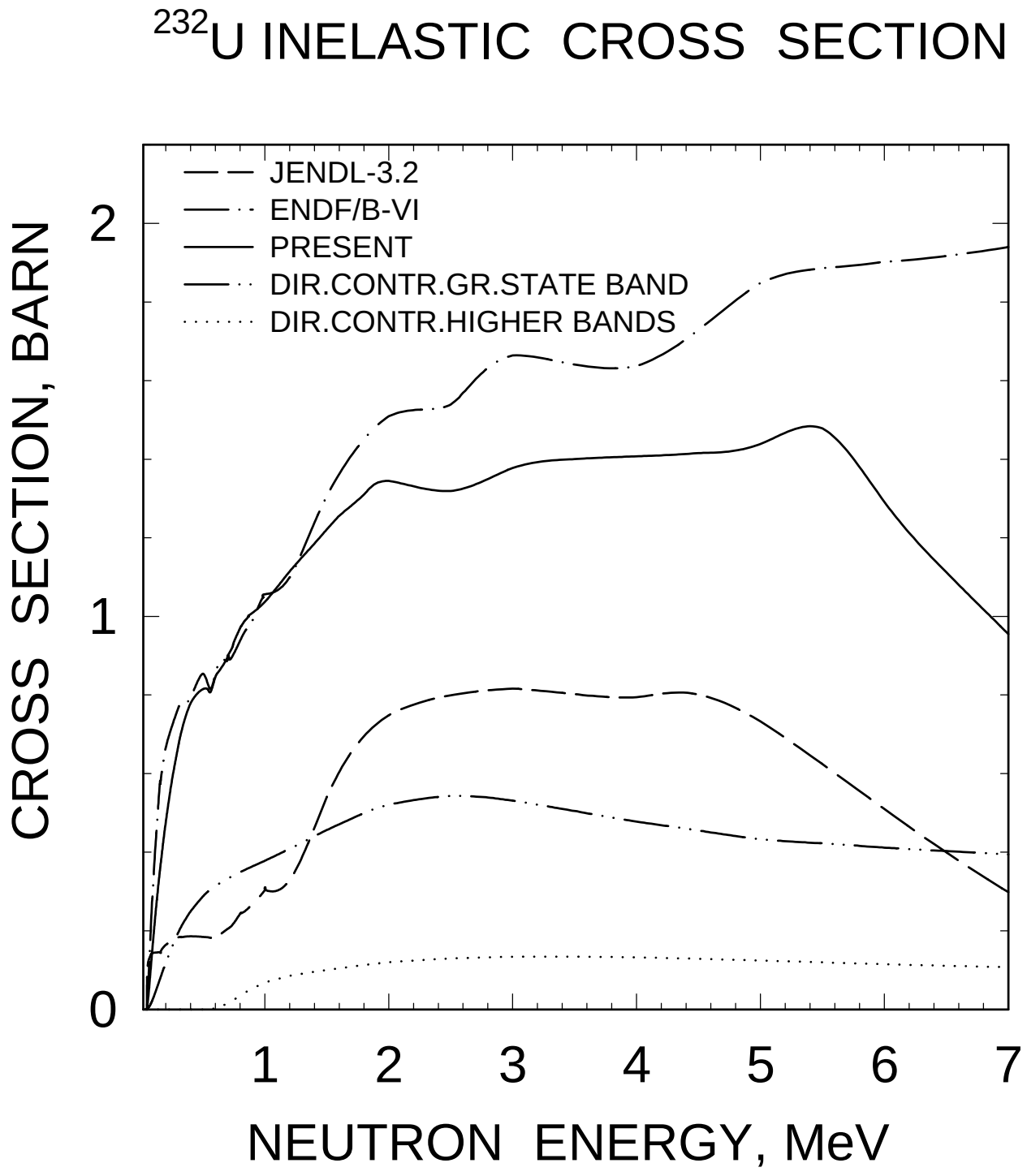
^{232}U INELASTIC CROSS SECTION
JENDL-3.2
ENDF/B-VI
PRESENT
DIR.CONTR.GR.STATE BAND
DIR.CONTR.HIGHER BANDS
CROSS SECTION, BARN
0
1
2
1
2
3
4
5
6
7
NEUTRON ENERGY, MeV

FIG. 45

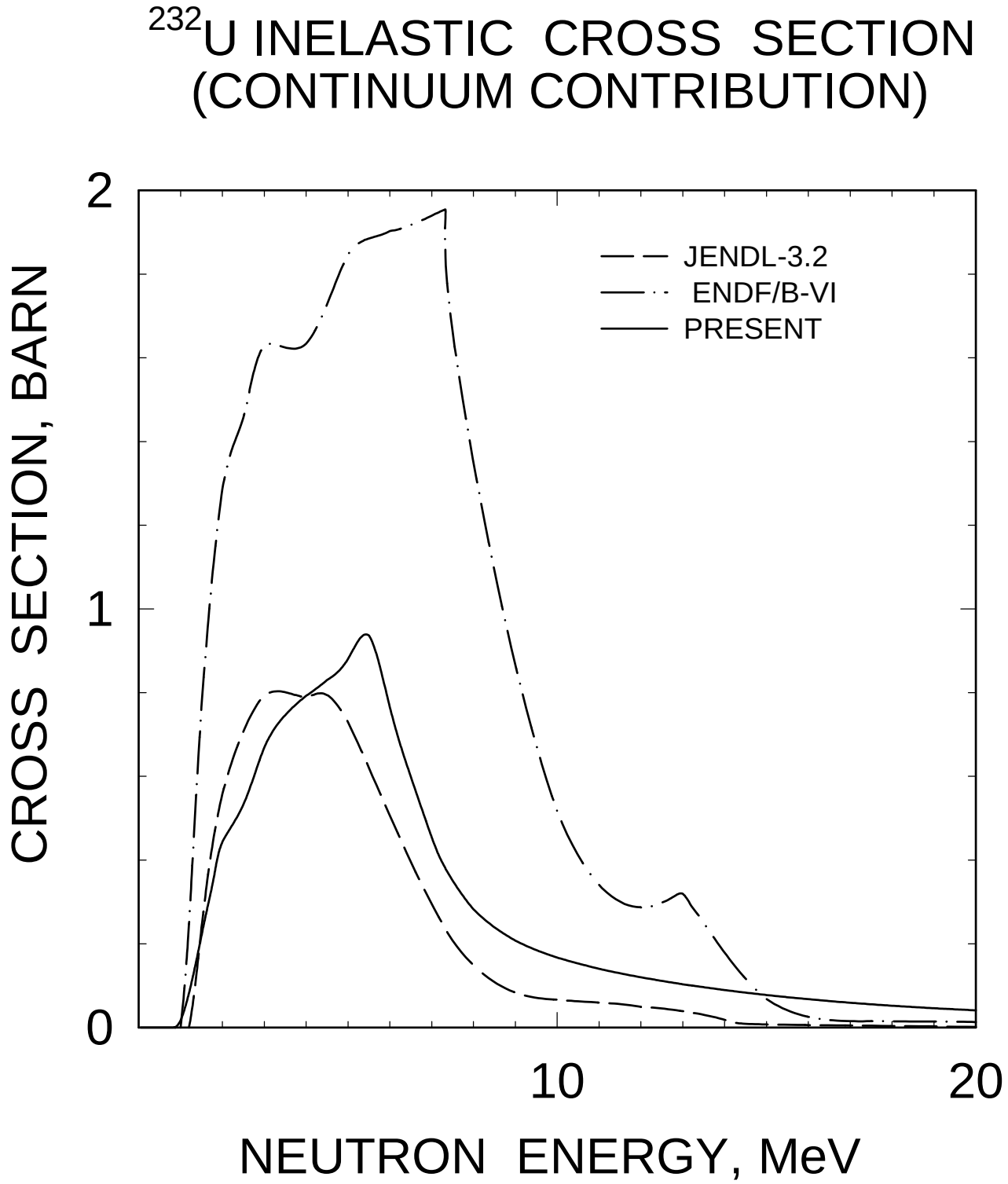
^{232}U INELASTIC CROSS SECTION
(CONTINUUM CONTRIBUTION)
JENDL-3.2
ENDF/B-VI
PRESENT
CROSS SECTION, BARN
2
1
0
10
20
NEUTRON ENERGY, MeV

FIG. 46

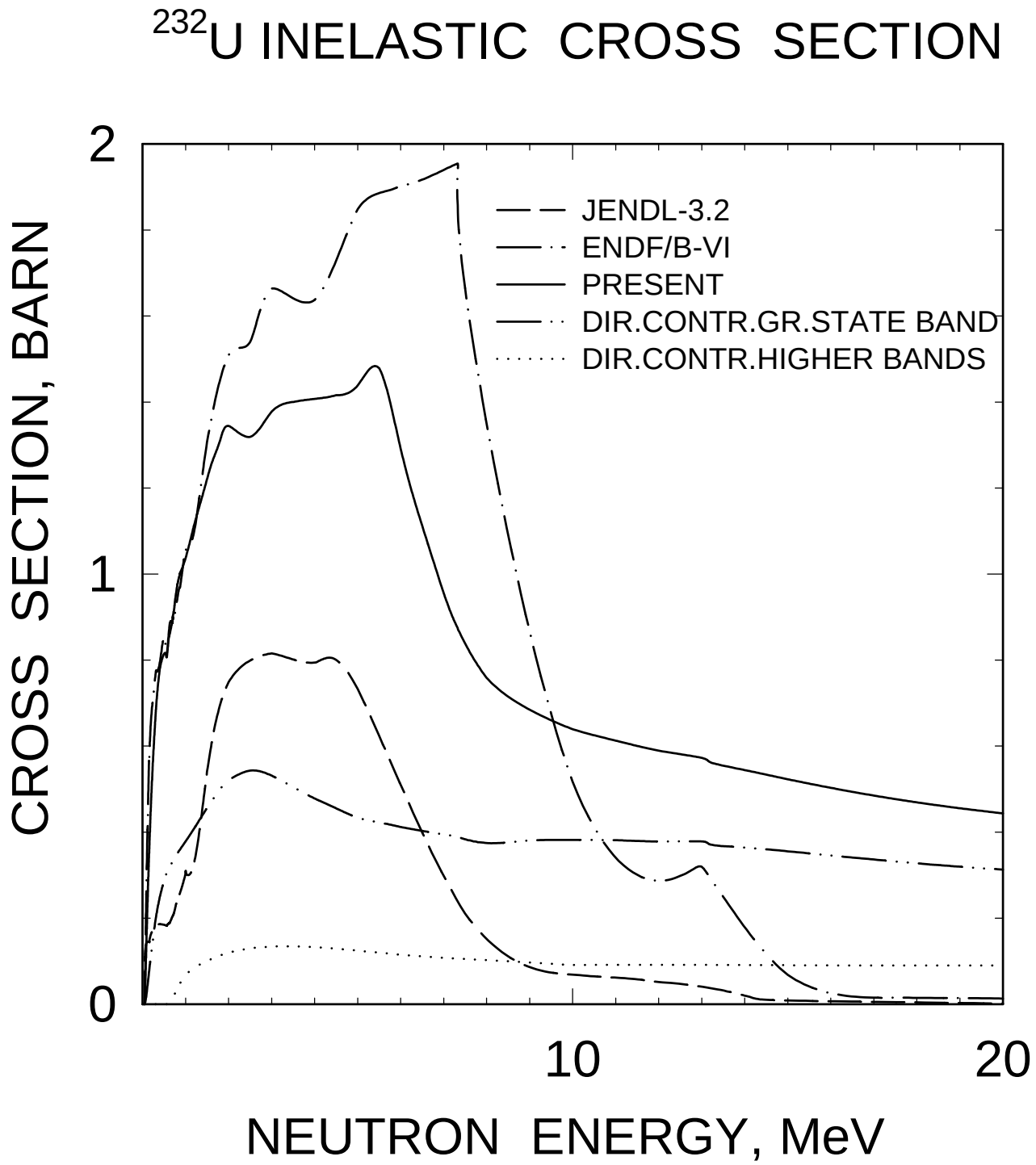
^{232}U INELASTIC CROSS SECTION
CROSS SECTION, BARN
NEUTRON ENERGY, MeV
0
1
2
10
20
JENDL-3.2
ENDF/B-VI
PRESENT
DIR.CONTR.GR.STATE BAND
DIR.CONTR.HIGHER BANDS

FIG. 47

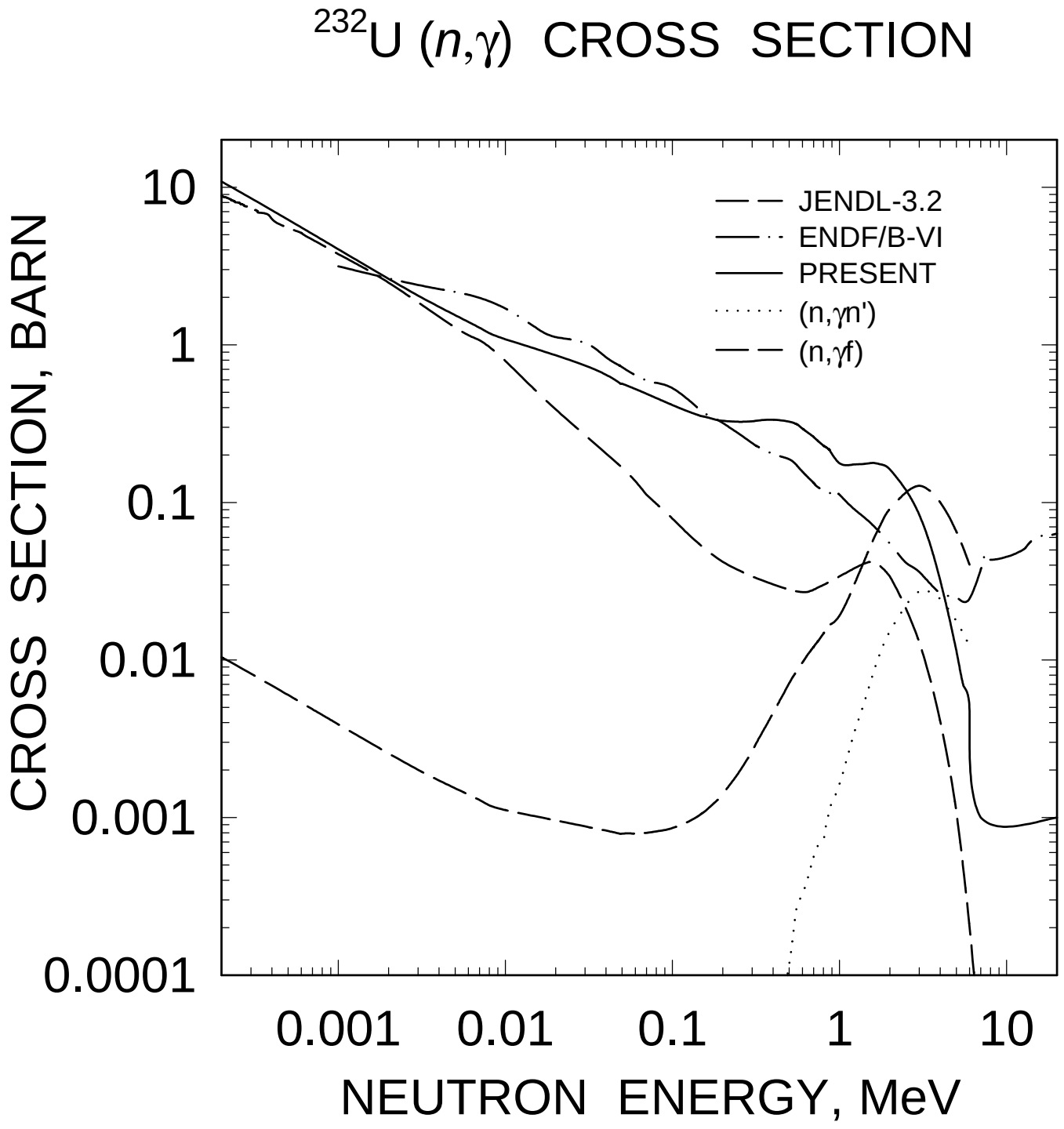
^{232}U (n,γ) CROSS SECTION
JENDL-3.2
ENDF/B-VI
PRESENT
(n,γn')
(n,γf)
CROSS SECTION, BARN
10
1
0.1
0.01
0.001
0.0001
0.001
0.01
0.1
1
10
NEUTRON ENERGY, MeV

FIG. 48

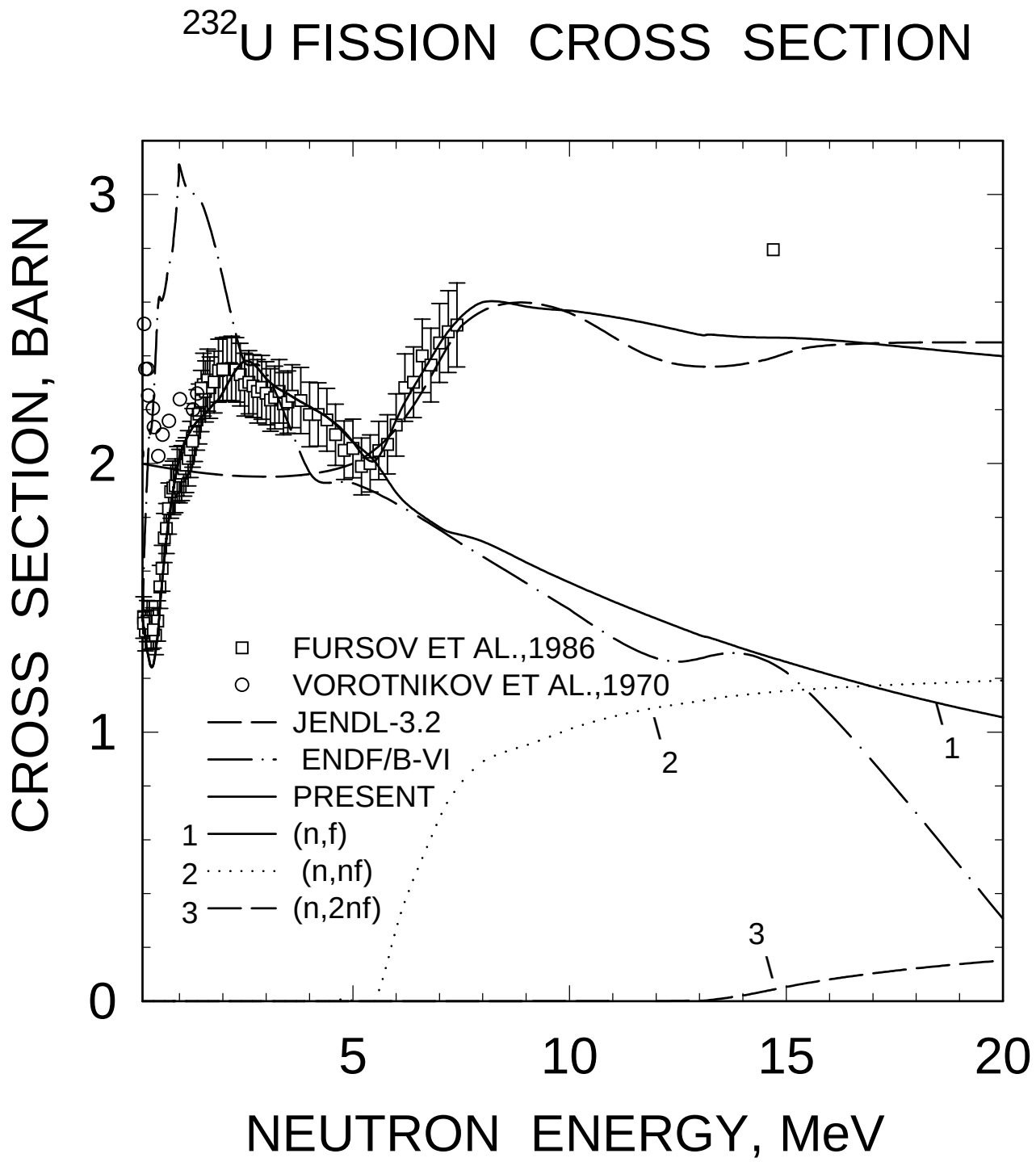
232U FISSION CROSS SECTION
CROSS SECTION, BARN
NEUTRON ENERGY, MeV
0
1
2
3
5
10
15
20
FURSOV ET AL.,1986
VOROTNIKOV ET AL.,1970
JENDL-3.2
ENDF/B-VI
PRESENT
1 (n,f)
2 (n,nf)
3 (n,2nf)
1
2
3

FIG. 49

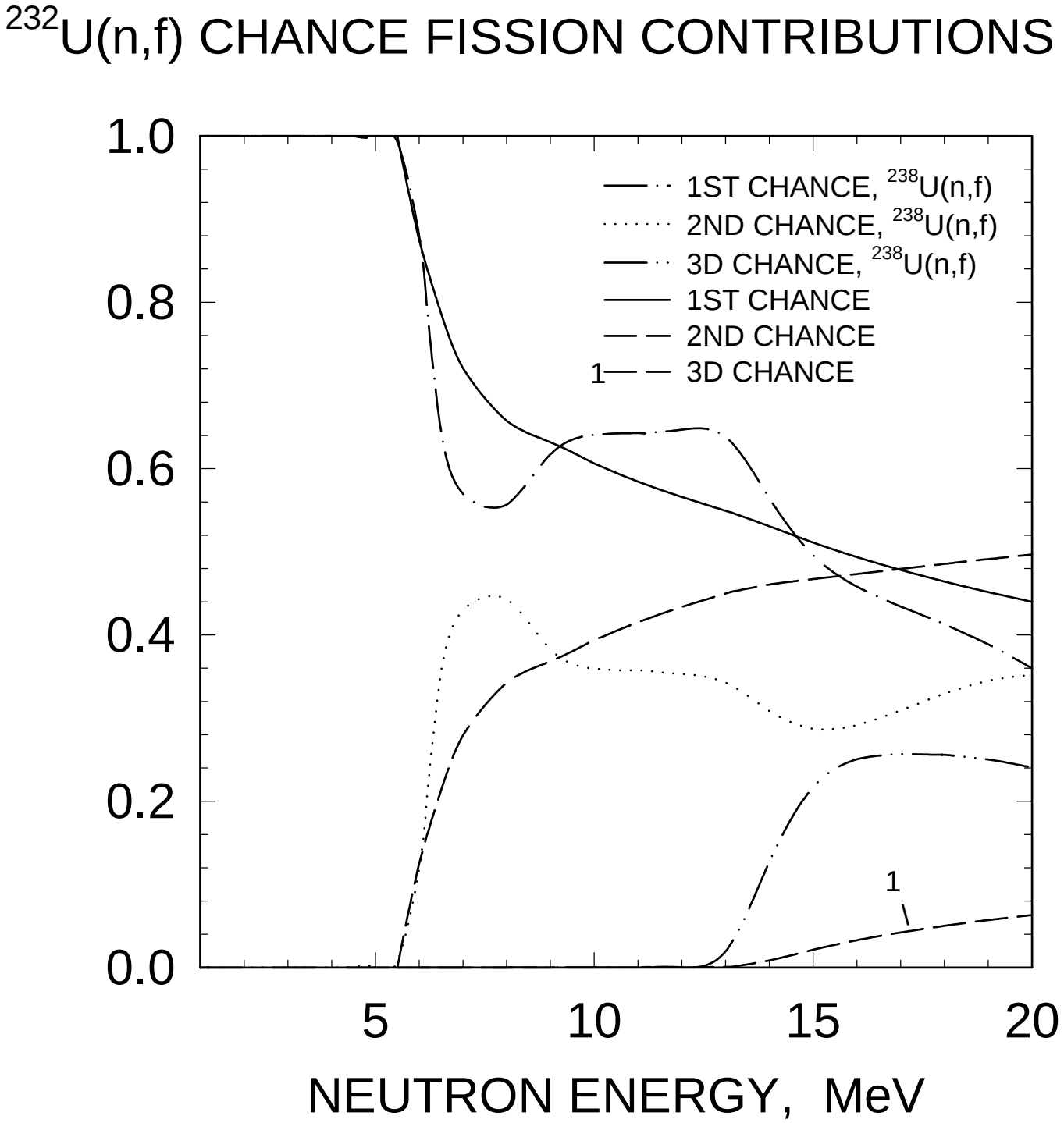
232U(n,f) CHANCE FISSION CONTRIBUTIONS
1.0
0.8
0.6
0.4
0.2
0.0
5
10
15
20
NEUTRON ENERGY, MeV
1ST CHANCE, 238U(n,f)
2ND CHANCE, 238U(n,f)
3D CHANCE, 238U(n,f)
1ST CHANCE
2ND CHANCE
3D CHANCE
1
1

FIG. 50

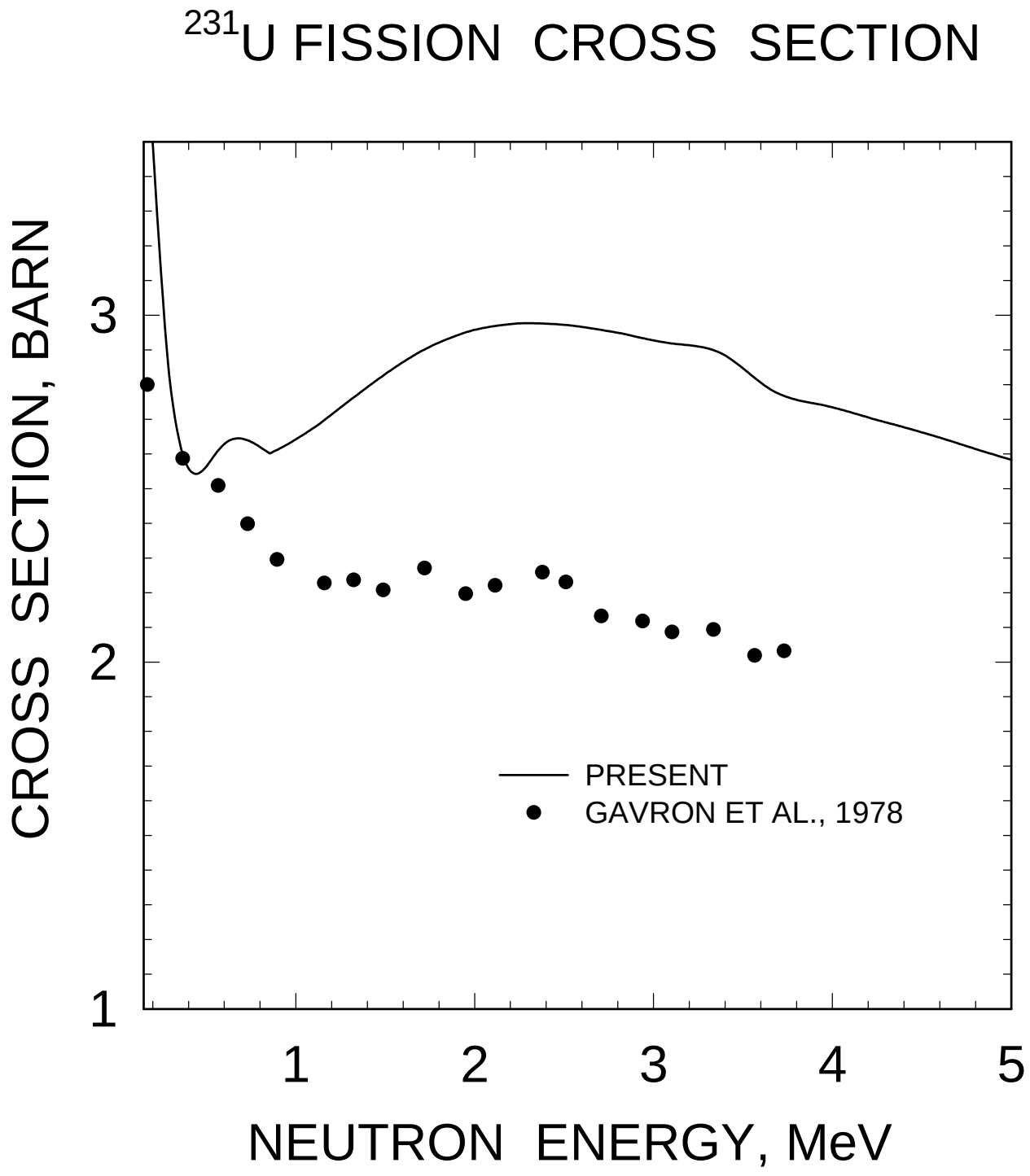
^{231}U FISSION CROSS SECTION
CROSS SECTION, BARN
3
2
1
1
2
3
4
5
NEUTRON ENERGY, MeV
PRESENT
GAVRON ET AL., 1978

FIG. 51

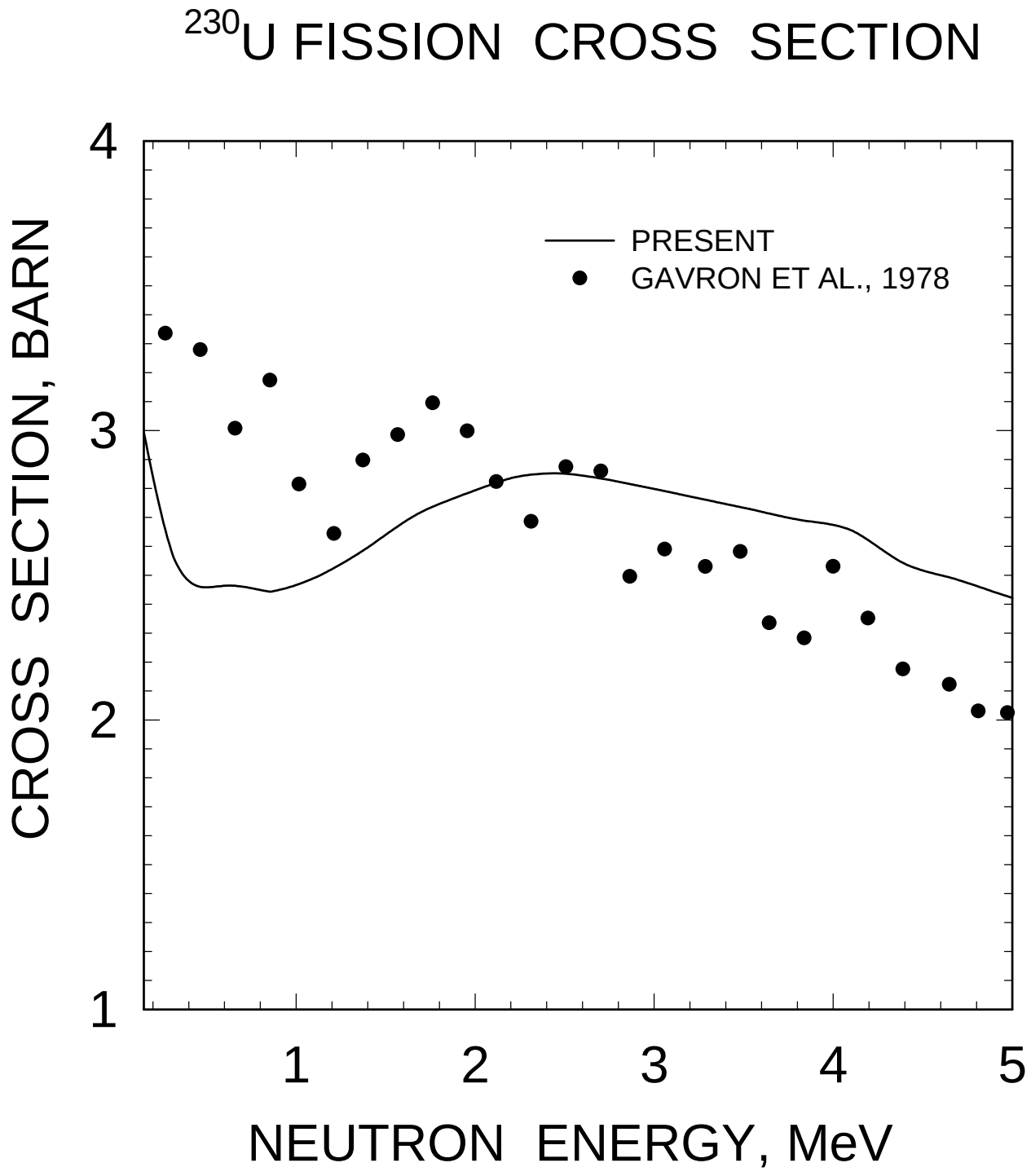
230U FISSION CROSS SECTION
PRESENT
GAVRON ET AL., 1978
CROSS SECTION, BARN
NEUTRON ENERGY, MeV
1
2
3
4
1
2
3
4
5

FIG. 52

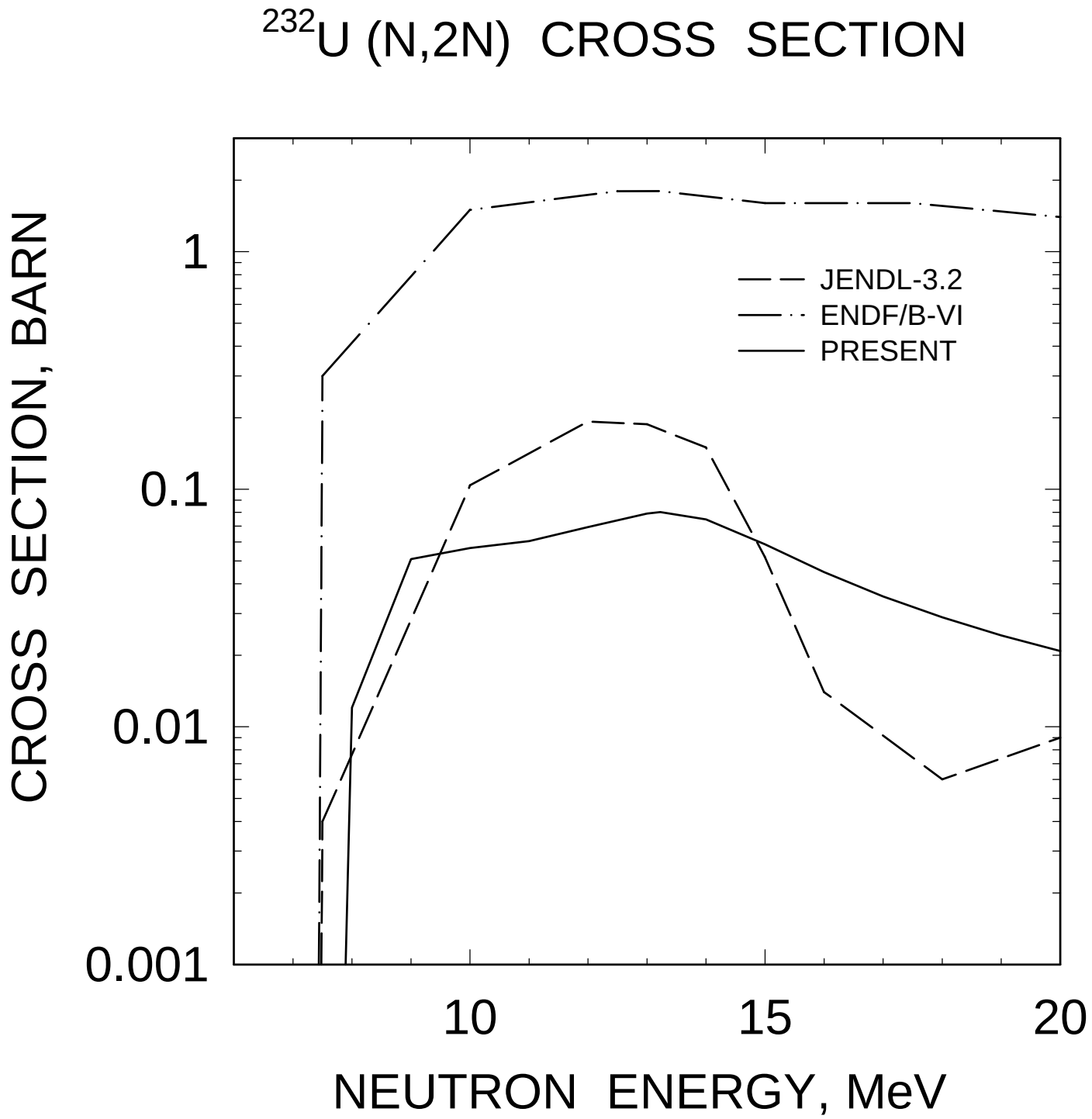
^{232}U (N,2N) CROSS SECTION
CROSS SECTION, BARN
1
0.1
0.01
0.001
10
15
20
NEUTRON ENERGY, MeV
JENDL-3.2
ENDF/B-VI
PRESENT

FIG. 53

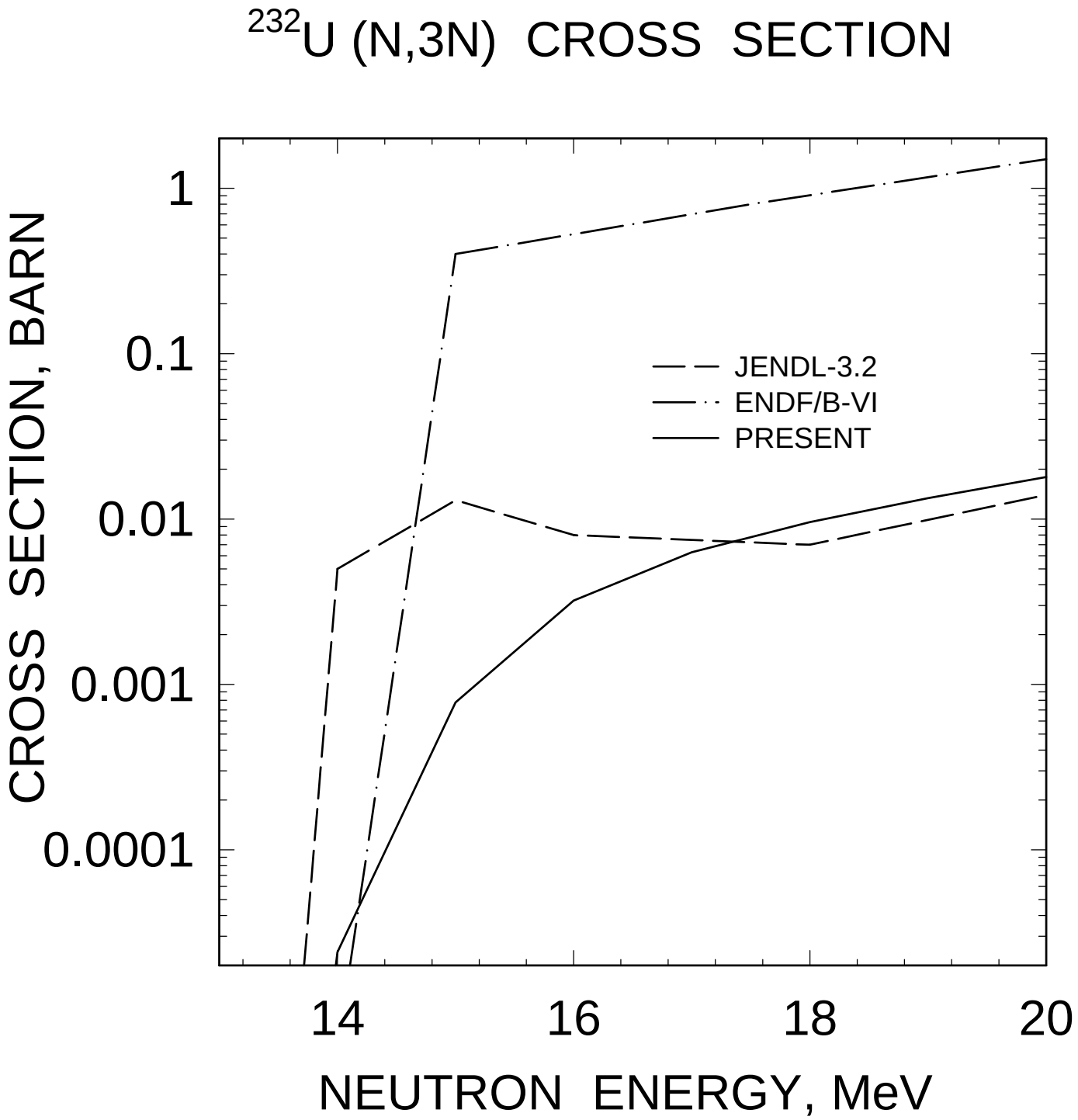
^{232}U (N,3N) CROSS SECTION
CROSS SECTION, BARN
1
0.1
0.01
0.001
0.0001
JENDL-3.2
ENDF/B-VI
PRESENT
14
16
18
20
NEUTRON ENERGY, MeV

FIG. 54

NEUTRON MULTIPLICITY AT THERMAL ENERGY

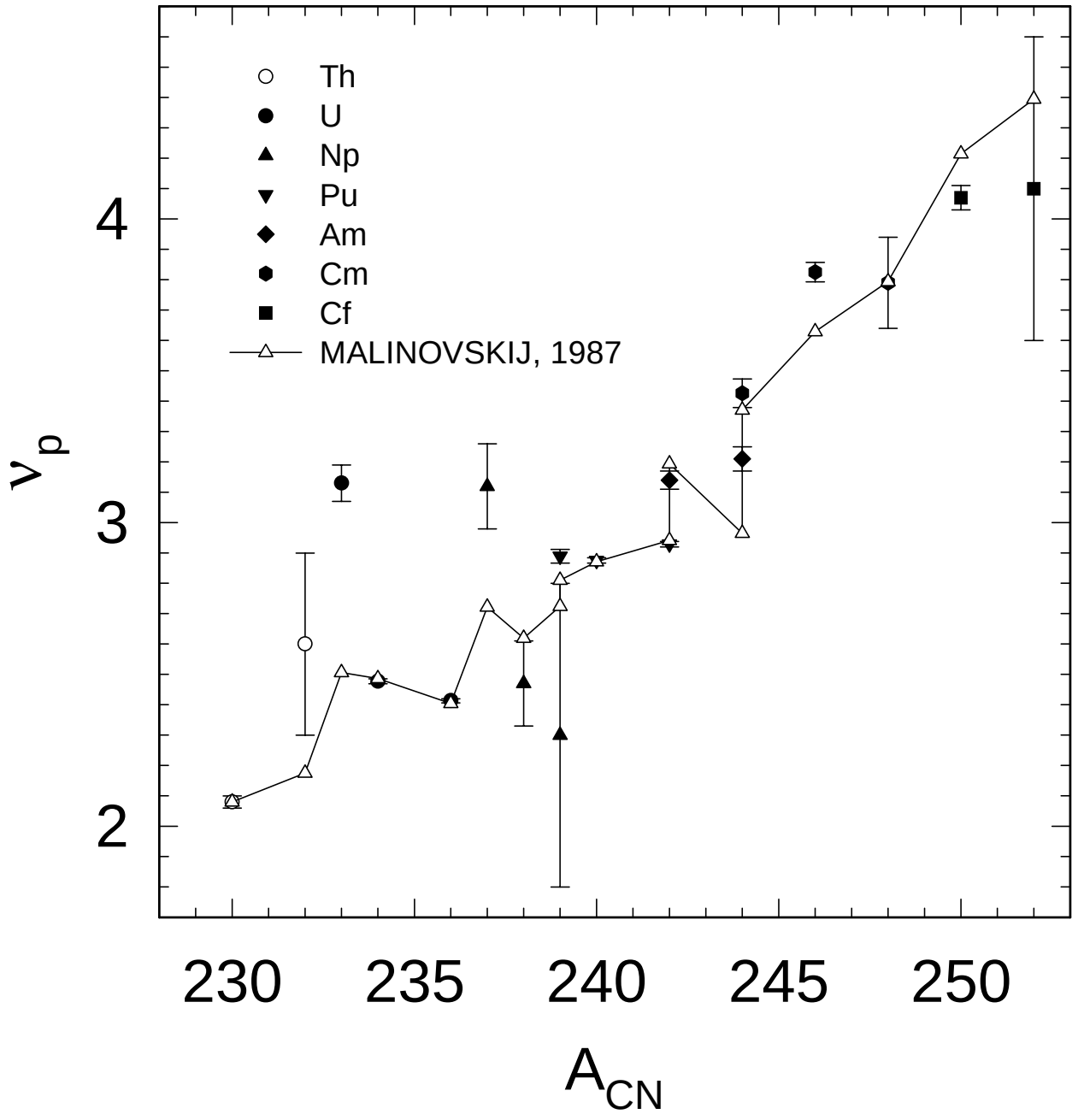

FIG. 55

NEUTRON MULTIPLICITY AT THERMAL ENERGY

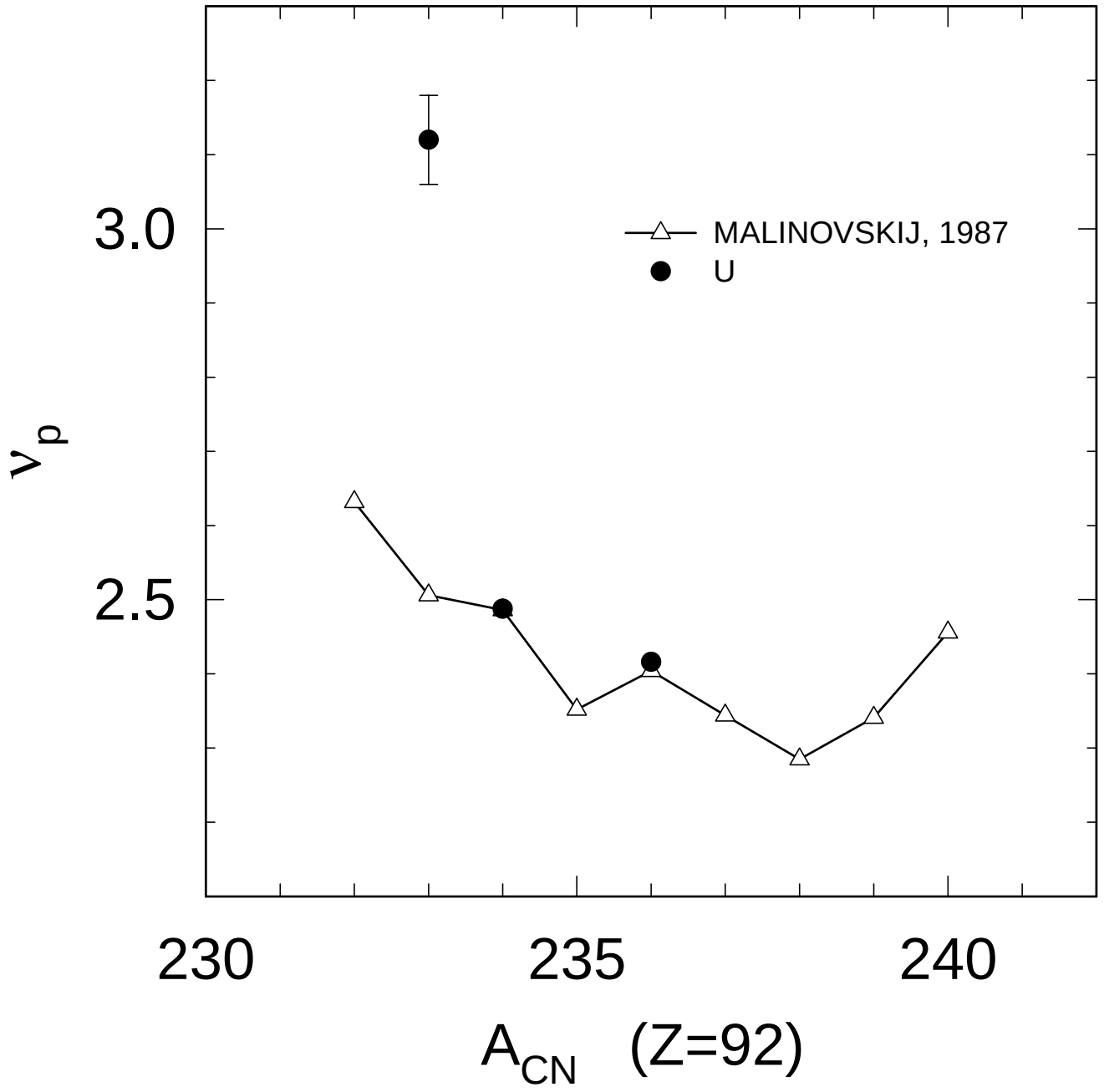

FIG. 56

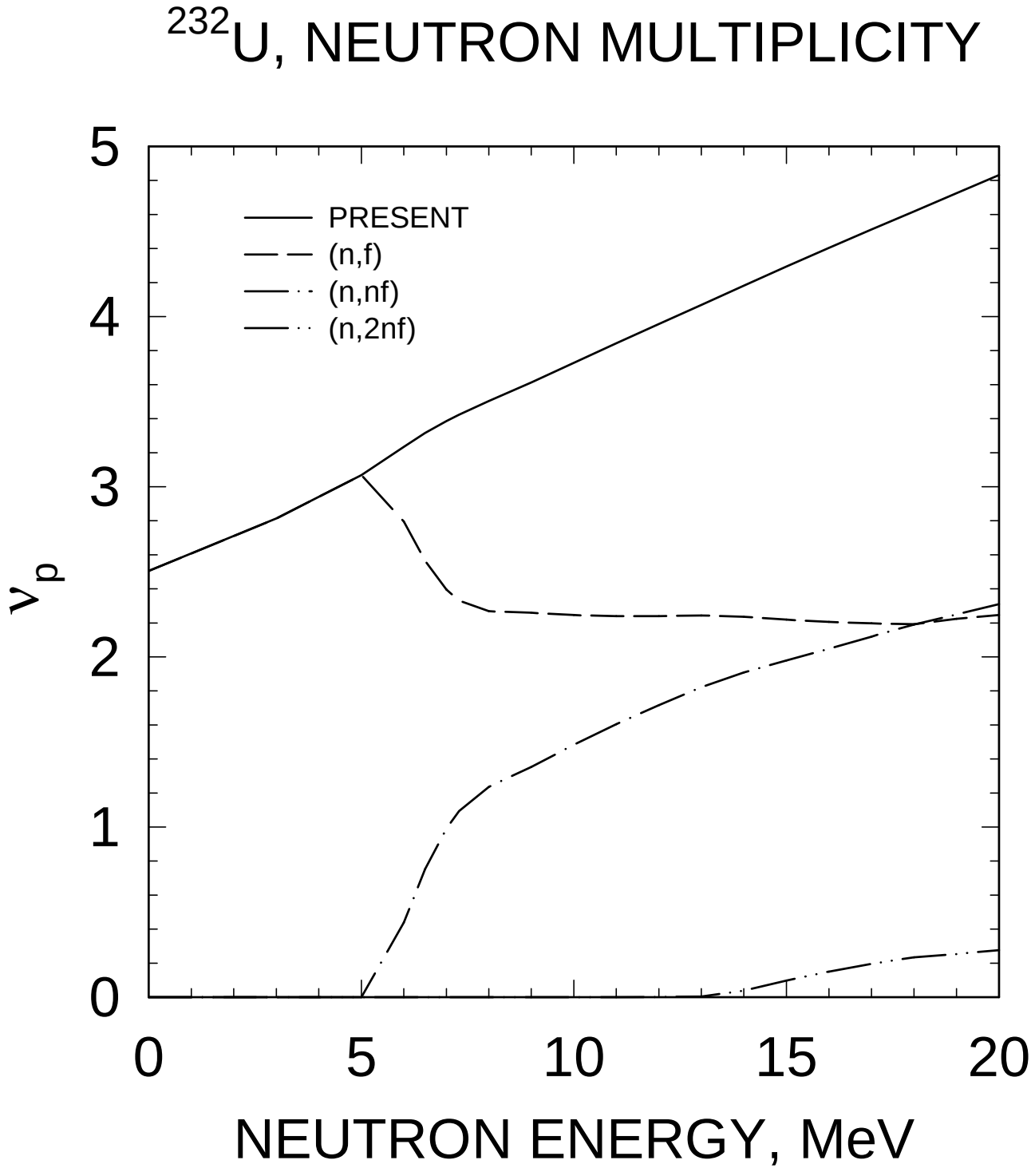
^{232}U, NEUTRON MULTIPLICITY
PRESENT
(n,f)
(n,nf)
(n,2nf)
ν_p
0
1
2
3
4
5
0
5
10
15
20
NEUTRON ENERGY, MeV

FIG. 57

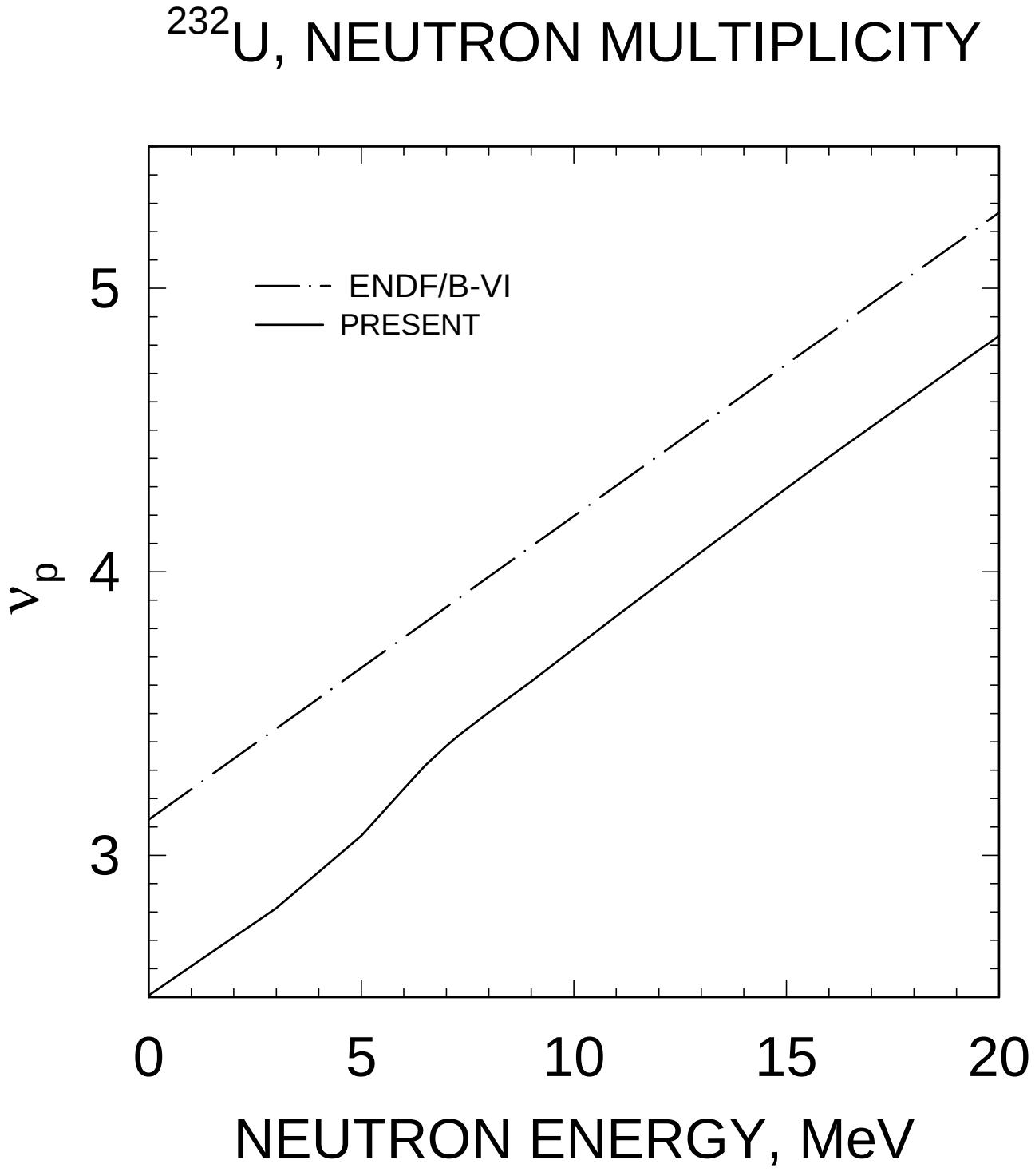
^{232}U, NEUTRON MULTIPLICITY
ENDF/B-VI
PRESENT
ν_p
5
4
3
0
5
10
15
20
NEUTRON ENERGY, MeV

FIG. 58

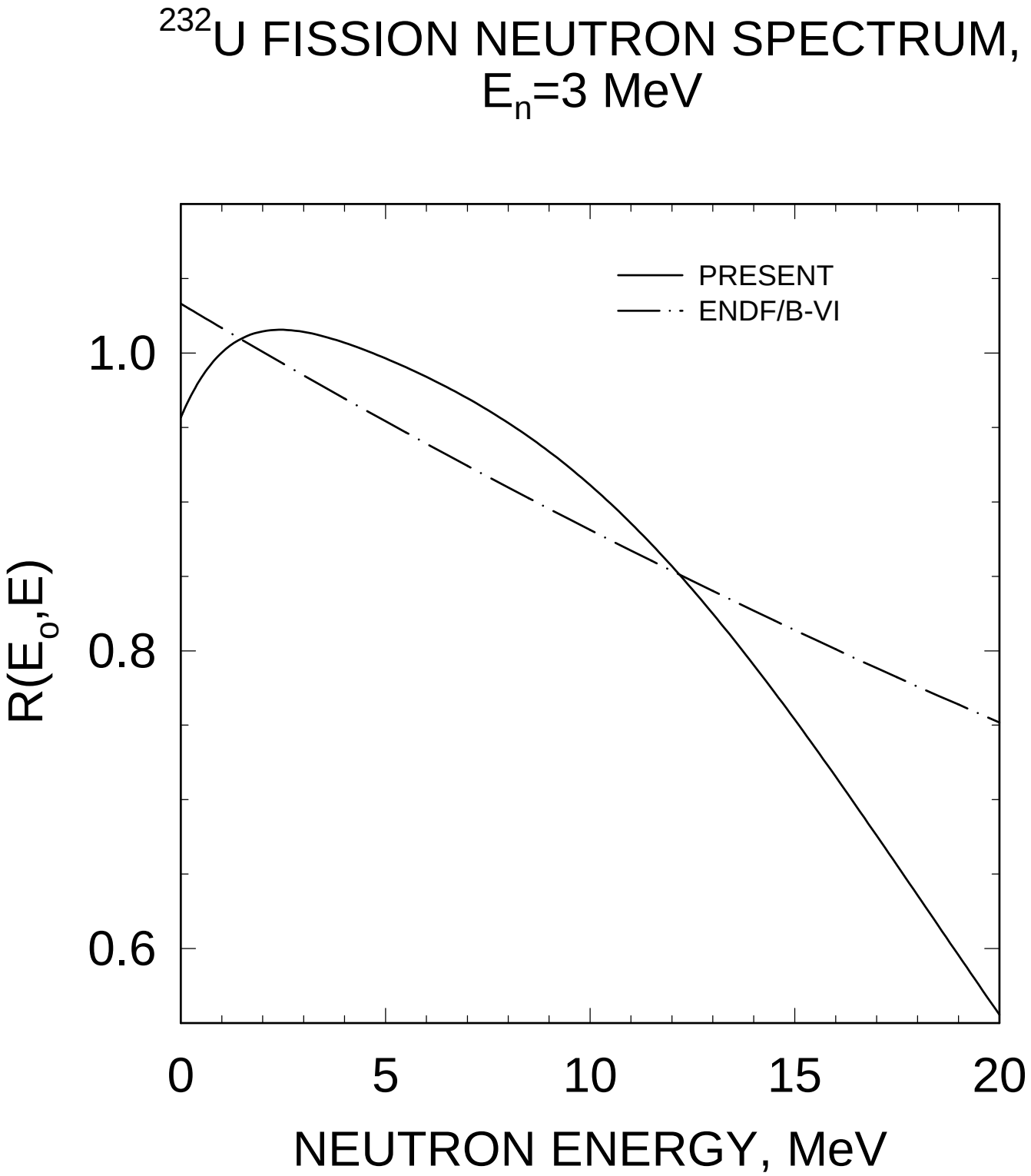
^{232}U FISSION NEUTRON SPECTRUM,
E_n=3 MeV
PRESENT
ENDF/B-VI
1.0
0.8
0.6
$R(E_o,E)$
0
5
10
15
20
NEUTRON ENERGY, MeV

FIG. 59

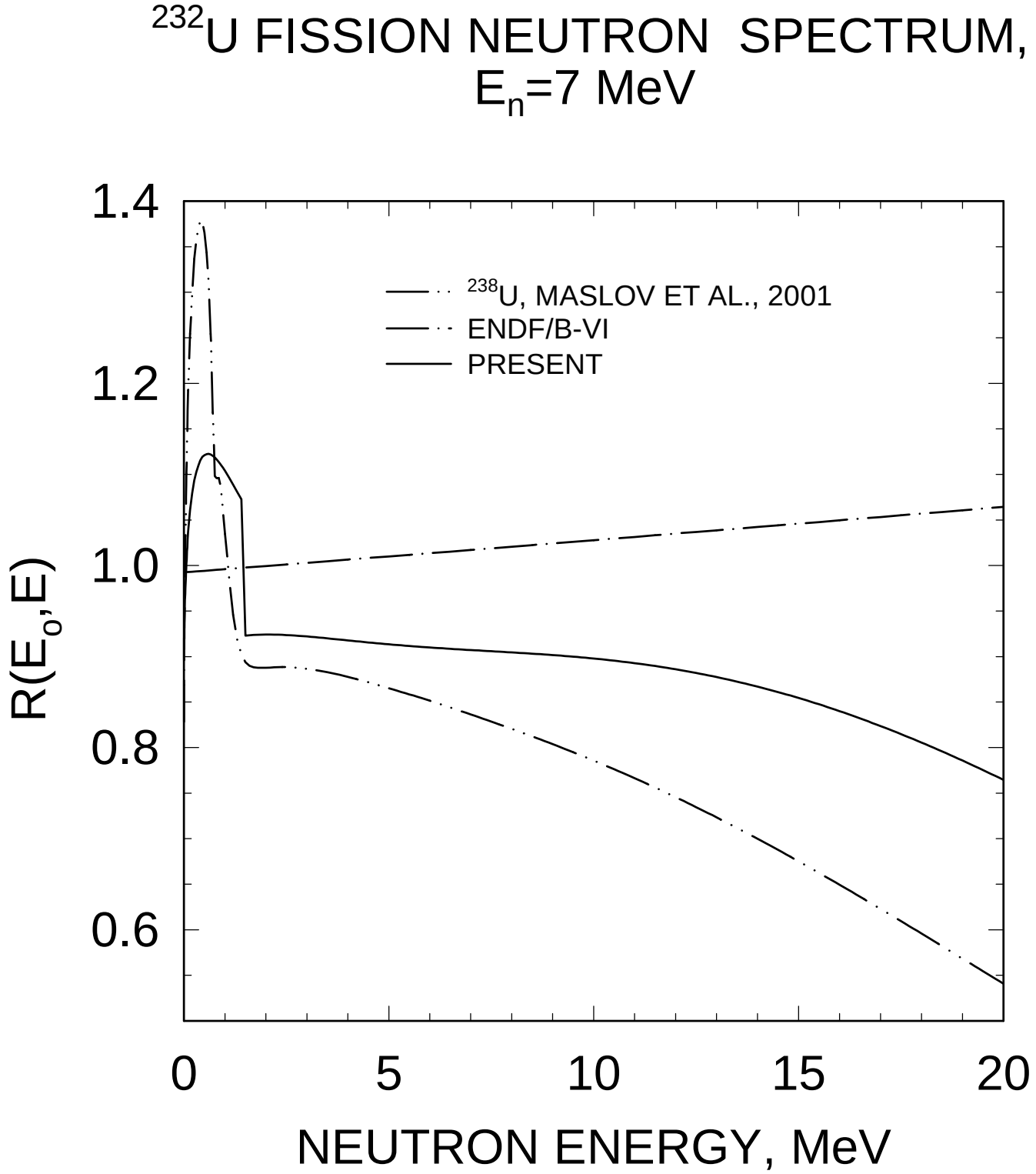
^{232}U FISSION NEUTRON SPECTRUM,
E_n=7 MeV
^{238}U, MASLOV ET AL., 2001
ENDF/B-VI
PRESENT
1.4
1.2
1.0
0.8
0.6
R(E_o,E)
0
5
10
15
20
NEUTRON ENERGY, MeV

FIG. 60

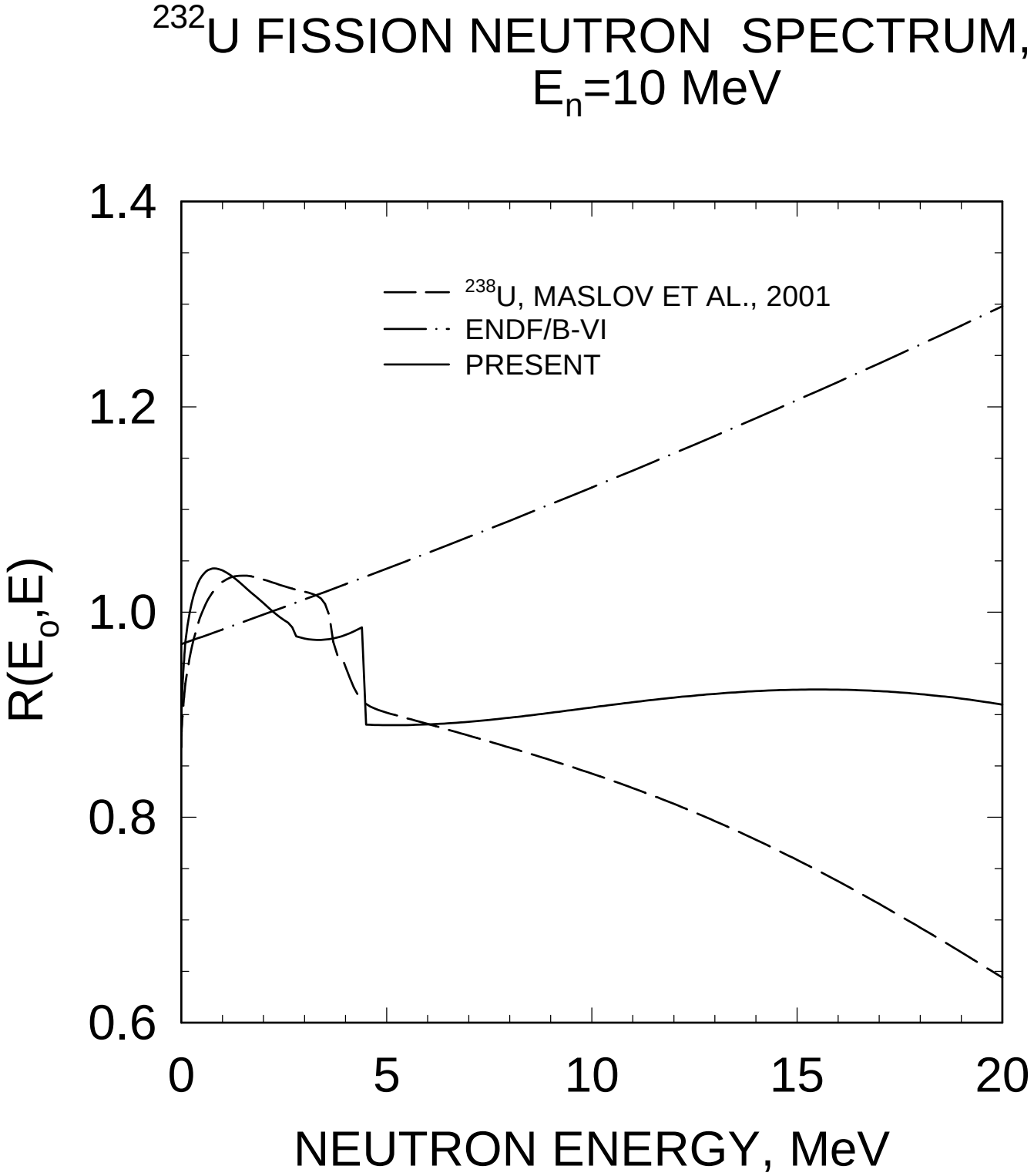
^{232}U FISSION NEUTRON SPECTRUM,
E_n=10 MeV
^{238}U, MASLOV ET AL., 2001
ENDF/B-VI
PRESENT
1.4
1.2
1.0
0.8
0.6
$R(E_o,E)$
0
5
10
15
20
NEUTRON ENERGY, MeV

FIG. 61

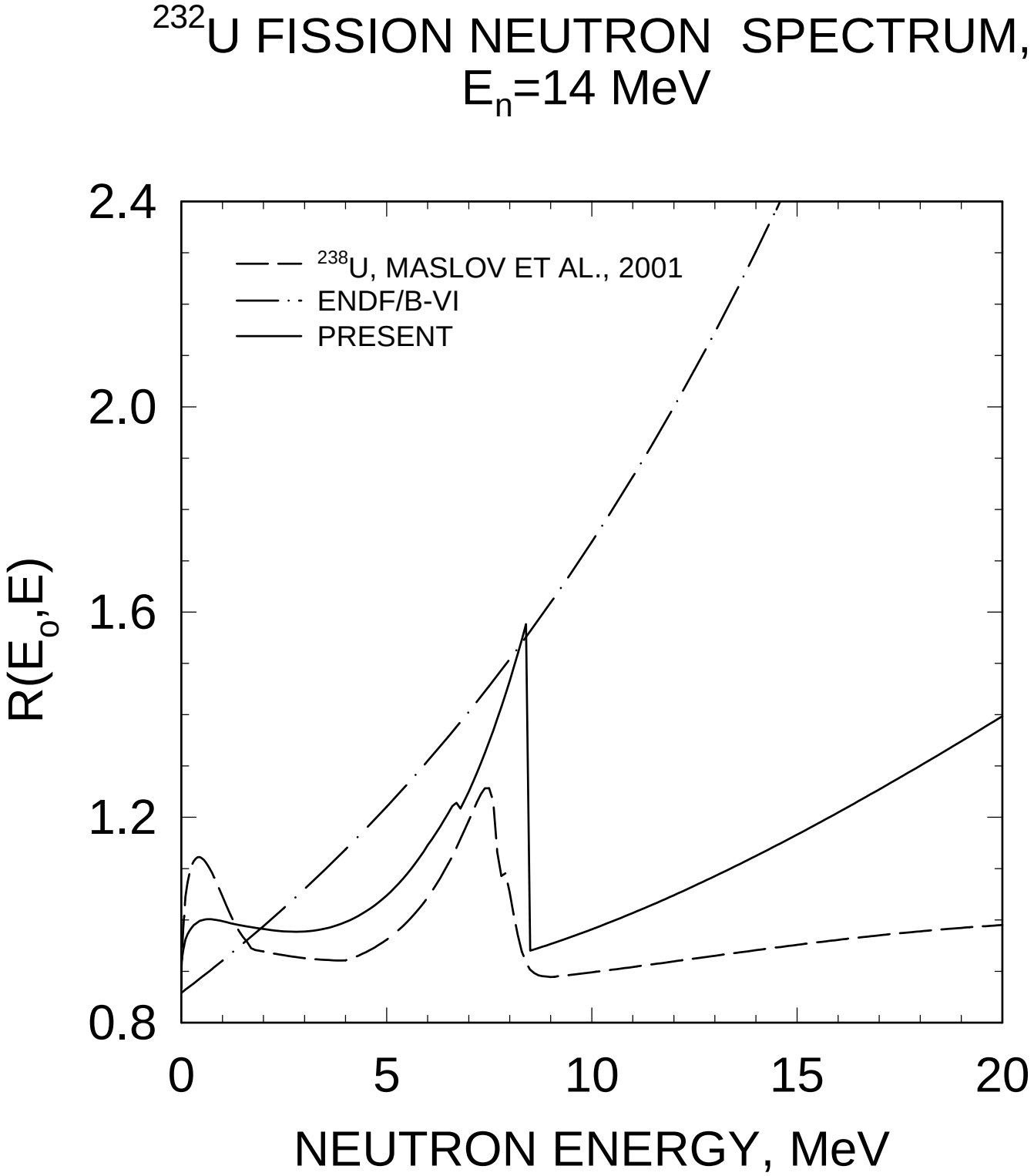
^{232}U FISSION NEUTRON SPECTRUM,
E_n=14 MeV
^{238}U, MASLOV ET AL., 2001
ENDF/B-VI
PRESENT
2.4
2.0
1.6
1.2
0.8
$R(E_o,E)$
0
5
10
15
20
NEUTRON ENERGY, MeV

FIG. 62

^{232}U FISSION NEUTRON SPECTRUM, E_n=20 MeV

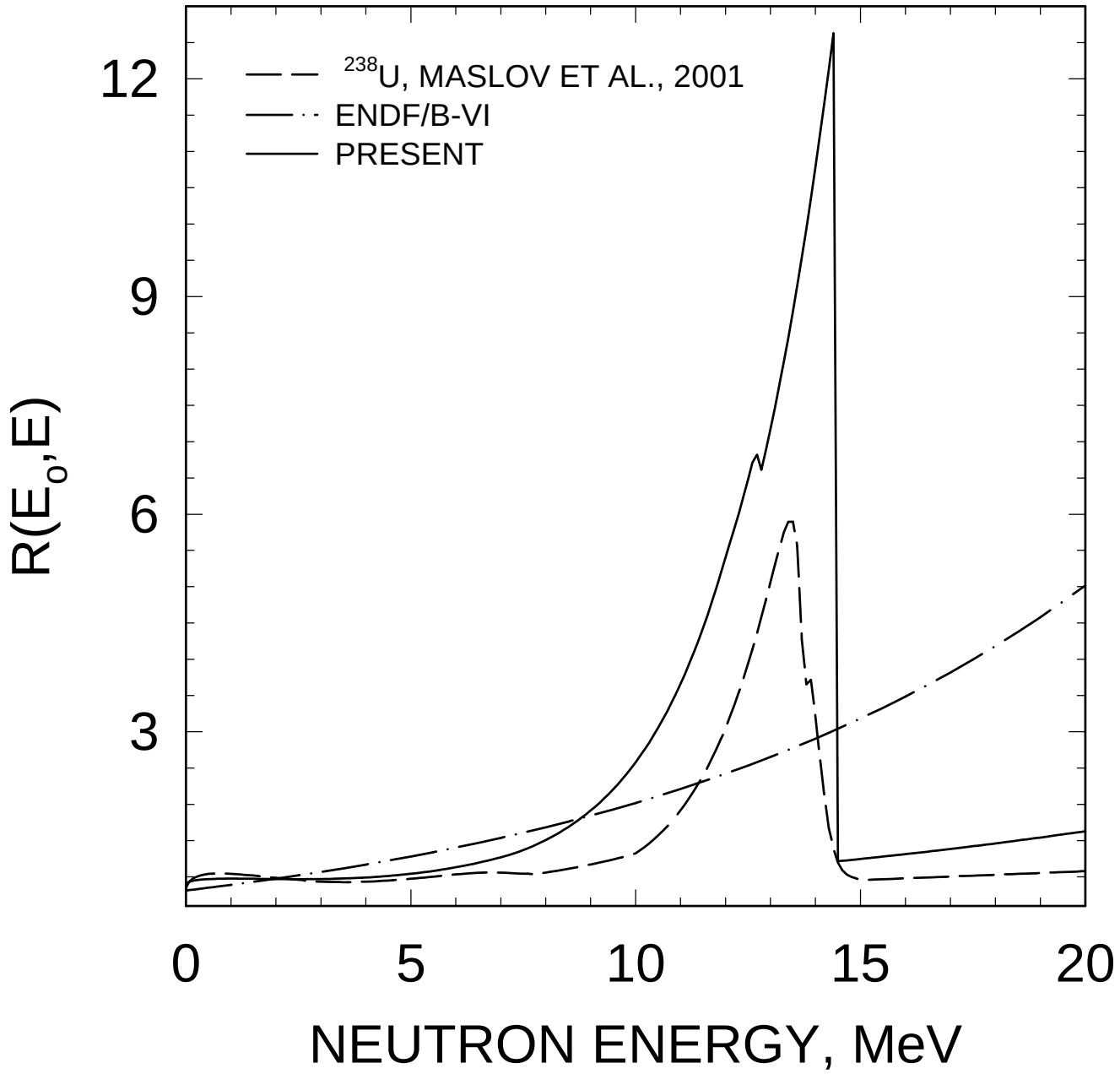

FIG. 63

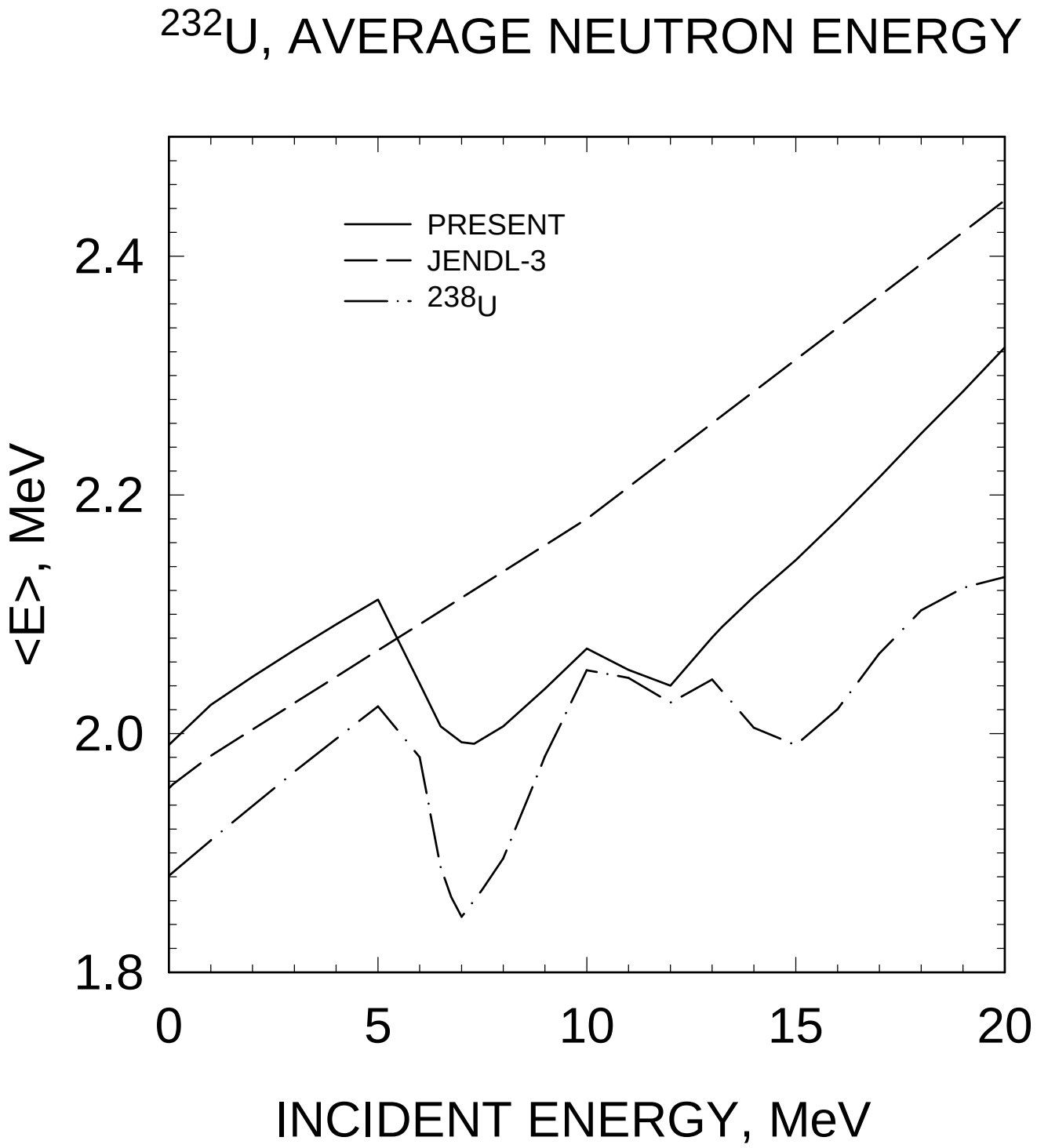
232U, AVERAGE NEUTRON ENERGY
PRESENT
JENDL-3
238U
2.4
2.2
2.0
1.8
<E>, MeV
0
5
10
15
20
INCIDENT ENERGY, MeV

FIG. 64

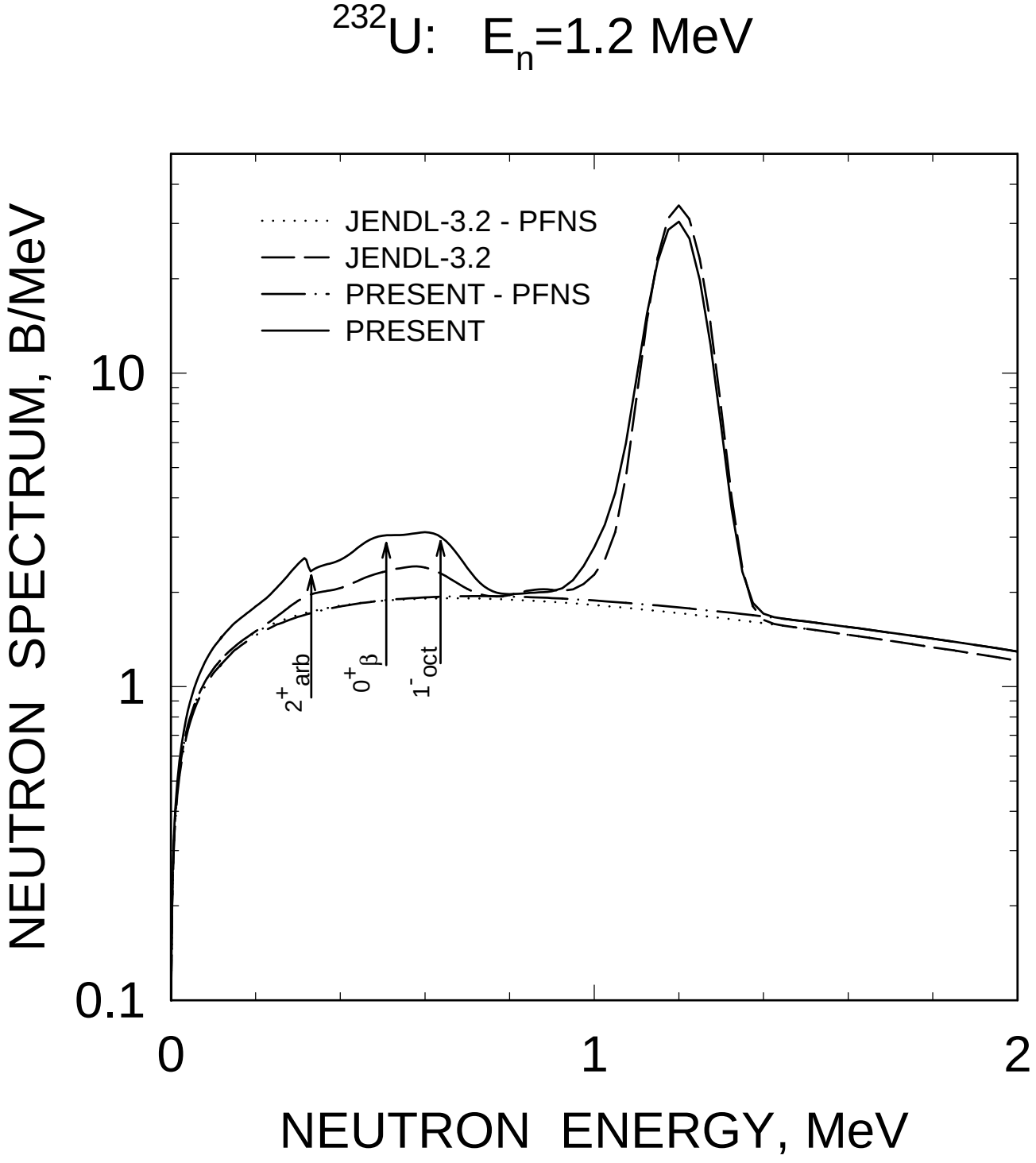
^{232}U: E_n=1.2 MeV
JENDL-3.2 - PFNS
JENDL-3.2
PRESENT - PFNS
PRESENT
2^+_{arb}
0^+_{β}
1^-_{oct}
NEUTRON SPECTRUM, B/MeV
10
1
0.1
0
1
2
NEUTRON ENERGY, MeV

FIG. 65

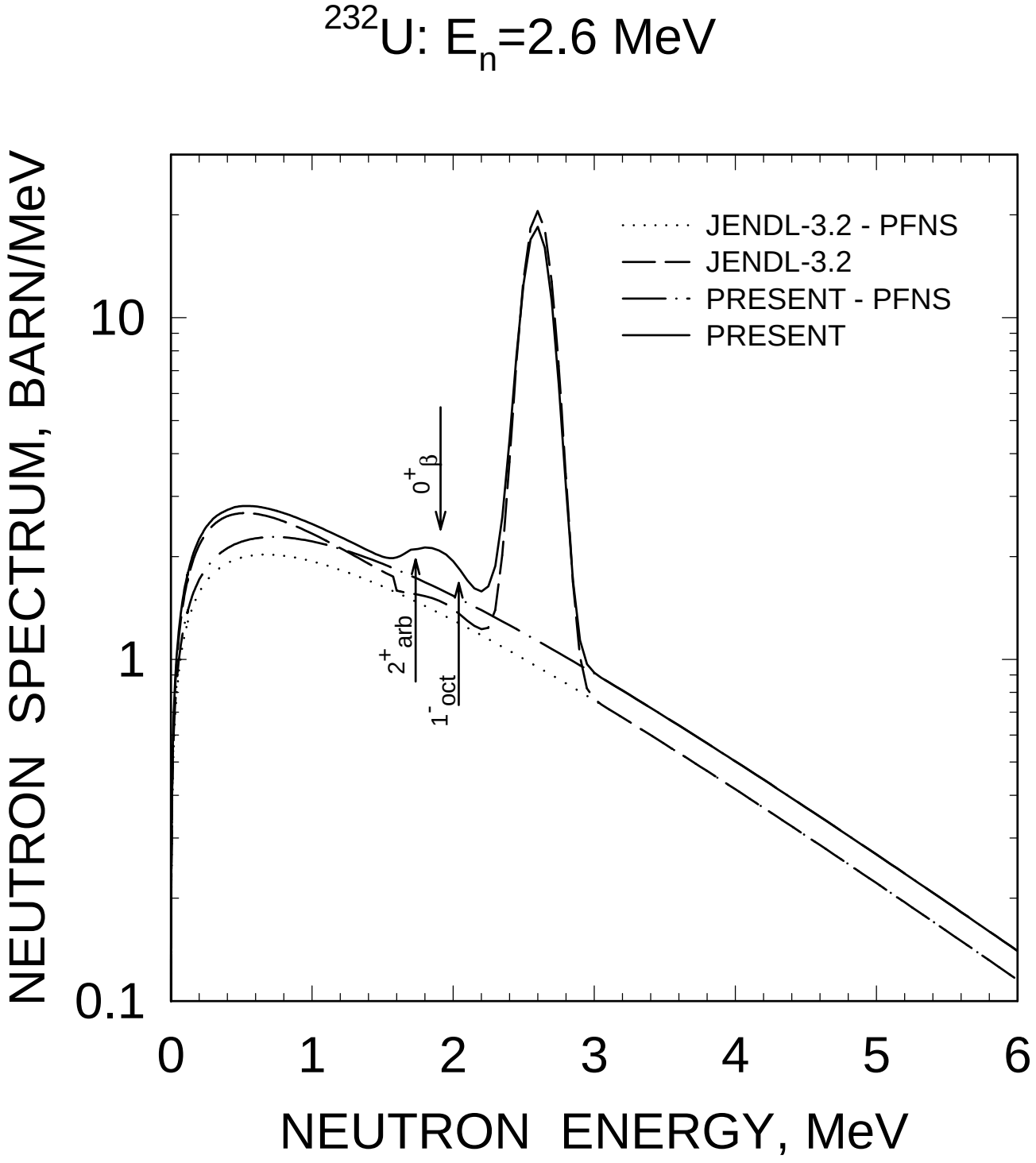
^{232}U: E_n=2.6 MeV
NEUTRON SPECTRUM, BARN/MeV
NEUTRON ENERGY, MeV
JENDL-3.2 - PFNS
JENDL-3.2
PRESENT - PFNS
PRESENT
0^+_β
2^+_{arb}
1^-_{oct}
0.1
1
10
0
1
2
3
4
5
6

FIG. 66

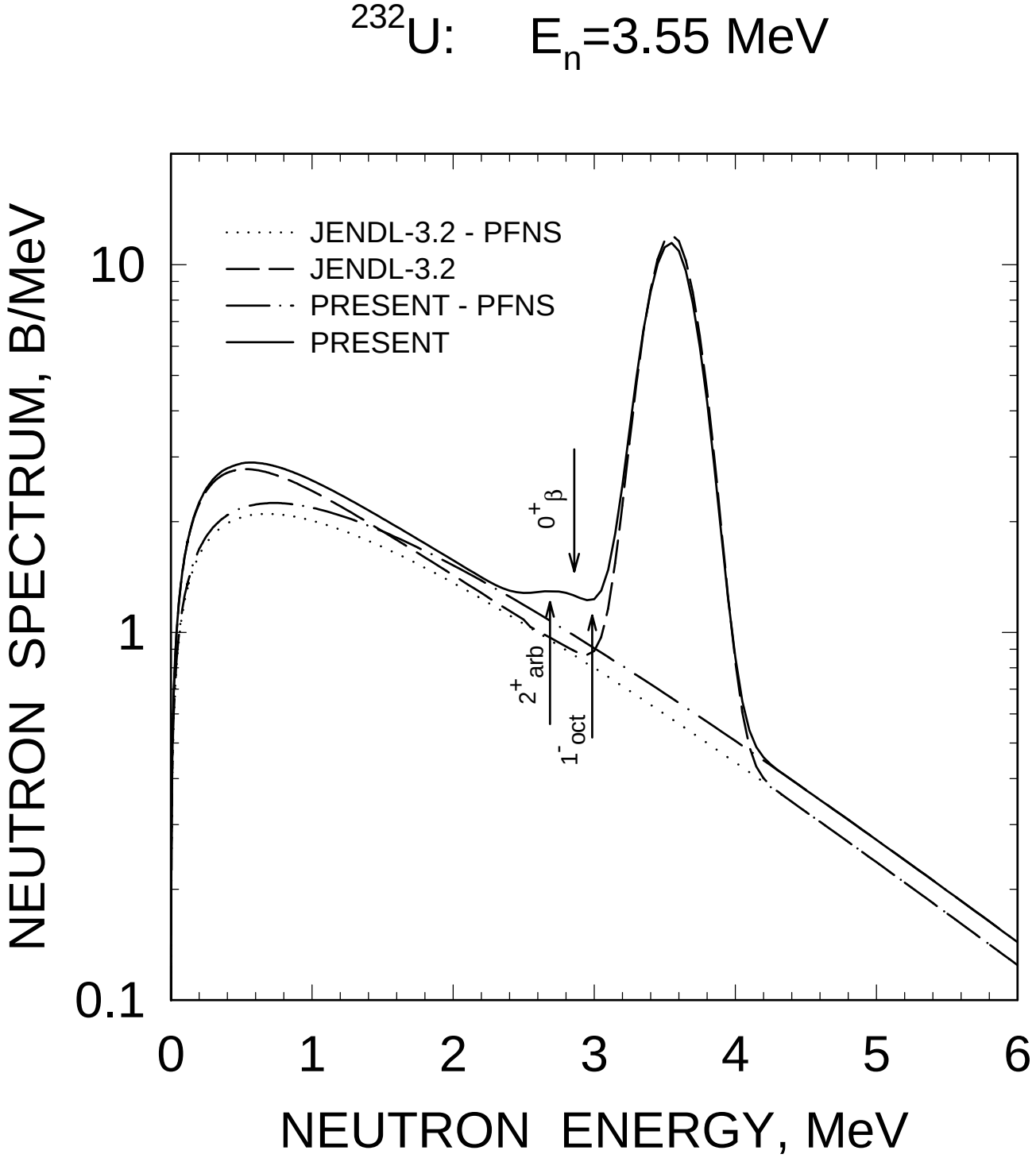
^{232}U: E_n=3.55 MeV
JENDL-3.2 - PFNS
JENDL-3.2
PRESENT - PFNS
PRESENT
0^+_β
2^+_{arb}
1^-_{oct}
NEUTRON SPECTRUM, B/MeV
10
1
0.1
0
1
2
3
4
5
6
NEUTRON ENERGY, MeV

FIG. 67

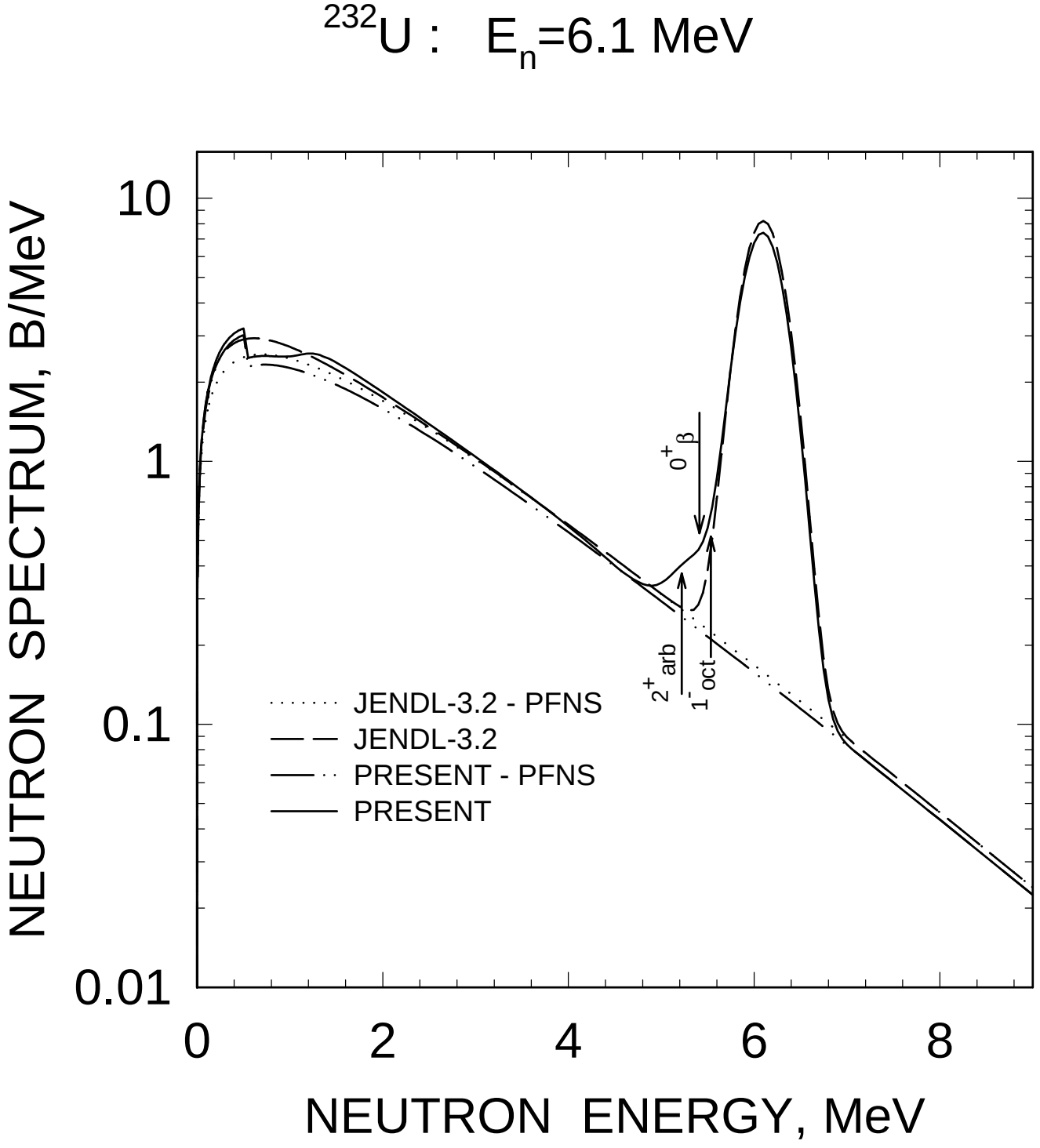
^{232}U : E_n=6.1 MeV
NEUTRON SPECTRUM, B/MeV
10
1
0.1
0.01
0
2
4
6
8
NEUTRON ENERGY, MeV
0^+_β
2^+_{arb}
1^-_{oct}
JENDL-3.2 - PFNS
JENDL-3.2
PRESENT - PFNS
PRESENT

FIG. 68

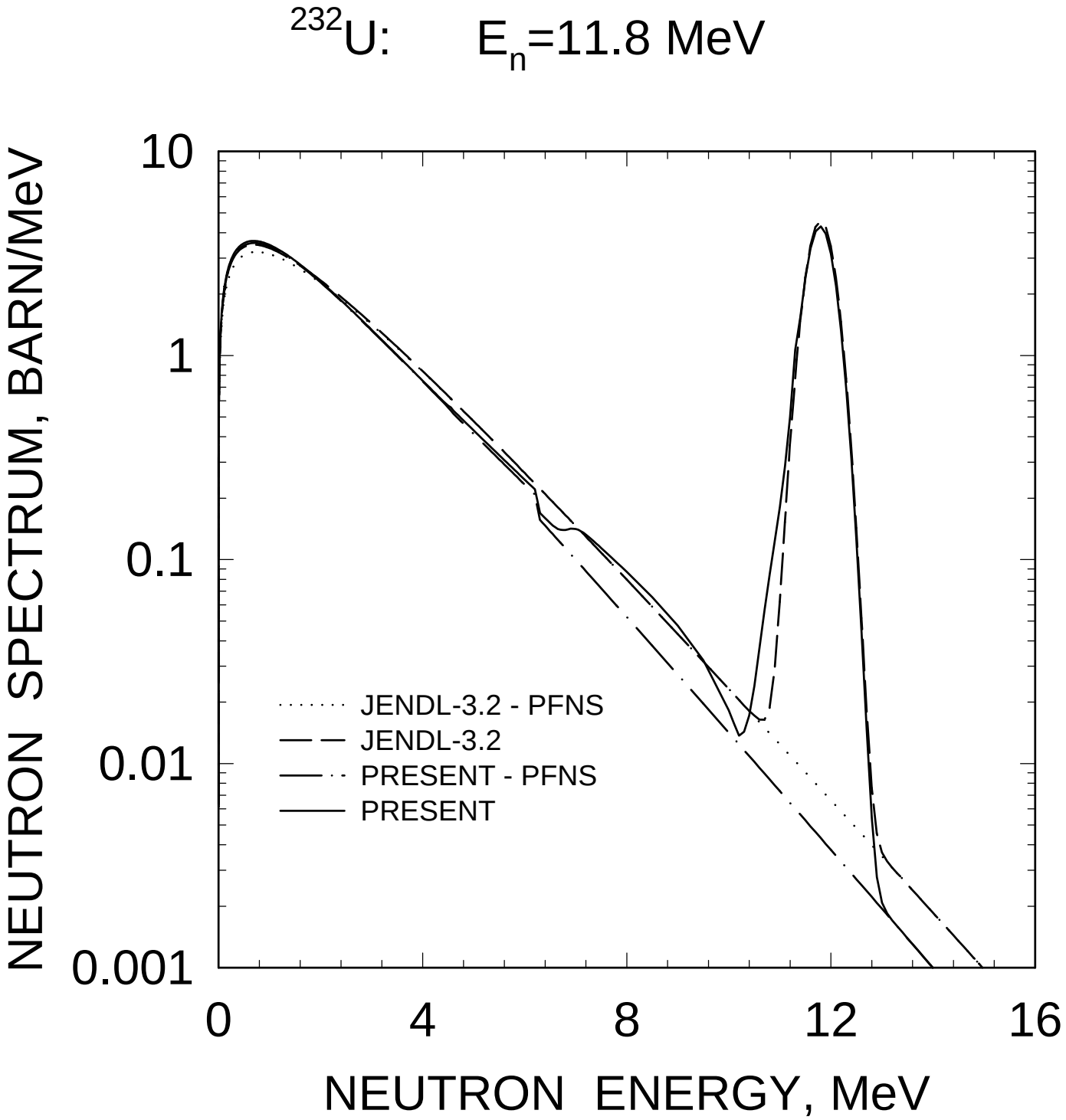
^{232}U: E_n=11.8 MeV
NEUTRON SPECTRUM, BARN/MeV
10
1
0.1
0.01
0.001
0
4
8
12
16
NEUTRON ENERGY, MeV
JENDL-3.2 - PFNS
JENDL-3.2
PRESENT - PFNS
PRESENT

FIG. 69

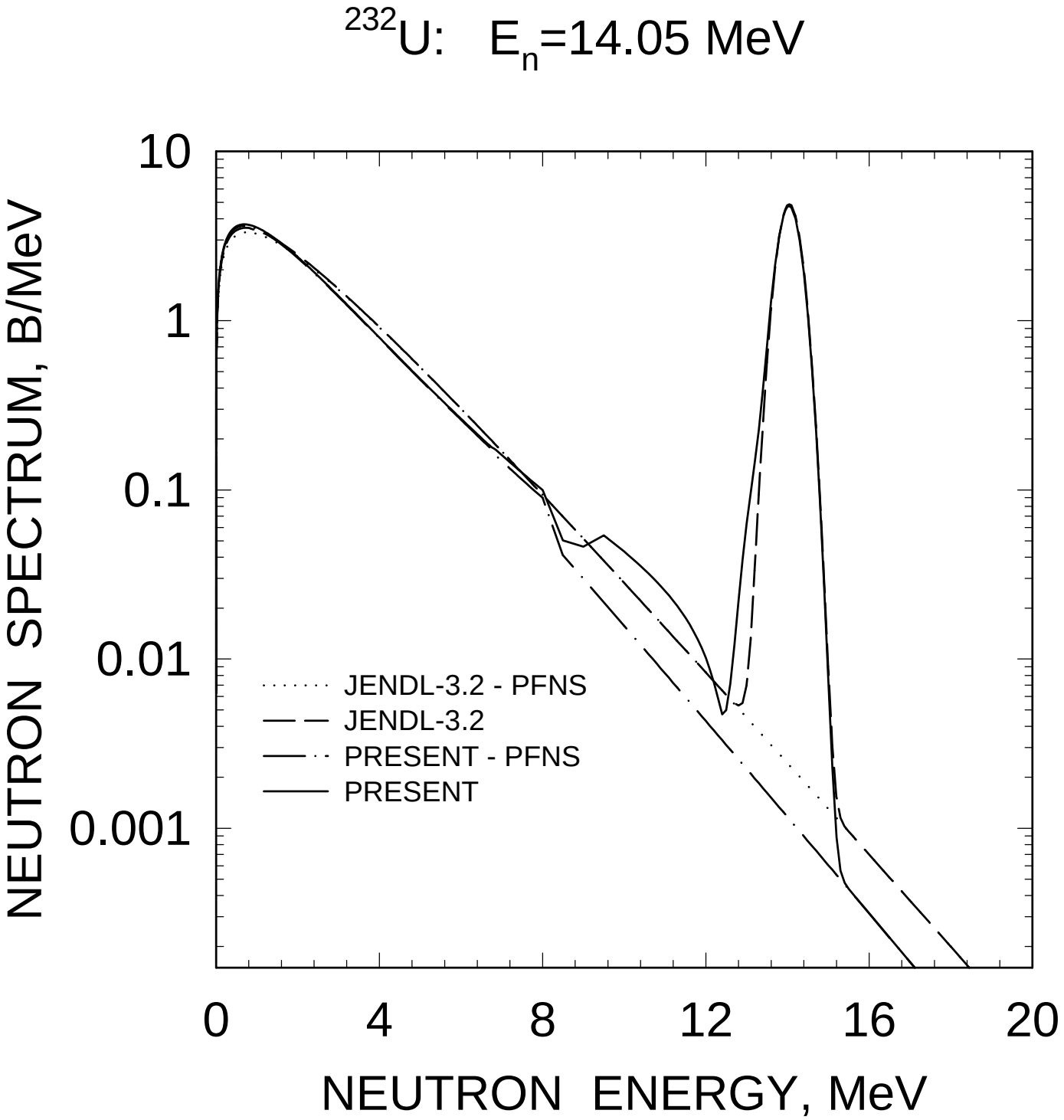
^{232}U: E_n=14.05 MeV
10
1
0.1
0.01
0.001
NEUTRON SPECTRUM, B/MeV
JENDL-3.2 - PFNS
JENDL-3.2
PRESENT - PFNS
PRESENT
0
4
8
12
16
20
NEUTRON ENERGY, MeV

FIG. 70

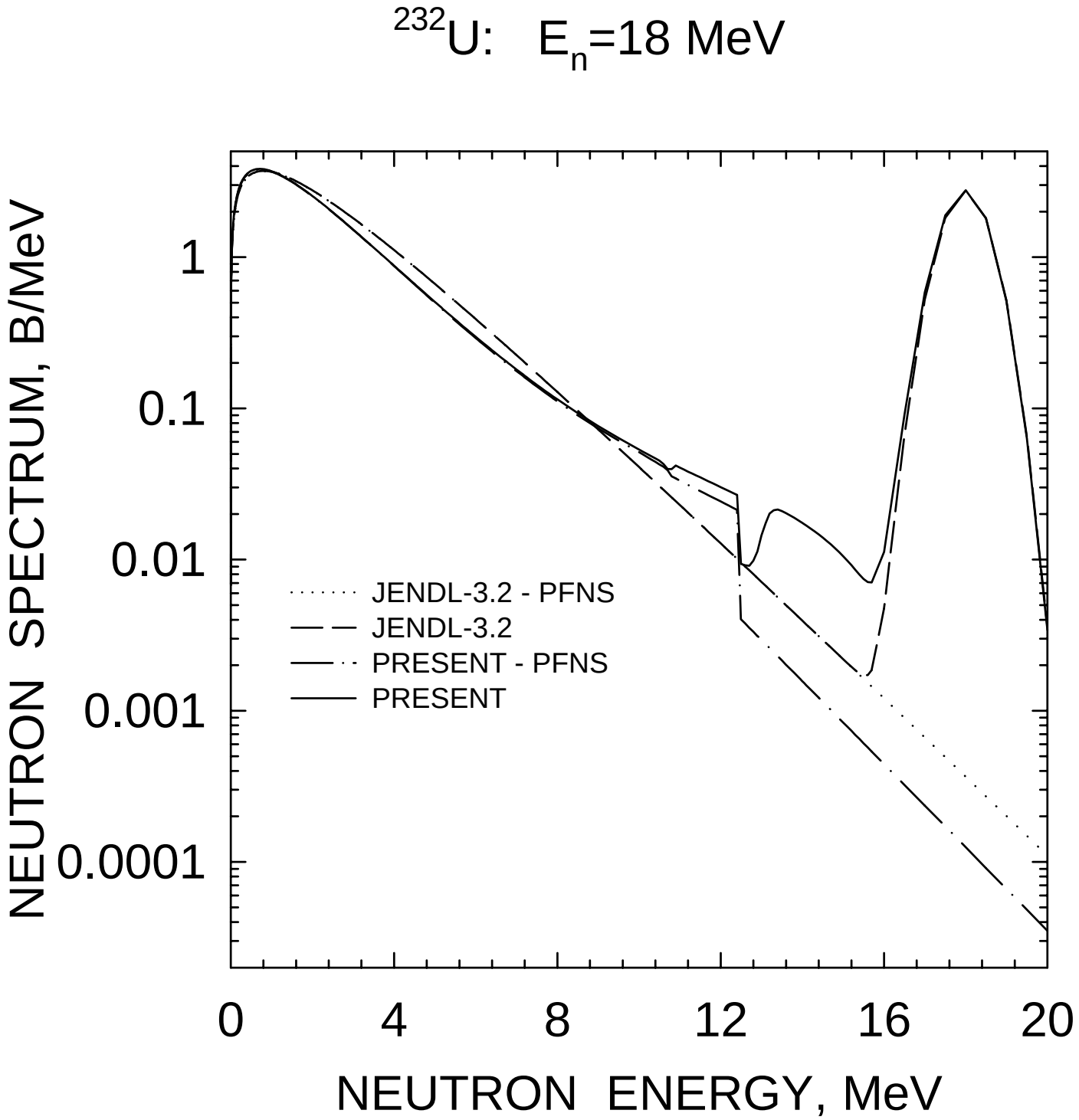
^{232}U: E_n=18 MeV
NEUTRON SPECTRUM, B/MeV
1
0.1
0.01
0.001
0.0001
0
4
8
12
16
20
NEUTRON ENERGY, MeV
JENDL-3.2 - PFNS
JENDL-3.2
PRESENT - PFNS
PRESENT

FIG. 71

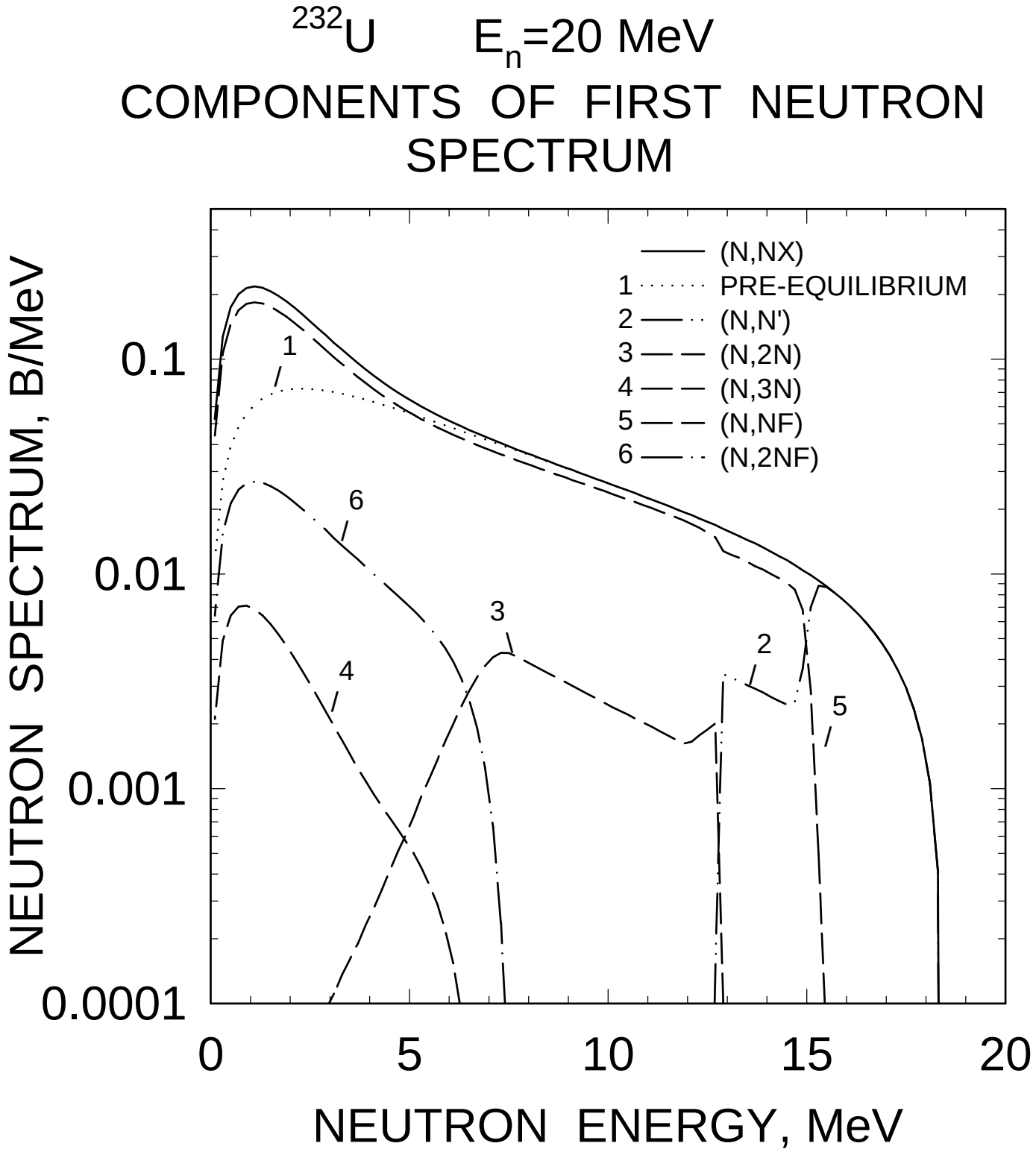
232U E_n=20 MeV
COMPONENTS OF FIRST NEUTRON SPECTRUM
(N,NX)
1 PRE-EQUILIBRIUM
2 (N,N')
3 (N,2N)
4 (N,3N)
5 (N,NF)
6 (N,2NF)
NEUTRON SPECTRUM, B/MeV
0.1
0.01
0.001
0.0001
0
5
10
15
20
NEUTRON ENERGY, MeV

FIG. 72

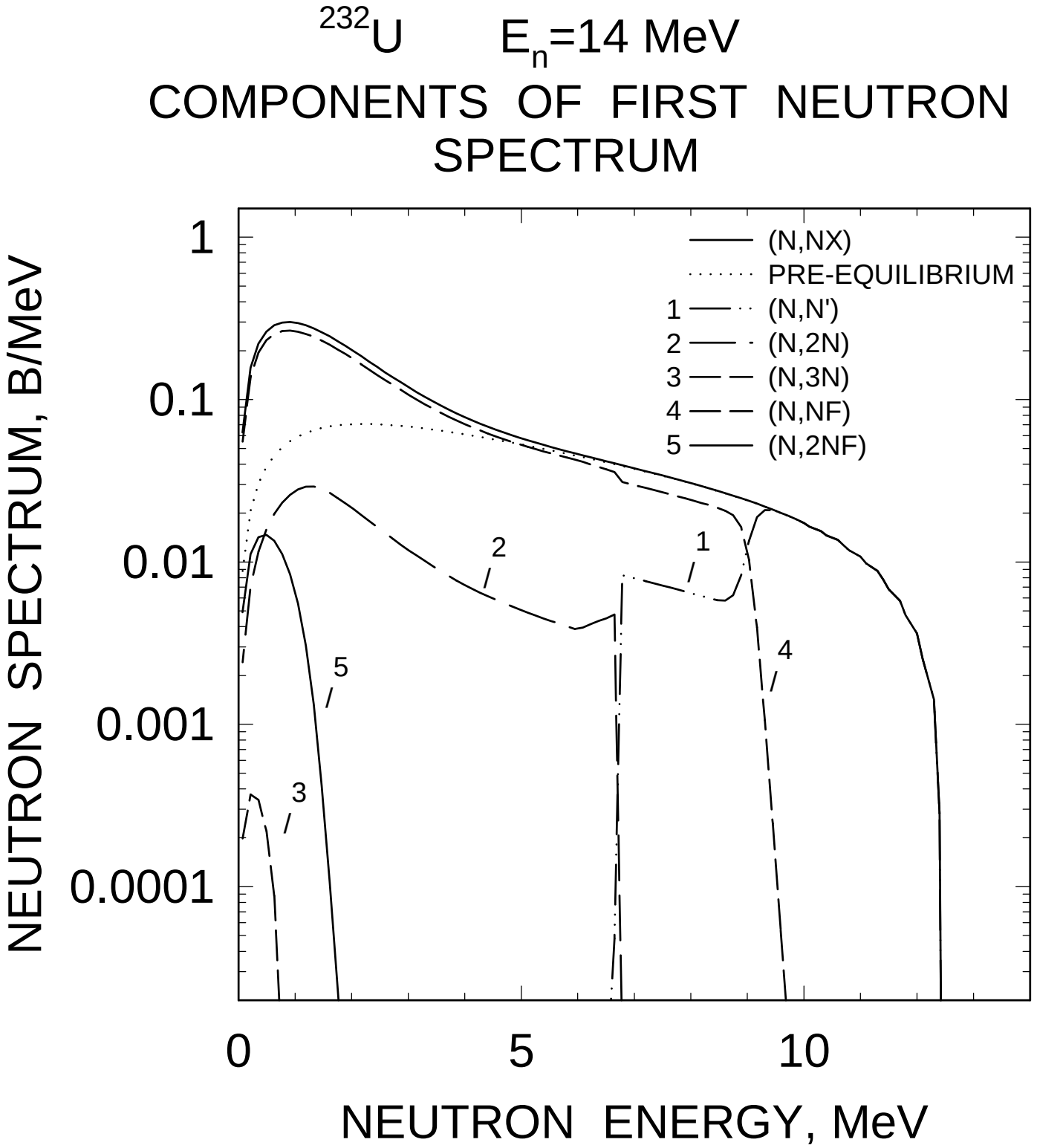
^{232}U E_n=14 MeV
COMPONENTS OF FIRST NEUTRON SPECTRUM
(N,NX)
PRE-EQUILIBRIUM
1 (N,N')
2 (N,2N)
3 (N,3N)
4 (N,NF)
5 (N,2NF)
NEUTRON SPECTRUM, B/MeV
1
0.1
0.01
0.001
0.0001
0
5
10
NEUTRON ENERGY, MeV

FIG. 73

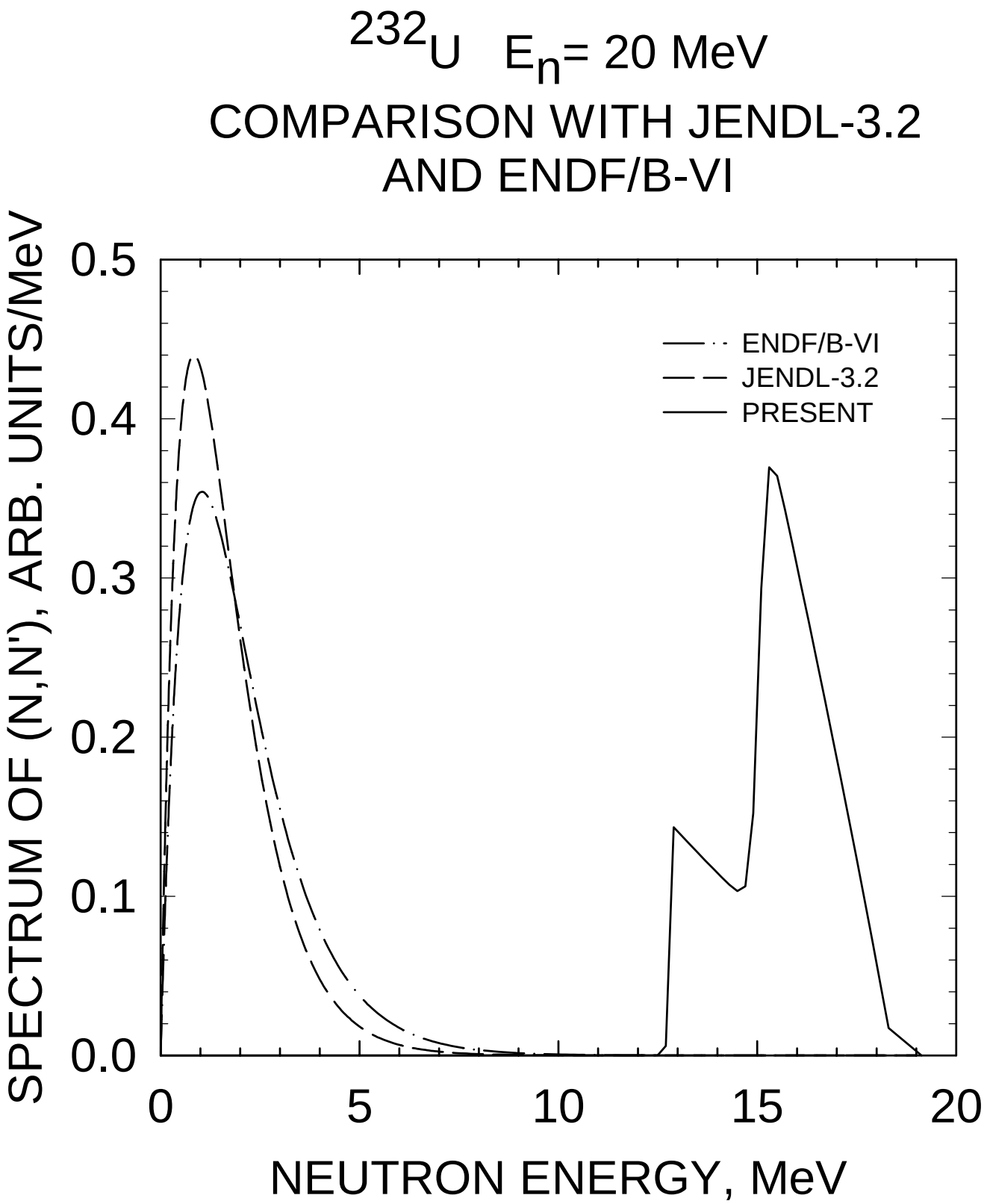
^{232}U E_n= 20 MeV
COMPARISON WITH JENDL-3.2
AND ENDF/B-VI
SPECTRUM OF (N,N'), ARB. UNITS/MeV
0.0
0.1
0.2
0.3
0.4
0.5
0
5
10
15
20
NEUTRON ENERGY, MeV
ENDF/B-VI
JENDL-3.2
PRESENT

FIG. 74

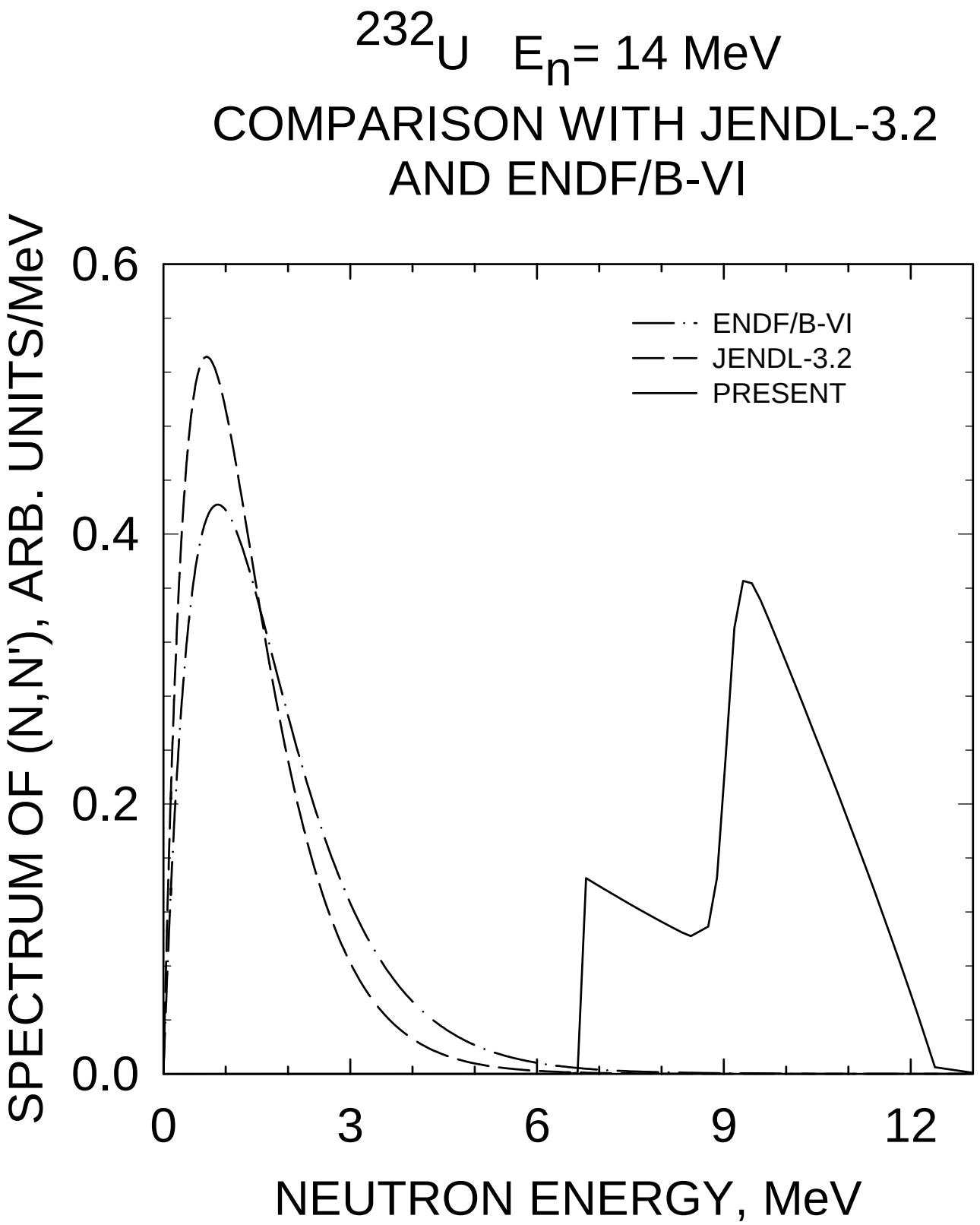
^{232}U E_n= 14 MeV
COMPARISON WITH JENDL-3.2
AND ENDF/B-VI
SPECTRUM OF (N,N'), ARB. UNITS/MeV
0.6
0.4
0.2
0.0
0
3
6
9
12
NEUTRON ENERGY, MeV
ENDF/B-VI
JENDL-3.2
PRESENT

FIG. 75

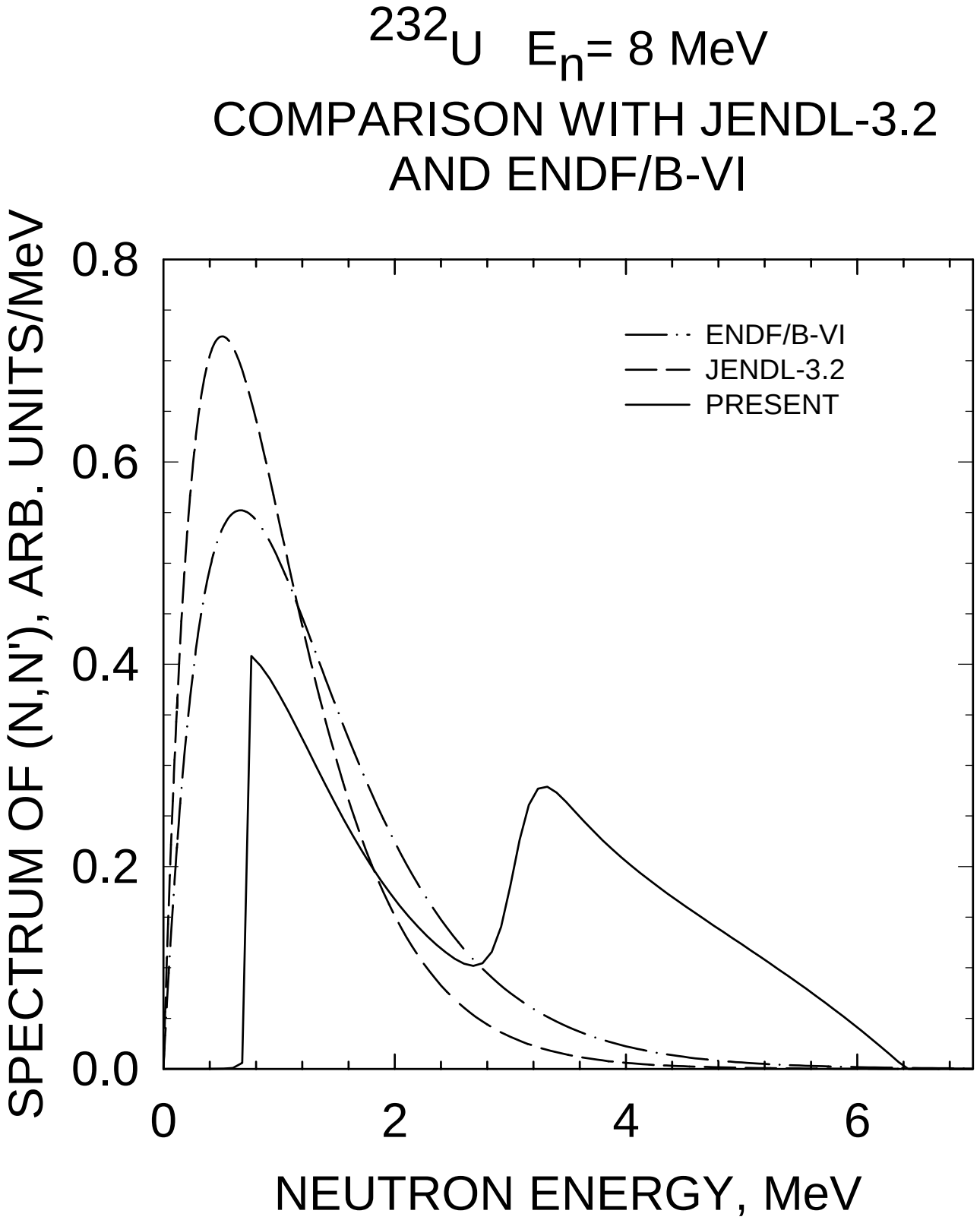
^{232}U E_n= 8 MeV
COMPARISON WITH JENDL-3.2
AND ENDF/B-VI
SPECTRUM OF (N,N'), ARB. UNITS/MeV
0.8
0.6
0.4
0.2
0.0
0
2
4
6
NEUTRON ENERGY, MeV
ENDF/B-VI
JENDL-3.2
PRESENT

FIG. 76

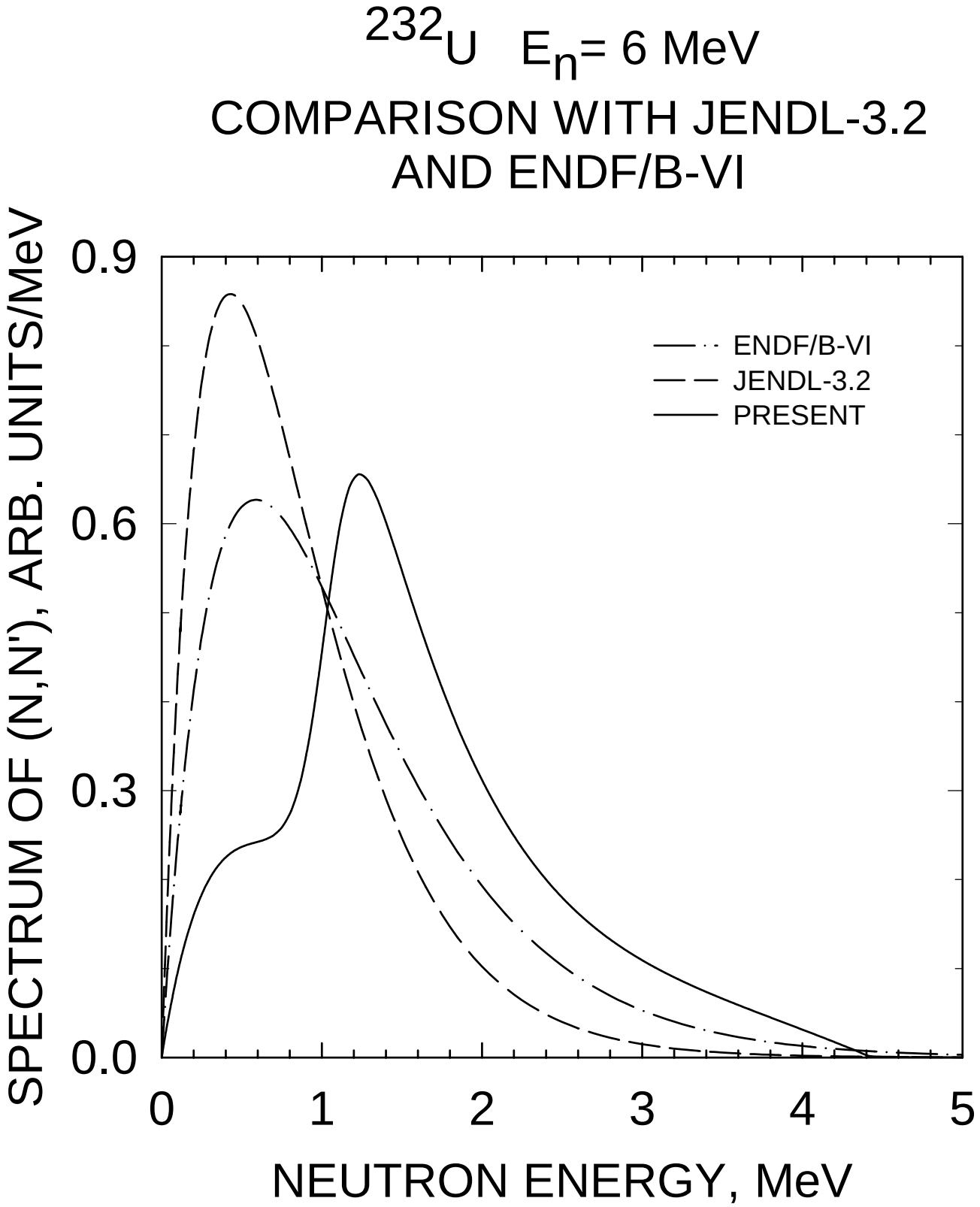
^{232}U E_n= 6 MeV
COMPARISON WITH JENDL-3.2
AND ENDF/B-VI
SPECTRUM OF (N,N'), ARB. UNITS/MeV
0.9
0.6
0.3
0.0
0
1
2
3
4
5
NEUTRON ENERGY, MeV
ENDF/B-VI
JENDL-3.2
PRESENT

FIG. 77

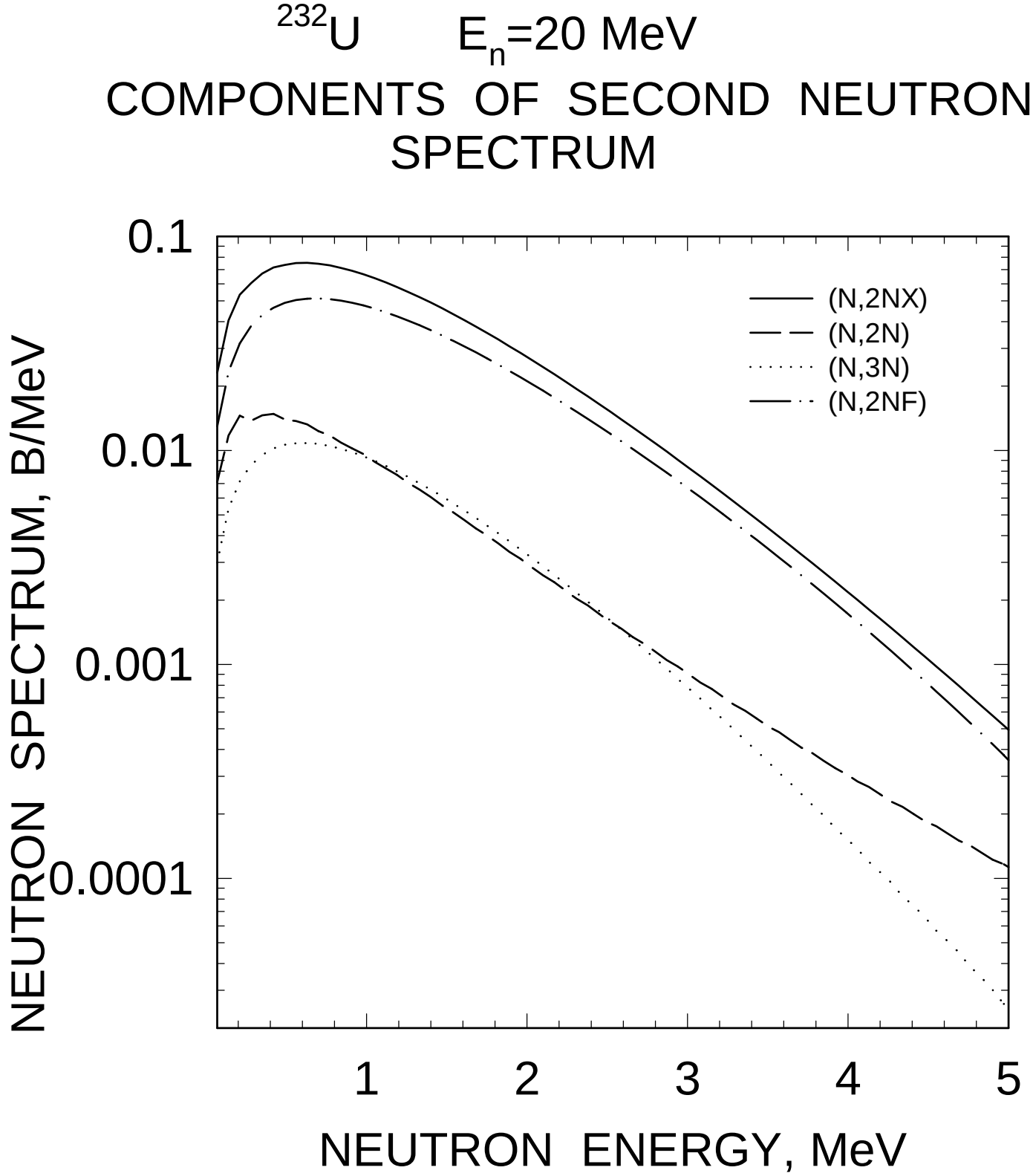
^{232}U E_n=20 MeV
COMPONENTS OF SECOND NEUTRON SPECTRUM
0.1
0.01
0.001
0.0001
NEUTRON SPECTRUM, B/MeV
(N,2NX)
(N,2N)
(N,3N)
(N,2NF)
1
2
3
4
5
NEUTRON ENERGY, MeV

FIG. 78

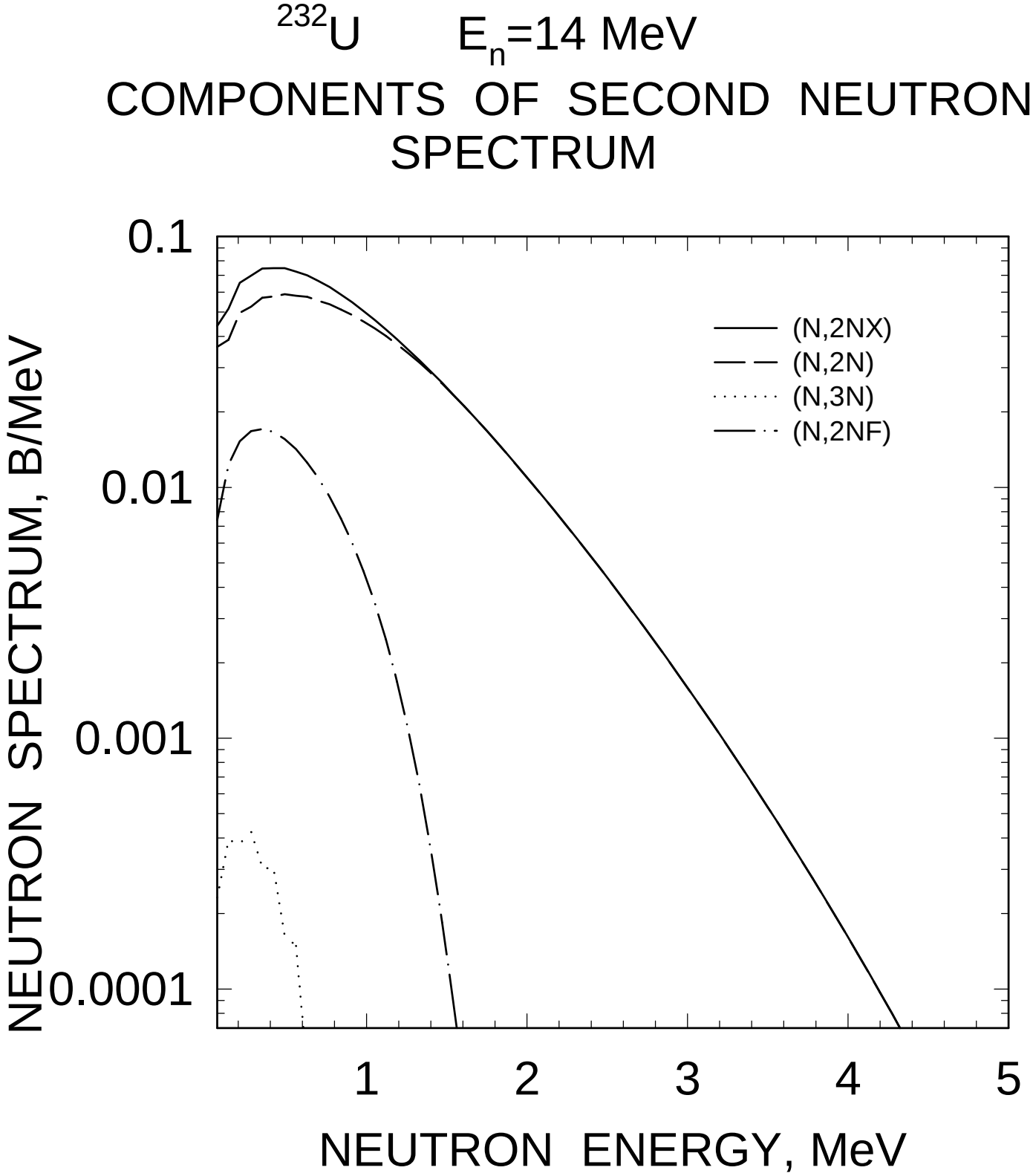
^{232}U E_n=14 MeV
COMPONENTS OF SECOND NEUTRON SPECTRUM
0.1
0.01
0.001
0.0001
NEUTRON SPECTRUM, B/MeV
(N,2NX)
(N,2N)
(N,3N)
(N,2NF)
1
2
3
4
5
NEUTRON ENERGY, MeV

FIG. 79

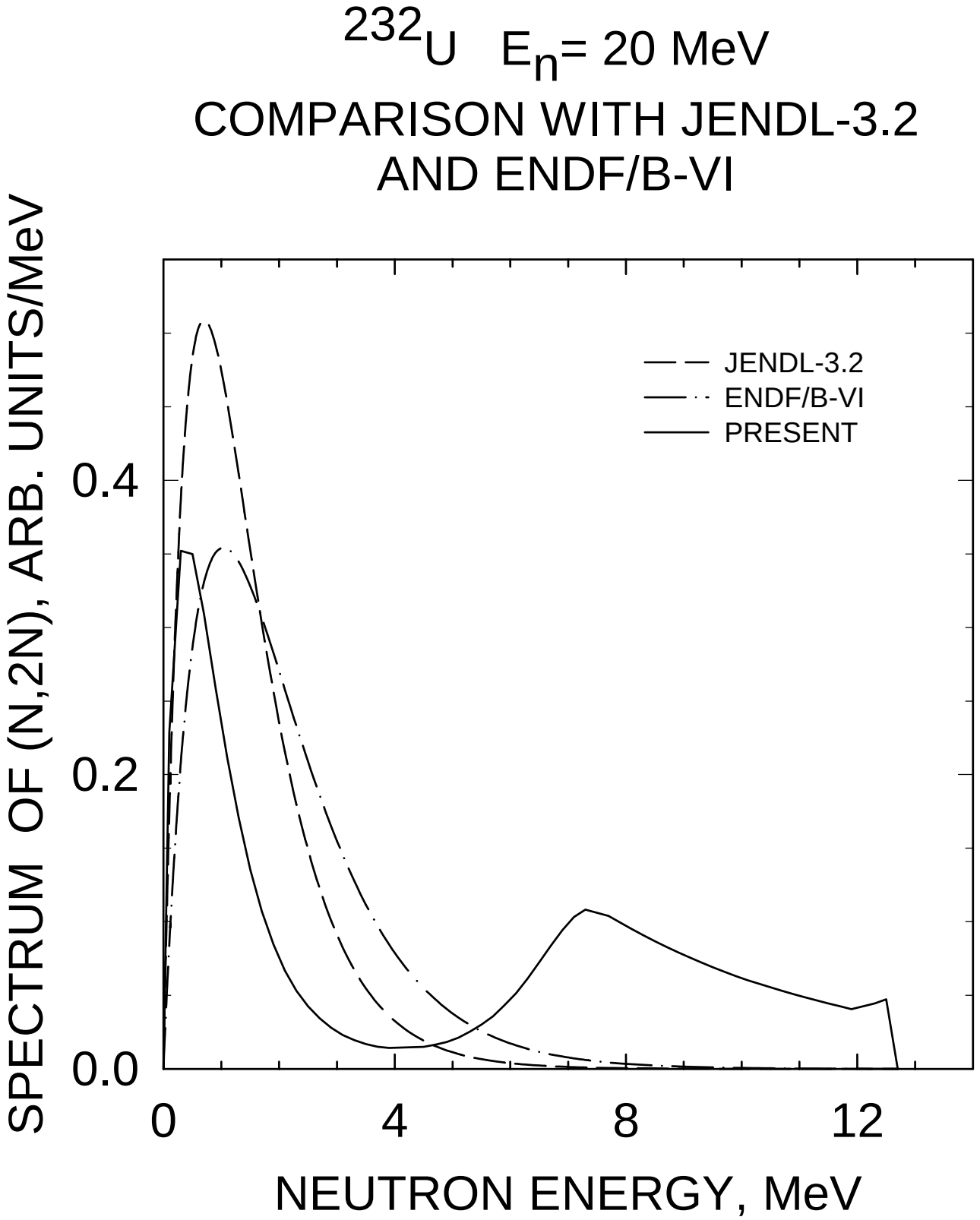
^{232}U E_n= 20 MeV
COMPARISON WITH JENDL-3.2
AND ENDF/B-VI
JENDL-3.2
ENDF/B-VI
PRESENT
SPECTRUM OF (N,2N), ARB. UNITS/MeV
0.0
0.2
0.4
0
4
8
12
NEUTRON ENERGY, MeV

FIG. 80

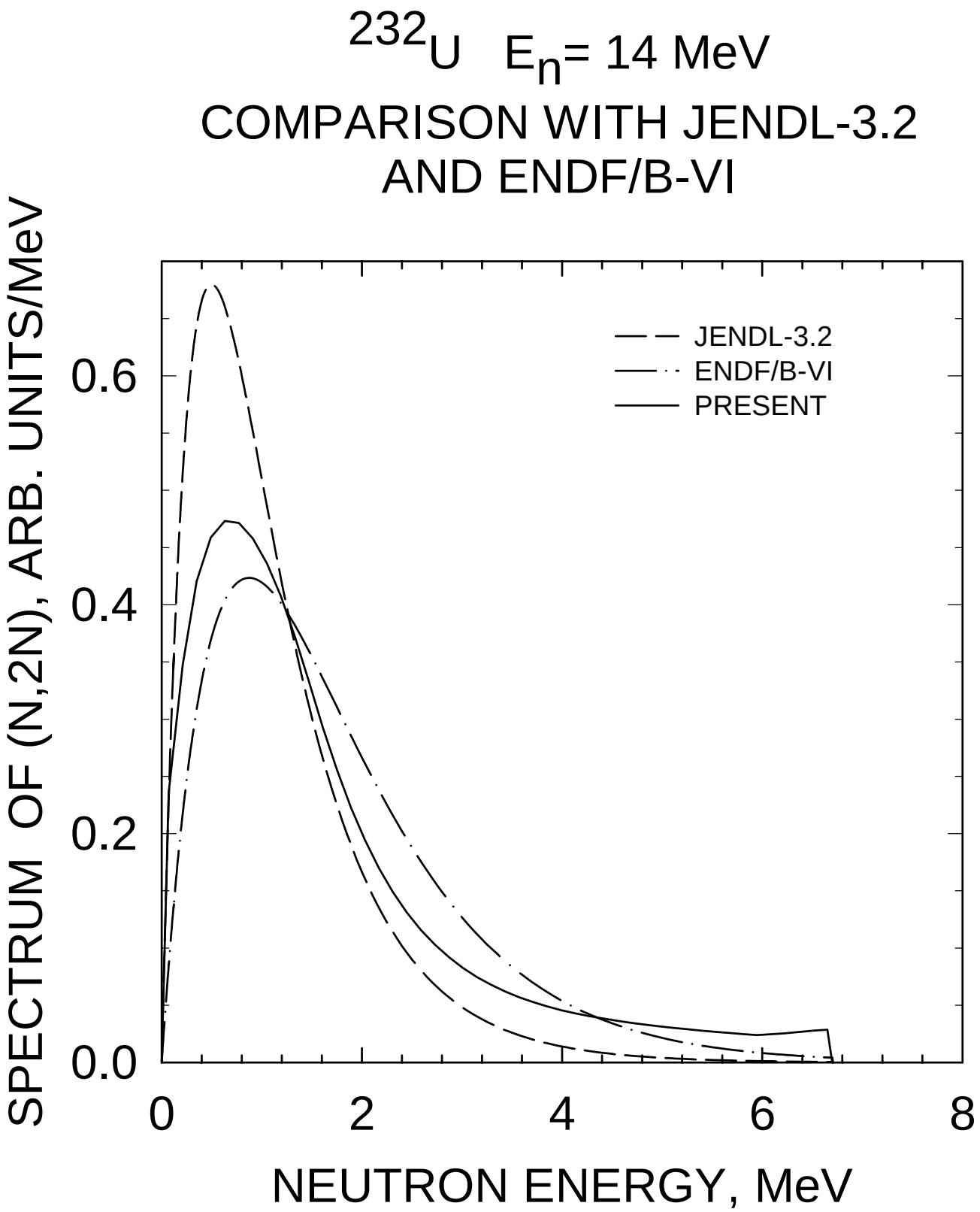
^{232}U E_n= 14 MeV
COMPARISON WITH JENDL-3.2
AND ENDF/B-VI
JENDL-3.2
ENDF/B-VI
PRESENT
SPECTRUM OF (N,2N), ARB. UNITS/MeV
0.0
0.2
0.4
0.6
0
2
4
6
8
NEUTRON ENERGY, MeV

FIG. 81

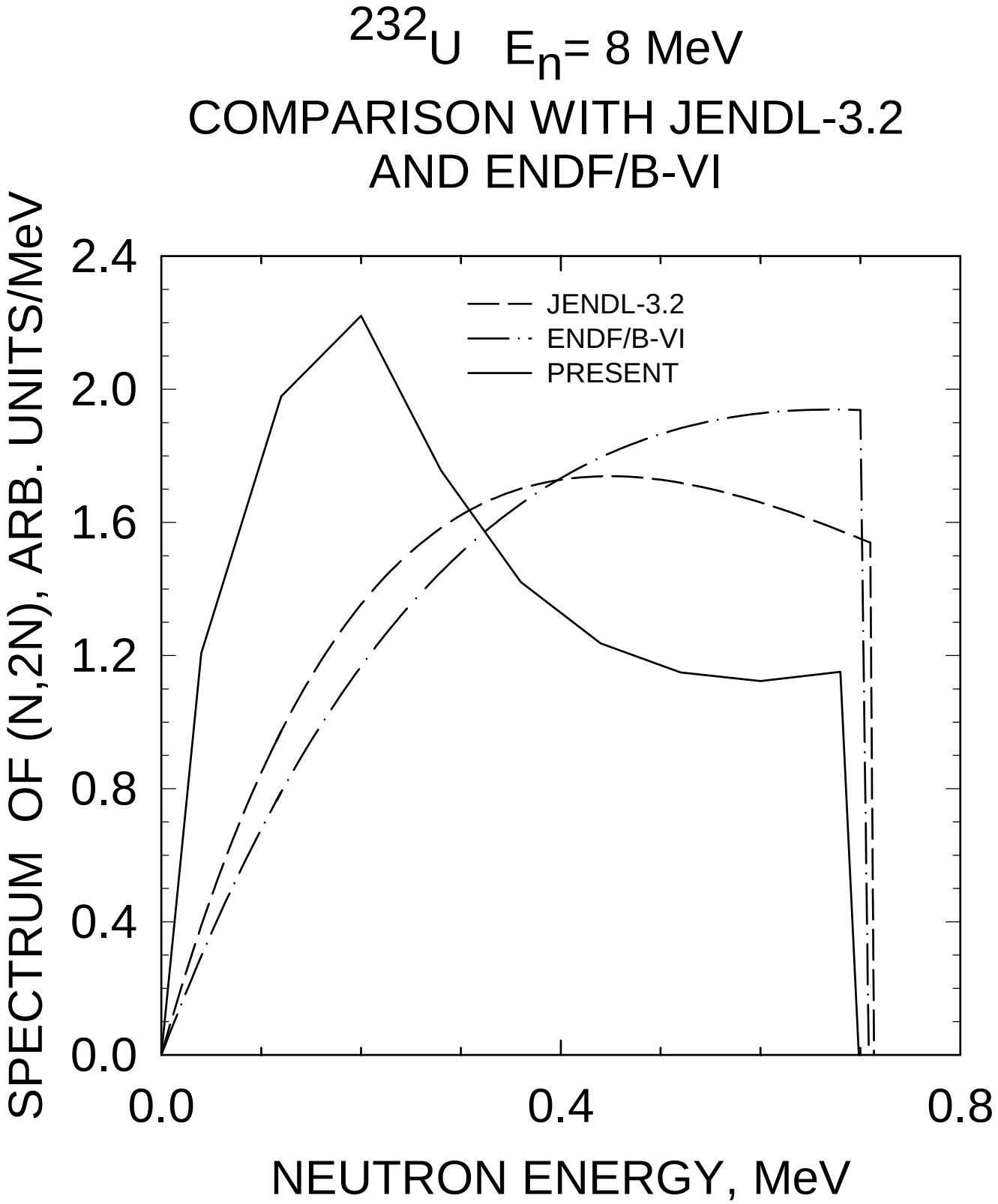
^{232}U E_n= 8 MeV
COMPARISON WITH JENDL-3.2
AND ENDF/B-VI
SPECTRUM OF (N,2N), ARB. UNITS/MeV
2.4
2.0
1.6
1.2
0.8
0.4
0.0
JENDL-3.2
ENDF/B-VI
PRESENT
0.0
0.4
0.8
NEUTRON ENERGY, MeV

FIG. 82

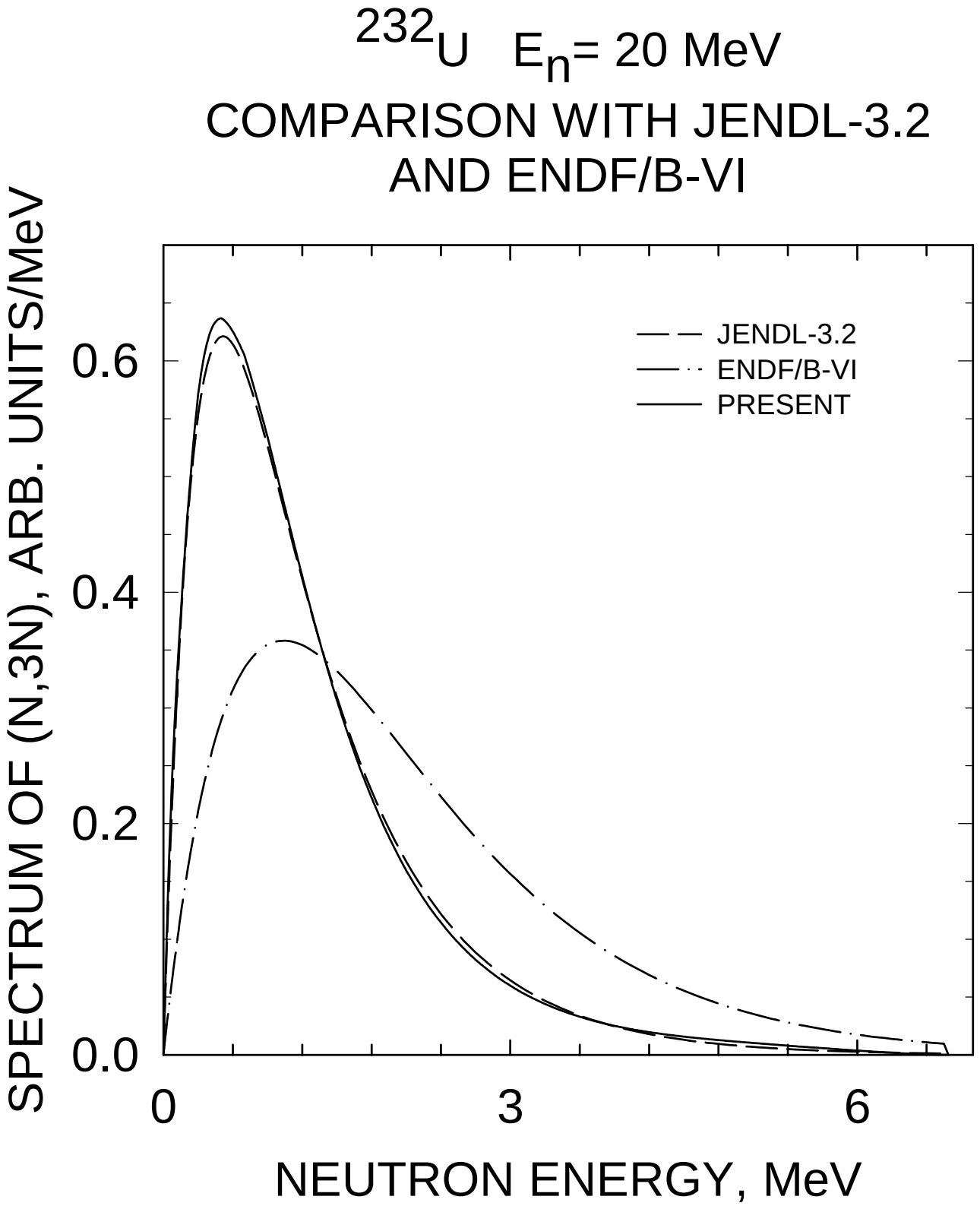
^{232}U E_n= 20 MeV
COMPARISON WITH JENDL-3.2
AND ENDF/B-VI
SPECTRUM OF (N,3N), ARB. UNITS/MeV
0.0
0.2
0.4
0.6
0
3
6
NEUTRON ENERGY, MeV
JENDL-3.2
ENDF/B-VI
PRESENT

FIG. 83

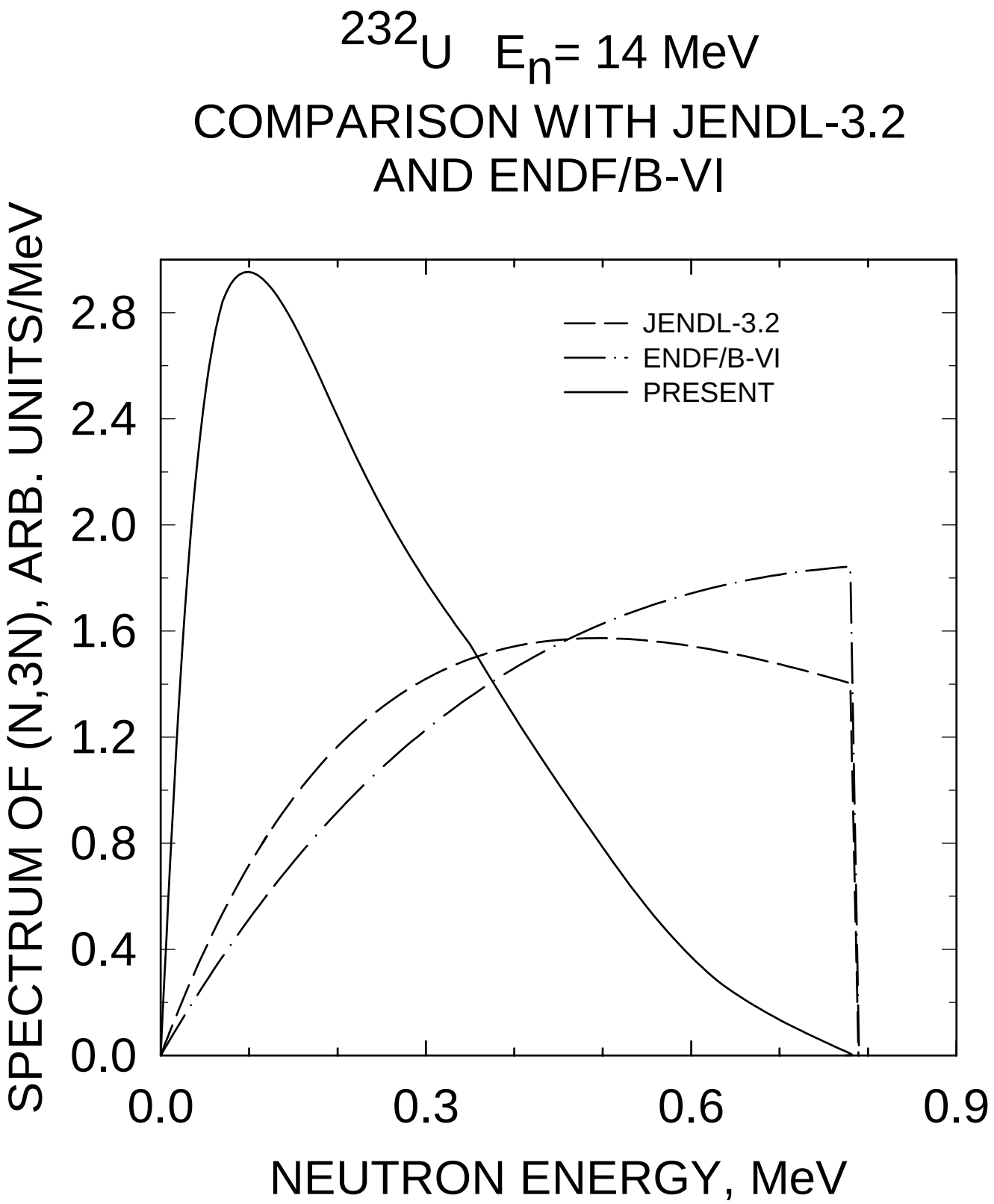
^{232}U E_n= 14 MeV
COMPARISON WITH JENDL-3.2
AND ENDF/B-VI
SPECTRUM OF (N,3N), ARB. UNITS/MeV
2.8
2.4
2.0
1.6
1.2
0.8
0.4
0.0
0.0
0.3
0.6
0.9
NEUTRON ENERGY, MeV
JENDL-3.2
ENDF/B-VI
PRESENT

FIG. 84

Nuclear Data Section
International Atomic Energy Agency
P.O. Box 100
A-1400 Vienna
Austria

e-mail: services@iaeand.iaea.org
fax: (43-1) 26007
cable: INATOM VIENNA
telex: 1-12645
telephone: (43-1) 2600-21710

Online: TELNET or FTP: iaeand.iaea.org
username: IAEANDS for interactive Nuclear Data Information System
usernames: ANONYMOUS for FTP file transfer;
FENDL2 for FTP file transfer of FENDL-2.0;
RIPL for FTP file transfer of RIPL;
NDSONL for FTP access to files saved in “NDIS” Telnet session.
Web: http://www-nds.iaea.org